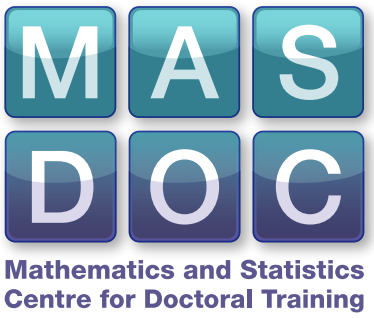

A Discontinuous Galerkin Finite Element Method for Quasi-Geostrophic Frontogenesis

by

Jorge Vicente Malik Lindley

Thesis

Submitted for the degree of

Doctor of Philosophy

Mathematics Institute

The University of Warwick

August 2017

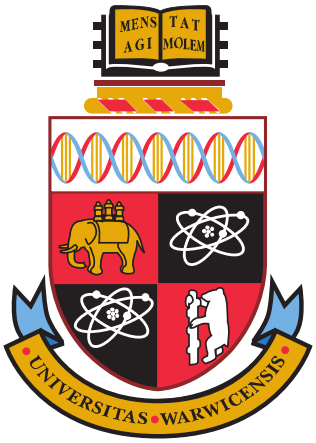

Contents

List of Tables

List of Figures

Acknowledgments

This work is supported by the UK Engineering and Physical Sciences Research Council (EPSRC) as part of the MASDOC Doctoral Training Centre at the University of Warwick. Grant No. EP/HO23364/1. High performance computing facilities provided by the Centre for Scientific Computing at the University of Warwick.

I would like to thank my family, especially my wife Indigo, for their support during my work. Many thanks to Robert Kerr and Andreas Dedner for supervising this project. Thanks also goes out to the staff and students of MASDOC at the University of Warwick for their support during my postgraduate research, and everyone in the archery club for making my time here very enjoyable.

Declarations

This thesis is submitted to the University of Warwick in support of my application for the degree of Doctor of Philosophy. It has been composed by myself and has not been submitted in any previous application for any degree. The work presented in this thesis was carried out by the author unless otherwise stated.

Chapters 1, 2 and 3 and Appendix A include a literature review and background material adapted from literature. Chapters 4, 5 and 6 and Appendix B contain original work with Robert Kerr and Andreas Dedner.

Abstract

In this thesis, a mixed continuous and discontinuous Galerkin finite element method is developed for the three-dimensional quasi-geostrophic equations, and is used to investigate the role that weather front formation plays in the transfer of energy to small scales that would produce a $k^{-5/3}$ energy spectrum as observed in the atmosphere. The quasi-geostrophic equations are used for computational efficiency and are found to be sufficient for producing simple fronts. Discontinuous Galerkin finite elements are used for the potential vorticity as continuous Galerkin methods perform poorly with advection dominated problems. The less dynamical vertical direction is discretised with finite differences to simplify the finite element method in the horizontal. Streamfunction boundary values are derived for free-slip boundary conditions in the three-dimensional model. The scheme is verified with numerical tests and is shown to converge at optimal rates until free-slip boundaries are introduced. Conservation of energy and enstrophy are shown numerically. Using the numerical method, a channel model simulation suggests that the bend up of fronts produced by a meandering zonal jet could be a viable mechanism for producing a $k^{-5/3}$ regime.

Abbreviations

DG Discontinuous Galerkin

EOC Experimental Order of Convergence

FEM Finite Element Method

GCM Global Circulation Model

KE Kinetic Energy

PDE Partial Differential Equation

PE Potential Energy

QG Quasi-Geostrophic

QGE Quasi-Geostrophic Equations

Nomenclature

Δ	Laplacian operator.
Δz	Vertical layer spacing.
Γ_{SW}	Side wall boundaries.
Γ_{TB}	Top and bottom boundaries.
Γ_B	Bottom boundary.
Γ_N	North boundary.
Γ_S	South boundary.
Γ_T	Top boundary.
Γ_h	Union of the edges of the elements in tessellation.
Θ	Zero-boundary value temperature.
β	Coriolis frequency gradient.
β_e	Penalty parameter.
γ	Coefficient of thermal expansion.
∇	Gradient operator.
ν	Viscosity.
ω	Relative vorticity.
ω_d	Dispersion relation.
∂_x	Partial derivative with respect to x.
∂_y	Partial derivative with respect to y.
∂_z	Partial derivative with respect to z.
φ	Latitude.
φ_0	Reference latitude.
ψ	Streamfunction.
Ψ	Streamfunction component with zero Dirichlet boundary condition.
ψ_N	North boundary streamfunction component.
ψ_S	South boundary streamfunction component.

ρ	Density.
$\boldsymbol{\tau}$	Unit tangent.
τ	Timestep.
$\boldsymbol{\tau}$	Stress tensor.
θ	Temperature.
θ_m	θ-method parameter.
a	Earth's radius.
$\mathcal{A}_H$	Horizontal momentum diffusion coefficient.
A_H	Horizontal momentum diffusion coefficient (non-dimensionalised).
$\mathcal{A}_V$	Vertical momentum diffusion coefficient.
A_V	Vertical momentum diffusion coefficient (non-dimensionalised).
$\mathcal{C}_D$	Bottom friction coefficient.
C_D	Bottom friction coefficient (non-dimensionalised).
C_N	Streamfunction North boundary value.
C_S	Streamfunction South boundary value.
D_z	Vertical finite difference operator.
$\mathcal{E}$	Total energy.
e	Edge of an element in the tessellation.
$\mathcal{E}_h$	Numerical energy.
$\boldsymbol{F}$	Forcing.
$\mathcal{F}$	Quasi-geostrophic forcing.
f_*	Reciprocal Coriolis parameter.
f_0	Coriolis frequency.
F_x	Zonal forcing.
F_y	Meridional forcing.
F_z	Vertical forcing.
g	Gravitational acceleration.
H	Vertical length scale.
h	Maximal element diameter in the tessellation.
H_t	External heating.
$\mathbb{H}_t$	QG external heating antiderivative.
$\mathcal{H}_t$	Quasi-geostrophic external heating.
$\mathcal{I}_h$	Interior intersections in the tessellation.
$\mathcal{I}_h^\partial$	Boundary intersections in the tessellation.

KE	Kinetic energy.
$\mathcal{K}_H$	Horizontal buoyancy diffusion coefficient.
K_H	Horizontal buoyancy diffusion coefficient (non-dimensionalised).
$\mathcal{K}_V$	Vertical buoyancy diffusion coefficient.
K_{V_1}	Vertical buoyancy diffusion coefficient (non-dimensionalised in QGE).
K_{V_2}	Vertical buoyancy diffusion coefficient (non-dimensionalised in temperature equation).
L	Horizontal length scale.
L_f	Rossby deformation length.
L_x	Zonal length.
L_y	Meridional length.
N	Brunt-Väisälä frequency.
$\mathcal{N}$	Number of vertical layers.
$\boldsymbol{n}$	Unit outer normal.
p	Pressure.
p_0	Hydrostatic pressure.
PE	Potential energy.
P^p	Space of polynomials of order p.
q	Potential vorticity.
q_s	Specific Humidity.
q_c	Potential vorticity free-slip correction term.
T	An element in the tessellation.
T	Time scale.
t	Time.
T_e^+	An element in the tessellation with edge e and normal $\boldsymbol{n}^+$.
T_e^-	An element in the tessellation with edge e and normal $\boldsymbol{n}^-$.
$\mathcal{T}_h$	Tessellation of polygons on the domain.
U	Horizontal velocity scale.
u	Full zonal velocity.
$\boldsymbol{u}$	Full velocity including geostrophic and ageostrophic components.
u_a	Ageostrophic zonal velocity.
$\boldsymbol{u_a}$	Ageostrophic velocity.

u_g	Geostrophic zonal velocity.
$\boldsymbol{u_g}$	Geostrophic velocity.
v	Full meridional velocity.
V_ψ	Streamfunction space.
V_{ψ_h}	Streamfunction discrete space.
v_a	Ageostrophic meridional velocity.
v_g	Geostrophic meridional velocity.
V_q	Potential vorticity space.
V_{q_h}	Potential vorticity discrete space.
W	Vertical velocity scale.
w	Full vertical velocity.
$\hat{\boldsymbol{x}}$	Zonal unit vector.
x	Zonal coordinate.
$\hat{\boldsymbol{y}}$	Meridional unit vector.
y	Meridional coordinate.
Z	Enstrophy.
$\hat{\boldsymbol{z}}$	Vertical unit vector.
z	Vertical coordinate.
Z_h	Numerical enstrophy.

Chapter 1

Introduction

An unsolved problem in atmospheric dynamics is the origin of the horizontal $k^{-5/3}$ energy regime for wavenumber magnitude k for mesoscales, smaller than the synoptic scale of about Rossby radius $L_f \approx 1000\,\text{km}$. Due to stratification, rotation and the thinness of the troposphere, most models would predict quasi-two-dimensional behaviour with a k^{-3} spectrum, which is what global forecast models consistently generate [9]. The $k^{-5/3}$ regime extends to scales far too large for a traditional three-dimensional turbulent cascade to work which is known to produce such an energy profile, therefore, other mechanisms must be considered. When frontal dynamics do not dominate and the atmosphere is predominantly stratified, the $k^{-5/3}$ regime can be explained by simulations of horizontally homogeneous stratified turbulence which display a horizontal $k^{-5/3}$ regime and a flow of kinetic energy to small scales [7, 31]. However, there is no reason for this to apply where frontal dynamics are dominant. Fronts generate small scale structures, but it is difficult to identify which possible source of spectra shallower than k^{-3} dominates. This is where reduced models are useful.

The goal of this thesis is to develop a finite element method for the three-dimensional quasi-geostrophic equations that can be used to see if front formation can also generate the observed transfer of kinetic energy to small scales. Ultimately such research is designed to advance the understanding of Earth's atmosphere to improve the accuracy of global circulation models and weather prediction.

1.1 Nature of the Atmosphere

The atmosphere is a large and complex fluid system that is driven by a multitude of processes including; planetary rotation, heating from the sun and planet surface, stratification, topological effects from mountain ranges and city landscapes, ocean currents, as well as anthropological activity. The vast scale of weather systems can be seen in Figure 1.1 and with such a large dynamical system depending on so many variables, one can see how the atmosphere can behave in a chaotic fashion and become difficult to predict.

Figure 1.1: "The Blue Marble" taken from Apollo 17. The scale of the cloud patterns stretches across the Earth's atmosphere. Image from NASA [94].

When studying the atmosphere, the effects of rotation, temperature gradients and stratification are of particular importance [39]. The rotation of the planet has a significant effect on the motion of flows within the atmosphere and is responsible for the behaviour of large scale flows such as cyclones. Strong horizontal temperature gradients combined with this rotation are responsible for powerful zonal jet streams that generate and carry weather systems around the planet. The stratification of the atmosphere refers to the decrease in density with height which organises the atmosphere into distinct layers as in Figure 1.2. This stratification has a significant effect on the flows within the atmospheric boundary layer (or troposphere), and can generate internal waves and drive baroclinic instability that creates large meanders in jet streams which can break off into large cyclones and anticyclones (see Appendix A for more information on jet streams and Rossby waves).

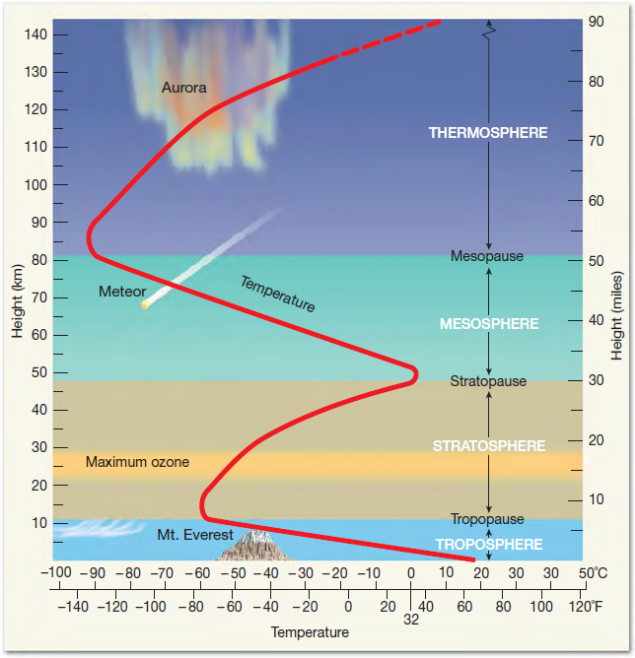

Figure 1.2: Structure of Earth's atmosphere. The red line indicates the temperature profile. The troposphere is the layer closest to the Earth's surface and contains the majority of weather systems. [Figure in [82], © 2013. Reprinted by permission of Pearson Education, Inc., New York, New York.]

The atmosphere is known as a geophysical fluid, that is a fluid motion of large enough scale to experience the effects discussed above. Geophysical fluids are fundamentally three-dimensional, however, the geophysical constraints (eg. stratification, rotation) suggest two-dimensional effects. Brethouwer et al. [31] demonstrated that atmospheric like turbulence can be simulated numerically, which displays strong stratification indicating some two-dimensional behaviour. It is well known that rapidly rotating flows can behave as a two-dimensional fluid as described by the Taylor-Proudman Theorem [39], which states that in such a flow the vertical derivative of the horizontal velocity must be zero. Although atmospheric flows are subjected to the rotation of the Earth, the rotation is not strong enough for three-dimensional effects to be ignored. The atmosphere experiences a wide range of flows, in particular high Reynolds number flows where inertial forces are large compared to viscous forces and the flow becomes turbulent.

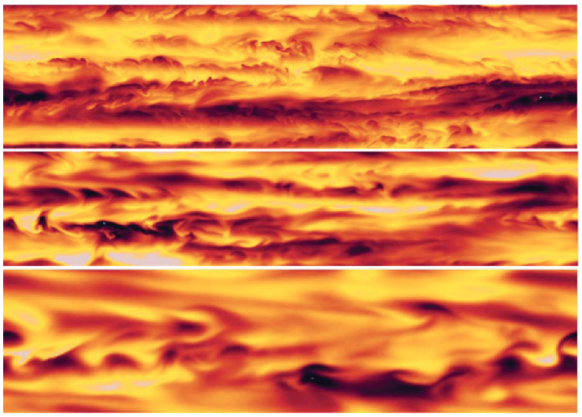

Figure 1.3: Horizontally homogeneous periodic calculation by Brethouwer, Billant, Lindborg and Chomaz [31]. Strong layering suggests two-dimensional dynamics. [Reprinted from [31] with permission from Cambridge University Press.]

1.2 Energy Cascades and Turbulence

Currently, there is no rigorous definition of turbulence. However, it may be characterised as a state of continuous instability where fully developed turbulence has a complex spatial structure with rapid, irregular velocity fluctuations at any particular point in space and motions on many different length scales [1, 115]. In a three-dimensional flow, isotropic turbulence can be characterised by the transfer of energy from large-scale eddies to smaller-scale eddies until the energy is dissipated by viscous effects. Turbulent flows can sometimes be identified by their energy spectrum. Consider a wavevector $\boldsymbol{k}$ whose components are the wavenumbers in the x, y and z directions. Denote the wavevector magnitude $k = |\boldsymbol{k}|$. Then the energy spectrum $E(k)$ of a three-dimensional flow is defined as

$$E(k) = \frac{k^2}{4\pi^2} \int \langle \boldsymbol{u}(\boldsymbol{x}) \cdot \boldsymbol{u}(\boldsymbol{x} + \boldsymbol{r}) \rangle \, e^{-i\boldsymbol{k}\cdot\boldsymbol{r}} \, d\boldsymbol{r} \tag{1.1}$$

such that

$$\mathcal{E} = \int_{k=0}^{\infty} E(k) \, dk \tag{1.2}$$

where $\mathcal{E}$ is the total energy of the system and $\langle \cdot \rangle$ is an ensemble average [40, 100]. As discussed below, a turbulent flow will exhibit an energy spectrum $E(k) \sim k^{-5/3}$. It should be noted that such an energy spectrum profile does not necessarily indicate that a flow is turbulent.

The most commonly quoted evidence for two-dimensional effects in geostrophic tur-

bulence is the existence of this $k^{-5/3}$ energy spectrum at mesoscales ($\sim$ 600 km to 2 km) in the stratosphere as seen in Figure 1.4. Nastrom and Gage [95] present the atmospheric wavenumber spectra of wind and temperature from over 6000 commercial aircraft flights. The spectra slopes follow a $k^{-5/3}$ regime in the range of scales from 2.5 km to 400 km. For larger scales, the slope steepens to k^{-3}. The spectra were found to be independent of latitude, season and location in the troposphere or stratosphere.

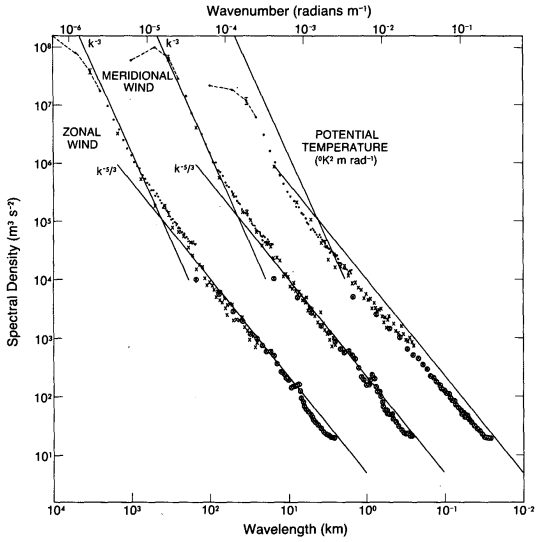

Figure 1.4: Nastrom and Gage energy spectrum, stratospheric measurements taken from Global Atmospheric Sampling Program (GASP) aircraft data. Wavenumber plotted against energy spectrum $E(k)$ on logarithmic axes. Meridional wind and temperature profiles are shifted one and two decades to the right, with the zonal wind being the left most profile. [Figure in [95]. © American Meteorological Society. Used with permission.]

There are two situations in which this energy spectrum is predicted to occur [117]: first in three-dimensional homogeneous isotropic turbulence with a downscale or forward energy cascade as predicted by Kolmogorov [71], and secondly in two-dimensional homogeneous isotropic turbulence on the large-scale side of energy injection with an upscale or inverse energy cascade as predicted by Kraichnan [73]. It is clear that the spectrum cannot be due to two-dimensional turbulence as the atmosphere is not two-dimensional. A forward energy cascade in three-dimensional turbulence is caused by eddy diffusion elongating vortex tubes and thereby increasing vorticity on smaller and smaller scales [34]. A purely three-dimensional argument is not supported since the scales at which the $k^{-5/3}$ regime is observed is far too large

for isotropic three-dimensional turbulence; at these large scales the atmosphere has greater dynamics in the horizontal than the vertical and is therefore not isotropic. Tung and Orlando [117] proposed that the spectrum observed in the atmosphere is produced by an injection of energy at synoptic scales (greater than 600 km) from thermal energy of the sun, with a forward energy cascade to small scales.

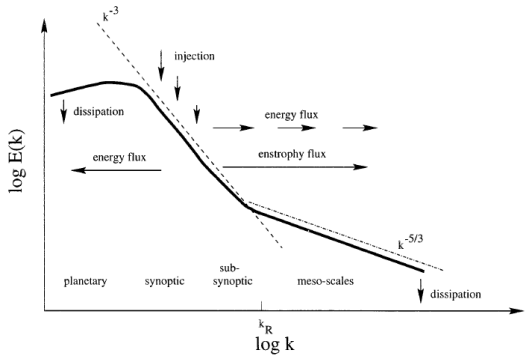

Figure 1.5: Energy and enstrophy cascades proposed by Tung and Orlando [117]. [Figure in [117]. © American Meteorological Society. Used with permission.]

Structure functions are useful for providing insight into the direction and strength of energy cascades. Let

$$\delta \boldsymbol{u} = \boldsymbol{u}(\boldsymbol{x} + \boldsymbol{r}) - \boldsymbol{u}(x) \tag{1.3}$$

be the velocity difference with separation $\boldsymbol{r}$, then the nth order structure function is

$$S_n(r) = \langle \delta \boldsymbol{u}^n \rangle, \tag{1.4}$$

where the angle brackets indicate a statistical average. The second order structure

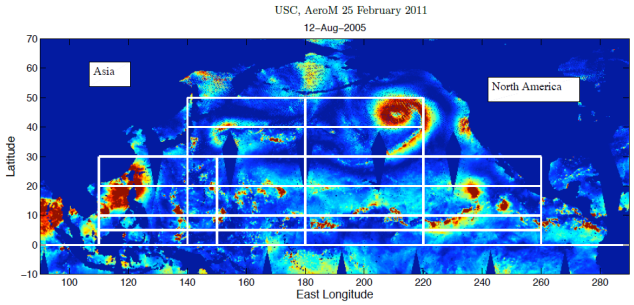

Figure 1.6: Scatterometer study area over the Pacific Ocean. Figure in [69].

function $S_2(r) \sim r^{2/3}$ corresponds to the energy spectrum $E(k) \sim k^{-5/3}$, [70]. In a study by King & Kerr (2009) [69], oceanic measurements were taken over the Pacific

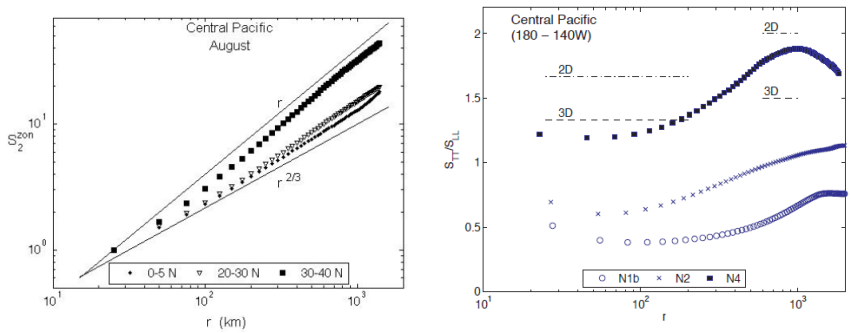

(a) (b)

Figure 1.7: Scatterometer data from Pacific Ocean showing (a) a $r^{2/3}$ regime in the second order structure function for small scales and (b) the dynamics are somewhere in between isotropic two-dimensional and three-dimensional turbulence (S_{LL} and S_{TT} denote the second order structure functions of two components of the velocity difference: along the separation $\boldsymbol{r}$ and orthogonal to $\boldsymbol{r}$). Figures in [69].

Ocean using backscattered microwaves emitted from a satellite, see Figure 1.6. They performed structure function analysis on this data and found that the second order structure function exhibited a $r^{2/3}$ profile for length scales below around 600km as seen in Figure 1.7. The data shown in Figure 1.7b indicates that the dynamics are neither purely three-dimensional nor two-dimensional but somewhere in between.

The $r^{2/3}$ (or $k^{-5/3}$) regime appears to be ubiquitous, it is observed in atmospheric measurements [35, 69, 76, 95], experiments and numerical simulations [8, 31, 55, 70, 77, 92]. Evidence for a forward energy cascade being responsible for this regime can be shown using third order structure functions. The three-dimensional forward energy cascade third order structure function is [52, 71],

$$S_3(r) = -\frac{4}{5}\epsilon r, \tag{1.5}$$

and is found in geostrophic turbulence [69, 76, 77] indicating a forward energy cascade as discussed in Section 1.3.

So, it appears that this energy spectrum is definitely there, however, the mechanisms underlying its formation are not understood. The first weather forecast simulations with a resolution of around 250 km gave a steeper k^{-3} spectrum instead of the expected $k^{-5/3}$, possibly due to numerical dissipation. However, new simulations with finer 25 km resolutions still have this regime (see Figure 1.9) and it is unknown why this is the case [9, 97, 98, 110, 114]. Until this is resolved, next generation General

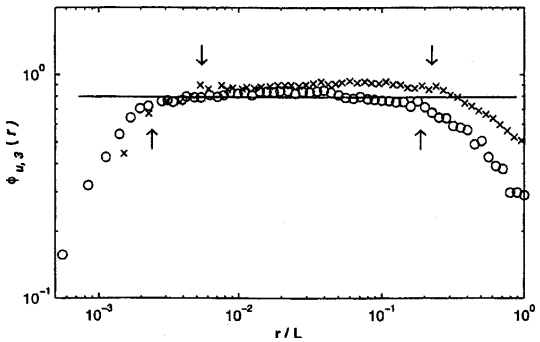

Figure 1.8: 4/5 Kolmogorov law for a third order structure function providing evidence for a cascade of energy to small scales. Figure in [70].

Circulation Models (GCM) will be flawed and will have repercussions in mesoscale numerical weather prediction. The underlying mechanisms leading to this problem is what this thesis intends to investigate. Augier [9] states that some GCMs have achieved a realistic $k^{-5/3}$ mesoscale regime, whilst others have not, possibly because of too much dissipation at synoptic scales. Yet, the mechanisms behind this regime are still unknown. GCMs simulate atmospheric flows on a global scale and cannot resolve small scale physical processes, such as frontogenesis, due to computational limitations. These sub-grid scale processes may be where the missing energy lies. Attempts to model these processes with stochastic schemes, to inject this energy into the scales resolved by the numerical model, produce more realistic energy spectra [97, 110]. Although, these techniques may be just compensating for model deficiencies.

Early studies aimed at trying to understand the mechanics of geostrophic turbulence in terms of two-dimensional turbulence and an inverse energy cascade [65, 83, 85, 90, 101, 124]. As first shown by McWilliams (1984) [85], two-dimensional turbulence displays the emergence of coherent vortices from the background turbulence. This is due to the inverse energy cascade where energy is transported from small scales to larger scales, whilst enstrophy (kinetic energy related to dissipation) cascades from large to small scales. This is in contrast to three-dimensional turbulence where energy observes a forward cascade due to vortex stretching and tilting [81, 83, 101]. Investigation into geostrophic turbulence using the barotropic (single layer) quasi-geostrophic equations revealed that the β-plane (effect of rotation and Earth's curvature, see Section 2.2) turbulence also exhibits coherent vortices. These vortices coexist with Rossby waves and the inverse energy cascade is inhibited for scales above $(U/\beta)^{1/2}$ for typical velocity U. This is typical of β-plane turbulence,

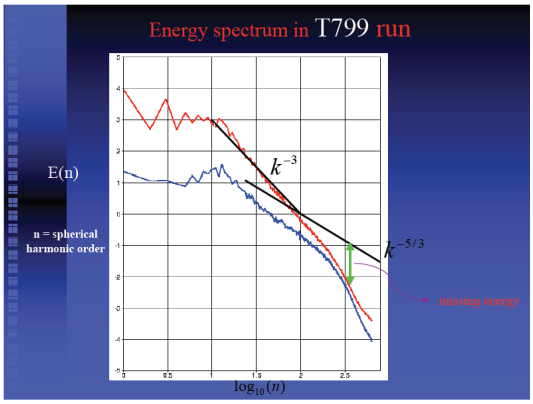

Figure 1.9: Missing energy in weather forecast models. Total kinetic energy spectrum from European Centre for Medium-Range Weather Forecasts (ECMWF) model with 25 km resolution (T799). Figure provided by Tim Palmer, similar figures in [97, 110].

however, the coherent vortices still had a significant effect on transport [101]. As geostrophic turbulence is not fully two-dimensional, the inverse energy cascade and the emergence of coherent vortices cannot fully describe the nature of geostrophic turbulence. Waves and jets also represent key components of geostrophic turbulence. Understanding these as well as their interaction with each other and topographical features is necessary for correct parameterisation in general circulation models [101].

In a further study of vortex interactions in geostrophic turbulence, McWilliams and Weiss (1999) [90] found that the vortex population decays much faster in geostrophic flows than two-dimensional flows. This suggests that the three-dimensional processes that amalgamate or destroy geostrophic vortices are more efficient than those in two-dimensional flows. They also observed that vortex interactions are much more frequent than in two-dimensional turbulence and vortices often aligned vertically to form tall vortex columns [83, 90]. Rossby waves have been suggested as a possible mechanism for this vortex alignment [65]. Hardenberg et al. (2000) [124] showed that there are important differences between continuous stratification and two-layer dynamics, indicating that further study of greater vertical resolution models is needed. Indeed Hardenberg found that the merging of baroclinic (stratified effects) vortices has a much more complex structure than in the barotropic case. Taller vortices become flattened over time and ejected vorticity filaments become curved in the vertical and spiral around the merging vortices. This can lead to a more rapid homogenization of the merging vortex cores in geostrophic turbulence.

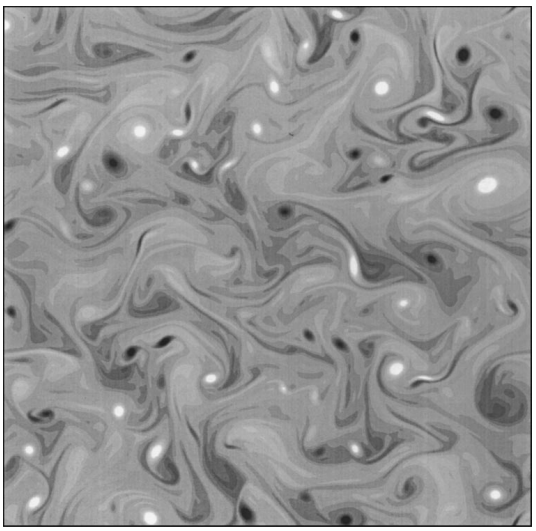

Figure 1.10: Relative vorticity field from a numerical simulation of freely decaying turbulence on the β-plane. Bright and dark tones indicate negative and positive vorticity respectively. Rossby waves coexist with coherent vortices, these vortices are generally smaller than those in pure two-dimensional or f-plane ($\beta = 0$) flows. Figure in [101].

Building on McWilliams and Weiss's research, Martinsen-Burrell and Weiss [83] broke down turbulent flows into vortex cores, strain cells and vortex filaments. They found that both two-dimensional and three-dimensional quasi-geostrophic turbulence indicated inverse cascades, whilst the vortex cores showed much steeper spectra indicating that the cores slow down the inverse cascade. A significant difference between the three-dimensional QG and the two-dimensional results was the background component of the three-dimensional QG flow contained many more vortex filaments than the two-dimensional flow. These filaments contain a greater amount of enstrophy and dominates the flow with a Gaussian probability density function (PDF) for the velocity. This Gaussian PDF is relevant for parameterising turbulent diffusion. It is noted, however, that physical measurements indicate non-Gaussian velocity fields which may be due to forcing from solar-driven advection and boundary forcing.

These earlier attempts to explain geostrophic turbulence in terms of two-dimensional dynamics with vortex merging and an inverse energy cascade provide useful insight into the similarities between the atmosphere and two-dimensional fluids. However, this cannot provide an explanation [76] for geostrophic turbulence since the atmosphere is clearly not two-dimensional. Whilst the atmosphere is strongly stratified,

vertical dynamics play an important role [59, 82] and there is strong evidence for a forward energy cascade [31, 77, 79].

1.3 Stratification and Geostrophic Turbulence

As seen in Figures 1.2 and 1.3, the atmosphere is stratified. This stratification can exhibit layering with two-dimensional effects and large horizontal structures which rules out isotropic three-dimensional turbulence as an explanation for the $k^{-5/3}$ inertial range. Geostrophic turbulence is a prominent research area as a result of this lack of understanding of the mechanics underlying the inertial range.

Work by Billant, Chomaz and Augier (2000-2012), [6, 7, 21, 22, 23, 24, 25, 26, 43] followed the idea that an instability could be responsible for the layering in strongly stratified fluids proposed by Herring and Métais (1989) [55, 92]. They arranged an experiment in a water tank and created two antiparallel vertical vortices using a double flap mechanism and tracked the vortices using dyes. They observed an instability distinct from the Crow (reconnection of vortex pairs) and short-wavelength instabilities known to appear in homogeneous fluids. The vortices formed a zigzag shape when viewed from the side, hence giving the instability its name. This instability is antisymmetric with respect to the plane separating the vortices and eventually the vortex pair is sliced into thin horizontal layers of independent pancake dipoles. These pancake like structures have been observed in laboratory experiments, numerical simulations and oceanic measurements and is known to enhance the energy dissipation through the vertical shear [23]. This has been proposed as an explanation for the significant difference between stratified turbulence and two-dimensional turbulence despite the majority of motion being horizontal [55]. Vertical motion is largely inhibited by stratification and leaves internal gravity waves and vertical vortices as the two main forms of vertical motion.

A recreation of the Billant and Chomaz's numerical experiments was done by Robert Kerr et al. [66]. A pair of counter-rotating vertical vortices with propagation aligned with the x-direction were perturbed. There were strong temperature gradients around the zigzag corners generated by the overturning of different densities (Figure 1.11). These strong temperature gradients instigate baroclinic enstrophy production which generates vorticity hence large horizontal velocities. It is proposed that baroclinic production of vorticity in two-dimensions is analogous to the

vortex stretching mechanism that generates turbulence.

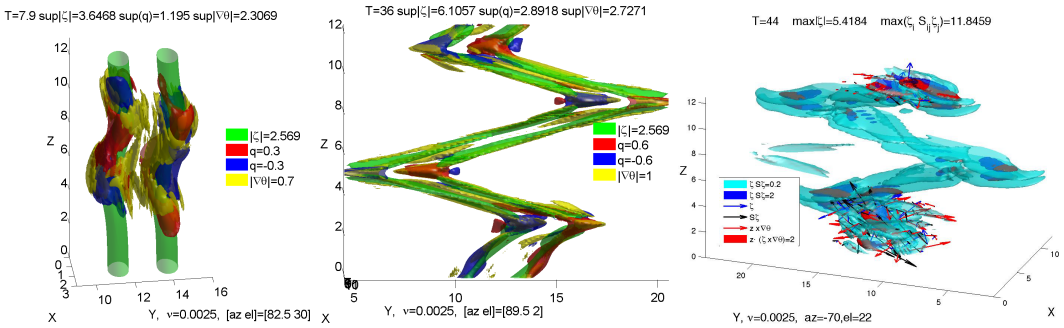

(a) (b) (c)

Figure 1.11: Zigzag instability formation. (a) Vortex pair shortly after initial perturbation. (b) Formation of zigzag instability. (c) Enstrophy production is strong in the corners of the instability. Images produced from calculation by Robert Kerr.

Brethouwer, Billant, Lindborg and Chomaz (2006) [31] performed scaling analysis and direct numerical simulations to provide evidence for a $k^{-5/3}$ regime in strongly stratified turbulent flows, that is for large Reynolds numbers $Re \gg 1$ and small Froude number $F_h \ll 1$. The Reynolds number UL/ν and Froude number U/NL (for typical velocity U, length L, viscosity ν and Brunt-Väisälä frequency N) were varied over a significant range to observe their influence on turbulence, length scales, energy spectra and instabilities. The aim was to contribute to a better understanding of the dynamics of strongly stratified flows, so that laboratory and numerical experiments may be more precisely designed to resemble geophysical flows.

The analysis reveals that two different regimes occur determined by the parameter $\mathscr{R} = ReF_h$, which is the ratio of vertical advection and diffusion terms. The strongly stratified turbulence regime is when $\mathscr{R} \gg 1$. This led to the hypothesis of three-dimensional turbulence in strongly stratified flows with an anisotropic forward energy cascade. Scaling arguments [31, 77] suggest that the horizontal kinetic and potential energy spectra of stratified turbulence follow the Kolmogorov regimes [40],

$$E_K(k) = C_1 \epsilon^{\frac{2}{3}} k^{-\frac{5}{3}}, \quad E_P(k) = C_2 \epsilon_P \epsilon^{-\frac{1}{3}} k^{-\frac{5}{3}} \tag{1.6}$$

for horizontal wavenumbers k and ϵ_P is the potential energy dissipation. It is also suggested that the vertical energy spectra have the form

$$E_K(k_v) \sim E_P(k_v) \sim N k_v^{-3} \tag{1.7}$$

for vertical wavenumbers k_v. The $\mathscr{R} \ll 1$ regime is less relevant to geophysical flows and large-scale dynamics are determined by a balance between inertial and viscous forces due to vertical shearing. Therefore, dissipation occurs mainly at large scales and no inertial cascade can develop.

Brethouwer's work concludes that $\mathscr{R} > 1$ is required for a clear transfer of kinetic and potential energy from large to small scales and emergence of an inertial range with a $k^{-5/3}$ regime. It also states that numerical simulation of strongly stratified turbulence with a clear inertial subrange is important to study further, but achieving $\mathscr{R} \gg 1$ and $F_h \ll 1$ at the same time is difficult with current computer resources. Whilst the upper ocean and middle atmosphere ($10-100\,\text{km}$ above sea level) fall into the category of strongly stratified flows, it is not always the case for the troposphere (below $10\,\text{km}$).

1.4 Frontogenesis

A horizontally homogeneous stratified mechanism, as described in the previous section, is one possible mechanism for generating $k^{-5/3}$ at small scales that is viable in the stratosphere. However, this doesn't appear to be the case in the troposphere as vertical motions play a crucial role. There is still strong evidence for a $k^{-5/3}$ law throughout the atmospheric boundary layer [95, 117], but not strong in terms of a horizontally homogeneous interpretation. Other possible mechanisms include effects of the ocean on the atmosphere, sea surface temperatures and frontogenesis.

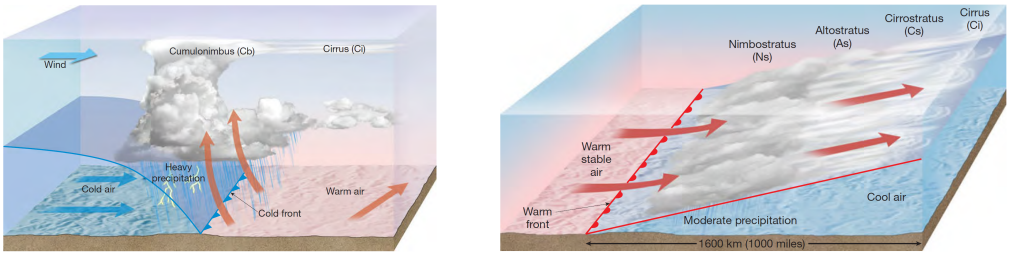

Figure 1.12: Illustration of the structures of cold (left) and warm (right) weather fronts. [Figure in [82], © 2013. Reprinted by permission of Pearson Education, Inc., New York, New York.]

Atmospheric fronts are regions of sharp temperature gradients that form boundaries between cold and warm air masses and are a prominent feature in weather forecasts. Cushman-Roisin and Beckers [39] provides a useful introduction to frontogenesis,

which is summarised in what follows. Cold fronts, depicted in weather charts as spiked lines, occur when a colder air mass overtakes a warmer air mass, therefore causing a temperature drop as it passes. Similarly, a warm front, depicted in weather charts as lines with semicircles, occurs when warm air overtakes a cold air mass, causing a temperature rise as is passes. The term front was coined by Vilhelm Bjerknes who initiated the study of fronts during World War I and related the meeting of air masses to the clash of military lines at a front. Fronts take around a day to form, which is a relatively fast process on atmospheric scales, suggesting that local heating is unimportant in the process and temperature changes are caused by advection. A simple example demonstrating how this can be achieved by advection is the horizontal velocity field

$$u = \alpha x, \;\; v = -\alpha y, \tag{1.8}$$

with α denoting a deformation rate. It is assumed that vertical velocity is zero over a flat surface. Now, suppose that this velocity field advects a temperature gradient that varies in the y-direction. Neglecting non-conservative processes gives the following equation for temperature θ,

$$\frac{d\theta}{dt} = \frac{\partial \theta}{\partial t} + u\frac{\partial \theta}{\partial x} + v\frac{\partial \theta}{\partial y} = 0. \tag{1.9}$$

Differentiating this with respect to x gives

$$\frac{d}{dt}\left(\frac{\partial \theta}{\partial x}\right) = -\alpha \frac{\partial \theta}{\partial x}. \tag{1.10}$$

Since the temperature gradient in the x-direction is initially zero it must remain zero. Therefore, the temperature gradient may change in intensity but not in direction. Differentiating with respect to y shows that the magnitude of the temperature gradient increases exponentially with time,

$$\frac{\partial \theta}{\partial y} = \left.\frac{\partial \theta}{\partial y}\right|_{t=0} e^{\alpha t}. \tag{1.11}$$

The evolution of an air parcel's y position is given by

$$\frac{dy}{dt} = v = -\alpha y \implies y = y_0 e^{-\alpha t}. \tag{1.12}$$

Therefore, all fluid parcels are converging toward $y = 0$ and the temperature gradient is increased by the advecting process. The intensifying temperature gradient

will produce a stronger thermal wind which changes the advecting wind velocity to accelerate the frontogenesis process and can produce an infinite temperature gradient in finite time. Cushman-Roisin and Beckers then notes that with accelerating dynamics and shorter length scales, a geostrophic approximation becomes invalid. Since fronts have sharp variations across the front and weak variations along the front, geostropy can be retained in one direction. This leads to a semi-geostrophic model used in [36, 38, 58, 61].

Cushman-Roisin and Beckers [39] continues to analyse frontogenesis under a semi-geostrophic model which predicts discontinuities at the top and bottom rigid boundaries. These discontinuities represent a frontal collapse and the solution becomes multi-valued after this point with the discontinuities propagating into the interior of the fluid. This model loses physical relevance at this point; in reality, dissipation keeps the temperature single valued and finite.

Frontogenesis drives the formation of weather systems in the atmosphere and can be modelled by modern numerical codes that simulate the full fluid equations. The aim is to generate frontogenesis as an alternative mechanism for a downscale energy cascade from a simple model. Frontogenesis has been observed in the three-layer quasi-geostrophic model of McWilliams and Chow (1981) [87]. This is the well-known two-layer model plus drag on the surface layer and a shear from the upper layer. The shear represents the thermal wind generated by a north-south temperature gradient. A jet developed in the centre and the jet became baroclinically unstable as in the atmosphere. Fronts and convective cells appeared naturally. Therefore, some signs of frontal formation can appear in a three-layer model with surface drag and an Eady model with an imposed thermal wind, that is a vertical shear that balances a temperature gradient. The goal of this project is to apply one of the latest numerical methods for accurate continuum simulations, discontinuous Galerkin methods, to this three-dimensional problem. The quasi-geostrophic equations, with forcing $\mathcal{F}$ and diffusion D, are written as [86]

$$\frac{\partial q}{\partial t} + J(\psi, q) = \mathcal{F} + D, \tag{1.13}$$

where the potential vorticity is

$$q = \Delta\psi + \frac{\partial}{\partial z}\left(\frac{f_0^2}{N^2}\frac{\partial \psi}{\partial z}\right) + \beta y, \tag{1.14}$$

for Coriolis frequency f_0 (see Section 2.2), streamfunction ψ and

$$J(\psi, q) = -\frac{\partial \psi}{\partial y}\frac{\partial q}{\partial x} + \frac{\partial \psi}{\partial x}\frac{\partial q}{\partial y} = (\boldsymbol{u_g} \cdot \nabla)q. \tag{1.15}$$

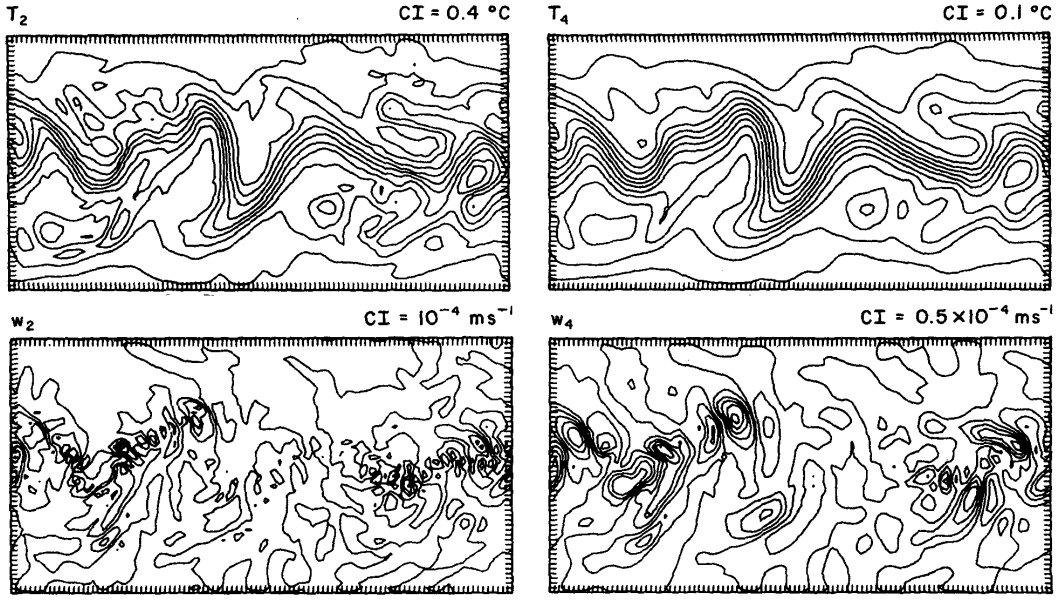

Figure 1.13: Instantaneous patterns from McWilliams channel simulation of temperature (top) and vertical velocity (bottom) at the fluid layer interfaces depicting an unstable jet. [Figure in [87]. © American Meteorological Society. Used with permission.]

The work in [87] provides a basis for the research in quasi-geostrophic frontogenesis presented in this thesis. In the 1981 paper, a numerical solution is calculated via second order finite difference methods. A jet stream forms much like in the Earth's atmosphere and front formations are observed. Further analysis within the paper shows that the kinetic energy spectrum displays a k^{-3} inertial range. McWilliams uses a layered model and not full three-dimensional equations. The results are also limited by the computational power available in the 1970's/80's. Similar results are found in [56, 89] with finer resolution studies displaying spectra slopes shallower than k^{-3} [93, 111].

There are many mechanisms involved in the formation of fronts, one of the most important being a horizontal deformation field acting upon a temperature gradient [61, 112, 128, 129, 130]. A deformation field with an axis of contraction perpendicular to a temperature gradient intensifies the gradient. Frontogenesis using the

primitive equations, Boussinesq equations and quasi-geostrophic equations has been achieved analytically [19, 61, 112, 130] and numerically [87, 128, 129].

Stone [112] presents an analytical solution for front formation within a horizontal wind deformation field acting on a horizontal temperature gradient using the Boussinesq equations to derive a quasi-geostrophic model. Stone credits Bergeron [19] for first proposing that atmospheric frontogenesis is caused by this configuration, this was met with criticism suggesting that such deformation fields do not persist for long enough to generate fronts. This criticism fails to account for the wide variations in the strength and duration of atmospheric deformation fields and it can be expected that some are capable of producing fronts, Stone refers to the work of Elliott and Brown [46] to support this.

Stone uses an initial temperature field with constant vertical and horizontal gradients. The top and bottom boundary conditions are chosen to be rigid so that vertical velocity is zero at these boundaries. The zonal direction extends to infinity and the meridional direction is periodic. The initial deformation field is then set with streamfunction $\psi = -x\sin(y)$, resembling an arrangement of low and high pressure cells. The asymptotic solution was solved analytically with appropriate approximations. The initial state develops characteristics of an atmospheric front. The solution was shown to develop regions of strong baroclinicity, large static stability and vertical circulations, with a steepening of the horizontal temperature gradient within a few hours, sufficient to account for observed rapid increases in the gradient in atmospheric frontogenesis. Additionally, the solution displays sharper gradients near the ground and zonal winds increasing with altitude due to the thermal wind relation, which are features of realistic fronts. Stone concludes that the analytical solution is in close agreement with observed atmospheric frontogenesis and therefore provides evidence that horizontal deformation fields are important in the phenomenon.

Williams [128] uses a numerical experiment with the Boussinesq equations to produce atmospheric frontogenesis, pointing out how the process of producing a front from initially large-scale motions of around 1000 km creates small-scale motions of the order of 100 km. It is also argued that the front produced by Stone [112] is not realistic because the potential vorticity q given in equation (1.14) is conserved by the quasi-geostrophic equations without forcing or diffusion, therefore an initially small potential vorticity must remain small.

The potential vorticity must be large at a true front: the first term in the potential vorticity equation is the relative vorticity, which will be a large positive value at a true front. The only way for the second term in (1.14) to become large and negative is for $\partial\theta/\partial z$ to become negative, where θ is the potential temperature. This would contradict the condition for a statically stable atmosphere. Therefore, the potential vorticity needs to be large at a true front which cannot evolve from an initial state where q was everywhere small. This implies that the quasi-geostrophic equations cannot produce a realistic front from large-scale initial conditions. The work by Stone [112] shows that the quasi-geostrophic equations can produce a pseudo front from a deformation field. The front does not tilt with height and the vorticity is zero at the front, which are not in agreement with observations in real atmospheric fronts.

Williams [128] tackles this by including the vertical and divergent parts of the horizontal deformation field in the advecting velocities. A finite difference approximation is used with an initial small-amplitude sinusoidal disturbance combined with an unstable baroclinic current. A horizontal to vertical grid spacing ratio of $\Delta x/\Delta z \approx 50$ is used to capture the slope of a cold front. The wavelength of the initial disturbance is selected to give the maximum growth rate according to Eady [44]. This disturbance grows exponentially over time and, once the amplitude is large enough, becomes distorted by the advecting terms to form a realistic frontal zone. The width of the frontal zone is limited by the numerical grid resolution and it is concluded that the width would attain zero in finite time in the absence of numerical errors. The time scale of frontogenesis in the numerical experiment is less than 24 hours. It is found that these numerical results are consistent with atmospheric observations [109]. Williams expresses that a satisfactory analytical solution describing the frontogenesis process would be useful.

Williams [130] expands on the quasi-geostrophic solution derived by Stone [112] in similar work. Williams' work differs from Stone's in that the deformation field extends to infinity and the initial variation in the temperature field is confined to a zone of finite width. This model is not necessarily more realistic in terms of atmospheric frontogenesis, but a complete solution is obtained. The model assumes incompressibility and that the atmosphere is bounded above and below by two rigid planes at a distance H apart, with the vertical velocity set to zero on these boundaries. The Coriolis parameter f is assumed to be constant and heating and friction are neglected. These approximations with the quasi-geostrophic equations

are the same in Stone's work. The deformation field used is

$$u_d = \left(\frac{U}{L}\right) x, \;\; v_d = -\left(\frac{U}{L}\right) y, \tag{1.16}$$

where U is a characteristic velocity scale and L a length scale. Note that this deformation field is similar to the one used by Stone especially near the centre since $\sin(x) \approx x$ for small x. The initial non-dimensional potential temperature field disturbance is

$$\theta'(x, y, 0) = -\left(\frac{2}{\pi}\right) \arctan(x). \tag{1.17}$$

An analytical solution is then derived where the asymptotic temperature field as $t \to \infty$ is given by

$$\theta'(x, y, \infty) = -\left(\frac{2}{\pi}\right) \arctan\left[\frac{\sinh(\pi x)}{\cos(\pi y)}\right], \tag{1.18}$$

which is the same form as Stone's approximate solution. It is also shown that if the initial temperature field $\theta = \theta_s(z) + \theta'$ satisfies the following conditions,

$$\begin{aligned} \frac{\partial}{\partial z}\theta'(x, y, 0) &= 0 \\ \theta'(x, y, 0) &= -\theta'(-x, y, 0) \\ \theta(\infty, y, 0) - \theta(-\infty, y, 0) &= -2, \end{aligned} \tag{1.19}$$

then the final solution as $t \to \infty$ will be independent of the initial state. A necessary condition for frontogenesis to occur is that the initial disturbance is of a scale larger than the Rossby radius of deformation

$$L_f = \frac{H}{f}\left(\frac{g}{\theta_0}\frac{\partial \theta_s}{\partial z}\right)^{\frac{1}{2}} = \frac{HN}{f} \tag{1.20}$$

where N is the Brunt-Väisälä frequency. For an initial disturbance with scale smaller than L_f, then frontolysis (weakening of the front) is expected to occur, except near the boundaries. As can be seen in Stone's work, the front is stronger near the top and bottom boundaries. Williams points out that, despite the restrictions, Stone's solution is very general. Williams claims that the production of a discontinuity requires the transfer of energy to small scales. Charney [34] shows that the quasi-geostrophic equations do not exhibit an energy cascade if the temperature is constant on each of the boundaries. This does not apply in Williams' work because the initial temperature field is not constant on the boundaries and the front forms. Williams

comments on the unrealistic nature of the front; the frontal zone does not tilt with height, and the vorticity at the front is zero. In contrast, realistic fronts have maximum vorticity at the frontal zone. It is also pointed out that the quasi-geostrophic equations cannot describe the entire frontogenesis process since as the frontal scale becomes small the local Rossby number will become large and the quasi-geostrophic approximation breaks down.

As mentioned, Charney [34] showed how the quasi-geostrophic equations require a surface temperature gradient for an energy cascade to occur and produce fronts, which is consistent with real world atmospheric fronts. This is due to a boundary term in the energy integral that evaluates to zero if the surface temperature is constant, this then violates energy conservation if a discontinuity were to appear. Charney also points out that the frontal motions in a quasi-geostrophic model cannot remain quasi-geostrophic because of the large velocity gradients and high Rossby numbers (QGE assume a small Rossby number).

Hoskins and Bretherton [61] also studied the geostrophic balance approximation across a front. They introduce several mechanism believed to be important in the formation of atmospheric fronts: (i) a horizontal deformation field, stretching in one horizontal dimension balanced by contraction in another, (ii) a horizontal shearing motion, (iii) a vertical deformation field balanced by vertical displacements, (iv) differential vertical motion, (v) latent heat release, (vi) surface friction, (vii) turbulence and mixing, and (viii) radiation. Their research confirms the time development of a horizontal deformation field acting upon a temperature gradient forms a vertical front in the quasi-geostrophic model. They claim that mechanisms (i) and (ii) are synoptic quasi-geostrophic scale motions whereas (iii) and (iv) are dominant on smaller frontal scales. Their research aims to show how the ageostrophic effects and true front formation arise as a response to the increasing temperature gradient. Hoskins and Bretherton refer to work by Edelmann [45] which used a five-layer model with a linear zonal thermal wind from the west with a maximum in the middle of the channel. In Edelmann's model, a small amplitude wave disturbance was imposed on this basic state which grew into a strong cyclone anticyclone system. This occurred regardless of whether surface friction or latent heat release was present, implying they are not essential for frontogenesis.

Hoskins and Bretherton [61] show that in an inviscid, adiabatic system, discontinuities in velocity and temperature can occur only at a boundary. This suggests

that frontogenesis will occur either at the surface (surface fronts) or at discontinuities in potential vorticity (upper tropospheric fronts). It is shown that the quasi-geostrophic equations describe an intensification of the temperature gradients and an increase in relative vorticity until the scaling assumptions required by the QGE breakdown. When the relative vorticity is no longer small compared to the Coriolis parameter, the ageostrophic motions become important and produce tilt of the front and motions up this slope. The vertical deformation field soon dominates and discontinuities tend to form at rigid boundaries in a finite time. Hoskins and Bretherton conclude that sharp surface fronts will form whenever quasi-geostrophic theory predicts a band of relative vorticity at the Earth's surface of magnitude comparable to the Coriolis parameter. Furthermore, the Boussinesq and rigid lid approximations are found to have little effect on the frontogenesis results.

Cullen and Purser [38] expands on the semi-geostrophic model used by Hoskins and Bretherton [61]. A finite difference approximation is used and takes the solution beyond the formation of a discontinuity where the front is found to propagate from the boundary to the fluid interior. Chynoweth and Sewell [36] also studied semi-geostrophic frontogenesis using Legendre transformations relating dual sets of variables and models fronts as a half-line of gradient discontinuity on a continuous convex surface, obtained as the self-intersection on a swallowtail surface. Convexification is used to remove non-physical multivaluedness. Chynoweth obtains a front which becomes steeper as it nears the ground. Holt [58] extended a Lagrangian model to study moist frontogenesis forced by a deformation flow. Holt found that adding cooling to the model to mimic evapouration effects had a significant effect on the overall evolution of the moist front. Whilst a semi-geostrophic model may increase accuracy in a simplified frontogenesis model, this accuracy would be lost in a more complex channel model where all fronts are not necessarily aligned with one axis. Therefore the quasi-geostrophic model is used for the research is this thesis.

Hoskins [60] points out that when upper atmospheric data became available in the 1950's, it could be seen that strong frontal regions occurred in the upper troposphere as well as near the surface of the Earth. Hoskins claims that experimental and observational data indicates that latent-heat release and other diabatic heating are not crucial to the frontogenesis process. Whilst a rigorous definition of a front is difficult to attain, Hoskins defines a front as a region whose length scale is comparable with the radius of deformation (NH/f) in one direction but much less in the cross direction. In this cross direction there are significant changes in buoyancy and

velocity with gradients tending to become very large in a finite time. The rotation of the fluid is crucial to the existence of the front.

Hoskins highlights two simple cases in which frontogenesis could occur. The first considered by Bergeron [19] is a simple deformation field $u = -\alpha x, v = \alpha y$. The second is a shear flow perpendicular to the temperature gradient investigated by Williams [128]. Hoskins concludes that quasi-geostrophic theory correctly suggests the formation of strong surface fronts with positive vorticity on the warm side of the front and that the front slopes in the vertical with warm air rising above the sloping cold region. Hoskins also highlights the role of the boundaries above and below the fluid; in the free atmosphere the ageostrophic circulation inhibits the formation of large gradients. However, quasi-geostrophic theory does not suggest the formation of frontal discontinuities in finite time, only exponential growth of gradients. More realistic models can be obtained by including the cross-front ageostrophic velocity producing the semi-geostrophic equations, or using the full primitive equations.

Therefore, it is certain that fronts can be produced using the quasi-geostrophic equations, even if they do not fully represent real atmospheric fronts. The quasi-geostrophic model will provide an indication of where frontogenesis will occur. The gap in research that this thesis will fill lies in a lack of numerical simulation of frontal dynamics using a finite element discretisation of the three-dimensional quasi-geostrophic equations with free-slip boundaries.

1.5 Finite Element Methods

The creation of finite element methods (FEM) has been attributed to the efforts of several groups and individuals that have contributed to the development of the modern method known as finite elements. A brief history of the method and an analysis of the contributors can be found in [54]. The development of FEM is often attributed to Courant, Argyris, Turner et al., Clough and Zienkiewicz. Clough gave the name finite element methods to the ideas and credited Turner for leading the development of the method in response to the need for solving complex engineering problems. Turner et al. [118] introduces triangular elements, derives the stiffness matrix and addresses convergence.

The idea behind FEM is to split the domain of a problem into a set of smaller

problems, or finite elements. The problem is then represented by a combination of equations on each element so that the global system can be solved. This is achieved using a form of Galerkin methods, where the problem is written into a weak formulation and approximation with basis functions. These elements can take many shapes, the most common of which are triangles and squares. This domain discretisation allows for meshes that represent very complex domains that may even change over time. This makes the finite element method useful for a wide range of applications across engineering and physics. The mesh flexibility of finite element methods is attractive for geophysical fluid flows, compared to the restrictive grids of finite difference and spectral methods.

However, these continuous Galerkin methods can perform poorly when attempting to simulate problems where the solution has sharp gradients or discontinuities. Such problems include shock waves, boundary layers and strong advection. This is where the discontinuous Galerkin finite element method is useful as it allows the solution to be discontinuous between elements. As the quasi-geostrophic model studied in this thesis is advection dominated and fronts contain sharp gradients by definition, a discontinuous approach seems prudent. The success of DG methods in this regard highlights them as a possible future solver for frontogenesis and atmospheric models.

Penalty terms are used to penalise discontinuities and enforce boundary conditions. Arnold et al. provides a unified analysis of the DG method for elliptic problems in [4]. The use of penalty methods for enforcing Dirichlet boundary conditions can be traced back to Lions (1968) [80] where elliptic problems with rough boundary data were considered. This approach was also used by Aubin (1970) [5] for finite difference approximations where he showed that the approximation converges to the analytical solution if the penalty parameter goes to infinity as the grid spacing goes to zero. In 1973, the penalty approach was used in the finite element method by Babuška [11] to weakly enforce zero Dirichlet boundary conditions. Convergence was not optimal because the weak formulation was inconsistent with the true solution to the strong problem. Nitsche [96] successfully implemented the penalty method with finite elements by including the boundary term produced by integration by parts in the weak formulation accompanied by another term to ensure symmetry of the discrete problem. Furthermore, Nitsche proved optimal order convergence if the penalty parameter scales with $1/h$ where h is the element size. It was soon realised that the continuity of the solution could be weakly enforced in the same way as Dirichlet boundary conditions with penalty terms [12].

One of the few papers that implement a finite element method for the quasi-geostrophic equations is by Erich Foster et al. [50, 51]. In his research he uses conforming finite elements to discretise the streamfunction formulation of the equations, requiring very complex elements. Foster describes the advantages of finite element methods, including natural treatment of boundaries and local grid adaptivity. It also mentions that there are very few instances of the numerical method being applied to the quasi-geostrophic equations. A streamfunction formulation of the equations is used yielding a fourth order partial differential equation, hence requiring the use of a high order C^1 element. Numerical tests are also done to verify the method and are found to be close to existing published results. A Mediterranean Sea mesh is also used to test the method on a complex domain (Figure 1.14). Results on this mesh had lower convergence rates than the theoretical results dictate which they attribute to the sharp corners of the domain. Foster concludes that the method met theoretical expectations, however, encouraged the use of non-conforming lower order finite element methods or other numerical techniques (finite difference, finite volume or spectral). This is probably due to the high computational cost that the method demanded.

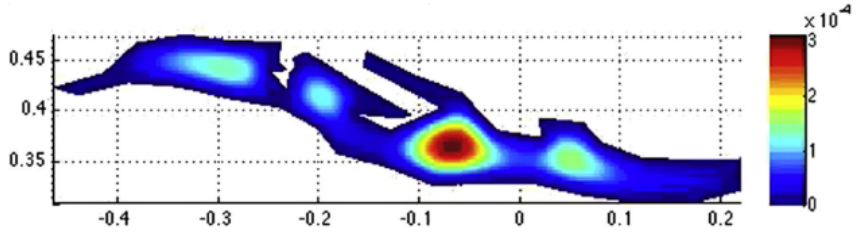

Figure 1.14: Streamfunction on a Mediterranean Sea mesh. [Reprinted from [51] with permission from Elsevier.]

Foster shows that a conforming method, whilst valid, is not the best approach. Although, it does confirm that finite element methods can be applied to quasi-geostrophic equations. Foster also takes on the task of dealing with the streamfunction formulation of the equations, something others seem to have avoided due to the high order partial differential equation (PDE) that it involves.

A paper by Bernsen et al. [20] constructs a mixed continuous and discontinuous Galerkin finite element discretization for a generalized vorticity streamfunction formulation in two spatial dimensions. This formulation consists of a hyperbolic (potential) vorticity equation and a linear elliptic equation for a transport streamfunc-

tion. This generalized formulation applies to three important systems in geophysical fluid dynamics; the incompressible Euler equations, the barotropic (where density depends only on pressure) quasi-geostrophic equations and the rigid-lid equations. Bernsen et al. considers multiple connected domains and shows energy is conserved in the system.

The equations in Bernsen's research are inviscid with potential vorticity $\xi = \xi(x, y, t)$ and streamfunction $\psi = \psi(x, y, t)$ in a bounded domain $\Omega \subset \mathbb{R}^2$.

$$\partial_t \xi / A + \nabla \cdot (\xi \overrightarrow{U}) = 0, \tag{1.21a}$$

$$\overrightarrow{U} = \nabla^{\perp} \psi, \tag{1.21b}$$

$$\nabla \cdot (A \nabla \psi) - B\psi + D = \xi / A, \tag{1.21c}$$

where the two-dimensional curl operator is given by $\nabla^{\perp} = [-\partial_y, \partial_x]^T$.

Choose the coefficients $A = 1, B = f_0^2/(gH), D = \beta y$ with Coriolis parameter $f_0 = 2\Omega_e \sin(\varphi_0)$ and $\beta = 2\Omega_e \cos(\varphi_0)/a$, where a is Earth's radius, φ_0 a typical value of the latitude and Ω_e Earth's rotation speed. Doing this reduces the general equations (1.21) to the quasi-geostrophic equations in two dimensions.

Another alternative approach to discretising the QGE is using a full discontinuous Galerkin method for the potential vorticity and streamfunction, then recreating the velocity and potential vorticity from the streamfunction using a Raviart-Thomas projection to recover divergence properties. The accuracy of the Raviart-Thomas projection is proven by Alexandre Ern [47], but, Alexandre's work applies the technique to a stationary problem. This approach was explored (Section B.2), however, results appeared to show this method to be insufficient as the reconstruction did not behave well once fed back into the equations and the numerical solution deteriorated over time. The method presented in Bernsen et al. [20] avoids this problem with the matched continuous/discontinuous method where the velocity is single valued at element boundaries due to the fact that the streamfunction is continuous. This method can be extended into three dimensions since the advecting velocity remains the same as (1.21b). Bernsen et al. does not consider viscous diffusion terms or full three-dimensionality.

Bernsen et al. considers treatment of free-slip boundary conditions on multiple

connected domains, important in geophysical and meteorological applications. The free-slip condition $\overrightarrow{U} \cdot \boldsymbol{n} = 0$, for outward unit normal $\boldsymbol{n}$ to the boundary, requires the streamfunction to take unknown values on the boundary that can depend on time. Although, the streamfunction boundary values were prescribed using exact solutions during numerical testing.

Energy conservation of the discretisation was shown for a $\theta-$method time discretisation, with energy fully conserved for $\theta = 1/2$. Despite this, the implicit method would require solving the full system in a large system matrix somehow treating the continuous and discontinuous parts appropriately. This could be the reason that numerical tests were performed using an explicit timestepping method, where tendency towards energy conservation was shown numerically.

Bernsen et al. derived error estimates, claiming convergence of order $O(h^p)$ for grid spacing h and p^{th} order basis functions. Regardless, numerical experiments tended to converge with an order higher than this. The test used for the quasi-geostrophic case is a travelling wave solution which serves as a useful numerical convergence test for the method presented in this thesis.

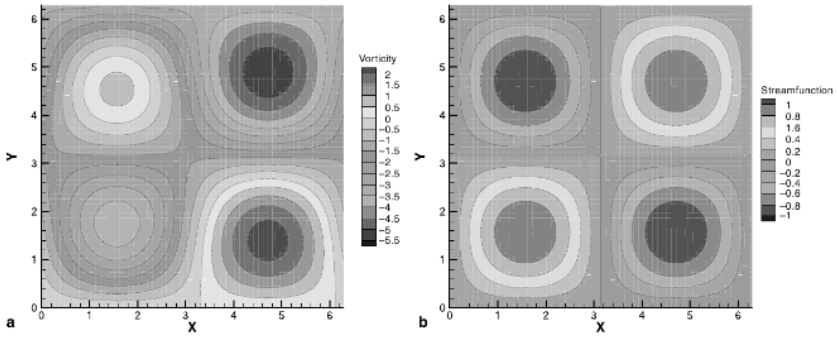

Figure 1.15: (a) Potential vorticity and (b) Streamfunction at $t = 12\pi$ for travellinig wave. [Reprinted from [20] with permission from Elsevier.]

Bernsen et al. [20] highlights a viable finite element method for the two-dimensional quasi-geostrophic equations. This provides an alternative in the geophysical field as traditionally fluid dynamics codes run on spectral methods which are awkward when dealing with topographic boundaries. Bernsen's research is important in highlighting that fluid dynamics simulations can be done with the flexible and powerful finite element methods that are becoming more popular within atmospheric simulations.

It is apparent that some work has gone towards implementing a finite element discretisation of the quasi-geostrophic equations, in particular for the two-dimensional case. However, there appears to be no work on a finite element method for the full three-dimensional quasi-geostrophic equations with complete free-slip boundary treatment. The main objective of this thesis is to develop such a scheme to fill this research gap and test it numerically whilst using the method to provide some investigation into weather front formation.

1.6 Thesis Outline

This thesis aims to develop a fully three-dimensional quasi-geostrophic code using finite element and finite difference methods. Previous numerical QGE codes have been restricted to two-dimensions with zero or approximate diffusive terms [20, 50, 51, 63] or two/three layer models [56, 87, 89]. This thesis extends this to a fully three-dimensional implementation with diffusive terms that are consistent with the model and generalised free-slip boundary conditions. The purpose of this new numerical method is to allow for the role of frontogenesis to be studied using a quasi-geostrophic model that is less computationally intensive than the primitive equations. This model is then used to investigate the bend up of fronts in a meandering jet as a possible mechanism underlying the $k^{-5/3}$ kinetic energy regime observed in the atmosphere.

A literature review in the introduction of this thesis outlines the current research that exists within this area as well as the progression of the finite element numerical techniques that will be used. This thesis begins by discussing the equations and assumptions involved in atmospheric modelling in Chapter 2 and deriving the three-dimensional quasi-geostrophic equations including diffusion and forcing terms which are seldom included in the literature [39, 99]. Energy equations for the QGE are also derived. The QGE are then prepared for discretisation by non-dimensionalisation of the equations, followed by a derivation of the top and bottom temperature equations required to satisfy vertical boundary conditions and formulation of the expressions used to calculate the streamfunction boundary values at the north and south walls. The mathematical framework needed to formulate finite element methods is provided in Chapter 3. In Chapter 4, a combination of finite element methods in the horizontal directions and finite difference methods in the vertical are used to de-

velop a discretisation of the quasi-geostrophic equations. Numerical tests are done in Chapter 5 to verify the method converges and exhibits expected vortex dynamics. Chapter 6 presents a discussion of the frontogenesis results produced by a turbulent jet channel model with a conclusion in Chapter 7.

Chapter 2

Atmospheric Equations

The equations of motion for a fluid are discussed and the quasi-geostrophic model is derived and non-dimensionalised. The difficulty in dealing with the boundary conditions in the three-dimensional quasi-geostrophic model is also explicitly treated which has not been widely studied for a continuous model in literature [51, 56, 84]. Boundary conditions are usually only treated for a three-layer model or simplified to assume that the streamfunction is zero on the boundary.

2.1 Equations of Motion

A fluid continuum is usually described mathematically using the Navier-Stokes equations, which were derived by Navier, Poisson, Saint-Venant and Stokes between 1827 and 1845 [1]. These equations in a rotating frame of reference provide the basis for atmospheric models. However, further equations are needed to described the movement of energy and water vapour in the atmosphere as these can change the properties of the atmosphere. For efficient numerical simulation of an atmospheric model, certain approximations can be made to produce the Primitive Equations. To study the key dynamics of the atmosphere, one can strip the equations down even further resulting in the quasi-geostrophic equations. The background information provided here can be found in Cushman-Roisin and Beckers [39] and McWilliams [86].

2.1.1 Navier-Stokes Equations

At the heart of any fluid flow, the equations that govern the flow are the Navier-Stokes equations [1, 39]. For a velocity $\boldsymbol{u} = (u, v, w)$, density ρ, pressure p and

forcing $\boldsymbol{F} = (F_x, F_y, F_z)$ the Navier-Stokes equations are

$$\rho\left(\frac{\partial u}{\partial t} + u\frac{\partial u}{\partial x} + v\frac{\partial u}{\partial y} + w\frac{\partial u}{\partial z}\right) = -\frac{\partial p}{\partial x} + \frac{\partial \tau^{xx}}{\partial x} + \frac{\partial \tau^{xy}}{\partial y} + \frac{\partial \tau^{xz}}{\partial z} + \rho F_x \tag{2.1a}$$

$$\rho\left(\frac{\partial v}{\partial t} + u\frac{\partial v}{\partial x} + v\frac{\partial v}{\partial y} + w\frac{\partial v}{\partial z}\right) = -\frac{\partial p}{\partial y} + \frac{\partial \tau^{yx}}{\partial x} + \frac{\partial \tau^{yy}}{\partial y} + \frac{\partial \tau^{yz}}{\partial z} + \rho F_y \tag{2.1b}$$

$$\rho\left(\frac{\partial w}{\partial t} + u\frac{\partial w}{\partial x} + v\frac{\partial w}{\partial y} + w\frac{\partial w}{\partial z}\right) = -\frac{\partial p}{\partial z} - \rho g + \frac{\partial \tau^{xz}}{\partial x} + \frac{\partial \tau^{yz}}{\partial y} + \frac{\partial \tau^{zz}}{\partial z} + \rho F_z, \tag{2.1c}$$

where the stress tensor

$$\boldsymbol{\tau} = \begin{bmatrix} \tau^{xx} & \tau^{xy} & \tau^{xz} \\ \tau^{yx} & \tau^{yy} & \tau^{yz} \\ \tau^{zx} & \tau^{zy} & \tau^{zz} \end{bmatrix} \tag{2.2}$$

represents the normal and shear stresses due to friction. The three equations represent the momentum in the x, y and z directions respectively. For an atmospheric model, rotation must be introduced to these equations as well as some other governing equations. For a given latitude φ and rotation Ω, the rotation vector of a three-dimensional rotating planet is $\boldsymbol{\Omega_e} = (0, \Omega\cos\varphi, \Omega\sin\varphi)$ [39]. The Navier-Stokes equations in this rotating frame are,

$$\rho\left(\frac{\partial u}{\partial t} + u\frac{\partial u}{\partial x} + v\frac{\partial u}{\partial y} + w\frac{\partial u}{\partial z} + f_* w - f v\right) = -\frac{\partial p}{\partial x} + \frac{\partial \tau^{xx}}{\partial x} + \frac{\partial \tau^{xy}}{\partial y} + \frac{\partial \tau^{xz}}{\partial z} + \rho F_x \tag{2.3a}$$

$$\rho\left(\frac{\partial v}{\partial t} + u\frac{\partial v}{\partial x} + v\frac{\partial v}{\partial y} + w\frac{\partial v}{\partial z} + f u\right) = -\frac{\partial p}{\partial y} + \frac{\partial \tau^{yx}}{\partial x} + \frac{\partial \tau^{yy}}{\partial y} + \frac{\partial \tau^{yz}}{\partial z} + \rho F_y \tag{2.3b}$$

$$\rho\left(\frac{\partial w}{\partial t} + u\frac{\partial w}{\partial x} + v\frac{\partial w}{\partial y} + w\frac{\partial w}{\partial z} - f_* u\right) = -\frac{\partial p}{\partial z} - \rho g + \frac{\partial \tau^{xz}}{\partial x} + \frac{\partial \tau^{yz}}{\partial y} + \frac{\partial \tau^{zz}}{\partial z} + \rho F_z, \tag{2.3c}$$

where $f = 2\Omega\sin\varphi$ is the Coriolis parameter and $f_* = 2\Omega\cos\varphi$ is the reciprocal Coriolis parameter. The centrifugal force is ignored since the Earth's slightly ellipsoidal shape causes the gravitational and centrifugal forces to result in a combined force that is aligned with the local vertical to the surface. This adjusted gravitational acceleration is what g represents. Note that the variables in these equations are now as they would be observed in the rotating frame of reference, that is from the viewpoint of someone standing on the surface of the Earth or a satellite in geostationary orbit. This provides equations for all the velocity components u, v and w, now equations for the pressure p and density ρ are required. An equation for the density is provided by conservation of mass. This means that any compressions in

the fluid must be balanced with an expansion elsewhere in the fluid. The *continuity equation* describes this behaviour,

$$\frac{\partial \rho}{\partial t} + \frac{\partial}{\partial x}(\rho u) + \frac{\partial}{\partial y}(\rho v) + \frac{\partial}{\partial z}(\rho w) = 0. \tag{2.4}$$

For pressure the *equation of state* must be considered, which for air is given by,

$$\rho = \frac{p}{RT(1 + 0.608 q_s)} \tag{2.5}$$

where $R = 287\,\mathrm{m^2 s^{-2} K^{-1}}$, T is absolute temperature and q_s is the specific humidity defined as the ratio of mass of water vapour to the total mass of air. Note that for seawater, salinity needs to be considered (see [39]). The introduction of the variables T and q_s requires further equations. One of these is the *energy equation* which arises from conservation of energy,

$$\rho C_v \left[\frac{\partial T}{\partial t} + \left(u \frac{\partial T}{\partial x} + v \frac{\partial T}{\partial y} + w \frac{\partial T}{\partial z} \right) \right] + p \left(\frac{\partial u}{\partial x} + \frac{\partial v}{\partial y} + \frac{\partial w}{\partial z} \right) = k_T \Delta T + H_t. \tag{2.6}$$

Here $C_v = 718\,\mathrm{J\ kg^{-1} K^{-1}}$ is the heat capacity, k_T is thermal conductivity of the fluid and H_t is external heating. Finally, the equation for specific humidity is

$$\frac{\partial q_s}{\partial t} + \left(u \frac{\partial q_s}{\partial x} + v \frac{\partial q_s}{\partial y} + w \frac{\partial q_s}{\partial z} \right) = k_q \Delta q_s, \tag{2.7}$$

where k_q is the specific humidity diffusion coefficient. This equation can be complicated by evapouration and condensation processes.

2.1.2 Boussinesq Approximation

The equations in their current form are quite complex and would be very costly to simulate numerically. A standard approximation to make in geophysical fluid dynamics is the *Boussinesq Approximation*. This approximation is based on the fact that the density of a geophysical fluid does not vary greatly from a mean value [39]. Therefore density can be expressed as

$$\rho = \rho_0 + \rho'(x, y, z, t) \tag{2.8}$$

where $|\rho'| \ll \rho_0$. Inserting this into the continuity equation (2.4) and ignoring terms of order ρ',

$$\frac{\partial u}{\partial x} + \frac{\partial v}{\partial y} + \frac{\partial w}{\partial z} = 0. \tag{2.9}$$

For the x and y momentum equations (2.3a) and (2.3b), any term multiplied by ρ is dominated by ρ_0 and terms multiplied by density variations can be ignored. With the assumption of a Newtonian fluid the stress tensor is defined as

$$\begin{aligned}
\tau^{xx} &= \mu\left(\frac{\partial u}{\partial x} + \frac{\partial u}{\partial x}\right), \tau^{xy} = \mu\left(\frac{\partial u}{\partial y} + \frac{\partial v}{\partial x}\right), \tau^{xz} = \mu\left(\frac{\partial u}{\partial z} + \frac{\partial w}{\partial x}\right) \\
\tau^{yy} &= \mu\left(\frac{\partial v}{\partial y} + \frac{\partial v}{\partial y}\right), \tau^{yz} = \mu\left(\frac{\partial v}{\partial z} + \frac{\partial w}{\partial y}\right), \tau^{zz} = \mu\left(\frac{\partial w}{\partial z} + \frac{\partial w}{\partial z}\right)
\end{aligned} \tag{2.10}$$

where μ is the coefficient of dynamic viscosity. Dividing the x and y momentum equations by ρ_0 and setting the kinematic viscosity $\nu = \mu/\rho_0$,

$$\frac{\partial u}{\partial t} + u\frac{\partial u}{\partial x} + v\frac{\partial u}{\partial y} + w\frac{\partial u}{\partial z} + f_* w - fv = -\frac{1}{\rho_0}\frac{\partial p}{\partial x} + \nu\Delta u + F_x \tag{2.11}$$

$$\frac{\partial v}{\partial t} + u\frac{\partial v}{\partial x} + v\frac{\partial v}{\partial y} + w\frac{\partial v}{\partial z} + fu = -\frac{1}{\rho_0}\frac{\partial p}{\partial y} + \nu\Delta v + F_y. \tag{2.12}$$

Now the z momentum equation (2.3c) requires treatment of the gravity term ρg. To do this define the hydrostatic pressure p_0 which varies only in z so that for some reference pressure P_0

$$p = p_0(z) + p'(x, y, z, t) \text{ where } p_0(z) = P_0 - \rho_0 g z. \tag{2.13}$$

This gives

$$\frac{dp_0}{dz} = -\rho_0 g, \tag{2.14}$$

then the z momentum equation becomes

$$\frac{\partial w}{\partial t} + u\frac{\partial w}{\partial x} + v\frac{\partial w}{\partial y} + w\frac{\partial w}{\partial z} - f_* u = -\frac{1}{\rho_0}\frac{\partial p'}{\partial z} - \frac{\rho' g}{\rho_0} + \nu\Delta w + F_z. \tag{2.15}$$

The $\rho' g$ term is important for buoyancy force in the equations, therefore ignoring it would result in a bad geophysical model. Finally, the energy equation (2.6) and specific humidity equation (2.7) can be linearised, then with the assumption that heat and water vapour diffuse at the same rate they can be combined into the equation

$$\frac{\partial \rho'}{\partial t} + u\frac{\partial \rho'}{\partial x} + v\frac{\partial \rho'}{\partial y} + w\frac{\partial \rho'}{\partial z} = \kappa\Delta\rho' + H_t. \tag{2.16}$$

Since the variables ρ and p do not appear explicitly in the equations, the prime notation on the variations ρ' and p' will be dropped from now on.

2.1.3 Eddy Coefficients

Geophysical flows are typically very turbulent. Since turbulence can manifest at many different scales, it requires very refined computational grids to sufficiently resolve a turbulent flow. This can be extremely computationally expensive, therefore, further modelling is required to be able to incorporate the effects of subgrid-scale turbulence into the simulation. The statistical average of a flow is described by the *Reynolds-averaged equations*. These equations are achieved by defining, for each variable u, v, w, p and ρ, the mean $\langle u \rangle$ and fluctuation u' such that

$$u = \langle u \rangle + u'. \tag{2.17}$$

Definition 2.1. *The* time average $\langle u \rangle$ *of a variable* u *is given by*

$$\langle u \rangle = \frac{1}{T} \int_{t_0}^{t_0+T} u \, dt, \tag{2.18}$$

for some time t_0 *and time scale* T *that is long enough to average the turbulent motions but short enough to retain the slow evolutions of the flow. The* fluctuation u' *is such that* $\langle u' \rangle = 0$.

To obtain a true time average take the limit as $T \to \infty$, but this would result in a stationary solution. Note that, by basic properties of a converging sequence, there will exist some time scale T such that integration from t_0 to T will be arbitrarily close to the true time average. Therefore, it is possible to numerically calculate such averages with a small error. Averaging over time on the governing equations and using the following property results in equations for the average fluid flow.

Proposition 2.2. *The time average of a product of two variables* u *and* v *is*

$$\langle uv \rangle = \langle u \rangle \langle v \rangle + \langle u'v' \rangle. \tag{2.19}$$

Proof. Using the definition of time averages,

$$\begin{aligned}\langle uv\rangle &= \int_{t_0}^{t_0+T} uv\,dt = \int_{t_0}^{t_0+T} (\langle u\rangle + u')(\langle v\rangle + v')\,dt \\ &= \int_{t_0}^{t_0+T} \langle u\rangle\langle v\rangle + \langle u\rangle v' + \langle v\rangle u' + u'v'\,dt \\ &= \int_{t_0}^{t_0+T} \langle u\rangle\langle v\rangle + u'v'\,dt + \langle u\rangle \underbrace{\int_{t_0}^{t_0+T} v'\,dt}_{0} + \langle v\rangle \underbrace{\int_{t_0}^{t_0+T} u'\,dt}_{0} \\ &= \langle u\rangle\langle v\rangle + \langle u'v'\rangle,\end{aligned} \tag{2.20}$$

where the last two terms vanish by the definition of fluctuations. Assuming that the limits as $T \to \infty$ exist (which is true of a fluid velocities, pressures and densities due to the bounded nature of a fluid system) this result also holds for a true time average. □

Using the continuity equation (2.9) to write the governing equations in conservative form and averaging over time, the x momentum equation becomes,

$$\frac{\partial\langle u\rangle}{\partial t} + \frac{\partial\langle uu\rangle}{\partial x} + \frac{\partial\langle vu\rangle}{\partial y} + \frac{\partial\langle wu\rangle}{\partial z} + f_*\langle w\rangle - f\langle v\rangle = -\frac{1}{\rho_0}\frac{\partial\langle p\rangle}{\partial x} + \nu\Delta\langle u\rangle + \langle F_x\rangle. \tag{2.21}$$

Definition 2.3. *Denote the three dimensional coordinate system as* $(x, y, z) = (x_1, x_2, x_3)$. *Let* $\boldsymbol{u} = (u_1, u_2, u_3)$ *be a velocity vector and* ρ *be some other fluid quantity. Then the* eddy viscosity approximation *is*

$$-\langle u_i'\rho'\rangle \approx \nu_e \frac{\partial\langle\rho\rangle}{\partial x_i}, \tag{2.22}$$

for some eddy viscosity coefficient ν_e.

Now apply Proposition 2.2 to the advection terms,

$$\begin{aligned}\frac{\partial\langle uu\rangle}{\partial x} + \frac{\partial\langle vu\rangle}{\partial y} + \frac{\partial\langle wu\rangle}{\partial z} = \quad & \frac{\partial(\langle u\rangle\langle u\rangle)}{\partial x} + \frac{\partial(\langle v\rangle\langle u\rangle)}{\partial y} + \frac{\partial(\langle w\rangle\langle u\rangle)}{\partial z} \\ & + \frac{\partial\langle u'u'\rangle}{\partial x} + \frac{\partial\langle v'u'\rangle}{\partial y} + \frac{\partial\langle w'u'\rangle}{\partial z}\end{aligned} \tag{2.23}$$

and make the standard eddy viscosity approximation for the Reynolds stresses $\langle u'u'\rangle$, $\langle u'v'\rangle$ and $\langle u'w'\rangle$ [86],

$$-\langle u'u'\rangle \approx \mathcal{A}_H \frac{\partial\langle u\rangle}{\partial x},\ -\langle v'u'\rangle \approx \mathcal{A}_H \frac{\partial\langle u\rangle}{\partial y},\ -\langle w'u'\rangle \approx \mathcal{A}_V \frac{\partial\langle u\rangle}{\partial z}, \tag{2.24}$$

where separate eddy viscosities $\mathcal{A}_H$ and $\mathcal{A}_V$ are used for the horizontal and vertical since the horizontal spatial dimensions typically cover a much larger area and therefore need to model a greater amount of subgrid-scale turbulence. Modelling turbulence with eddy coefficients which may depend on grid properties and vary in spatial dimensions is a form of *subgrid-scale parameterisation*. Performing similar approximations for the y and z momentum equations,

$$\frac{du}{dt} + f_* w - fv = -\frac{1}{\rho_0}\frac{\partial p}{\partial x} + \frac{\partial}{\partial x}\left(\mathcal{A}_H \frac{\partial u}{\partial x}\right) + \frac{\partial}{\partial y}\left(\mathcal{A}_H \frac{\partial u}{\partial y}\right) + \frac{\partial}{\partial z}\left(\mathcal{A}_V \frac{\partial u}{\partial z}\right) + F_x \tag{2.25a}$$

$$\frac{dv}{dt} + fu = -\frac{1}{\rho_0}\frac{\partial p}{\partial y} + \frac{\partial}{\partial x}\left(\mathcal{A}_H \frac{\partial v}{\partial x}\right) + \frac{\partial}{\partial y}\left(\mathcal{A}_H \frac{\partial v}{\partial y}\right) + \frac{\partial}{\partial z}\left(\mathcal{A}_V \frac{\partial v}{\partial z}\right) + F_y \tag{2.25b}$$

$$\frac{dw}{dt} - f_* u = -\frac{1}{\rho_0}\frac{\partial p}{\partial z} - \frac{g\rho}{\rho_0} + \frac{\partial}{\partial x}\left(\mathcal{A}_H \frac{\partial w}{\partial x}\right) + \frac{\partial}{\partial y}\left(\mathcal{A}_H \frac{\partial w}{\partial y}\right) + \frac{\partial}{\partial z}\left(\mathcal{A}_V \frac{\partial w}{\partial z}\right) + F_z \tag{2.25c}$$

where it is understood that all variables have been replaced with averages, therefore, the angle bracket notation is omitted. Observe that the viscosity coefficient ν has been absorbed into the eddy coefficients. The above equations have also used the material time derivative

$$\frac{du}{dt} = \frac{\partial u}{\partial t} + u\frac{\partial u}{\partial x} + v\frac{\partial u}{\partial y} + w\frac{\partial u}{\partial z}. \tag{2.26}$$

Similarly, for the energy equation use the horizontal eddy viscosity $\mathcal{K}_H$ and vertical eddy diffusivity $\mathcal{K}_V$. It is acceptable to use $\mathcal{K}_H = \mathcal{A}_H$, however, the coefficients are differentiated here for reasons that will become apparent when deriving the quasi-geostrophic equations in Section 2.3. The vertical eddy diffusivity $\mathcal{K}_V$ is distinguished from the vertical momentum eddy viscosity $\mathcal{A}_V$ for reasons discussed in [39],

$$\frac{\partial \rho}{\partial t} + u\frac{\partial \rho}{\partial x} + v\frac{\partial \rho}{\partial y} + w\frac{\partial \rho}{\partial z} = \frac{\partial}{\partial x}\left(\mathcal{K}_H \frac{\partial \rho}{\partial x}\right) + \frac{\partial}{\partial y}\left(\mathcal{K}_H \frac{\partial \rho}{\partial y}\right) + \frac{\partial}{\partial z}\left(\mathcal{K}_V \frac{\partial \rho}{\partial z}\right) + H_t. \tag{2.27}$$

The continuity equation is unchanged by the decomposition of variables into mean

and fluctuations. A commonly used horizontal eddy viscosity is given by [39],

$$\mathcal{A}_H = \Delta x \Delta y \sqrt{\left(\frac{\partial u}{\partial x}\right)^2 + \left(\frac{\partial v}{\partial y}\right)^2 + \frac{1}{2}\left(\frac{\partial u}{\partial y} + \frac{\partial v}{\partial x}\right)^2}. \tag{2.28}$$

2.1.4 Scales of Motion

In order to simplify the equations further, scales are introduced for each of the variables involved. For the horizontal lengths x and y assign a scale L with typical atmospheric values of around 10^5m. In the vertical z assign H with typical values much less than horizontal length scales around 10^3 m. Time t has the scale T with geophysical values typically 10^4 s. Also, assign horizontal velocity scales U and V to variables u and v with typical values of 10 ms^{-1}, and W to the vertical velocity w. Finally, P and $\Delta\rho$ denote the scales of pressure p and density fluctuations ρ respectively.

Within geophysical fluid dynamics it is assumed that the time scale is greater than or of the same order of the time scales involved with rotation effects,

$$T \gtrsim \frac{1}{\Omega} \tag{2.29}$$

and velocity and length scales satisfy

$$\frac{U}{L} \lesssim \Omega. \tag{2.30}$$

Also, assume that the horizontal area of the domain is much larger than the vertical direction

$$H \ll L. \tag{2.31}$$

By considering the continuity equation (2.9) one can determine that W/H is less than or on the order of U/L otherwise $\partial w/\partial z = 0$ and w is constant in the vertical, therefore,

$$W \lesssim \frac{HU}{L} \tag{2.32}$$

and by (2.31)

$$W \ll U, \tag{2.33}$$

meaning geophysical flows are close to two-dimensional. Now, observing the scales

of the Coriolis terms in the $x-$momentum equation (2.25a),

$$f_* w \sim \Omega W \text{ and } fv \sim \Omega U. \tag{2.34}$$

Since $W \ll U$, the first of these terms can be neglected.

Due to the importance of rotation in geophysical fluids, assume the pressure gradient term scales as the Coriolis terms,

$$\frac{P}{\rho_0 L} = \Omega U. \tag{2.35}$$

Furthermore, assume that dissipation processes are smaller than Coriolis forces,

$$\frac{\mathcal{A}_H U}{L^2} \lesssim \Omega U, \ \frac{\mathcal{A}_V U}{H^2} \lesssim \Omega U, \tag{2.36}$$

but not small enough to be neglected otherwise the model would lose the effects of subgrid-scale turbulence. This scaling also applies to the $y-$momentum equation (2.25b). The vertical momentum equation (2.25c)

$$\begin{aligned} &\frac{\partial w}{\partial t} + u\frac{\partial w}{\partial x} + v\frac{\partial w}{\partial y} + w\frac{\partial u}{\partial z} - f_* u = \\ &-\frac{1}{\rho_0}\frac{\partial p}{\partial z} - \frac{g\rho}{\rho_0} + \frac{\partial}{\partial x}\left(\mathcal{A}_H \frac{\partial w}{\partial x}\right) + \frac{\partial}{\partial y}\left(\mathcal{A}_H \frac{\partial w}{\partial y}\right) + \frac{\partial}{\partial z}\left(\mathcal{A}_V \frac{\partial w}{\partial z}\right) + F_z, \end{aligned} \tag{2.37}$$

can be simplified further by observing the scales of each term,

$$\frac{W}{T}, \frac{UW}{L}, \frac{UW}{L}, \frac{W^2}{H}, \Omega U, \frac{P}{\rho_0 H}, \frac{g\Delta\rho}{\rho_0}, \frac{\mathcal{A}_H W}{L^2}, \frac{\mathcal{A}_H W}{L^2}, \frac{\mathcal{A}_V W}{L^2}, F_z. \tag{2.38}$$

For the first term $W/T \lesssim \Omega W \ll \Omega U$ by (2.29) and (2.33). Using (2.30), (2.32) and (2.33) it can be seen that the advection terms are also much less than ΩU:

$$\frac{UW}{L} \lesssim \Omega W \ll \Omega U \quad \text{and} \quad \frac{W^2}{H} \lesssim \frac{WU}{L} \lesssim \Omega W \ll \Omega U. \tag{2.39}$$

Therefore, the first four terms are dominated by the Coriolis term and can be neglected. However, the Coriolis term is also small compared to the vertical pressure gradient since by (2.33) and (2.35)

$$\Omega U \sim \frac{P}{\rho_0 L} \ll \frac{P}{\rho_0 H}. \tag{2.40}$$

Finally, assuming that diffusion and external forcing cannot dominate Coriolis terms

$$\frac{\mathcal{A}_H U}{L^2} \lesssim \Omega W \ll \Omega U \quad \text{and} \quad \frac{\mathcal{A}_V U}{H^2} \lesssim \Omega W \ll \Omega U, \tag{2.41}$$

and can therefore be neglected. The most dominant terms in the $z-$momentum equation forms the *hydrostatic balance*

$$0 = -\frac{1}{\rho_0}\frac{\partial p}{\partial z} - \frac{g\rho}{\rho_0}. \tag{2.42}$$

That is the pressure exerted by the air close to the ground is balanced by the weight of the air above. The hydrostatic balance approximation holds when $H \ll L$ as is generally true in geophysical flows, this does not hold if the horizontal and vertical length scales become comparable.

2.1.5 Primitive Equations

As previously seen, the Boussinesq approximation assumes that the density of a fluid ρ does not depart very much from a reference density ρ_0, this assumption means that the variations in density have no effect on the flow except for buoyancy forces. Applying the Boussinesq and hydrostatic approximations to the Navier-Stokes equations produces the *primitive equations*, which are used as the basis of atmospheric modelling. For a full three-dimensional velocity $\boldsymbol{u} = (u, v, w)$, pressure p and density ρ the equations are,

$$\begin{aligned}
&\frac{\partial u}{\partial t} + u\frac{\partial u}{\partial x} + v\frac{\partial u}{\partial y} + w\frac{\partial u}{\partial z} - fv = \\
&-\frac{1}{\rho_0}\frac{\partial p}{\partial x} + \frac{\partial}{\partial x}\left(\mathcal{A}_H\frac{\partial u}{\partial x}\right) + \frac{\partial}{\partial y}\left(\mathcal{A}_H\frac{\partial u}{\partial y}\right) + \frac{\partial}{\partial z}\left(\mathcal{A}_V\frac{\partial u}{\partial z}\right) + F_x && \text{(2.43a)}\\
&\frac{\partial v}{\partial t} + u\frac{\partial v}{\partial x} + v\frac{\partial v}{\partial y} + w\frac{\partial v}{\partial z} + fu = \\
&-\frac{1}{\rho_0}\frac{\partial p}{\partial y} + \frac{\partial}{\partial x}\left(\mathcal{A}_H\frac{\partial v}{\partial x}\right) + \frac{\partial}{\partial y}\left(\mathcal{A}_H\frac{\partial v}{\partial y}\right) + \frac{\partial}{\partial z}\left(\mathcal{A}_V\frac{\partial v}{\partial z}\right) + F_y && \text{(2.43b)}\\
&0 = -\frac{\partial p}{\partial z} - \rho g && \text{(2.43c)}\\
&\frac{\partial u}{\partial x} + \frac{\partial v}{\partial y} + \frac{\partial w}{\partial z} = 0 && \text{(2.43d)}\\
&\frac{\partial \rho}{\partial t} + u\frac{\partial \rho}{\partial x} + v\frac{\partial \rho}{\partial y} + w\frac{\partial \rho}{\partial z} = \\
&\frac{\partial}{\partial x}\left(\mathcal{K}_H\frac{\partial \rho}{\partial x}\right) + \frac{\partial}{\partial y}\left(\mathcal{K}_H\frac{\partial \rho}{\partial y}\right) + \frac{\partial}{\partial z}\left(\mathcal{K}_V\frac{\partial \rho}{\partial z}\right) + H_t, && \text{(2.43e)}
\end{aligned}$$

where ρ_0 is a reference density, g is gravitational acceleration, $f = 2\Omega \sin\varphi$ is the Coriolis parameter (for a latitude φ) and $\mathcal{A}_H$, $\mathcal{A}_V$, $\mathcal{K}_H$ and $\mathcal{K}_V$ are eddy viscosity and diffusivity coefficients. The first three equations govern x, y and z momentum. The fourth equation is the continuity equation and the fifth is the energy equation.

2.2 Rotation and the Shallow Water Equations

The Earth is a rotating body with a rotation rate 2π radians per day $\approx 0.73 \times 10^{-4}$ rad s^{-1}. With the Earth's atmosphere being thin on a planetary scale, one can use a Cartesian coordinate frame with rotation about a vertical axis aligned with the direction of gravity. Whilst small scale motions experience very little influence from rotation, large scales motions will be affected. However, due to the thinness of the atmosphere, only the vertical component of Earth's rotation is significant as seen in section 2.1.4 (although this isn't necessarily true close to the equator). For the Earth's true rotation vector $\boldsymbol{\Omega_e} = (0, \Omega\cos\varphi, \Omega\sin\varphi)$ with its direction pointing outward through the North Pole, consider the local vertical component

$$\boldsymbol{\Omega} = (\boldsymbol{\Omega_e} \cdot \hat{\boldsymbol{z}}) = |\boldsymbol{\Omega_e}| \sin(\varphi)\hat{\boldsymbol{z}} = (0, 0, \Omega\sin\varphi), \tag{2.44}$$

where φ is the latitude and the unit vector in the vertical $\hat{\boldsymbol{z}} = (0, 0, 1)$. The magnitude $\Omega = |\boldsymbol{\Omega}|$ is positive in the Northern Hemisphere and negative in the Southern Hemisphere. The Coriolis parameter $f = 2\Omega\sin\varphi$ can be approximated using a Taylor expansion around a reference latitude φ_0. Let the meridional coordinate y be measured from the reference latitude φ_0 then $\varphi = \varphi_0 + y/a$ for Earth's radius $a \approx 6.4 \times 10^6$m [86], where y/a is a small perturbation such that $\varphi - \varphi_0 \ll 1$. The Coriolis parameter may then be approximated as

$$f = 2\Omega\sin\varphi_0 + 2\Omega\cos\varphi_0(\varphi - \varphi_0) + ... = f_0 + \beta y + ... \tag{2.45}$$

The Coriolis frequency and its gradient are defined as

$$f_0 = 2\Omega\sin\varphi_0 \text{ and } \beta = \frac{2\Omega}{a}\cos\varphi_0. \tag{2.46}$$

In the Northern Hemisphere f_0 is positive and in the Southern Hemisphere it is negative, whilst vanishing at the equator and being the strongest at the poles. The β parameter is positive everywhere and is largest at the equator. This is known as the f-plane approximation when the typical length scale L is small and the β term is dropped, this comes from the visualisation of a plane tangent to the surface of the

planet at the expansion point. Otherwise, when L/a is not negligible, the β term is used to approximate the curvature of the Earth and is known as the β-plane approximation. This approximation means the rotation does not introduce nonlinear terms into the governing equations, therefore, making them easier to solve. If L/a is large then this approximation to Ω cannot be justified.

Atmospheric flows usually have very large horizontal length scales compared to the vertical length scale. For such a thin fluid layer it is reasonable to approximate the motion with the Shallow-Water Equations (SWE) [39, 86],

$$\frac{\partial \boldsymbol{u}_\perp}{\partial t} + (\boldsymbol{u}_\perp \cdot \nabla)\boldsymbol{u}_\perp - f\hat{\boldsymbol{z}} \times \boldsymbol{u}_\perp = -g\nabla\eta, \tag{2.47}$$

$$\frac{\partial h}{\partial t} + \nabla \cdot (h\boldsymbol{u}_\perp) = 0 \tag{2.48}$$

with $\boldsymbol{u}_\perp = (u, v)$ the horizontal velocity, f Coriolis frequency, g gravitational acceleration, η the surface deviations and $h = H + \eta - B$ the depth of the fluid. H is the mean fluid depth and $B(x, y)$ is a bottom topography. These equations can be derived from the Primitive Equations by assuming no viscosity, no density variation ($\rho = 0$) and integrating the continuity equation (2.43d) over the fluid depth.

2.3 Quasi-geostrophic Equations

The Quasi-Geostrophic Equations (QGE) are approximations to the shallow water equations for small Rossby numbers U/Lf, that is when inertial forces are an order of magnitude smaller than the Coriolis and pressure forces [86]. The flow is purely geostrophic if the Rossby number is equal to zero. The QGE are a popular model for large scale atmospheric motions [20, 51, 64, 86, 87]. The QGE are simplified enough to allow for efficient numerical simulation, whilst still containing the underlying characteristics of atmospheric or oceanic flows. The assumptions used in the QGE approximation include the hydrostatic balance, β-plane approximation, geostrophic balance and the eddy viscosity parameterisation [39, 51]. For completeness, a derivation of the QGE is presented which can be found in standard fluid dynamics and atmospheric modelling texts [39, 86][1], a more rigorous derivation can be found in Pedlosky [99]. Forcing and diffusion terms are included in the following derivation for this thesis, because they are often neglected in the literature.

The underlying assumptions of the QGE are that the velocities are relatively small,

[1]The derivation presented here closely follows that in Cushman-Roisin and Beckers [39].

so that the flow is close to geostrophic (pressure gradient balances with Coriolis force), and there is a maintained state of stratification. That is the density profile takes the form

$$\rho = \bar{\rho}(z) + \rho'(x, y, z, t), \tag{2.49}$$

where $|\rho'| \ll |\bar{\rho}|$. Substituting this along with $p = \bar{p}(z) + p'(x, y, z, t)$ into the primitive equations (2.43) and using the β-plane,

$$\begin{aligned}
\frac{du}{dt} - f_0 v - \beta y v = &-\frac{1}{\rho_0}\frac{\partial p'}{\partial x} + \frac{\partial}{\partial x}\left(\mathcal{A}_H \frac{\partial u}{\partial x}\right) + \frac{\partial}{\partial y}\left(\mathcal{A}_H \frac{\partial u}{\partial y}\right) \\
&+ \frac{\partial}{\partial z}\left(\mathcal{A}_V \frac{\partial u}{\partial z}\right) + F_x
\end{aligned} \tag{2.50a}$$

$$\begin{aligned}
\frac{dv}{dt} + f_0 u + \beta y u = &-\frac{1}{\rho_0}\frac{\partial p'}{\partial y} + \frac{\partial}{\partial x}\left(\mathcal{A}_H \frac{\partial v}{\partial x}\right) + \frac{\partial}{\partial y}\left(\mathcal{A}_H \frac{\partial v}{\partial y}\right) \\
&+ \frac{\partial}{\partial z}\left(\mathcal{A}_V \frac{\partial v}{\partial z}\right) + F_y
\end{aligned} \tag{2.50b}$$

$$0 = -\frac{\partial p'}{\partial z} - \rho' g \tag{2.50c}$$

$$\frac{\partial u}{\partial x} + \frac{\partial v}{\partial y} + \frac{\partial w}{\partial z} = 0 \tag{2.50d}$$

$$\begin{aligned}
\frac{\partial \rho'}{\partial t} + u\frac{\partial \rho'}{\partial x} + v\frac{\partial \rho'}{\partial y} + w\frac{\partial \bar{\rho}}{\partial z} = &\frac{\partial}{\partial x}\left(\mathcal{K}_H \frac{\partial \rho'}{\partial x}\right) + \frac{\partial}{\partial y}\left(\mathcal{K}_H \frac{\partial \rho'}{\partial y}\right) + \frac{\partial}{\partial z}\left(\mathcal{K}_V \frac{\partial \rho'}{\partial z}\right) \\
&+ \frac{\partial}{\partial z}\left(\mathcal{K}_V \frac{\partial \bar{\rho}}{\partial z}\right) + H_t,
\end{aligned} \tag{2.50e}$$

where the $w\partial\rho'/\partial z$ term has been dropped since it is dominated by $w\partial\bar{\rho}/\partial z$. The $\mathcal{K}_V \partial\rho'/\partial z$ term is retained to avoid losing the subgrid-scale motions that it models. Only the perturbations of density and pressure appear in the hydrostatic balance equation (2.50c) since the average stratification and pressure are in hydrostatic balance ($\partial\bar{p}/\partial z = -\bar{\rho}g$).

For the quasi-geostrophic approximation, assume that advective velocities are weak, making the Rossby number (U/fL) small. Also, assume that the time scale is long compared to the inertial time scale ($2\pi/f_0$), so that the acceleration terms are small. For the β-plane approximation $|\beta y| \ll f_0$. With these assumptions the dominant terms in the momentum equations are in geostrophic equilibrium,

$$-f_0 v = -\frac{1}{\rho_0}\frac{\partial \rho'}{\partial x} \tag{2.51a}$$

$$f_0 u = -\frac{1}{\rho_0}\frac{\partial \rho'}{\partial y}. \tag{2.51b}$$

A system in complete geostrophic balance has no vertical velocity and does not vary in time. Therefore, to deviate from this basic state, consider a non-geostrophic (or ageostrophic) component of of velocity (u_a, v_a) so that,

$$u = u_g + u_a, \;\; v = v_g + v_a, \tag{2.52}$$

where the geostrophic components are defined as

$$u_g = -\frac{1}{f_0\rho_0}\frac{\partial p'}{\partial y}, \;\; v_g = \frac{1}{f_0\rho_0}\frac{\partial p'}{\partial x}. \tag{2.53}$$

Now, in the horizontal momentum equations of (2.50) replace the velocities in all terms, except the Coriolis term, with the geostrophic velocity approximation (2.53). Since the Coriolis terms are assumed to be more dominant, they retain the full velocity. Vertical advection is neglected as it is small compared to horizontal velocity which is already small compared to Coriolis terms. The horizontal momentum equations now become,

$$\begin{aligned}
&-\frac{1}{\rho_0 f_0}\frac{\partial^2 p'}{\partial y \partial t} - \frac{1}{\rho_0^2 f_0^2} J\left(p', \frac{\partial p'}{\partial y}\right) - f_0 v - \frac{\beta y}{\rho_0 f_0}\frac{\partial p'}{\partial x} = && \text{(2.54a)}\\
&-\frac{1}{\rho_0}\frac{\partial p'}{\partial x} - \frac{1}{\rho_0 f_0}\frac{\partial}{\partial x}\left(\mathcal{A}_H \frac{\partial^2 p'}{\partial x \partial y}\right) - \frac{1}{\rho_0 f_0}\frac{\partial}{\partial y}\left(\mathcal{A}_H \frac{\partial^2 p'}{\partial y^2}\right) - \frac{1}{\rho_0 f_0}\frac{\partial}{\partial z}\left(\mathcal{A}_V \frac{\partial^2 p'}{\partial z \partial y}\right) + F_x\\
&\frac{1}{\rho_0 f_0}\frac{\partial^2 p'}{\partial x \partial t} + \frac{1}{\rho_0^2 f_0^2} J\left(p', \frac{\partial p'}{\partial x}\right) + f_0 u - \frac{\beta y}{\rho_0 f_0}\frac{\partial p'}{\partial y} = && \text{(2.54b)}\\
&-\frac{1}{\rho_0}\frac{\partial p'}{\partial y} - \frac{1}{\rho_0 f_0}\frac{\partial}{\partial x}\left(\mathcal{A}_H \frac{\partial^2 p'}{\partial x^2}\right) - \frac{1}{\rho_0 f_0}\frac{\partial}{\partial y}\left(\mathcal{A}_H \frac{\partial^2 p'}{\partial y \partial x}\right) - \frac{1}{\rho_0 f_0}\frac{\partial}{\partial z}\left(\mathcal{A}_V \frac{\partial^2 p'}{\partial z \partial x}\right) + F_y
\end{aligned}$$

where the Jacobian operator is defined as

$$J(a, b) = -\frac{\partial a}{\partial y}\frac{\partial b}{\partial x} + \frac{\partial a}{\partial x}\frac{\partial b}{\partial y}. \tag{2.55}$$

Rearranging for velocities u and v,

$$\begin{aligned}
u = u_g + u_a = &-\frac{1}{\rho_0 f_0}\frac{\partial p'}{\partial y} - \frac{1}{\rho_0 f_0^2}\frac{\partial^2 p'}{\partial x \partial t} - \frac{1}{\rho_0^2 f_0^3} J\left(p', \frac{\partial p'}{\partial x}\right) + \frac{\beta y}{\rho_0 f_0^2}\frac{\partial p'}{\partial y} && \text{(2.56a)}\\
&- \frac{1}{\rho_0 f_0^2}\left[\frac{\partial}{\partial x}\left(\mathcal{A}_H \frac{\partial^2 p'}{\partial x^2}\right) + \frac{\partial}{\partial y}\left(\mathcal{A}_H \frac{\partial^2 p'}{\partial y \partial x}\right) + \frac{\partial}{\partial z}\left(\mathcal{A}_V \frac{\partial^2 p'}{\partial z \partial x}\right)\right] + \frac{1}{f_0} F_y\\
v = v_g + v_a = &\;\; \frac{1}{\rho_0 f_0}\frac{\partial p'}{\partial x} - \frac{1}{\rho_0 f_0^2}\frac{\partial^2 p'}{\partial y \partial t} - \frac{1}{\rho_0^2 f_0^3} J\left(p', \frac{\partial p'}{\partial y}\right) - \frac{\beta y}{\rho_0 f_0^2}\frac{\partial p'}{\partial x} && \text{(2.56b)}\\
&+ \frac{1}{\rho_0 f_0^2}\left[\frac{\partial}{\partial x}\left(\mathcal{A}_H \frac{\partial^2 p'}{\partial x \partial y}\right) + \frac{\partial}{\partial y}\left(\mathcal{A}_H \frac{\partial^2 p'}{\partial y^2}\right) + \frac{\partial}{\partial z}\left(\mathcal{A}_V \frac{\partial^2 p'}{\partial z \partial y}\right)\right] - \frac{1}{f_0} F_x
\end{aligned}$$

which provides a better approximation for the velocity than the purely geostrophic velocity approximation in (2.51). Substituting this into the continuity equation (2.50d) yields

$$\begin{aligned}\frac{\partial w}{\partial z} = \quad & \frac{1}{\rho_0 f_0^2}\left[\frac{\partial}{\partial t}\Delta p' + \frac{1}{\rho_0 f_0}J(p',\Delta p') + \beta\frac{\partial p'}{\partial x}\right] \\ & - \frac{1}{\rho_0 f_0^2}\left[\frac{\partial^2}{\partial x^2}\left(\mathcal{A}_H\frac{\partial^2 p'}{\partial x^2}\right) + 2\frac{\partial^2}{\partial x\partial y}\left(\mathcal{A}_H\frac{\partial^2 p'}{\partial x\partial y}\right) + \frac{\partial^2}{\partial y^2}\left(\mathcal{A}_H\frac{\partial^2 p'}{\partial y^2}\right)\right. \\ & \left. + \frac{\partial^2}{\partial x\partial z}\left(\mathcal{A}_V\frac{\partial^2 p'}{\partial x\partial z}\right) + \frac{\partial^2}{\partial y\partial z}\left(\mathcal{A}_V\frac{\partial^2 p'}{\partial y\partial z}\right)\right] + \frac{1}{f_0}\left(\frac{\partial F_x}{\partial y} - \frac{\partial F_y}{\partial x}\right),\end{aligned} \tag{2.57}$$

where it is understood from now on that $\Delta = \partial^2/\partial x^2 + \partial^2/\partial y^2$ is the two-dimensional Laplacian operator (similarly $\nabla = (\partial/\partial x, \partial/\partial y)$ is the two-dimensional gradient operator). Observe that the vertical velocity is indeed of the order of ageostrophic terms. The right hand side of the above equation is formed only from ageostrophic components, hence justifying the neglect of vertical velocity in advection terms.

Considering the density equation (2.50e), the density perturbations and horizontal velocities are small and vertical velocity even smaller compared to the dominant Coriolis forces. Therefore, the geostrophic velocity approximation is sufficient for this equation and the ageostrophic corrections (2.56) are not necessary. This gives the equation

$$\begin{aligned}\frac{\partial \rho'}{\partial t} + \frac{1}{\rho_0 f_0}J(p',\rho') - \frac{\rho_0 N^2}{g}w = \quad & \frac{\partial}{\partial x}\left(\mathcal{K}_H\frac{\partial \rho'}{\partial x}\right) + \frac{\partial}{\partial y}\left(\mathcal{K}_H\frac{\partial \rho'}{\partial y}\right) + \frac{\partial}{\partial z}\left(\mathcal{K}_V\frac{\partial \rho'}{\partial z}\right) \\ & + \frac{\partial}{\partial z}\left(\mathcal{K}_V\frac{\partial \bar{\rho}}{\partial z}\right) + H_t \\ = \quad & \frac{\partial}{\partial x}\left(\mathcal{K}_H\frac{\partial \rho'}{\partial x}\right) + \frac{\partial}{\partial y}\left(\mathcal{K}_H\frac{\partial \rho'}{\partial y}\right) + \frac{\partial}{\partial z}\left(\mathcal{K}_V\frac{\partial \rho'}{\partial z}\right) \\ & - \frac{\rho_0}{g}\frac{\partial}{\partial z}\left(\mathcal{K}_V N^2\right) + H_t,\end{aligned} \tag{2.58}$$

where the stratification or Brunt-Väisälä frequency is

$$N^2(z) = -\frac{g}{\rho_0}\frac{d\bar{\rho}}{dz}. \tag{2.59}$$

Now dividing by N^2/g, taking a z-derivative and using the hydrostatic balance

(2.50c) to eliminate density perturbations ρ',

$$\begin{aligned}
&\frac{\partial}{\partial t}\left[\frac{\partial}{\partial z}\left(\frac{1}{N^2}\frac{\partial p'}{\partial z}\right)\right] + \frac{1}{\rho_0 f_0} J\left[p', \frac{\partial}{\partial z}\left(\frac{1}{N^2}\frac{\partial p'}{\partial z}\right)\right] + \rho_0 \frac{\partial w}{\partial z} = \\
&\frac{\partial^2}{\partial x \partial z}\left(\frac{\mathcal{K}_H}{N^2}\frac{\partial^2 p'}{\partial x \partial z}\right) + \frac{\partial^2}{\partial y \partial z}\left(\frac{\mathcal{K}_H}{N^2}\frac{\partial^2 p'}{\partial y \partial z}\right) + \frac{\partial}{\partial z}\left(\frac{1}{N^2}\frac{\partial}{\partial z}\left(\mathcal{K}_V \frac{\partial^2 p'}{\partial z^2}\right)\right) \\
&+ \frac{\partial}{\partial z}\left(\frac{\rho_0}{N^2}\frac{\partial}{\partial z}\left(\mathcal{K}_V N^2\right)\right) - \frac{\partial}{\partial z}\left(\frac{g}{N^2} H_t\right).
\end{aligned} \tag{2.60}$$

Observe that the fourth term on the right hand side of the above equation vanishes when N^2 is constant or of the form $c_1 \exp(c_2 z)$ for constants c_1 and c_2. Due to the tendency for the atmosphere to follow such a density profile, this term will be dropped. The equations (2.57) and (2.60) provide equations for pressure perturbations p' and vertical stretching $\partial w/\partial z$. Eliminating the vertical stretching gives an equation for p',

$$\begin{aligned}
&\frac{\partial}{\partial t}\left[\Delta p' + \frac{\partial}{\partial z}\left(\frac{f_0^2}{N^2}\frac{\partial p'}{\partial z}\right)\right] + \frac{1}{\rho_0 f_0} J\left[p', \Delta p' + \frac{\partial}{\partial z}\left(\frac{f_0^2}{N^2}\frac{\partial p'}{\partial z}\right)\right] + \beta \frac{\partial p'}{\partial x} = \\
&\frac{\partial^2}{\partial x^2}\left(\mathcal{A}_H \frac{\partial^2 p'}{\partial x^2}\right) + 2\frac{\partial^2}{\partial x \partial y}\left(\mathcal{A}_H \frac{\partial^2 p'}{\partial x \partial y}\right) + \frac{\partial^2}{\partial y^2}\left(\mathcal{A}_H \frac{\partial^2 p'}{\partial y^2}\right) \\
&+ \frac{\partial^2}{\partial x \partial z}\left(\mathcal{A}_V \frac{\partial^2 p'}{\partial x \partial z}\right) + \frac{\partial^2}{\partial y \partial z}\left(\mathcal{A}_V \frac{\partial^2 p'}{\partial y \partial z}\right) \\
&+ \frac{\partial^2}{\partial x \partial z}\left(\mathcal{K}_H \frac{f_0^2}{N^2}\frac{\partial^2 p'}{\partial x \partial z}\right) + \frac{\partial^2}{\partial y \partial z}\left(\mathcal{K}_H \frac{f_0^2}{N^2}\frac{\partial^2 p'}{\partial y \partial z}\right) + \frac{\partial}{\partial z}\left(\frac{f_0^2}{N^2}\frac{\partial}{\partial z}\left(\mathcal{K}_V \frac{\partial^2 p'}{\partial z^2}\right)\right) \\
&- g\frac{\partial}{\partial z}\left(\frac{f_0^2}{N^2} H_t\right) + \rho_0 f_0 \left(\frac{\partial F_y}{\partial x} - \frac{\partial F_x}{\partial y}\right).
\end{aligned} \tag{2.61}$$

For simplification, choose the eddy coefficients to be constants (which may depend on discretisation parameters). Also, define the following forcing terms for convenience,

$$\mathcal{H}_t = -\frac{g}{\rho_0 f_0} H_t \text{ and } \mathcal{F} = \left(\frac{\partial F_y}{\partial x} - \frac{\partial F_x}{\partial y}\right) = (\nabla \times \boldsymbol{F}) \cdot \hat{\boldsymbol{z}}. \tag{2.62}$$

Finally, define the streamfunction $\psi = p'/\rho_0 f_0$ and divide through by $\rho_0 f_0$. Now, the quasi-geostrophic equations for nonlinear motions in a continuously stratified fluid on a beta plane with diffusion are:

$$\begin{aligned}
\frac{\partial q}{\partial t} + J(\psi, q) = \quad & \mathcal{F} + \frac{\partial}{\partial z}\left(\frac{f_0^2}{N^2}\mathcal{H}_t\right) + \mathcal{A}_H \Delta^2 \psi + \mathcal{A}_V \frac{\partial^2 \Delta \psi}{\partial z^2} \\
& + \mathcal{K}_H \frac{\partial}{\partial z}\left(\frac{f_0^2}{N^2}\frac{\partial \Delta \psi}{\partial z}\right) + \mathcal{K}_V \frac{\partial}{\partial z}\left(\frac{f_0^2}{N^2}\frac{\partial^3 \psi}{\partial z^3}\right)
\end{aligned} \tag{2.63}$$

where the potential vorticity is introduced

$$q = \Delta\psi + \frac{\partial}{\partial z}\left(\frac{f_0^2}{N^2}\frac{\partial\psi}{\partial z}\right) + \beta y, \tag{2.64}$$

which is a conserved quantity in the absence of diffusion or external sources/sinks. There has been extensive work on the QGE one-layer (assumption that flow is homogeneous in vertical direction) and $\mathcal{N}$-layer models, the work in this thesis will use the continuous model above.

Numerical approximations often use an eddy viscosity on the potential vorticity to approximation diffusive processes [39], however, the above derived diffusion terms provide a more accurate and consistent model. The following recapitulates the quasi-geostrophic model that was just derived. The QGE are written,

$$\frac{\partial q}{\partial t} + J(\psi, q) = \mathcal{F} + D \tag{2.65a}$$

for forcing $\mathcal{F}$ and diffusion terms D, where ψ is the streamfunction and the potential vorticity is

$$q = \Delta\psi + \frac{\partial}{\partial z}\left(\frac{f_0^2}{N^2}\frac{\partial\psi}{\partial z}\right) + \beta y \tag{2.65b}$$

and the Jacobian is

$$J(\psi, q) = -\frac{\partial\psi}{\partial y}\frac{\partial q}{\partial x} + \frac{\partial\psi}{\partial x}\frac{\partial q}{\partial y} = (\boldsymbol{u_g}\cdot\nabla)q. \tag{2.65c}$$

The parameter β is the Coriolis parameter that multiplies the latitudinal coordinate y, f_0 is the Coriolis frequency and N is the Brunt-Väisälä frequency given by

$$N^2 = -\frac{g}{\rho_0}\frac{\partial\bar{\rho}}{\partial z}, \tag{2.65d}$$

for density ρ and gravitational acceleration g. The horizontal geostrophic velocity $\boldsymbol{u_g}$ is given by the two-dimensional curl of the streamfunction

$$\boldsymbol{u_g} = \nabla^{\perp}\psi = \begin{pmatrix} -\dfrac{\partial\psi}{\partial y} \\ +\dfrac{\partial\psi}{\partial x} \end{pmatrix}. \tag{2.65e}$$

Possible diffusion terms D, as derived above, and a surface friction term as intro-

duced in McWilliams [84] are

$$\text{Vertical Momentum Diffusion } D_{VM} = \mathcal{A}_V \frac{\partial^2 \Delta\psi}{\partial z^2}, \tag{2.66}$$

$$\text{Horizontal Momentum Diffusion } D_{HM} = \mathcal{A}_H \Delta^2 \psi, \tag{2.67}$$

$$\text{Vertical Buoyancy Diffusion } D_{VB} = \mathcal{K}_V \frac{\partial}{\partial z}\left(\frac{f_0^2}{N^2}\frac{\partial^3 \psi}{\partial z^3}\right), \tag{2.68}$$

$$\text{Horizontal Buoyancy Diffusion } D_{HB} = \mathcal{K}_H \frac{\partial}{\partial z}\left(\frac{f_0^2}{N^2}\frac{\partial \Delta\psi}{\partial z}\right), \tag{2.69}$$

$$\text{Surface Friction } \mathcal{F}_{SF} = \mathcal{C}_D \Delta\psi. \tag{2.70}$$

The parameter $\mathcal{A}_V$ is the viscosity for vertical momentum diffusion, $\mathcal{A}_H$ is the horizontal momentum diffusion coefficient, $\mathcal{K}_V$ is the vertical buoyancy diffusion coefficient, $\mathcal{K}_H$ is the horizontal buoyancy diffusion coefficient and $\mathcal{C}_D$ is the surface friction coefficient. Ageostrophic horizontal velocities u_a and v_a, vertical velocity w, temperature θ, pressure p' and density ρ' fluctuations can be recovered from the streamfunction as follows [39, 84, 86], for a reference density ρ_0 and thermal expansion coefficient γ,

$$u_g = -\frac{\partial \psi}{\partial y} \tag{2.71a}$$

$$v_g = \frac{\partial \psi}{\partial x} \tag{2.71b}$$

$$u_a = -\frac{1}{f_0}\frac{\partial^2 \psi}{\partial t \partial x} - \frac{1}{f_0} J\left(\psi, \frac{\partial \psi}{\partial x}\right) + \frac{\beta}{f_0} y \frac{\partial \psi}{\partial y} - \frac{1}{f_0}\frac{\partial}{\partial x}\left[\mathcal{A}_H \Delta\psi + \mathcal{A}_V \frac{\partial^2 \psi}{\partial z^2}\right] + \frac{F_y}{f_0} \tag{2.71c}$$

$$v_a = -\frac{1}{f_0}\frac{\partial^2 \psi}{\partial t \partial y} - \frac{1}{f_0} J\left(\psi, \frac{\partial \psi}{\partial y}\right) - \frac{\beta}{f_0} y \frac{\partial \psi}{\partial x} + \frac{1}{f_0}\frac{\partial}{\partial y}\left[\mathcal{A}_H \Delta\psi + \mathcal{A}_V \frac{\partial^2 \psi}{\partial z^2}\right] - \frac{F_x}{f_0} \tag{2.71d}$$

$$w = -\frac{f_0}{N^2}\left[\frac{\partial^2 \psi}{\partial t \partial z} + J\left(\psi, \frac{\partial \psi}{\partial z}\right) - \mathcal{K}_V \frac{\partial^3 \psi}{\partial z^3} - \mathcal{K}_H \frac{\partial \Delta\psi}{\partial z} - \mathcal{H}_t\right] \tag{2.71e}$$

$$p' = \rho_0 f_0 \psi \tag{2.71f}$$

$$\rho' = -\frac{\rho_0 f_0}{g}\frac{\partial \psi}{\partial z} \tag{2.71g}$$

$$\theta = \frac{f_0}{\gamma g}\frac{\partial \psi}{\partial z}, \tag{2.71h}$$

Note that the model is inconsistent, when considering boundaries, unless $\mathcal{K}_H = \mathcal{A}_V = 0$ because each diffusion term requires a condition preventing momentum or buoyancy flux across the boundaries [84]. This would require a sixth order PDE,

however, the QGE is only a fourth order PDE. At this point the horizontal buoyancy diffusion is removed from the model ($\mathcal{K}_H = 0$) and vertical momentum diffusion is retained for now as it is sometimes used in numerical models [87]. Assume that the domain is periodic or contained by side walls in the horizontal and there are rigid top and bottom boundaries, then these equations are complimented with the following no-flow through and no-flux boundary conditions imposed on side walls Γ_{SW} and top/bottom boundaries Γ_{TB}:

$$\frac{\partial \psi}{\partial \boldsymbol{\tau}} = \mathcal{A}_H \frac{\partial^2 \psi}{\partial \boldsymbol{n}^2} = \mathcal{K}_H \frac{\partial^2 \psi}{\partial z \partial \boldsymbol{n}} = 0 \text{ on side walls } \Gamma_{SW}, \tag{2.72a}$$

$$w = \mathcal{K}_V \frac{\partial^2 \psi}{\partial z^2} = 0 \text{ and } \mathcal{A}_V \frac{\partial \nabla \psi}{\partial z} = 0 \text{ on top and bottom boundaries } \Gamma_{TB}, \tag{2.72b}$$

where $\boldsymbol{n}$ and $\boldsymbol{\tau}$ are the horizontal outer unit normal and tangent vectors to the side wall boundaries. Observe that the first condition $\frac{\partial \psi}{\partial \boldsymbol{\tau}} = 0$ on Γ_{SW} means that the streamfunction takes some value $C_i(z,t)$ on each connected side wall Γ_i which depends on height and time only.

2.3.1 Energetics

Definition 2.4. *(Kinetic and Potential Energy)*
Define the energy in the system in a domain Ω as [39, 56],

$$\mathcal{E} = \int_\Omega \frac{1}{2} |\nabla \psi|^2 \, \mathrm{d}\boldsymbol{x} + \int_\Omega \frac{1}{2} \frac{f_0^2}{N^2} \left(\frac{\partial \psi}{\partial z} \right)^2 \mathrm{d}\boldsymbol{x}. \tag{2.73}$$

Observing that $|\nabla \psi|^2 = \psi_y^2 + \psi_x^2 = u^2 + v^2$ makes it clear that the first integral is equivalent to kinetic energy. This leaves the second integral as an expression for available potential energy, which is defined as the difference between the existing potential energy and the potential energy in the unperturbed basic stratification state. Therefore, the Kinetic Energy *is defined as*

$$KE = \int_\Omega \frac{1}{2} |\nabla \psi|^2 \, \mathrm{d}\boldsymbol{x} \tag{2.74}$$

and the Potential Energy *as*

$$PE = \int_\Omega \frac{1}{2} \frac{f_0^2}{N^2} \left(\frac{\partial \psi}{\partial z} \right)^2 \mathrm{d}\boldsymbol{x}. \tag{2.75}$$

Theorem 2.5. *The energy $\mathcal{E}$ is conserved by the quasi-geostrophic equations* (2.65) *when diffusion and external forcing are zero.*

Proof. Substituting (2.65b) into (2.65a) with $\mathcal{F} = 0$ and $D = 0$, multiplying by the streamfunction ψ and integrating over the domain Ω,

$$\int_\Omega \frac{\partial}{\partial t}(\Delta\psi)\psi + \int_\Omega \frac{\partial^2}{\partial t \partial z}\left(\frac{f_0^2}{N^2}\frac{\partial \psi}{\partial z}\right)\psi + \int_\Omega \nabla\cdot(\boldsymbol{u_g}\Delta\psi)\psi + \int_\Omega \frac{\partial}{\partial z}\nabla\cdot\left(\boldsymbol{u_g}\frac{f_0^2}{N^2}\frac{\partial\psi}{\partial z}\right)\psi = 0, \tag{2.76}$$

where the final term follows from

$$\begin{aligned}
\frac{\partial}{\partial z}\nabla\cdot\left(\boldsymbol{u_g}\frac{f_0^2}{N^2}\frac{\partial\psi}{\partial z}\right) &= \frac{\partial}{\partial z}\left((\boldsymbol{u_g}\cdot\nabla)\frac{f_0^2}{N^2}\frac{\partial\psi}{\partial z} + \underbrace{(\nabla\cdot\boldsymbol{u_g})}_{=0}\frac{f_0^2}{N^2}\frac{\partial\psi}{\partial z}\right) \\
&= \left(\frac{\partial \boldsymbol{u_g}}{\partial z}\cdot\nabla\right)\frac{f_0^2}{N^2}\frac{\partial\psi}{\partial z} + (\boldsymbol{u_g}\cdot\nabla)\frac{\partial}{\partial z}\left(\frac{f_0^2}{N^2}\frac{\partial\psi}{\partial z}\right) \\
&= \frac{f_0^2}{N^2}\left(\frac{\partial^2\psi}{\partial y\partial z}\frac{\partial^2\psi}{\partial x\partial z} - \frac{\partial^2\psi}{\partial y\partial z}\frac{\partial^2\psi}{\partial x\partial z}\right) + (\boldsymbol{u_g}\cdot\nabla)\frac{\partial}{\partial z}\left(\frac{f_0^2}{N^2}\frac{\partial\psi}{\partial z}\right) \\
&= (\boldsymbol{u_g}\cdot\nabla)\frac{\partial}{\partial z}\left(\frac{f_0^2}{N^2}\frac{\partial\psi}{\partial z}\right).
\end{aligned} \tag{2.77}$$

Applying integration by parts and multiplying by -1 gives

$$\begin{aligned}
&\int_\Omega \frac{\partial}{\partial t}(\nabla\psi)\cdot\nabla\psi - \int_{\Gamma_{SW}}\frac{\partial}{\partial t}(\nabla\psi\cdot\boldsymbol{n})\psi + \int_\Omega \frac{\partial}{\partial t}\left(\frac{f_0^2}{N^2}\frac{\partial\psi}{\partial z}\right)\frac{\partial\psi}{\partial z} - \int_{\Gamma_{TB}}\frac{\partial}{\partial t}\left(\frac{f_0^2}{N^2}\frac{\partial\psi}{\partial z}\right)\psi \\
&+ \int_\Omega (\boldsymbol{u_g}\Delta\psi)\cdot\nabla\psi - \int_{\Gamma_{SW}}(\boldsymbol{u_g}\cdot\boldsymbol{n})\Delta\psi\psi + \int_\Omega \nabla\cdot\left(\boldsymbol{u_g}\frac{f_0^2}{N^2}\frac{\partial\psi}{\partial z}\right)\frac{\partial\psi}{\partial z} \\
&- \int_{\Gamma_{TB}}\nabla\cdot\left(\boldsymbol{u_g}\frac{f_0^2}{N^2}\frac{\partial\psi}{\partial z}\right)\psi = 0.
\end{aligned} \tag{2.78}$$

The fifth and sixth terms vanish since $\boldsymbol{u_g} \perp \nabla\psi$ and $\boldsymbol{u_g}\cdot\boldsymbol{n} = 0$ on Γ_{SW}. The second term vanishes since $\psi = \sum_i C_i(z,t)\mathbb{1}_{\Gamma_i}$ on $\Gamma_{SW} = \bigcup_i \Gamma_i$ (where $\mathbb{1}_{\Gamma_i}$ is an indicator function of Γ_i) then

$$\int_{\Gamma_{SW}}\frac{\partial}{\partial t}(\nabla\psi\cdot\boldsymbol{n})\psi = \sum_i C_i(z,t)\frac{\partial}{\partial t}\int_{\Gamma_i}(\boldsymbol{u_g}\cdot\boldsymbol{\tau}) = 0 \tag{2.79}$$

by Kelvin's Circulation Theorem [1]. The seventh term vanishes as follows,

$$\begin{aligned}
\int_\Omega \nabla\cdot\left(\boldsymbol{u_g}\frac{f_0^2}{N^2}\frac{\partial\psi}{\partial z}\right)\frac{\partial\psi}{\partial z} &= \int_\Omega \frac{1}{2}\nabla\cdot\left(\boldsymbol{u_g}\frac{f_0^2}{N^2}\left(\frac{\partial\psi}{\partial z}\right)^2\right) \\
&= \int_{\Gamma_{SW}}\frac{1}{2}(\boldsymbol{u_g}\cdot\boldsymbol{n})\frac{f_0^2}{N^2}\left(\frac{\partial\psi}{\partial z}\right)^2 = 0,
\end{aligned} \tag{2.80}$$

where the last step follows by the divergence theorem. Now,

$$\begin{aligned}&\frac{\partial}{\partial t}\int_\Omega \frac{1}{2}|\nabla\psi|^2 + \frac{\partial}{\partial t}\int_\Omega \frac{1}{2}\frac{f_0^2}{N^2}\left(\frac{\partial\psi}{\partial z}\right)^2 \\ &= \int_{\Gamma_{TB}} \frac{\partial}{\partial t}\left(\frac{f_0^2}{N^2}\frac{\partial\psi}{\partial z}\right)\psi + \int_{\Gamma_{TB}} \nabla\cdot\left(\boldsymbol{u_g}\frac{f_0^2}{N^2}\frac{\partial\psi}{\partial z}\right)\psi = -\int_{\Gamma_{TB}} f_0 w\psi = 0 \end{aligned} \tag{2.81}$$

since $w = 0$ on the top and bottom boundaries. Therefore $\partial\mathcal{E}/\partial t = 0$. □

Definition 2.6. *(Enstrophy)*
Define the enstrophy *in the system in a domain* Ω *as [39, 119],*

$$Z = \int_\Omega \frac{1}{2}|q|^2 \,\mathrm{d}\boldsymbol{x}. \tag{2.82}$$

Theorem 2.7. *The enstrophy* Z *is conserved by the quasi-geostrophic equations* (2.65) *when diffusion and external forcing are zero.*

Proof. Assuming $\mathcal{F} = 0$ and $D = 0$, multiply (2.65a) by q and use incompressibility to get

$$q\frac{\partial q}{\partial t} + q\nabla\cdot(\boldsymbol{u_g}q) = 0. \tag{2.83}$$

Applying the chain rule gives

$$\frac{1}{2}\frac{\partial q^2}{\partial t} + \frac{1}{2}\nabla\cdot(\boldsymbol{u_g}q^2) = 0. \tag{2.84}$$

Integrating over the domain Ω, applying the divergence theorem to the second integral and using the no-flow boundary condition gives

$$\frac{\partial}{\partial t}\int_\Omega \frac{1}{2}q^2 = 0. \tag{2.85}$$

Therefore, $\partial Z/\partial t = 0$. □

The kinetic energy equation is found by substituting potential vorticity (2.65b) into the QGE (2.65a), multiplying by $-\psi$ and integrating over the domain. After, apply integration by parts with boundary terms vanishing as in the proof of Theorem 2.5,

$$\frac{\partial KE}{\partial t} = f_0\int_\Omega w\frac{\partial\psi}{\partial z} - \int_\Omega \mathcal{A}_H\Delta^2\psi\psi - \int_\Omega \mathcal{A}_V\frac{\partial^2\Delta\psi}{\partial z^2}\psi - \int_\Omega \mathcal{F}\psi. \tag{2.86}$$

Similarly, by multiplying the vertical velocity equation (2.71e) by $f_0\partial\psi/\partial z$, integrating over the domain and applying integration by parts gives the potential energy

equation

$$\frac{\partial PE}{\partial t} = -f_0 \int_\Omega w \frac{\partial \psi}{\partial z} - \int_\Omega \mathcal{K}_V \frac{f_0^2}{N^2} \left(\frac{\partial^2 \psi}{\partial z^2} \right)^2 - \int_\Omega \mathcal{K}_H \frac{f_0^2}{N^2} \left(\frac{\partial \nabla \psi}{\partial z} \right)^2 + \int_\Omega \frac{f_0^2}{N^2} \mathcal{H}_t \frac{\partial \psi}{\partial z} \tag{2.87}$$

where boundary terms vanish due to the boundary conditions in (2.72).

2.3.2 Non-dimensionalisation

It is convenient to non-dimensionalise equations when simulating them numerically. The quasi-geostrophic equations,

$$\frac{\partial q}{\partial t} + J(\psi, q) = \mathcal{F} + D, \tag{2.88}$$

for forcing $\mathcal{F}$ and additional diffusive terms D, where the potential vorticity is

$$q = \Delta \psi + \frac{\partial}{\partial z} \left(\frac{f_0^2}{N^2} \frac{\partial \psi}{\partial z} \right) + \beta y. \tag{2.89}$$

can be non-dimensionalised as follows. Let L be a characteristic horizontal length scale, H a vertical length scale, U a velocity scale and N_0 a reference Brunt-Väisälä frequency, then the non-dimensional variables, denoted with a *, are

$$x^* = \frac{x}{L}, y^* = \frac{y}{L}, z^* = \frac{z}{H}, t^* = \frac{Ut}{L}, q^* = \frac{Lq}{U}, \psi^* = \frac{\psi}{UL}, \beta^* = \frac{\beta L^2}{U}, N^* = \frac{N}{N_0}. \tag{2.90}$$

Non-dimensionalising equation (2.89) first gives

$$\frac{U}{L} q^* = \frac{U}{L} \Delta^* \psi^* + \frac{UL f_0^2}{H^2 N_0^2} \frac{\partial}{\partial z^*} \left(\frac{1}{N^{*2}} \frac{\partial \psi^*}{\partial z^*} \right) + \frac{U \beta^*}{L} y^*. \tag{2.91}$$

Then dividing through by U/L gives

$$q^* = \Delta^* \psi^* + \frac{L^2 f_0^2}{H^2 N_0^2} \frac{\partial}{\partial z^*} \left(\frac{1}{N^{*2}} \frac{\partial \psi^*}{\partial z^*} \right) + \beta^* y^* \tag{2.92}$$

$$= \Delta^* \psi^* + \frac{1}{Bu} \frac{\partial}{\partial z^*} \left(\frac{f_0^2}{N^2} \frac{\partial \psi^*}{\partial z^*} \right) + \beta^* y^*, \tag{2.93}$$

where the Burger number Bu is defined as,

$$Bu = \left(\frac{H N_0}{L f_0} \right)^2 = \left(\frac{L_f}{L} \right)^2, \tag{2.94}$$

with the Rossby deformation radius $L_f = HN_0/f_0$. Substituting the non-dimensional variables into equation (2.88) gives

$$\frac{U^2}{L^2}\frac{\partial q^*}{\partial t^*} + \frac{U^2}{L^2}J(\psi^*, q^*) = \mathcal{F} + D, \tag{2.95}$$

and dividing by U^2/L^2,

$$\frac{\partial q^*}{\partial t^*} + J(\psi^*, q^*) = \frac{L^2}{U^2}\mathcal{F} + \frac{L^2}{U^2}D. \tag{2.96}$$

Turn attention to the diffusion terms,

$$D = \mathcal{A}_V\frac{\partial^2\Delta\psi}{\partial z^2} + \mathcal{A}_H\Delta^2\psi + \mathcal{K}_V\frac{\partial}{\partial z}\left(\frac{f_0^2}{N^2}\frac{\partial^3\psi}{\partial z^3}\right) - \mathcal{C}_D\Delta\psi, \tag{2.97}$$

where the last term is the surface friction. Non-dimensionalising these terms gives

$$\begin{aligned}\frac{L^2}{U^2}D = D^* &= \mathcal{A}_V\frac{L^2}{U^2}\frac{UL}{L^2H^2}\frac{\partial^2\Delta^*\psi^*}{\partial z^{*2}} + \mathcal{A}_H\frac{L^2}{U^2}\frac{UL}{L^4}\Delta^{*2}\psi^* \\ &\quad + \mathcal{K}_V\frac{L^2}{U^2}\frac{f_0^2UL}{N_0^2H^4}\frac{\partial}{\partial z^*}\left(\frac{1}{N^{*2}}\frac{\partial^3\psi^*}{\partial z^{*3}}\right) - \mathcal{C}_D\frac{L^2}{U^2}\frac{UL}{L^2}\Delta^*\psi^*, \\ &= A_V\frac{\partial^2\Delta^*\psi^*}{\partial z^{*2}} + A_H\Delta^{*2}\psi^* + K_{V_1}\frac{\partial}{\partial z}\left(\frac{1}{N^2}\frac{\partial^3\psi^*}{\partial z^3}\right) - C_D\Delta^*\psi^*\end{aligned} \tag{2.98}$$

with non-dimensional coefficients

$$\begin{aligned}A_V &= \frac{\mathcal{A}_V L}{UH^2}, \\ A_H &= \frac{\mathcal{A}_H}{UL}, \\ K_{V_1} &= \frac{\mathcal{K}_V L^3 f_0^2}{UH^4N_0^2}, \\ C_D &= \frac{\mathcal{C}_D L}{U}.\end{aligned} \tag{2.99}$$

Assuming any additional forcing terms can be suitably non-dimensionalised as $\mathcal{F}^*$, and dropping the superscript notation so that all variables from here on represent non-dimensional quantites, the final non-dimensionalised equations are,

$$\frac{\partial q}{\partial t} + J(\psi, q) = \mathcal{F} + A_V\frac{\partial^2\Delta\psi}{\partial z^2} + A_H\Delta^2\psi + K_{V_1}\frac{\partial}{\partial z}\left(\frac{1}{N^2}\frac{\partial^3\psi}{\partial z^3}\right) - C_D\Delta\psi \tag{2.100a}$$

$$q = \Delta\psi + Bu^{-1}\frac{\partial}{\partial z}\left(\frac{1}{N^2}\frac{\partial\psi}{\partial z}\right) + \beta y. \tag{2.100b}$$

2.3.3 Auxiliary and Boundary Conditions

Assume a three-dimensional domain $\Omega \times [0, H] = [0, L_x] \times [0, L_y] \times [0, H]$. Impose no-flow through the north-south ($y = 0, L_y$) boundaries, periodicity on the east-west boundaries and no-flow through on the top and bottom ($z = 0, H$) boundaries. For simplicity set $L_y = L$ and then the non-dimensional domain becomes $[0, L_x/L] \times [0, 1] \times [0, 1]$ which allows for a greater range in the zonal direction. The full non-dimensionalised quasi-geostrophic model with external forcing $\mathcal{F} = (\nabla \times \boldsymbol{F}) \cdot \hat{\boldsymbol{z}}$, bottom friction and horizontal and vertical diffusion is,

$$\frac{\partial q}{\partial t} + (\boldsymbol{u_g} \cdot \nabla) q = (\nabla \times \boldsymbol{F}) \cdot \hat{\boldsymbol{z}} + A_H \Delta^2 \psi + K_{V_1} \frac{\partial}{\partial z} \left(\frac{1}{N^2} \frac{\partial^3 \psi}{\partial z^3} \right) - C_D \Delta \psi, \quad (2.101a)$$

$$q = \Delta \psi + Bu^{-1} \frac{\partial}{\partial z} \left(\frac{1}{N^2} \frac{\partial \psi}{\partial z} \right) + \beta y, \quad (2.101b)$$

where in this case $\nabla\times$ is the three dimensional curl operator on the external forcing $\boldsymbol{F} = (F_x, F_y, F_z)$. This forcing $\boldsymbol{F}$ is in fact the same term from the Primitive Equations (2.43) if forcing is applied. The reason for writing the forcing in this form becomes apparent in the auxiliary conditions. For a three-dimensional domain with rigid walls at the north, south, top and bottom and periodic in the zonal (east-west) direction, the equations are complimented with free-slip boundary conditions, where there is no normal velocity or diffusive flux at the walls [84];

$$\frac{\partial \psi}{\partial \boldsymbol{\tau}} = A_H \frac{\partial^2 \psi}{\partial \boldsymbol{n}^2} = 0 \text{ on } \Gamma_N \cup \Gamma_S, \quad (2.102a)$$

$$w = K_{V_1} \frac{\partial^2 \psi}{\partial z^2} = 0 \text{ on } \Gamma_T \cup \Gamma_B, \quad (2.102b)$$

where $\Gamma_N, \Gamma_S, \Gamma_T, \Gamma_B$ are north, south, top and bottom boundaries respectively with unit normal $\boldsymbol{n}$ and tangent $\boldsymbol{\tau}$. Note that on the north and south walls $\nabla \psi \cdot \boldsymbol{\tau} = -\boldsymbol{u_g} \cdot \boldsymbol{n} = 0$ and $0 = \partial^2 \psi / \partial \boldsymbol{n}^2 = \partial^2 \psi / \partial y^2 = \omega$ since $\partial^2 \psi / \partial x^2 = 0$ on these boundaries. For the top and bottom boundaries it is required that vertical velocity $w = 0$, therefore, from equation (2.71e)

$$w = -\frac{1}{N^2} \left[\frac{\partial^2 \psi}{\partial t \partial z} + J\left(\psi, \frac{\partial \psi}{\partial z} \right) - K_{V_2} \frac{\partial^3 \psi}{\partial z^3} - \mathcal{H}_t \right] = 0 \text{ on } \Gamma_T \cup \Gamma_B. \quad (2.103)$$

Taking care to realise that non-dimensionalising vertical velocity (order $f_0 U^2 / H N_0^2$) gives the non-dimensional constant $K_{V_2} = \mathcal{K}_V L / U H^2$. This differs from the con-

stant K_{V_1} that results from non-dimensionalising the main equation since the length scale L is not necessarily equal to the Rossby deformation length $L_f = HN_0/f_0$. Indeed, K_{V_2} is equal to the coefficient $K_{V_1} = \mathcal{K}_V L^3 f_0^2/UH^4N_0^2$ if $L = L_f$.

The zero normal velocity boundary condition ($\boldsymbol{u_g} \cdot \boldsymbol{n} = -\nabla\psi \cdot \boldsymbol{\tau} = 0$) results in the streamfunction adopting an unknown value on the boundary that may depend on time t or height z. That is,

$$\psi = C_N(z,t) \text{ on } \Gamma_N, \tag{2.104a}$$

$$\psi = C_S(z,t) \text{ on } \Gamma_S. \tag{2.104b}$$

For the quasi-geostrophic equations to provide an accurate solution to the primitive equations, the model needs to satisfy some auxiliary conditions. These conditions will determine the unknown streamfunction values on the horizontal walls. The work on quasi-geostrophic models by McWilliams [84] gives the following auxiliary conditions. For a two-dimensional horizontal domain Ω and a fixed height z,

$$\oint_{\Gamma_S} \left(\frac{\partial}{\partial \boldsymbol{n}} \left(\frac{\partial \psi}{\partial t} - A_H \Delta\psi + C_D\psi \right) - \boldsymbol{F} \cdot \hat{\boldsymbol{s}} \right) d\boldsymbol{s} = 0, \tag{2.105a}$$

$$\int_\Omega w \, dxdy = 0. \tag{2.105b}$$

The line integral in the first condition is in the clockwise direction as though the southern boundary forms and island in a basin contained by the northern boundary.

The following derivation is not taken from literature. Suppose ψ is a solution to the quasi-geostropic equations (2.101), satisfying boundary conditions (2.102). Then for a fixed level of z, let

$$\psi = \Psi + \psi_N C_N + \psi_S C_S, \tag{2.106}$$

where ψ solves (2.101b) with $\Psi = 0$ on $\Gamma_N \cup \Gamma_S$. The other two components ψ_N and ψ_S solve

$$\Delta\psi_N + Bu^{-1} \frac{\partial}{\partial z} \left(\frac{1}{N^2} \frac{\partial \psi_N}{\partial z} \right) = \Delta\psi_S + Bu^{-1} \frac{\partial}{\partial z} \left(\frac{1}{N^2} \frac{\partial \psi_S}{\partial z} \right) = 0, \tag{2.107}$$

on the interior with

$$\psi_N = \begin{cases} 1 & \text{on } \Gamma_N \\ 0 & \text{on } \Gamma_S \end{cases}, \tag{2.108}$$

and

$$\psi_S = \begin{cases} 0 & \text{on } \Gamma_N \\ 1 & \text{on } \Gamma_S \end{cases}. \tag{2.109}$$

The unique solutions for $\psi_N = y$ and $\psi_S = 1 - y$ can be shown analytically and numerically. Substituting the streamfunction decomposition (2.106) into the first auxiliary condition in (2.105), and using the fact that the outward unit normal at the south boundary is $\boldsymbol{n} = (0, -1)$,

$$\begin{aligned} &\oint\!\!\!\!\!\!\diagup_{\Gamma_S} \left(-\frac{\partial^2 \Psi}{\partial t \partial y} - \frac{\partial^2 \psi_N C_N}{\partial t \partial y} - \frac{\partial^2 \psi_S C_S}{\partial t \partial y} + A_H \Delta \frac{\partial}{\partial y}(\Psi + C_N \psi_N + C_S \psi_S) \right) dx \\ &+ \oint\!\!\!\!\!\!\diagup_{\Gamma_S} \left(-C_D \frac{\partial}{\partial y}(\Psi + C_N \psi_N + C_S \psi_S) - F_x \right) dx = 0. \end{aligned} \tag{2.110}$$

Substituting in the analytical solutions for ψ_N and ψ_S gives

$$\oint\!\!\!\!\!\!\diagup_{\Gamma_S} \left(-\frac{\partial^2 \Psi}{\partial t \partial y} - \frac{\partial C_N}{\partial t} + \frac{\partial C_S}{\partial t} + A_H \Delta \frac{\partial \Psi}{\partial y} - C_D \left[\frac{\partial \Psi}{\partial y} + C_N - C_S \right] - F_x \right) dx = 0. \tag{2.111}$$

Moving the x-independent terms out of the integral and rearranging gives

$$\frac{\partial}{\partial t}(C_N - C_S) = \oint\!\!\!\!\!\!\diagup_{\Gamma_S} \left(-\frac{\partial^2 \Psi}{\partial t \partial y} + A_H \Delta \frac{\partial \Psi}{\partial y} - C_D \left[\frac{\partial \Psi}{\partial y} + C_N - C_S \right] - F_x \right) dx. \tag{2.112}$$

A second condition on the values of C_N and C_S can be obtained by substituting the streamfunction decomposition (2.106) into the second auxiliary condition in (2.105).

$$0 = \int_\Omega w \, dxdy = \int_\Omega \left(\frac{\partial^2 \psi}{\partial t \partial z} + \nabla \cdot \left(\boldsymbol{u_g} \frac{\partial \psi}{\partial z} \right) - K_{V_2} \frac{\partial^3 \psi}{\partial z^3} - \mathcal{H}_t \right) dxdy. \tag{2.113}$$

Using the divergence theorem on the advection term causes it to vanish since the normal component of velocity is zero at the boundaries. Now,

$$\begin{aligned} &\int_\Omega \left(\frac{\partial^2 \Psi}{\partial t \partial z} + \frac{\partial^2}{\partial t \partial z}(C_N \psi_N + C_S \psi_S) - K_{V_2} \left[\frac{\partial^3 \Psi}{\partial z^3} + \frac{\partial^3}{\partial z^3}(C_N \psi_N + C_S \psi_S) \right] \right) dxdy \\ &- \int_\Omega \mathcal{H}_t \, dxdy = 0 \end{aligned} \tag{2.114}$$

which rearranges to

$$\frac{\partial^2}{\partial t \partial z}(C_N + C_S) = \frac{2L}{L_x} \int_\Omega \left(-\frac{\partial^2 \Psi}{\partial t \partial z} + K_{V_2} \frac{\partial^3 \Psi}{\partial z^3} + \mathcal{H}_t \right) dxdy + K_{V_2} \left[\frac{\partial^3 C_N}{\partial z^3} + \frac{\partial^3 C_S}{\partial z^3} \right]. \tag{2.115}$$

Observe that, the integrals of ψ_N and ψ_S over a horizontal plane both evaluate to $L_x/2L$ since the horizontal domain is $[0, L_x/L] \times [0, 1]$. Integrating with respect to z produces an arbitrary constant that can depend only on time which is set to zero as it will not affect the dynamics. This leaves

$$\frac{\partial}{\partial t}(C_N + C_S) = \frac{2L}{L_x}\int_\Omega \left(-\frac{\partial \Psi}{\partial t} + K_{V_2}\frac{\partial^2 \Psi}{\partial z^2} + \mathbb{H}_t\right) dxdy + K_{V_2}\frac{\partial^2}{\partial z^2}(C_N + C_S) \tag{2.116}$$

where $\mathbb{H}_t = \int \mathcal{H}_t \, dz$ is the antiderivative of $\mathcal{H}_t$ with respect to z. Adding and subtracting equations (2.112) and (2.116) provides expressions for how the boundary values change with time,

$$\begin{aligned}\frac{\partial}{\partial t}C_N =& \frac{L}{L_x}\int_\Omega \left(-\frac{\partial \Psi}{\partial t} + K_{V_2}\frac{\partial^2 \Psi}{\partial z^2} + \mathbb{H}_t\right) dxdy + \frac{K_{V_2}}{2}\frac{\partial^2}{\partial z^2}(C_N + C_S) \\ &+ \frac{1}{2}\oint_{\Gamma_S} \left(-\frac{\partial^2 \Psi}{\partial t \partial y} + A_H \Delta \frac{\partial \Psi}{\partial y} - C_D \frac{\partial \Psi}{\partial y} + C_D(C_S - C_N) - F_x\right) dx,\end{aligned} \tag{2.117a}$$

$$\begin{aligned}\frac{\partial}{\partial t}C_S =& \frac{L}{L_x}\int_\Omega \left(-\frac{\partial \Psi}{\partial t} + K_{V_2}\frac{\partial^2 \Psi}{\partial z^2} + \mathbb{H}_t\right) dxdy + \frac{K_{V_2}}{2}\frac{\partial^2}{\partial z^2}(C_N + C_S) \\ &- \frac{1}{2}\oint_{\Gamma_S} \left(-\frac{\partial^2 \Psi}{\partial t \partial y} + A_H \Delta \frac{\partial \Psi}{\partial y} - C_D \frac{\partial \Psi}{\partial y} + C_D(C_S - C_N) - F_x\right) dx.\end{aligned} \tag{2.117b}$$

It must also be ensured that this solution created by combining the zero-boundary solution Ψ with the boundary values C_N and C_S satisfies the zero vertical velocity condition (2.103) at the top and bottom boundaries. Substituting the streamfunction decomposition (2.106) into this condition (2.103),

$$\begin{aligned}&\frac{\partial^2 \Psi}{\partial t \partial z} + (\boldsymbol{u_g} \cdot \nabla)\frac{\partial \Psi}{\partial z} - K_{V_2}\frac{\partial^3 \Psi}{\partial z^3} + \frac{\partial^2}{\partial t \partial z}(C_N \psi_N + C_S \psi_S) \\ &+(\boldsymbol{u_g} \cdot \nabla)\frac{\partial}{\partial z}(C_N \psi_N + C_S \psi_S) - K_{V_2}\frac{\partial^3}{\partial z^3}(C_N \psi_N + C_S \psi_S) - \mathcal{H}_t = 0,\end{aligned} \tag{2.118}$$

on Γ_T and Γ_B. Since C_N and C_S are equal to the streamfunction ψ evaluated at

the north and south boundaries

$$\begin{aligned}
&\frac{\partial^2 C_N}{\partial t \partial z}\psi_N + \frac{\partial^2 C_S}{\partial t \partial z}\psi_S - K_{V_2}\left[\frac{\partial^3 C_N}{\partial z^3}\psi_N + \frac{\partial^3 C_S}{\partial z^3}\psi_S\right] \\
&= \left[\frac{\partial^2 \psi}{\partial t \partial z} + (\boldsymbol{u_g}\cdot\nabla)\frac{\partial \psi}{\partial z} - K_{V_2}\frac{\partial^3 \psi}{\partial z^3}\right]\Bigg|_{\Gamma_N}\psi_N + \left[\frac{\partial^2 \psi}{\partial t \partial z} + (\boldsymbol{u_g}\cdot\nabla)\frac{\partial \psi}{\partial z} - K_{V_2}\frac{\partial^3 \psi}{\partial z^3}\right]\Bigg|_{\Gamma_S}\psi_S \\
&= -\frac{N^2}{f_0}(w|_{\Gamma_N}\psi_N + w|_{\Gamma_S}\psi_S) + \mathcal{H}_t|_{\Gamma_N}\psi_N + \mathcal{H}_t|_{\Gamma_S}\psi_S \qquad (2.119) \\
&= \mathcal{H}_t|_{\Gamma_N}\psi_N + \mathcal{H}_t|_{\Gamma_S}\psi_S
\end{aligned}$$

where $w = 0$ has been used on the top and bottom boundaries and $(\boldsymbol{u_g}\cdot\nabla)C_N = (\boldsymbol{u_g}\cdot\nabla)C_S = 0$ on the side walls. Therefore, the boundary condition on Ψ at the top and bottom is

$$\frac{\partial^2 \Psi}{\partial t \partial z} + (\boldsymbol{u_g}\cdot\nabla)\frac{\partial \Psi}{\partial z} - K_{V_2}\frac{\partial^3 \Psi}{\partial z^3} = v_g\frac{\partial}{\partial z}(C_S - C_N) + \mathcal{H}_t - \mathcal{H}_t|_{\Gamma_N}\psi_N - \mathcal{H}_t|_{\Gamma_S}\psi_S. \qquad (2.120)$$

Similarly, one must also make a correction to the potential vorticity equation (2.101b). Substituting the streamfunction decomposition into this equation,

$$\begin{aligned}
q &= \Delta\Psi + Bu^{-1}\frac{\partial}{\partial z}\left(\frac{1}{N^2}\frac{\partial \Psi}{\partial z}\right) + Bu^{-1}\frac{\partial}{\partial z}\left(\frac{1}{N^2}\frac{\partial}{\partial z}(C_N\psi_N + C_S\psi_S)\right) + \beta y \\
&= \Delta\Psi + Bu^{-1}\frac{\partial}{\partial z}\left(\frac{1}{N^2}\frac{\partial \Psi}{\partial z}\right) + \beta y \qquad (2.121) \\
&+ Bu^{-1}\left[\left(\frac{\partial C_N}{\partial z}\frac{\partial N^{-2}}{\partial z} + N^{-2}\frac{\partial^2 C_N}{\partial z^2}\right)\psi_N + \left(\frac{\partial C_S}{\partial z}\frac{\partial N^{-2}}{\partial z} + N^{-2}\frac{\partial^2 C_S}{\partial z^2}\right)\psi_S\right].
\end{aligned}$$

Notice that the extra term only comes from the vertical derivatives since $\Delta\psi_N = \Delta\psi_S = 0$ and C_N and C_S depend on t and z only. This can be simplified further when $A_H \neq 0$ so that $\Delta\psi = 0$ on Γ_N and Γ_S; since C_N and C_S are the values of the full streamfunction solution ψ at the boundaries,

$$\begin{aligned}
q|_{\Gamma_N} &= \left[\Delta\psi + Bu^{-1}\frac{\partial}{\partial z}\left(\frac{1}{N^2}\frac{\partial \psi}{\partial z}\right) + \beta y\right]\Bigg|_{\Gamma_N} = \left[Bu^{-1}\frac{\partial}{\partial z}\left(\frac{1}{N^2}\frac{\partial \psi}{\partial z}\right) + \beta y\right]\Bigg|_{y=1} \\
&= Bu^{-1}\frac{\partial}{\partial z}\left(\frac{1}{N^2}\frac{\partial C_N}{\partial z}\right) + (\beta y)|_{\Gamma_N} \\
&\Rightarrow Bu^{-1}\frac{\partial}{\partial z}\left(\frac{1}{N^2}\frac{\partial C_N}{\partial z}\right) = (q - \beta y)|_{\Gamma_N} \qquad (2.122)
\end{aligned}$$

where the boundary condition $\Delta\psi = 0$ on Γ_N has been used. Likewise, for the south

boundary

$$Bu^{-1}\frac{\partial}{\partial z}\left(\frac{1}{N^2}\frac{\partial C_S}{\partial z}\right) = (q-\beta y)|_{\Gamma_S}. \tag{2.123}$$

So, the correction is now

$$q = \Delta\Psi + Bu^{-1}\frac{\partial}{\partial z}\left(\frac{1}{N^2}\frac{\partial \Psi}{\partial z}\right) + \beta y + (q-\beta y)|_{\Gamma_N}\psi_N + (q-\beta y)|_{\Gamma_S}\psi_S. \tag{2.124}$$

Chapter 3

Mathematical Framework

This chapter presents the mathematical framework required for finite element theory. Finite element methods revolve around Sobolev spaces which are vector spaces of functions equipped with a norm on the functions and their weak derivatives. These are the natural spaces to use as the finite element method involves formulating the problem in a weak sense and then approximating the solution in a finite dimensional subspace using a tessellation of the domain. The material here can be found in standard texts on partial differential equations and finite element methods [4, 48, 105].

3.1 Sobolev Spaces

Definition 3.1. *(Inner Product)*
Let f and g be square integrable functions $f, g : \Omega \to \mathbb{R}$, on a domain $\Omega \subset \mathbb{R}^d$ for dimension d. Then their inner product is defined as

$$(f, g) := \int_\Omega f g \, d\boldsymbol{x}. \tag{3.1}$$

Definition 3.2. *(Lebesgue Space)*
The Lebesgue space $L^p(\Omega)$ consists of all those functions that are measurable (limit of a sequence of step functions almost everywhere) and whose pth power is Lebesgue integrable;

$$L^p(\Omega) = \{f : f \text{ measurable and } ||f||_{L^p} < \infty\}, \tag{3.2}$$

where

$$||f||_{L^p} = \left(\int_\Omega |f|^p \, d\boldsymbol{x} \right)^{\frac{1}{p}}. \tag{3.3}$$

Lebesgue spaces are Banach spaces when equipped with their norms.

Definition 3.3. *(Sobolev Space)*
Let $k \geq 0$ and α be a multi-index with $|\alpha| \leq k$. Then the Sobolev space $W^{k,p}(\Omega)$ is defined as

$$W^{k,p}(\Omega) = \{f \in L^p(\Omega) : D^\alpha f \in L^p(\Omega), 0 \leq |\alpha| \leq k\}, \tag{3.4}$$

where $D^\alpha f$ is the order α weak derivative of f. The space is equipped with the norm

$$||f||_{W^{k,p}} = \left(\sum_{0 \leq |\alpha| \leq k} ||D^\alpha f||_{L^p}^p \right)^{1/p}. \tag{3.5}$$

$W^{k,p}(\Omega)$ is a Banach space and separable if $1 \leq p < \infty$. Denote $W^{k,2}(\Omega)$ as $H^k(\Omega)$, also define $H_0^k(\Omega)$ as the closure in $H^k(\Omega)$ of infinitely differentiable functions compactly supported in Ω which can be heuristically defined as

$$H_0^k(\Omega) = \{f \in H^k(\Omega) : D^\alpha f = 0 \text{ on } \partial\Omega \text{ for } |\alpha| \leq k-1\}. \tag{3.6}$$

Finite element methods rely on the division of a domain into a grid or tessellation.

Definition 3.4. *(Tessellation)*
A tessellation *of a polyhedral domain Ω is a partitioning $\mathcal{T}_h$ of Ω into closed polygons or polyhedra such that*

$$\overline{\Omega} = \bigcup_{T \in \mathcal{T}_h} T, \tag{3.7}$$

and the elements $T \in \mathcal{T}_h$ have pairwise disjoint interiors. Define the maximal element diameter as

$$h := \max_{T \in \mathcal{T}_h} h_T \quad \text{where} \quad h_T := \max_{x,y \in T} |x - y|. \tag{3.8}$$

Discontinuous Galerkin finite element methods allow for discontinuities in the solution between elements in a tessellation. A discontinuous solution therefore requires an adjustment to the Sobolev space definition to allow for these discontinuities. These broken Sobolev spaces depend on a subdivision of the domain defined above.

Definition 3.5. *(Broken Sobolev Space)*
Let $\mathcal{T}_h$ be a tessellation of Ω, then the broken Sobolev spaces *needed for a discontinuous Galerkin finite element framework are defined as*

$$H^m(\mathcal{T}_h) = \left\{ v \in L^2(\Omega) : v|_T \in H^m(T) \text{ for all } T \in \mathcal{T}_h \right\}. \tag{3.9}$$

For the discontinuous Galerkin approach, one must also pay attention to the values on the element intersections.

Definition 3.6. *(Intersections)*
Let $\mathcal{T}_h$ be a tessellation of Ω . Then define the set of interior intersections *in $\mathcal{T}_h$ as*

$$\mathcal{I}_h = \{e \subset \Omega : e = \overline{T_e^+} \cap \overline{T_e^-} \text{ for } T_e^+, T_e^- \in \mathcal{T}_h \text{ with } T_e^+ \neq T_e^- \text{ and } |e| \neq 0\} \quad (3.10)$$

and the set of boundary intersections *as*

$$\mathcal{I}_h^\partial = \{e \subset \partial\Omega : e = \overline{T} \cap \partial\Omega \text{ is an edge of } T \in \mathcal{T}_h\}. \quad (3.11)$$

This definition has used the notation T_e^+, T_e^- to define two elements with $e \subset \partial T_e^\pm$. Outer unit normals to $\partial T_e^\pm$ are similarly denoted $\boldsymbol{n}_e^\pm$.

Functions in broken Sobolev spaces can have two values on interior intersections. Therefore, it is useful to define the jump and average operators which map $u \in H^m(\mathcal{T}_h)$ to $L^2(\Gamma_h)$ functions, where $\Gamma_h = \bigcup_{e \in \mathcal{I}_h \cup \mathcal{I}_h^\partial} e$ denotes the union of the edges of the elements $T \in \mathcal{T}_h$.

Definition 3.7. *(Jumps and Averages)*
For $v \in H^m(\mathcal{T}_h)$ define the average and jump operators over an intersection $e \in \mathcal{I}_h$ as

$$\{v\} = \frac{1}{2}\left(v|_{T_e^+} + v|_{T_e^-}\right), \quad [v] = \left(v|_{T_e^+}\boldsymbol{n}_e^+ + v|_{T_e^-}\boldsymbol{n}_e^-\right) \text{ on } e \in \mathcal{I}_h. \quad (3.12)$$

For vector valued functions $\boldsymbol{u} \in (H^m(\mathcal{T}_h))^d$ define

$$\{\boldsymbol{u}\} = \frac{1}{2}\left(\boldsymbol{u}|_{T_e^+} + \boldsymbol{u}|_{T_e^-}\right), \quad [\boldsymbol{u}] = \left(\boldsymbol{u}|_{T_e^+} \cdot \boldsymbol{n}_e^+ + \boldsymbol{u}|_{T_e^-} \cdot \boldsymbol{n}_e^-\right) \text{ on } e \in \mathcal{I}_h. \quad (3.13)$$

For boundary intersections $e \in \mathcal{I}_h^\partial$ define

$$\{v\} = v, \quad [v] = (v - g_D)\boldsymbol{n}, \quad \{\boldsymbol{u}\} = \boldsymbol{u}, \quad [\boldsymbol{u}] = (\boldsymbol{u} - \boldsymbol{f_D}) \cdot \boldsymbol{n} \text{ on } e \in \mathcal{I}_h^\partial, \quad (3.14)$$

where g_D and $\boldsymbol{f_D}$ are given boundary data for v and $\boldsymbol{u}$ respectively. The notation $v|_{T_e^+}$ denotes the trace of v in element T_e^+ along edge e.

The following jump and average operator properties will be required to manipulate the terms involved with a discontinuous formulation.

Lemma 3.8. *(Properties of Jumps and Averages)*
Consider functions $\boldsymbol{u} \in (H^1(\mathcal{T}_h))^d$ and $v \in H^1(\mathcal{T}_h)$ and an edge $e \in \mathcal{I}_h \cup \mathcal{I}_h^\partial$ then

1. $[\boldsymbol{u}v] = \{\boldsymbol{u}\} \cdot [v] + [\boldsymbol{u}] \{v\}$ *on* $e \in \mathcal{I}_h$.

2. $[\boldsymbol{u}v] = \{\boldsymbol{u}\} \cdot [v] + [g_D \boldsymbol{u}]$ *on* $e \in \mathcal{I}_h^\partial$.

3. $[\boldsymbol{u}v] = [\boldsymbol{u}]v$ *for* $v \in C^0(\Omega)$.

4. $[\boldsymbol{u}] = 0, \{\boldsymbol{u}\} = \boldsymbol{u}$ *if* $\boldsymbol{u} \in (H^1(\Omega))^d$

Proof. To prove the first equality, consider an interior intersection $e \in \mathcal{I}_h$, then

$$\begin{aligned}
[\boldsymbol{u}] \{v\} + \{\boldsymbol{u}\} \cdot [v] = & \quad \frac{1}{2} \left(\boldsymbol{u}|_{T_e^+} \cdot \boldsymbol{n}_e^+ + \boldsymbol{u}|_{T_e^-} \cdot \boldsymbol{n}_e^- \right) \cdot \left(v|_{T_e^+} + v|_{T_e^-} \right) \\
& + \frac{1}{2} \left(\boldsymbol{u}|_{T_e^+} + \boldsymbol{u}|_{T_e^-} \right) \left(v|_{T_e^+} \boldsymbol{n}_e^+ + v|_{T_e^-} \boldsymbol{n}_e^- \right) \\
= & \quad \frac{1}{2} \Big(2\boldsymbol{u}|_{T_e^+} v|_{T_e^+} \cdot \boldsymbol{n}_e^+ + 2\boldsymbol{u}|_{T_e^-} v|_{T_e^-} \cdot \boldsymbol{n}_e^- \\
& + \boldsymbol{u}|_{T_e^+} v|_{T_e^-} \cdot \boldsymbol{n}_e^+ + \boldsymbol{u}|_{T_e^+} v|_{T_e^-} \cdot \boldsymbol{n}_e^- \\
& + \boldsymbol{u}|_{T_e^-} v|_{T_e^+} \cdot \boldsymbol{n}_e^+ + \boldsymbol{u}|_{T_e^-} v|_{T_e^+} \cdot \boldsymbol{n}_e^- \Big) \\
= & \quad \boldsymbol{u}|_{T_e^+} v|_{T_e^+} \cdot \boldsymbol{n}_e^+ + \boldsymbol{u}|_{T_e^-} v|_{T_e^-} \cdot \boldsymbol{n}_e^- = [\boldsymbol{u}v]. \qquad (3.15)
\end{aligned}$$

For the second equality, take a boundary intersection $e \in \mathcal{I}_h^\partial$, then

$$\{\boldsymbol{u}\} \cdot [v] = (v - g_D) \boldsymbol{n} \cdot \boldsymbol{u} = [\boldsymbol{u}v] - [g_D \boldsymbol{u}] \qquad (3.16)$$

where it is assumed that the boundary data $\boldsymbol{f_D} = 0$ for $\boldsymbol{u}$. The third and forth equalities follow easily by the continuity of the functions. □

A key component that is vital to the finite element method in the formulation of the weak problem is integration by parts, the continuous form is as follows.

Theorem 3.9. *(Integration by Parts)*
Suppose that $\Omega \subset \mathbb{R}^d$ *is a domain, consider* $\boldsymbol{u} \in (H^1(\Omega))^r$ *and* $v \in H^1(\Omega)$ *then*

$$\int_\Omega \nabla \cdot \boldsymbol{u} v \, d\Omega = \int_{\partial\Omega} \boldsymbol{u} \cdot \boldsymbol{n} v \, d\Gamma - \int_\Omega \boldsymbol{u} \cdot \nabla v \, d\Omega, \qquad (3.17)$$

for unit outer normal $\boldsymbol{n}$ *to the surface* $\Gamma = \partial\Omega$ *formed by the boundary of the domain.*

Proof. Apply the divergence theorem to $\boldsymbol{u}v$, (see [48]). □

This will also need to be applied to functions in broken Sobolev spaces for the discontinuous Galerkin weak formulations.

Theorem 3.10. *(Integration by Parts for Broken Sobolev Spaces)*
Suppose that $\mathcal{T}_h$ is a tessellation of the domain Ω, consider $\boldsymbol{u} \in (H^2(\mathcal{T}_h))^r$ and $v \in H^2(\mathcal{T}_h)$ then

$$\sum_{T\in\mathcal{T}_h}\int_T \nabla\cdot\boldsymbol{u}v = \sum_{e\in\mathcal{I}_h\cup\mathcal{I}_h^\partial}\int_e [v]\cdot\{\boldsymbol{u}\} + \sum_{e\in\mathcal{I}_h\cup\mathcal{I}_h^\partial}\int_e [\boldsymbol{u}]\{v\} - \sum_{T\in\mathcal{T}_h}\int_T \boldsymbol{u}\cdot\nabla v. \quad (3.18)$$

Proof. First apply integration by parts in Theorem 3.9 to get

$$\sum_{T\in\mathcal{T}_h}\int_T \nabla\cdot\boldsymbol{u}v = \sum_{T\in\mathcal{T}_h}\left(\int_{\partial T}\boldsymbol{u}\cdot\boldsymbol{n}v - \int_T \boldsymbol{u}\cdot\nabla v\right). \quad (3.19)$$

Now, each intersection $e \in \mathcal{I}_h$ appears two times in the boundary term; once for $T = T_e^+$ with normal $\boldsymbol{n}_e^+$ and another for $T = T_e^-$ with normal $\boldsymbol{n}_e^-$. Therefore, by writing the boundary term as a sum over the element intersections

$$\begin{aligned}\sum_{T\in\mathcal{T}_h}\int_T \nabla\cdot\boldsymbol{u}v &= \sum_{e\in\mathcal{I}_h}\int_e\left(\boldsymbol{u}|_{T_e^+}\cdot\boldsymbol{n}_e^+ v|_{T_e^+} + \boldsymbol{u}|_{T_e^-}\cdot\boldsymbol{n}_e^- v|_{T_e^-}\right) + \sum_{e\in\mathcal{I}_h^\partial}\int_e \boldsymbol{u}\cdot\boldsymbol{n}v \\ &\quad - \sum_{T\in\mathcal{T}_h}\int_T \boldsymbol{u}\cdot\nabla v \qquad (3.20)\\ &= \sum_{e\in\mathcal{I}_h\cup\mathcal{I}_h^\partial}\int_e [\boldsymbol{u}v] - \sum_{T\in\mathcal{T}_h}\int_T \boldsymbol{u}\cdot\nabla v\end{aligned}$$

which follows from the definition of the jump operator with zero Dirichlet $\boldsymbol{g_D} = 0$ or no-flow $\boldsymbol{u}\cdot\boldsymbol{n} = 0$ boundary conditions. □

The proof of Theorem 3.10 is only for the cases of zero Dirichlet or no-flow boundary conditions as these are the only cases that will be required.

3.2 Weak Formulations

The concept of finite element methods is centred around a Galerkin approach where the problem is formulated in weak or variational form. To demonstrate the method, suppose one is tasked with the problem of finding a solution $u : \Omega \to \mathbb{R}$ such that

$$-\Delta u + u = f, \quad \text{in } \Omega, \quad (3.21a)$$

$$u = 0 \quad \text{on } \partial\Omega, \quad (3.21b)$$

for some function $f \in C^0(\overline{\Omega}, \mathbb{R})$. Using the space $V = H_0^1(\Omega)$, multiply (3.21a) by a test function $v \in V$, integrate over the domain Ω and apply integration by parts where the boundary term vanishes since $v \in V$. Defining the bilinear form

$$a(u, v) = \int_\Omega \nabla u \cdot \nabla v + uv \, dx \tag{3.22}$$

and the linear form using the inner product

$$l(v) = (f, v) = \int_\Omega fv \, dx \tag{3.23}$$

allows one to write the weak formulation of the problem as: find $u \in V$ such that

$$a(u, v) = l(v) \;\; \forall v \in V. \tag{3.24}$$

This can be shown to be equivalent to the strong form of the problem (3.21) given certain regularity assumptions on f and the domain boundary $\partial\Omega$ [116]. A finite element method can now be implemented by creating a tessellation $\mathcal{T}_h$ of the domain and defining a finite dimensional discrete subspace $V_h \subset V$ that approximates a solution by a combination of piecewise polynomials. The problem is then to find a discrete solution $u_h \in V_h$ such that

$$a(u_h, v_h) = l(v_h) \;\; \forall v_h \in V_h. \tag{3.25}$$

Note that, the discrete solution and finite element space depend upon a parameter h that is the grid spacing determined by a maximal length within the polygons of the tessellation. High accuracy solutions are then obtained by letting $h \to 0$ so that $u_h \to u$.

3.3 Lax Milgram

The following theorem is important in variational theory and shows that the finite element numerical method will have a unique solution.

Theorem 3.11. *(Lax Milgram)*
For a bilinear form $a : V \times V \to \mathbb{R}$ and linear functional $l : V \to \mathbb{R}$, consider the following variational problem; find $u \in V$ such that $a(u, v) = l(v)$ for all $v \in V$. Suppose the following conditions hold,

1. *$a(\cdot, \cdot)$ is bounded, that is there exists a $C_a > 0$ such that $|a(u, v)| \leq C_a \|u\|_V \|v\|_V$ for all $u, v \in V$.*

2. *$a(\cdot,\cdot)$ is coercive, that is there exists an $\alpha > 0$ such that $a(v,v) \geq \alpha \|v\|_V^2$ for all $v \in V$.*

3. *$l(\cdot)$ is bounded, that is there exists a $C_l > 0$ such that $|l(v)| \leq C_l \|v\|_V$ for all $v \in V$.*

Then the variational problem has a unique solution and the solution u satisfies

$$\|u\| \leq \frac{1}{\alpha} \|l\|_{V^*} \tag{3.26}$$

Proof. See [48]. □

3.4 Non-zero Boundary Conditions

Lax Milgram can be used to show that there is a unique solution to the weak problem (3.24). However, suppose that a problem has non-zero Dirichlet boundary given by $g \in H^1(\Omega)$: find $u : \Omega \to \mathbb{R}$ such that

$$-\Delta u + u = f, \quad \text{in } \Omega, \tag{3.27a}$$

$$u = g \quad \text{on } \partial\Omega. \tag{3.27b}$$

Lax Milgram cannot be directly applied to the weak formulation for u since the space $V_g = \left\{ w \in H^1(\Omega) : w = v + g, \text{ for some } v \in H_0^1(\Omega) \right\}$ is not a linear space. Although, one may solve the problem: find $u_0 = u - g \in V$ with $g \in H^1(\Omega)$ such that

$$a(u_0, v) = l(v) - a(g, v) =: l_0(v), \ \ \forall v \in V. \tag{3.28}$$

Lax Milgram is applicable to this problem and so there is a unique solution u_0, therefore, there exists a unique $u = u_0 + g$. This allows the implementation of a finite element method for non-zero boundaries by solving for the solution u_0 and then combining this with the function g to get the desired solution u.

3.5 Interior Penalty Discontinuous Galerkin Method

When using a discontinuous space to solve problem (3.27), the weak formulation must consider the sum of elements of the tessellation $\mathcal{T}_h$ instead of the whole domain

when integrating, so that the bilinear form becomes for $u, v \in H^2(\mathcal{T}_h)$

$$a_{DG}(u,v) = \sum_{T\in\mathcal{T}_h}\int_T (\nabla u\cdot\nabla v + uv) - \sum_{e\in\mathcal{I}_h\cup\mathcal{I}_h^\partial}\int_e \{\nabla u\}\cdot[v] - \sum_{e\in\mathcal{I}_h\cup\mathcal{I}_h^\partial}\int_e \{\nabla v\}\cdot[u] + \sum_{e\in\mathcal{I}_h\cup\mathcal{I}_h^\partial}\beta_e\int_e [u]\cdot[v], \tag{3.29}$$

where integration by parts for broken Sobolev spaces (Theorem 3.10) has been used and the $[\nabla u]\{v\}$ term has been neglected since the jump of the gradient of the true solution $[\nabla u] = 0$. The third term has been added to make the problem symmetric, allowing for more efficient numerical solvers to be used. A penalty term with penalty parameter β_e has been added to penalise jumps in the solution for stability and to weakly enforce boundary conditions. In a discontinuous Galerkin method, the boundary conditions are enforced weakly within the formulation itself rather than as a requirement in the solution space. The addition of these terms also ensure uniqueness of the solution without affecting the consistency with the original problem since $[u] = 0$. The solution is required to be in $H^2(\mathcal{T}_h)$, so that the traces of ∇u and ∇v are well defined (see trace theorems in [105]) and $a_{DG}(\cdot,\cdot)$ is a bilinear form. This formulation is known as the *symmetric interior penalty method* [3].

Chapter 4

Finite Element Discretisation

Finite element methods involve discretising the domain into a tessellation of elements, usually square or triangular, and solving the equations in a distributional sense using local basis functions. These methods were developed for solving complex engineering problems and have been used for a long time in the field [4, 54]. Finite element methods have recently become popular within fluid dynamics and atmospheric simulation as it allows for easy treatment of complex boundaries and multiply connected domains with high order accuracy [20, 51, 63, 102, 107, 127]. This chapter presents a discretisation of the quasi-geostrophic equations using a combination of finite elements in the horizontal directions and finite differences in the less dynamical vertical direction.

4.1 Numerical Scheme

The numerical scheme will work on a cuboid domain $\Omega \times [0,1] = [0, L_x/L] \times [0,1] \times [0,1]$ using the method of lines in the vertical z direction and a finite element method on a mesh on the horizontal layers. Denote each layer Ω_j for $j = 0, ..., \mathcal{N}$ with equal spacing Δz with Ω_0 on the bottom of the domain ($z = 0$) and $\Omega_\mathcal{N}$ at the top ($z = 1$). Once the horizontal has been discretised, finite difference approximations will be used to discretise vertical derivatives with $\psi_j : \Omega_j \to \mathbb{R}$ denoting $\psi|_{\Omega_j} = \psi(x, y, j\Delta z)$, that is the function ψ evaluated at level j. Boundary conditions given by equation (2.102) are no-flow through the rigid north, south, top and bottom boundaries. Therefore, the advecting horizontal velocity $\boldsymbol{u_g} = \nabla^\perp \psi$ must satisfy $\boldsymbol{u_g} \cdot \boldsymbol{n} = 0$ at the north ($y = 1$) and south ($y = 0$) walls and the vertical velocity w must also satisfy $w = 0$ on the top $\Gamma_T := \Omega_\mathcal{N}$ and bottom $\Gamma_B := \Omega_0$ boundaries. In the case where diffusion is present, there must also be no diffusive flux at these

walls as stated in (2.102). The east-west boundaries are periodic.

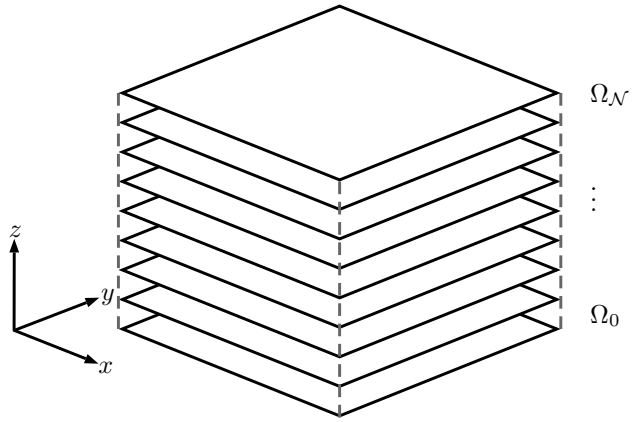

Figure 4.1: Domain split into $\mathcal{N}+1$ horizontal layers with equal spacing Δz. Each layer is divided up with the same tessellation $\mathcal{T}_h$.

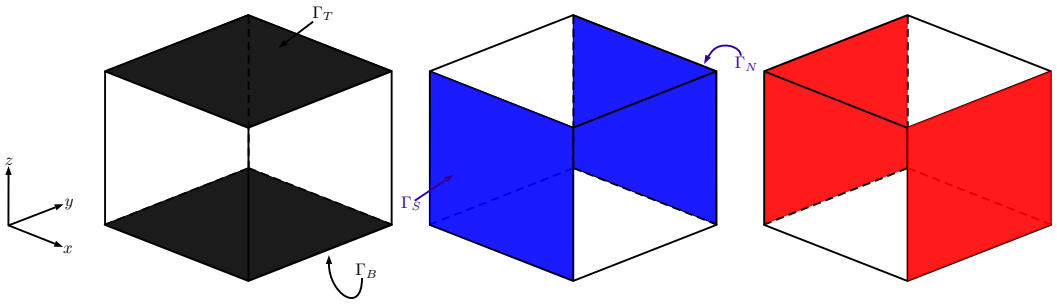

Figure 4.2: Domain boundaries. Black: top and bottom boundaries with no-flow through condition $w = 0$ (and no flux $\partial^2\psi/\partial z^2 = 0$ if vertical buoyancy diffusion present), Blue: north and south boundaries with no-flow through condition $\boldsymbol{u_g}\cdot\boldsymbol{n} = 0$ (and no flux $\partial^2\psi/\partial y^2 = 0$ if horizontal momentum diffusion present), Red: periodic east and west boundaries.

4.1.1 Finite Element Spatial Discretisation

The method solves for potential vorticity q in a discontinuous space with continuous streamfunction ψ. This ensures velocity is not discontinuous across element intersections in the normal direction and an upwind flux can be used without instability issues. This can been seen from $\boldsymbol{u_g}\cdot\boldsymbol{n} = \nabla^\perp\psi\cdot\boldsymbol{n} = -\nabla\psi\cdot\boldsymbol{\tau}$, where $\nabla^\perp = (-\partial_y, \partial_x)$ and $\nabla = (\partial_x, \partial_y)$ are the two-dimensional curl and gradient operators. Then because the streamfunction ψ is continuous, the gradient in the tangential direction at the element boundary is single valued, and so is the normal component of velocity. This method was implemented using the two-dimensional, inviscid QGE by Bernsen

et al. (2006), [20], the work presented here will extend this to the three-dimensional QGE with diffusion, forcing and free-slip boundary conditions providing a more useful atmospheric model. Recall the non-dimensionalised quasi-geostrophic equations (2.100) from Section 2.3.2,

$$\frac{\partial q}{\partial t} + J(\psi, q) = \mathcal{F} + A_H \Delta^2 \psi + K_{V_1} \frac{\partial}{\partial z}\left(\frac{1}{N^2}\frac{\partial^3 \psi}{\partial z^3}\right) - C_D \Delta \psi \tag{4.1a}$$

$$q = \Delta \psi + Bu^{-1} \frac{\partial}{\partial z}\left(\frac{1}{N^2}\frac{\partial \psi}{\partial z}\right) + \beta y. \tag{4.1b}$$

The heating term $\mathcal{H}_t$ has been absorbed into $\mathcal{F}$ since they serve the same purpose with regards to discretising the main equations. The Laplacian and gradient operators are two-dimensional. Define the relative vorticity $\omega := \Delta\psi = \partial^2\psi/\partial x^2 + \partial^2\psi/\partial y^2$ and substitute this into equation (4.1a) to get

$$\frac{\partial q}{\partial t} + (\boldsymbol{u_g} \cdot \nabla) q = \mathcal{F} + A_H \Delta \omega + K_{V_1} \frac{\partial}{\partial z}\left(\frac{1}{N^2}\frac{\partial^3 \psi}{\partial z^3}\right) - C_D \omega, \tag{4.2}$$

where relative vorticity can be alternatively calculated as

$$\omega = q - \beta y - \frac{\partial}{\partial z}\left(\frac{Bu^{-1}}{N^2}\frac{\partial \psi}{\partial z}\right). \tag{4.3}$$

Consider the two-dimensional domain $\Omega = [0, L_x/L] \times [0, 1] \subset \mathbb{R}^2$. The problem is, find $\psi : \Omega \times [0,1] \times [0,\infty) \to \mathbb{R}$ (and therefore $q : \Omega \times [0,1] \times [0,\infty) \to \mathbb{R}$, $\boldsymbol{u_g} : \Omega \times [0,1] \times [0,\infty) \to \mathbb{R}$ and $\omega : \Omega \times [0,1] \times [0,\infty) \to \mathbb{R}$) such that (4.1b), (4.2) and (4.3) are satisfied, subject to the boundary conditions (2.102),

$$\frac{\partial \psi}{\partial \boldsymbol{\tau}} = A_H \frac{\partial^2 \psi}{\partial \boldsymbol{n}^2} = 0 \text{ on } \Gamma_N \cup \Gamma_S, \tag{4.4a}$$

$$w = K_{V_1} \frac{\partial^2 \psi}{\partial z^2} = 0 \text{ on } \Gamma_T \cup \Gamma_B, \tag{4.4b}$$

and auxiliary conditions (2.105),

$$\oint_{\Gamma_S} \left(\frac{\partial}{\partial \boldsymbol{n}}\left(\frac{\partial \psi}{\partial t} - A_H \Delta \psi + C_D \psi\right) - \boldsymbol{F} \cdot \hat{\boldsymbol{s}}\right) d\boldsymbol{s} = 0, \tag{4.5a}$$

$$\int_\Omega w \, dxdy = 0, \tag{4.5b}$$

with initial condition

$$\psi(x, y, z, 0) = \psi^0 \text{ for } (x, y, z) \in \Omega \times [0, 1], \tag{4.6}$$

for some given $\psi^0 : \Omega \times [0,1] \to \mathbb{R}$ which determines all other initial fields.

Now, define the space that will be applicable to continuous solutions as

$$V_\psi := \left\{ \phi \in H^1(\Omega) : \phi = 0 \text{ on } \Gamma_N \cup \Gamma_S \right\}. \tag{4.7}$$

The north Γ_N and south Γ_S boundaries are as shown in Figure 4.2. Consider a tessellation $\mathcal{T}_h$ of the two-dimensional domain Ω, let $V_q = H^2(\mathcal{T}_h)$, then define finite element spaces $V_{q_h}^p$ and $V_{\psi_h}^p$ of piecewise polynomials such that $V_{q_h}^p \subset V_q$ and $V_{\psi_h}^p \subset V_\psi$. Define the p^{th} order continuous discrete space

$$V_{\psi_h}^p = \left\{ v \in C^0(\Omega) \cap V_\psi : v|_T \in P^p(T) \text{ for all } T \in \mathcal{T}_h \right\} \tag{4.8}$$

and the p^{th} order discontinuous discrete space

$$V_{q_h}^p = \left\{ v \in V_q : v|_T \in P^p(T) \text{ for all } T \in \mathcal{T}_h \right\} \tag{4.9}$$

where p is the degree of the polynomial space P^p. For quadrilateral elements, the space of polynomial products $Q^p = \{p : p = p_1 p_2, \text{ for } p_1, p_2 \in P^p\}$ is used instead of P^p. The order of finite element methods are determined by the order of the discrete space used, hence the order of the polynomials on each element. To simplify notation, define the finite element spaces $V_{\psi_h} := V_{\psi_h}^p$ and $V_{q_h} := V_{q_h}^p$ where it is understood that the order p of these spaces may be varied during implementation and need not be identical.

To begin the finite element discretisation in the horizontal directions, consider a fixed vertical height z and a two-dimensional horizontal domain Ω so that the weak formulation required by the finite element method may be obtained. The existence of global weak solutions to the QGE is shown in [103]. Assume that the true solutions $\psi, q, \omega, \boldsymbol{u_g}$ are smooth. Transform the first equation into a weak form by multiplying (4.2) by a test function $\varphi \in V_q$, integrating over an element $T \in \mathcal{T}_h$ and summing over all elements to get

$$\begin{aligned} \sum_{T\in\mathcal{T}_h} \int_T \frac{\partial q}{\partial t}\varphi = &- \sum_{T\in\mathcal{T}_h} \int_T J(\psi, q)\varphi + \sum_{T\in\mathcal{T}_h} \int_T A_H \Delta\omega\varphi + \sum_{T\in\mathcal{T}_h} \int_T K_{V_1} \frac{\partial}{\partial z}\left(\frac{1}{N^2}\frac{\partial^3\psi}{\partial z^3}\right)\varphi \\ &- \sum_{T\in\mathcal{T}_h} \int_T C_D\omega\varphi + \sum_{T\in\mathcal{T}_h} \int_T \mathcal{F}\varphi. \end{aligned} \tag{4.10}$$

The third and fifth terms on the right hand side require no further manipulation

within the weak form as no horizontal gradients are involved and the vertical derivatives just need to be discretised using an appropriate finite difference approximation. The bottom friction term (forth term on the right hand side) can be rewritten using (4.3) so that

$$\sum_{T\in\mathcal{T}_h}\int_T C_D\omega\varphi = C_D\sum_{T\in\mathcal{T}_h}\int_T\left(q-\beta y-\frac{\partial}{\partial z}\left(\frac{Bu^{-1}}{N^2}\frac{\partial\psi}{\partial z}\right)\right)\varphi \tag{4.11}$$

which allows for the q term to be treated implicitly during the time discretisation, although stability constraints should be dominated by the non-linear advection term. Notice that the advection term can be written in conservative form

$$J(\psi,q)=\frac{\partial\psi}{\partial x}\frac{\partial q}{\partial y}-\frac{\partial\psi}{\partial y}\frac{\partial q}{\partial x}=\boldsymbol{u_g}\cdot\nabla q=\nabla\cdot(\boldsymbol{u_g}q), \tag{4.12}$$

due to incompressibility ($\nabla\cdot\boldsymbol{u_g}=\partial_x u_g+\partial_y v_g=\partial_{xy}\psi-\partial_{yx}\psi=0$). Now, apply the discontinuous form of integration by parts from Theorem 3.10, noting that $\mathcal{I}_h^\partial$ is the set of edges on the north and south boundaries only,

$$\begin{aligned}\sum_{T\in\mathcal{T}_h}\int_T\nabla\cdot(\boldsymbol{u_g}q)\varphi &= \sum_{e\in\mathcal{I}_h\cup\mathcal{I}_h^\partial}\int_e[\boldsymbol{u_g}q\varphi]-\sum_{T\in\mathcal{T}_h}\int_T q\boldsymbol{u_g}\cdot\nabla\varphi\\ &= \sum_{e\in\mathcal{I}_h\cup\mathcal{I}_h^\partial}\int_e[\boldsymbol{u_g}q]\{\varphi\}+\sum_{e\in\mathcal{I}_h}\int_e\{\boldsymbol{u_g}q\}\cdot[\varphi]+\sum_{e\in\mathcal{I}_h^\partial}\int_e\underbrace{\boldsymbol{u_g}\cdot\boldsymbol{n}_e^+}_{0}q\varphi\\ &\quad-\sum_{T\in\mathcal{T}_h}\int_T q\boldsymbol{u_g}\cdot\nabla\varphi\\ &= \sum_{e\in\mathcal{I}_h}\int_e\hat{\boldsymbol{u}}_e(q)\cdot[\varphi]-\sum_{T\in\mathcal{T}_h}\int_T q\boldsymbol{u_g}\cdot\nabla\varphi,\end{aligned} \tag{4.13}$$

where the $[\boldsymbol{u_g}q]$ term was dropped since the normal velocity components are single valued at element edges $[\boldsymbol{u_g}]=(\boldsymbol{u_g}|_{T_e^+}-\boldsymbol{u_g}|_{T_e^-})\cdot\boldsymbol{n}_e^+=0$ and the true solution satisfies $[q]=0$. The following upwind numerical flux has been introduced for numerical stability [105],

$$\hat{\boldsymbol{u}}_e(q)=\begin{cases}q|_{T_e^+}\boldsymbol{u_g} & \text{if } \boldsymbol{u_g}\cdot\boldsymbol{n}_e^+\geq 0\\ q|_{T_e^-}\boldsymbol{u_g} & \text{if } \boldsymbol{u_g}\cdot\boldsymbol{n}_e^+<0\end{cases} \tag{4.14}$$

with $\boldsymbol{n}_e^+$ denoting the outer unit normal at an element edge e of element T_e^+. This is equal to $\{\boldsymbol{u_g}q\}$ for smooth solutions $\boldsymbol{u_g}$ and q. The upwind flux is introduced here in anticipation of substitution of the discrete solutions, where the potential vorticity

will be discontinuous on element intersections and (4.14) will become meaningful. Finally, turning attention to the horizontal momentum diffusion term

$$\sum_{T\in\mathcal{T}_h}\int_T A_H\Delta\omega\varphi = -\sum_{T\in\mathcal{T}_h}\int_T A_H\nabla\omega\cdot\nabla\varphi + \sum_{e\in\mathcal{I}_h\cup\mathcal{I}_h^\partial}\int_e A_H\{\nabla\omega\}\cdot[\varphi] + \cancelto{0}{\sum_{e\in\mathcal{I}_h\cup\mathcal{I}_h^\partial}\int_e A_H[\nabla\omega]\{\varphi\}}, \tag{4.15}$$

where the last term is ignored for simplicity, this is possible since the true vorticity solution ω is smooth and has no jumps hence $[\nabla\omega]=0$. One can also add a penalty term to penalise jumps in the solution and improve stability of the numerical method [105]

$$P^{\beta_e}(\omega,\varphi) = \sum_{e\in\mathcal{I}_h\cup\mathcal{I}_h^\partial}\beta_e\int_e[\omega]\cdot[\varphi], \tag{4.16}$$

and a symmetry term

$$S(\omega,\varphi) = \sum_{e\in\mathcal{I}_h\cup\mathcal{I}_h^\partial}\int_e A_H\{\nabla\varphi\}\cdot[\omega], \tag{4.17}$$

without effecting consistency since for the continuous solution $[\omega]=0$. Here $\beta_e>0$ is a penalty parameter. Now,

$$\sum_{T\in\mathcal{T}_h}\int_T A_H\Delta\omega\varphi = -\sum_{T\in\mathcal{T}_h}\int_T A_H\nabla\omega\cdot\nabla\varphi + \sum_{e\in\mathcal{I}_h\cup\mathcal{I}_h^\partial}\int_e A_H\{\nabla\omega\}\cdot[\varphi] + \sum_{e\in\mathcal{I}_h\cup\mathcal{I}_h^\partial}\int_e A_H\{\nabla\varphi\}\cdot[\omega] - \sum_{e\in\mathcal{I}_h\cup\mathcal{I}_h^\partial}\beta_e\int_e[\omega]\cdot[\varphi]. \tag{4.18}$$

Boundary intersection terms are calculated using the boundary condition $\omega=0$ on Γ_N and Γ_S. This will weakly enforce the no-flux boundary condition on the north and south walls within the discontinuous Galerkin finite element method. A weak

formulation for (4.2) is now find $q \in V_q$ such that

$$\begin{aligned}\sum_{T\in\mathcal{T}_h}\int_T \frac{\partial q}{\partial t}\varphi = &-\sum_{e\in\mathcal{I}_h}\int_e \hat{\boldsymbol{u}}_e(q)\cdot[\varphi] + \sum_{T\in\mathcal{T}_h}\int_T q\boldsymbol{u_g}\cdot\nabla\varphi \\ &-\sum_{T\in\mathcal{T}_h}\int_T A_H\nabla\omega\cdot\nabla\varphi + \sum_{e\in\mathcal{I}_h\cup\mathcal{I}_h^\partial}\int_e A_H\{\nabla\omega\}\cdot[\varphi] \\ &+\sum_{e\in\mathcal{I}_h\cup\mathcal{I}_h^\partial}\int_e A_H\{\nabla\varphi\}\cdot[\omega] - \sum_{e\in\mathcal{I}_h\cup\mathcal{I}_h^\partial}\beta_e\int_e[\omega]\cdot[\varphi] \\ &+\sum_{T\in\mathcal{T}_h}\int_T K_{V_1}\frac{\partial}{\partial z}\left(\frac{1}{N^2}\frac{\partial^3\psi}{\partial z^3}\right)\varphi \\ &-\sum_{T\in\mathcal{T}_h}\int_T C_D\omega\varphi + \sum_{T\in\mathcal{T}_h}\int_T \mathcal{F}\varphi \end{aligned} \tag{4.19}$$

for all $\varphi \in V_q$.

From Section 2.3.3, equation (4.1b) can be expressed using the streamfunction decomposition $\psi = \Psi + \psi_N C_N + \psi_S C_S$ to get

$$q - q_c = \Delta\Psi + Bu^{-1}\frac{\partial}{\partial z}\left(\frac{1}{N^2}\frac{\partial\Psi}{\partial z}\right) + \beta y. \tag{4.20}$$

where $q_c := (q-\beta y)|_{\Gamma_N}\psi_N + (q-\beta y)|_{\Gamma_S}\psi_S$ is defined for conciseness. Multiplying by a test function $\xi \in V_\psi$ and integrating over the domain Ω

$$-\int_\Omega \nabla\Psi\cdot\nabla\xi + \underbrace{\int_{\partial\Omega}\nabla\Psi\cdot\boldsymbol{n}\xi}_{0} + \int_\Omega\frac{\partial}{\partial z}\left(\frac{Bu^{-1}}{N^2}\frac{\partial\Psi}{\partial z}\right)\xi = \int_\Omega (q-q_c-\beta y)\xi \tag{4.21}$$

where the second term vanishes since $\xi \in V_\psi$ is zero on the boundary. A weak formulation for (4.1b) is therefore: find $\Psi \in V_\psi$ such that

$$-\int_\Omega \nabla\Psi\cdot\nabla\xi + \int_\Omega\frac{\partial}{\partial z}\left(\frac{Bu^{-1}}{N^2}\frac{\partial\Psi}{\partial z}\right)\xi = \int_\Omega (q-q_c-\beta y)\xi \tag{4.22}$$

for all $\xi \in V_\psi$.

4.1.2 Vertical and Time Discretisation

The weak formulations (4.19) and (4.22) have been derived above with smooth solutions to express the quasi-geostrophic equations in a form suitable for applying a

finite difference method in the horizontal directions. Now, substitute the smooth solutions with the discrete solutions so that the finite difference approximations and time discretisations can be applied. With the notation $q_j^n \approx q(x, y, j\Delta z, n\tau)$ denoting the approximation at timestep n and vertical level j, the full solution is written $q^n = (q_0^n, ..., q_{\mathcal{N}}^n) \in V_{q_h}^{\mathcal{N}+1} = V_{q_h}(\Omega_0) \times ... \times V_{q_h}(\Omega_{\mathcal{N}})$. Other variables ψ, $\boldsymbol{u_g}$, ω and $\mathcal{F}$ are discretised in a similar fashion. The terms on the right hand side of (4.19) are treated explicitly, except for the bottom friction term where a θ_m-method allows for the possibility of a semi-implicit scheme (the subscript on θ_m is only used to avoid confusion with the temperature variable θ that will be introduced in Section 4.1.3).

A fourth order central finite difference approximation is used in the vertical allowing a simplification of the finite element discretisation restricted to the horizontal. This high order method is used to reduce the impact of the low vertical resolution on the accuracy of the numerical solutions (see Chapter 5). The finite difference approximation of an mth order derivative of ψ at vertical level $j \in \{0, ..., \mathcal{N}\}$ will take the form

$$\frac{\partial^m}{\partial z^m}\psi_j(x, y) \approx \sum_{i=0}^{\mathcal{N}} \frac{\alpha_i(j, m)}{\Delta z^m}\psi_i(x, y) =: D_z^{(m)}\psi_i, \tag{4.23}$$

for coefficients $\alpha_0, ..., \alpha_{\mathcal{N}}$ depending on the centre of the approximation and order of the derivative. Table 4.1 presents the coefficients used in this fourth order scheme.

Derivative (m)	Point $(i-j)$						
	-3	-2	-1	0	1	2	3
1		1/12	$-2/3$	0	2/3	$-1/12$	
2		$-1/12$	4/3	$-5/2$	4/3	$-1/12$	
3	1/8	-1	13/8	0	13/8	1	$-1/8$
4	$-1/6$	2	$-13/2$	28/2	$-13/2$	2	$-1/6$

Table 4.1: Fourth order central finite difference coefficients as calculated in [49].

For example, the second order derivative of $\psi(x, y)$ at level j is given by

$$\frac{\partial^2}{\partial z^2}\psi_j(x, y) \approx D_z^{(2)}\psi_j = \left.\frac{-\frac{1}{12}\psi_{j-2} + \frac{4}{3}\psi_{j-1} - \frac{5}{2}\psi_j + \frac{4}{3}\psi_{j+1} - \frac{1}{12}\psi_{j+2}}{\Delta z^2}\right|_{(x,y)}. \tag{4.24}$$

After applying the vertical and time discretisations, (4.19) becomes: for each $j \in \{0, ..., \mathcal{N}\}$

$$\sum_{T\in\mathcal{T}_h}\int_T (1+\mu)\, q_j^{n+1}\varphi = \sum_{T\in\mathcal{T}_h}\int_T q_j^n\varphi + \tau\sum_{T\in\mathcal{T}_h}\int_T q_j^n \boldsymbol{u_g}_j^n\cdot\nabla\varphi - \tau\sum_{e\in\mathcal{I}_h}\int_e \hat{\boldsymbol{u}}_e^n(q_j^n)\cdot[\varphi]$$
$$- \tau\sum_{T\in\mathcal{T}_h}\int_T A_H\nabla\omega_j^n\cdot\nabla\varphi + \tau\sum_{e\in\mathcal{I}_h\cup\mathcal{I}_h^\partial}\int_e A_H\{\nabla\omega_j^n\}\cdot[\varphi]$$
$$+ \tau\sum_{e\in\mathcal{I}_h\cup\mathcal{I}_h^\partial}\int_e A_H\{\nabla\varphi\}\cdot[\omega_j^n] - \tau\sum_{e\in\mathcal{I}_h\cup\mathcal{I}_h^\partial}\beta_e\int_e[\omega_j^n]\cdot[\varphi]$$
$$+ \tau\sum_{T\in\mathcal{T}_h}\int_T K_{V_1}D_z^{(1)}\left(\frac{1}{N^2}D_z^{(3)}\psi_j^n\right)\varphi$$
$$- \tau C_D\sum_{T\in\mathcal{T}_h}\int_T\left((1-\theta_m)q_j^n - \beta y - D_z^{(1)}\left(\frac{Bu^{-1}}{N^2}D_z^{(1)}\psi_j^n\right)\right)\varphi$$
$$+ \tau\sum_{T\in\mathcal{T}_h}\int_T \mathcal{F}_j^{n+1}\varphi \text{ for all } \varphi\in V_{q_h}, \tag{4.25}$$

where $\mu := \tau C_D\theta_m$ and the z-derivatives of order m have been discretised by finite difference operators $D_z^{(m)}$. Recall the upwind numerical flux is

$$\hat{\boldsymbol{u}}_e(q_j^n) = \begin{cases} q_j^n|_{T_e^+}\boldsymbol{u_g}_j^n & \text{if } \boldsymbol{u_g}_j^n\cdot\boldsymbol{n}_e^+ \geq 0 \\ q_j^n|_{T_e^-}\boldsymbol{u_g}_j^n & \text{if } \boldsymbol{u_g}_j^n\cdot\boldsymbol{n}_e^+ < 0 \end{cases}. \tag{4.26}$$

The relative vorticity solution does not require a weak formulation as it can be calculated directly as

$$\omega_j^n = q_j^n - \beta y - D_z^{(1)}\left(\frac{Bu^{-1}}{N^2}D_z^{(1)}\psi_j^n\right). \tag{4.27}$$

Similarly the geostrophic velocity is calculated directly as

$$\boldsymbol{u_g}_j^n = \nabla^\perp\psi_j^n. \tag{4.28}$$

For (4.22), taking a test function $\xi\in V_{\psi_h}$ with support on an arbitrary element $T\in\mathcal{T}_h$ and summing over all elements

$$-\sum_{T\in\mathcal{T}_h}\int_T\nabla\Psi\cdot\nabla\xi + \sum_{T\in\mathcal{T}_h}\int_T\frac{\partial}{\partial z}\left(\frac{Bu^{-1}}{N^2}\frac{\partial\Psi}{\partial z}\right)\xi = \sum_{T\in\mathcal{T}_h}\int_T(q-q_c-\beta y)\xi \tag{4.29}$$

and substituting the discrete streamfunction solution $\Psi_j^{n+1} \in V_{\psi_h}$ gives

$$
\begin{aligned}
&- \sum_{T\in\mathcal{T}_h} \int_T \nabla\Psi_j^{n+1} \cdot \nabla\xi + \sum_{T\in\mathcal{T}_h} \int_T D_z^{(1)} \left(\frac{Bu^{-1}}{N^2} D_z^{(1)} \Psi_j^{n+1} \right) \xi \\
&= \sum_{T\in\mathcal{T}_h} \int_T (q_j^{n+1} - {q_c}_j^{n+1} - \beta y)\xi
\end{aligned} \tag{4.30}
$$

for all $\xi \in V_{\psi_h}$.

The problem discretised spatially in the horizontal and in time is now encapsulated by defining the bilinear forms $a_1 : V_{\psi_h} \times V_{\psi_h} \to \mathbb{R}$ and $a_2 : V_{\psi_h} \times V_{\psi_h} \to \mathbb{R}$,

$$
a_1(u,v) = \sum_{T\in\mathcal{T}_h} \int_T uv, \tag{4.31}
$$

$$
a_2(u,v) = \sum_{T\in\mathcal{T}_h} \int_T \nabla u \cdot \nabla v \tag{4.32}
$$

with $a_1 : V_{q_h} \times V_{q_h} \to \mathbb{R}$ also defined as in (4.31) without ambiguity as it will be clear which bilinear form is used. Also, define the linear forms $l_{1,j} : V_{q_h} \to \mathbb{R}$ and $l_{2,j} : V_{\psi_h} \to \mathbb{R}$,

$$
\begin{aligned}
l_{1,j}^n(\varphi) = \quad & \sum_{T\in\mathcal{T}_h} \int_T q_j^n \varphi + \tau \sum_{T\in\mathcal{T}_h} \int_T q_j^n \boldsymbol{u_g}_j^n \cdot \nabla\varphi - \tau \sum_{e\in\mathcal{I}_h} \int_e \hat{\boldsymbol{u}}_e^n(q_j^n) \cdot [\varphi] \\
& - \tau \sum_{T\in\mathcal{T}_h} \int_T A_H \nabla\omega_j^n \cdot \nabla\varphi + \tau \sum_{e\in\mathcal{I}_h\cup\mathcal{I}_h^\partial} \int_e A_H \{\nabla\omega_j^n\} \cdot [\varphi] \\
& + \tau \sum_{e\in\mathcal{I}_h\cup\mathcal{I}_h^\partial} \int_e A_H \{\nabla\varphi\} \cdot [\omega_j^n] - \tau \sum_{e\in\mathcal{I}_h\cup\mathcal{I}_h^\partial} \beta_e \int_e [\omega_j^n] \cdot [\varphi] \\
& + \tau \sum_{T\in\mathcal{T}_h} \int_T K_{V_1} D_z^{(1)} \left(\frac{1}{N^2} D_z^{(3)} \psi_j^n \right) \varphi \\
& - \tau C_D \sum_{T\in\mathcal{T}_h} \int_T \left((1-\theta_m) q_j^n - \beta y - D_z^{(1)} \left(\frac{Bu^{-1}}{N^2} D_z^{(1)} \psi_j^n \right) \right) \varphi \\
& + \tau \sum_{T\in\mathcal{T}_h} \int_T \mathcal{F}_j^{n+1} \varphi,
\end{aligned} \tag{4.33}
$$

$$
l_{2,j}^n(\xi) = \sum_{T\in\mathcal{T}_h} \int_T (q_j^n - {q_c}_j^n - \beta y)\xi. \tag{4.34}
$$

For each $j \in \{0, ..., \mathcal{N}\}$, given q_j^n and Ψ_j^n find $q_j^{n+1} \in V_{q_h}$ and $\Psi_j^{n+1} \in V_{\psi_h}$ such that

$$(1+\mu)a_1(q_j^{n+1}, \varphi) = l_{1,j}^n(\varphi) \text{ for all } \varphi \in V_{q_h}, \tag{4.35a}$$

$$\text{and } -a_2(\Psi_j^{n+1}, \xi) + a_1(D_z^{(1)}(Bu^{-1}N^{-2}D_z^{(1)}\Psi_j^{n+1}), \xi) = l_{2,j}^{n+1}(\xi) \text{ for all } \xi \in V_{\psi_h} \tag{4.35b}$$

where

$$\mu = \tau C_D \theta_m. \tag{4.36}$$

This is not yet complete, as the finite difference operators in the vertical require boundary conditions.

4.1.3 Top and Bottom Boundary Treatment

Treatment of the vertical boundaries is complicated by the nature of the qausi-geostrophic model. The model requires no-flow through at the top and bottom boundaries, that is the vertical velocity $w = 0$. From (2.103) it is, therefore, required that

$$w = -\frac{1}{N^2}\left[\frac{\partial^2\psi}{\partial t \partial z} + J\left(\psi, \frac{\partial\psi}{\partial z}\right) - K_{V_2}\frac{\partial^3\psi}{\partial z^3} - \mathcal{H}_t\right] = 0 \text{ on } \Gamma_T \cup \Gamma_B. \tag{4.37}$$

Rearranging this gives

$$\frac{\partial^2\psi}{\partial t \partial z} + J\left(\psi, \frac{\partial\psi}{\partial z}\right) = K_{V_2}\frac{\partial^3\psi}{\partial z^3} + \mathcal{H}_t \text{ on } \Gamma_T \cup \Gamma_B, \tag{4.38}$$

where the non-dimensional constant $K_{V_2} = \mathcal{K}_V L/UH^2$. Notice that this is equal to $K_{V_1} = \mathcal{K}_V L^3 f_0^2/UH^4 N_0^2$ if the horizontal length scale L is equal to the Rossby radius $L = L_f = HN_0/f_0$. The quasi-geostrophic model defines temperature θ (non-dimensionalised from equation (2.71h)) as

$$\theta = \frac{\partial\psi}{\partial z}. \tag{4.39}$$

Therefore, equation (4.38) is an advection-diffusion equation for temperature on the top and bottom boundaries, with advection in the horizontal xy-directions and diffusion in the vertical z-direction. Equation (4.38) can be written as

$$\frac{\partial\theta}{\partial t} + J(\psi, \theta) = K_{V_2}\frac{\partial^2\theta}{\partial z^2} + \mathcal{H}_t \text{ on } \Gamma_T \cup \Gamma_B. \tag{4.40}$$

This will provide the boundary data necessary to complete the finite difference approximations for the streamfunction. To implement this let θ_j^n for $j = 0, \mathcal{N}$ be the discrete solution of θ at the top and bottom boundaries at timestep n. Then provided θ_j^n is known, calculate θ_j^{n+1} using a finite element discretisation of (4.40). This data can then be used as the vertical Neumann boundary condition on the streamfunction

$$\frac{\partial \psi^{n+1}}{\partial z} = \theta_0^{n+1} \text{ at } z = 0, \tag{4.41a}$$

$$\frac{\partial \psi^{n+1}}{\partial z} = \theta_{\mathcal{N}}^{n+1} \text{ at } z = 1, \tag{4.41b}$$

for each timestep. This is implemented by using a finite element discretisation in the horizontal and finite difference approximation in the vertical to solve for θ at the boundary layers. A discontinuous Galerkin approach is applied for the finite element discretisation as was done for the potential vorticity for improved accuracy and stability for the non-linear advection term. Multiplying (4.40) by a discontinuous test function $\varphi \in V_q$, integrating over an element $T \in \mathcal{T}_h$ and summing over all elements gives

$$\sum_{T \in \mathcal{T}_h} \int_T \left(\frac{\partial \theta}{\partial t} + \nabla \cdot (\boldsymbol{u_g} \theta) \right) \varphi = \sum_{T \in \mathcal{T}_h} \int_T \left(K_{V_2} \frac{\partial^2 \theta}{\partial z^2} + \mathcal{H}_t \right) \varphi. \tag{4.42}$$

This equation only holds on the horizontal planes at $z = 0, 1$, that is $\Omega_0 = \Gamma_B$ and $\Omega_{\mathcal{N}} = \Gamma_T$. Similar to the discretisation of the potential vorticity, after integration by parts and using an upwind numerical flux, for $z = 0, 1$ (or $j = 1, \mathcal{N}$),

$$\begin{aligned} \sum_{T \in \mathcal{T}_h} \int_T \theta_j^{n+1} \varphi = \sum_{T \in \mathcal{T}_h} \int_T \theta_j^n \varphi + \tau \sum_{T \in \mathcal{T}_h} \int_T \left(\boldsymbol{u_g}_j^n \theta_j^n \cdot \nabla \varphi + K_{V_2} D_z^{(2)} \theta_j^n \varphi \right) \\ - \tau \sum_{e \in \mathcal{I}_h} \int_e \hat{\boldsymbol{u}}_e^n \left(\theta_j^n \right) \cdot [\varphi] + \tau \sum_{e \in \mathcal{T}_h} \int_T \mathcal{H}_t{}_j^{n+1} \varphi \end{aligned} \tag{4.43}$$

where the vertical z derivatives are discretised using finite differences and the numerical flux $\hat{\boldsymbol{u}}_e$ is given by

$$\hat{\boldsymbol{u}}_e \left(\theta_j^n \right) = \begin{cases} \theta_j^n \big|_{T_{e^+}} \boldsymbol{u_g}_j^n & \text{if } \boldsymbol{u_g}_j^n \cdot \boldsymbol{n}_e^+ \geq 0 \\ \theta_j^n \big|_{T_{e^-}} \boldsymbol{u_g}_j^n & \text{if } \boldsymbol{u_g}_j^n \cdot \boldsymbol{n}_e^+ < 0 \end{cases}. \tag{4.44}$$

In the case of no vertical diffusion $\mathcal{K}_V = 0$ and heating $\mathcal{H}_t = 0$, the values of temperature at the north and south boundaries of the top and bottom layers will not

be altered from the initial values by equation (4.40). Otherwise, there are no prescribed values for temperature at the horizontal walls. However, it is known from the no-flow through boundary condition that $\partial\psi/\partial x = 0$ along the north and south boundaries Γ_N and Γ_S, therefore along this boundary $\partial^2\psi/\partial x\partial z = \partial\theta/\partial x = 0$ and so temperature should not vary in the x-direction along the north and south boundaries.

For $\mathcal{K}_V = 0$ temperature simply needs to be advected on the top and bottom boundaries to provide Neumann data for the streamfunction ψ. If $p \in \{-3, -2, -1, \mathcal{N}+1, \mathcal{N}+2, \mathcal{N}+3\}$ is the ghost point level, let

$$q = \begin{cases} 2\mathcal{N} - p & \text{if } p > \mathcal{N} \\ -p & \text{if } p < 0 \end{cases}, \tag{4.45}$$

and the Neumann value provided by the temperature solution

$$g_N = \begin{cases} \theta_{\mathcal{N}}^{n+1} & \text{if } p > \mathcal{N} \\ \theta_0^{n+1} & \text{if } p < 0 \end{cases}, \tag{4.46}$$

then using a second order central finite difference approximation at the top and bottom boundaries, the values of the ghost points outside the domain are given by

$$\psi_p^{n+1} = \psi_q^{n+1} - (q-p)\Delta z g_N. \tag{4.47}$$

This reduces the accuracy of the approximation to second order in the vertical at the boundaries, which can propagate into the interior solution over time.

For $\mathcal{K}_V \neq 0$ there is the additional no-flux boundary condition $\partial^2\psi/\partial z^2 = 0$ at the top and bottom boundaries. This must be combined with the Neumann data provided by the temperature equation (4.38) in the finite difference discretisation. The interior temperature is calculated using the relation (4.39) with a finite difference approximation of the vertical derivative of the streamfunction. Finite differences are calculated at the top and bottom boundaries using ghost points outside the domain with values defined in terms of the boundary data and the interior nodes. The vertical diffusion term $K_{V_2}\partial^2\theta/\partial z^2$ in (4.40) can be calculated using zero Neumann data for temperature ($\partial\theta/\partial z = 0$ on Γ_N and Γ_S). Otherwise, streamfunction ghost points are found using the fourth and sixth order finite difference expressions for $\partial\psi/\partial z = g_N$ and $\partial^2\psi/\partial z^2 = 0$ at $z = 0, 1$. The values of the streamfunction at the

ghost points are then

$$\psi_{-1} = \frac{15}{4}\psi_0 - 3\psi_1 + \frac{1}{4}\psi_2 + \frac{3}{2}\Delta z g_N \tag{4.48a}$$

$$\psi_{-2} = 30\psi_0 - 32\psi_1 + 3\psi_2 + 24\Delta z g_N \tag{4.48b}$$

$$\psi_{-3} = \frac{575}{4}\psi_0 - 16\psi_1 + \frac{81}{4}\psi_2 - \psi_3 + \frac{243}{2}\Delta z g_N \tag{4.48c}$$

$$\psi_{\mathcal{N}+1} = \frac{15}{4}\psi_0 - 3\psi_1 + \frac{1}{4}\psi_2 - \frac{3}{2}\Delta z g_N \tag{4.48d}$$

$$\psi_{\mathcal{N}+2} = 30\psi_0 - 32\psi_1 + 3\psi_2 - 24\Delta z g_N \tag{4.48e}$$

$$\psi_{\mathcal{N}+3} = \frac{575}{4}\psi_0 - 16\psi_1 + \frac{81}{4}\psi_2 - \psi_3 - \frac{243}{2}\Delta z g_N. \tag{4.48f}$$

When applying free-slip boundary conditions, top and bottom boundary conditions are required on the zero-boundary component Ψ that is used to calculate the stream-function boundary values. This can be provided in a similar way by solving the zero-boundary temperature equation given by (2.120), which can be written as

$$\frac{\partial \Theta}{\partial t} + (\boldsymbol{u_g} \cdot \nabla)\Theta - K_{V_2}\frac{\partial^2 \Theta}{\partial z^2} = v_g \frac{\partial}{\partial z}(C_S - C_N) + \mathcal{H}_t - \mathcal{H}_t|_{\Gamma_N}\psi_N - \mathcal{H}_t|_{\Gamma_S}\psi_S \tag{4.49}$$

where $\Theta := \partial\Psi/\partial z$. The discretised form of this equation becomes for $j = 1, \mathcal{N}$,

$$\begin{aligned}\sum_{T\in\mathcal{T}_h}\int_T \Theta_j^{n+1}\varphi = \sum_{T\in\mathcal{T}_h}\int_T \Theta_j^n\varphi + \tau\sum_{T\in\mathcal{T}_h}\int_T \left(\boldsymbol{u_g}_j^n\Theta_j^n\cdot\nabla\varphi + K_{V_2}D_z^{(2)}\Theta_j^n\varphi\right) \\ - \tau\sum_{e\in\mathcal{I}_h}\int_e \hat{\boldsymbol{u}}_e^n\left(\Theta_j^n\right)\cdot[\varphi] + \tau\sum_{e\in\mathcal{T}_h}\int_T v_{g_j}^n D_z^{(1)}(C_S{}_j^n - C_N{}_j^n)\varphi \\ + \tau\sum_{e\in\mathcal{T}_h}\int_T (\mathcal{H}_t{}_j^{n+1} - \mathcal{H}_t{}_j^{n+1}|_{\Gamma_N}\psi_N - \mathcal{H}_t{}_j^{n+1}|_{\Gamma_S}\psi_S)\varphi\end{aligned} \tag{4.50}$$

for all $\varphi \in V_{q_h}$. Vertical derivatives of Ψ are calculated the same as for ψ in (4.47) or (4.48) with

$$g_N = \begin{cases}\Theta_{\mathcal{N}}^{n+1} & \text{if } p > \mathcal{N} \\ \Theta_0^{n+1} & \text{if } p < 0\end{cases}. \tag{4.51}$$

4.1.4 Free-Slip Boundary Treatment

As stated in Section 3.4, the problem may be solved with zero Dirichlet boundary and then the boundary data g can be added onto this solution. Unfortunately, in this case the boundary data is not explicitly known. To satisfy the free-slip boundary condition $\partial\psi/\partial\boldsymbol{\tau} = 0$ on Γ_N and Γ_S, the derived relations (2.117) are used to find the

values of the streamfunction ψ on the north and south boundaries. These equations are advanced in time using a forward Euler discretisation and the integrals are calculated using a numerical quadrature. The integral relations in (2.117) require the zero-boundary streamfunction component $\Psi = \psi - C_N\psi_N - C_S\psi_S$ to be solved using equations (2.124) and (2.120). This can be done using the discrete problems (4.35) and (4.50). The solution Ψ^{n+1} can then be used to find ${C_N}^{n+1}$ and ${C_S}^{n+1}$ as

$$\begin{aligned}
{C_N}_j^{n+1} = {C_N}_j^n &+ \tau\frac{L}{L_x}\int_\Omega\left(\frac{\Psi_j^n - \Psi_j^{n+1}}{\tau} + K_{V_2}D_z^{(2)}\Psi_j^n + {\mathbb{H}_t}_j^n\right)dxdy \\
&+ \frac{\tau}{2}\oint_{\Gamma_S}\left(\frac{\partial}{\partial y}\left(\frac{\Psi_j^n - \Psi_j^{n+1}}{\tau}\right) + A_H\Delta\frac{\partial\Psi_j^n}{\partial y} - C_D\frac{\partial\Psi_j^n}{\partial y}\right)dx \quad (4.52a) \\
&+ \frac{\tau}{2}\oint_{\Gamma_S}\left(C_D(C_S{}_j^n - C_N{}_j^n) - {F_x}_j^n\right)dx + \tau\frac{K_{V_2}}{2}D_z^{(2)}(C_N{}_j^n + C_S{}_j^n), \\
{C_S}_j^{n+1} = {C_S}_j^n &+ \tau\frac{L}{L_x}\int_\Omega\left(\frac{\Psi_j^n - \Psi_j^{n+1}}{\tau} + K_{V_2}D_z^{(2)}\Psi_j^n + {\mathbb{H}_t}_j^n\right)dxdy \\
&- \frac{\tau}{2}\oint_{\Gamma_S}\left(\frac{\partial}{\partial y}\left(\frac{\Psi_j^n - \Psi_j^{n+1}}{\tau}\right) + A_H\Delta\frac{\partial\Psi_j^n}{\partial y} - C_D\frac{\partial\Psi_j^n}{\partial y}\right)dx \quad (4.52b) \\
&- \frac{\tau}{2}\oint_{\Gamma_S}\left(C_D(C_S{}_j^n - C_N{}_j^n) - {F_x}_j^n\right)dx + \tau\frac{K_{V_2}}{2}D_z^{(2)}(C_N{}_j^n + C_S{}_j^n).
\end{aligned}$$

The streamfunction is then calculated as $\psi^{n+1} = \Psi^{n+1} + {C_N}^{n+1}\psi_N + {C_S}^{n+1}\psi_S$. The full algorithm is detailed in Section 4.4.

4.1.5 Matrix Formulation

For the numerical method to be implemented, it must be formulated as a matrix problem so that it can be solved computationally. To write the problem in matrix form, express the solutions q_j^n and Ψ_j^n at each vertical level j in terms of a linear combination of basis functions,

$$q_j^n = \sum_k c_k(j,n)\varphi_k, \tag{4.53}$$

$$\Psi_j^n = \sum_k d_k(j,n)\xi_k \tag{4.54}$$

for constants $c_k(j,n), d_k(j,n) \in \mathbb{R}$ and basis functions $\{\varphi_k\}_k \subset V_{q_h}$ and $\{\xi_k\}_k \subset V_{\psi_h}$ of the finite-dimensional discrete solution spaces. For information on how these bases are constructed see [30]. Substituting (4.53) into (4.35a) and taking the test

function to be a basis function $\varphi_l \in V_{q_h}$

$$\sum_k (1+\mu) c_k(j, n+1) a_1(\varphi_k, \varphi_l) = l^n_{1,j}(\varphi_l). \tag{4.55}$$

Assuming the discrete space has $P = \dim(V_{q_h})$ basis functions, one may write the solution coefficients (known as degrees of freedom) in a vector

$$\boldsymbol{c}^n_j = \begin{bmatrix} c_1(j,n) \\ c_2(j,n) \\ c_3(j,n) \\ \vdots \\ c_P(j,n) \end{bmatrix} \tag{4.56}$$

and defining the finite element matrix and right hand side vector

$$A = \begin{bmatrix} a_1(\varphi_1,\varphi_1) & \dots & a_1(\varphi_P,\varphi_1) \\ \vdots & \ddots & \vdots \\ a_1(\varphi_1,\varphi_P) & \dots & a_1(\varphi_P,\varphi_P) \end{bmatrix}, \quad F^n_j = \begin{bmatrix} l^n_{1,j}(\varphi_1) \\ \vdots \\ l^n_{1,j}(\varphi_P) \end{bmatrix} \tag{4.57}$$

the matrix problem at each level $j \in \{0, ..., \mathcal{N}\}$ is

$$(1+\mu) A \boldsymbol{c}^{n+1}_j = F^n_j. \tag{4.58}$$

The full problem for equation (4.25) in matrix form is then

$$\begin{bmatrix} L^0 & 0 & 0 & 0 & \cdots & 0 \\ 0 & L^0 & 0 & 0 & \cdots & 0 \\ 0 & \ddots & \ddots & \ddots & \vdots & \vdots \\ \vdots & \cdots & 0 & 0 & L^0 & 0 \\ 0 & \cdots & 0 & 0 & 0 & L^0 \end{bmatrix} \begin{bmatrix} \boldsymbol{c}^{n+1}_0 \\ \boldsymbol{c}^{n+1}_1 \\ \vdots \\ \boldsymbol{c}^{n+1}_{\mathcal{N}-1} \\ \boldsymbol{c}^{n+1}_{\mathcal{N}} \end{bmatrix} = \begin{bmatrix} F^n_0 \\ F^n_1 \\ \vdots \\ F^n_{\mathcal{N}-1} \\ F^n_{\mathcal{N}} \end{bmatrix} \tag{4.59}$$

with

$$L^0 = (1+\mu) A. \tag{4.60}$$

For equation (4.35b) which recovers the streamfunction,

$$
\begin{aligned}
&-\sum_{T\in\mathcal{T}_h}\int_T \nabla\Psi_j^{n+1}\cdot\nabla\xi+\sum_{T\in\mathcal{T}_h}\int_T D_z^{(1)}\left(\frac{Bu^{-1}}{N^2}D_z^{(1)}\Psi_j^{n+1}\right)\xi\\
&=\sum_{T\in\mathcal{T}_h}\int_T (q_j^{n+1}-{q_c}_j^{n+1}-\beta y)\xi, \qquad (4.61)
\end{aligned}
$$

for all $\xi\in V_{\psi_h}$. For simplicity, a second order centred difference is used below to demonstrate the matrix problem, so that

$$
\begin{aligned}
D_z^{(1)}\left(\frac{Bu^{-1}}{N^2}D_z^{(1)}\Psi_j^{n+1}\right)&=\lambda_j(\Psi_{j+1}^{n+1}-\Psi_{j-1}^{n+1})+\mu_j(\Psi_{j+1}^{n+1}-2\Psi_j^{n+1}+\Psi_{j-1}^{n+1}), \qquad (4.62)\\
\lambda_j&=\frac{Bu^{-1}}{4\Delta z^2}\left(N_{j+1}^{-2}-N_{j-1}^{-2}\right), \qquad (4.63)\\
\mu_j&=N_j^{-2}\frac{Bu^{-1}}{\Delta z^2}. \qquad (4.64)
\end{aligned}
$$

See Table 4.1 for the fourth order scheme. Recall the bilinear forms

$$
\begin{aligned}
a_1(\Psi,\xi)&=\sum_{T\in\mathcal{T}_h}\int_T \Psi\xi \qquad (4.65)\\
a_2(\Psi,\xi)&=\sum_{T\in\mathcal{T}_h}\int_T \nabla\Psi\cdot\nabla\xi, \qquad (4.66)
\end{aligned}
$$

and the linear form

$$
l_{2,j}^n(\xi)=\sum_{T\in\mathcal{T}_h}\int_T (q_j^n-{q_c}_j^n-\beta y)\xi, \qquad (4.67)
$$

the problem can be written as; for each $j\in\{0,...,\mathcal{N}\}$ find $\Psi_j\in V_{\psi_h}$ such that

$$
\begin{aligned}
-a_2(\Psi_j^{n+1},\xi)+\lambda_j a_1(\Psi_{j+1}^{n+1}-\Psi_{j-1}^{n+1},\xi)+\mu_j a_1(\Psi_{j+1}^{n+1}-2\Psi_j^{n+1}+\Psi_{j-1}^{n+1},\xi)&\\
=l_{2,j}^{n+1}(\xi)\ \forall\xi\in V_{\psi_h}. \qquad (4.68)&
\end{aligned}
$$

Substituting in the approximation written as a linear combination of basis functions (4.54)

$$
\begin{aligned}
\sum_k &-d_k(j,n+1)a_2(\xi_k,\xi_l)+\lambda_j(d_k(j+1,n+1)-d_k(j-1,n+1))a_1(\xi_k,\xi_l)\\
&+\mu_j(d_k(j+1,n+1)-2d_k(j,n+1)+d_k(j-1,n+1)a_1(\varphi_k,\xi_l))=l_{2,j}^n(\xi_l), \qquad (4.69)
\end{aligned}
$$

Writing the vector for the streamfunction solution coefficients for $Q = \dim(V_{\psi_h})$,

$$\boldsymbol{d}_j^n = \begin{bmatrix} d_1(j,n) \\ d_2(j,n) \\ d_3(j,n) \\ \vdots \\ d_Q(j,n) \end{bmatrix}, \tag{4.70}$$

and defining

$$A_i = \begin{bmatrix} a_i(\xi_1,\xi_1) & \dots & a_i(\xi_Q,\xi_1) \\ \vdots & \ddots & \vdots \\ a_i(\xi_1,\xi_Q) & \dots & a_i(\xi_Q,\xi_Q) \end{bmatrix}, \quad G_j^n = \begin{bmatrix} l_{2,j}^n(\xi_1) \\ \vdots \\ l_{2,j}^n(\xi_Q) \end{bmatrix} \tag{4.71}$$

gives

$$(\mu_j + \lambda_j)A_1\boldsymbol{d}_{j+1}^{n+1} - (A_2 + 2\mu_j A_1)\boldsymbol{d}_j^{n+1} + (\mu_j - \lambda_j)A_1\boldsymbol{d}_{j-1}^{n+1} = G_j^{n+1}. \tag{4.72}$$

Finally, (4.30) is given in matrix form as

$$\begin{bmatrix} L_0^0 & L_1^{\partial+} & L_2^{\partial+} & 0 & \cdots & 0 \\ L_0^- & L_1^0 & L_2^+ & 0 & \cdots & 0 \\ 0 & \ddots & \ddots & \ddots & \vdots & \vdots \\ \vdots & \cdots & 0 & L_{\mathcal{N}-2}^- & L_{\mathcal{N}-1}^0 & L_{\mathcal{N}}^+ \\ 0 & \cdots & 0 & L_{\mathcal{N}-2}^{\partial-} & L_{\mathcal{N}-1}^{\partial-} & L_{\mathcal{N}}^0 \end{bmatrix} \begin{bmatrix} \boldsymbol{d}_0^{n+1} \\ \boldsymbol{d}_1^{n+1} \\ \vdots \\ \boldsymbol{d}_{\mathcal{N}-1}^{n+1} \\ \boldsymbol{d}_{\mathcal{N}}^{n+1} \end{bmatrix} = \begin{bmatrix} G_0^{n+1} \\ G_1^{n+1} \\ \vdots \\ G_{\mathcal{N}-1}^{n+1} \\ G_{\mathcal{N}}^{n+1} \end{bmatrix} \tag{4.73}$$

where

$$\begin{aligned} L_j^- &= (\mu_j - \lambda_j)A_1, \\ L_j^0 &= -(A_2 + 2\mu_j A_1), \\ L_j^+ &= (\mu_j + \lambda_j)A_1 \end{aligned} \tag{4.74}$$

and $L_j^{\partial\pm}$ depend upon the order of the finite difference approximation, see Section 4.1.3 for the treatment of the vertical boundary conditions.

For constant Brunt-Väisälä frequency N, the values $\lambda_j = 0$ and so $L_j^+ = L_j^-$. This means the matrix is symmetric except for the top and bottom rows due to the vertical boundary conditions. Therefore, it cannot be guaranteed that a conjugate gradient method can be used to solve this system. However, a preconditioner may allow the

method to converge. Otherwise, a bi-conjugate gradient or GMRES method will be required to recover the streamfunction ψ. A direct solver such as a block Thomas algorithm may also be efficient for solving the system.

4.1.6 Timestep Restriction

After applying a suitable finite element space discretisation, one is left with solving the system of ordinary differential equations of the form

$$\left(\frac{\partial q}{\partial t}, \varphi\right) = f(t, q), \tag{4.75}$$

for some function f. An explicit Euler time discretisation is used as detailed in the previous discretisations, that is

$$\left(q^{n+1}, \varphi\right) = (q^n, \varphi) + \tau f(t, q^n) \tag{4.76}$$

with the exception of the bottom friction term which has the option of a theta method as seen in (4.25). This explicit timestepping means the system matrices only need to be assembled once. An implicit method would require linearisation of the advection term, therefore, making the matrix depend on previous timestep data or requiring several iterations to solve each timestep. This would be very computationally expensive. Furthermore, a fully implicit method would require all equations to be assembled into a single system matrix increasing the complexity of the problem. The bottom friction term does have the option of using a theta method which causes the matrix to depend on the timestep τ, but only requires the matrix to be reassembled if the timestep changes.

A standard timestep restriction used in advection dominated problems is the Courant-Friedrichs-Lewy (CFL) condition [20],

$$\Delta t < \frac{h}{\|\boldsymbol{u_g}\|_\infty}, \tag{4.77}$$

for supremum norm

$$\|\boldsymbol{u_g}\|_\infty = \sup\{|\boldsymbol{u_g}(\boldsymbol{x})| : \boldsymbol{x} \in \Omega \times [0,1]\}. \tag{4.78}$$

It has also been shown, [37, 74], that DG methods with a Runge-Kutta time dis-

cretisation require the timestep restriction

$$\Delta t < \frac{h}{\|\boldsymbol{u_g}\|_\infty (2p+1)}, \tag{4.79}$$

where p is the order of the polynomial basis functions of the discrete space, this is used as the timestep restriction in the implementation.

4.2 Full Discretisation Summary

The full problem is now summarised using the bilinear forms

$$a_1(u,v) = \sum_{T\in\mathcal{T}_h} \int_T uv, \tag{4.80}$$

$$a_2(u,v) = \sum_{T\in\mathcal{T}_h} \int_T \nabla u \cdot \nabla v \tag{4.81}$$

and linear forms

$$\begin{aligned} l^n_{1,j}(\varphi) = \quad & \sum_{T\in\mathcal{T}_h} \int_T q_j^n \varphi + \tau \sum_{T\in\mathcal{T}_h} \int_T q_j^n \boldsymbol{u_g}_j^n \cdot \nabla\varphi - \tau \sum_{e\in\mathcal{I}_h} \int_e \hat{\boldsymbol{u}}_e^n(q_j^n)\cdot[\varphi] \\ & - \tau \sum_{T\in\mathcal{T}_h} \int_T A_H \nabla\omega_j^n \cdot \nabla\varphi + \tau \sum_{e\in\mathcal{I}_h\cup\mathcal{I}_h^\partial} \int_e A_H\{\nabla\omega_j^n\}\cdot[\varphi] \\ & + \tau \sum_{e\in\mathcal{I}_h\cup\mathcal{I}_h^\partial} \int_e A_H\{\nabla\varphi\}\cdot[\omega_j^n] - \tau \sum_{e\in\mathcal{I}_h\cup\mathcal{I}_h^\partial} \beta_e \int_e [\omega_j^n]\cdot[\varphi] \\ & + \tau \sum_{T\in\mathcal{T}_h} \int_T K_{V_1} D_z^{(1)} \left(\frac{1}{N^2} D_z^{(3)} \psi_j^n\right)\varphi \\ & - \tau C_D \sum_{T\in\mathcal{T}_h} \int_T \left((1-\theta_m)q_j^n - \beta y - D_z^{(1)}\left(\frac{Bu^{-1}}{N^2} D_z^{(1)}\psi_j^n\right)\right)\varphi \\ & + \tau \sum_{T\in\mathcal{T}_h} \int_T \mathcal{F}_j^{n+1}\varphi, \end{aligned} \tag{4.82}$$

$$l^n_{2,j}(\xi) = \quad \sum_{T\in\mathcal{T}_h} \int_T (q_j^n - \beta y - (q_j^n - \beta y)|_{\Gamma_N}\psi_N - (q_j^n - \beta y)|_{\Gamma_S}\psi_S)\xi, \tag{4.83}$$

$$l^n_{3,j}(\phi) = \sum_{T\in\mathcal{T}_h}\int_T \theta^n_j\varphi + \tau\sum_{T\in\mathcal{T}_h}\int_T \left(\boldsymbol{u_g}^n\theta^n_j\cdot\nabla\varphi + K_{V_2}D^{(2)}_z\theta^n_j\varphi\right)$$
$$- \tau\sum_{e\in\mathcal{I}_h}\int_e \hat{\boldsymbol{u}}^n_e\left(\theta^n_j\right)\cdot[\varphi] + \tau\sum_{e\in\mathcal{T}_h}\int_T \mathcal{H}^{n+1}_{t_j}\varphi, \tag{4.84}$$

$$l^n_{4,j}(\phi) = \sum_{T\in\mathcal{T}_h}\int_T \Theta^n_j\varphi + \tau\sum_{T\in\mathcal{T}_h}\int_T \left(\boldsymbol{u_g}^n\Theta^n_j\cdot\nabla\varphi + K_{V_2}D^{(2)}_z\Theta^n_j\varphi\right)$$
$$- \tau\sum_{e\in\mathcal{I}_h}\int_e \hat{\boldsymbol{u}}^n_e\left(\Theta^n_j\right)\cdot[\varphi] + \tau\sum_{e\in\mathcal{T}_h}\int_T {v_g}^n_j D^{(1)}_z(C_S{}^n_j - C_N{}^n_j)\varphi$$
$$+ \tau\sum_{e\in\mathcal{T}_h}\int_T(\mathcal{H}^{n+1}_{t_j} - \mathcal{H}^{n+1}_{t_j}|_{\Gamma_N}\psi_N - \mathcal{H}^{n+1}_{t_j}|_{\Gamma_S}\psi_S)\varphi. \tag{4.85}$$

Provided with initial data q^0, θ^0 and ψ^0, the discrete formulation of the PDEs in (4.1) is; for each $j \in \{0, ..., \mathcal{N}\}$, given q^n_j and $\psi^n_j = \Psi^n_j + {C_N}^n_j\psi_N + {C_S}^n_j\psi_S$ find $q^{n+1}_j \in V_{q_h}$ and $\Psi^{n+1}_j \in V_{\psi_h}$ such that

$$(1 + \tau C_D\theta_m)a_1(q^{n+1}_j, \varphi) = l^n_{1,j}(\varphi) \text{ for all } \varphi \in V_{q_h}, \tag{4.86}$$

$$\text{and } -a_2(\Psi^{n+1}_j, \xi) + a_1(D^{(1)}_z(Bu^{-1}N^{-2}D^{(1)}_z\Psi^{n+1}_j), \xi) = l^{n+1}_{2,j}(\xi) \text{ for all } \xi \in V_{\psi_h}, \tag{4.87}$$

where vertical derivatives are discretised using the fourth order finite difference method detailed in Section 4.1.2. The no-flow through ($\partial\psi/\partial\boldsymbol{\tau} = -\boldsymbol{u_g}\cdot\boldsymbol{n} = 0$) and no-flux ($\partial^2\psi/\partial\boldsymbol{n}^2 = \omega = 0$) boundary conditions at the north and south walls are enforced weakly through the penalty terms in (4.86). However, the zero Dirichlet boundary condition on Ψ is strongly enforced through the discrete space V_{ψ_h} when solving (4.87) with the streamfunction boundary values ${C_N}^n$ and ${C_S}^n$ calculated each timestep using (4.52). Therefore, this culminates in a weak enforcement of the free-slip boundaries. Figure 4.3 details the solution algorithm.

The top/bottom Neumann boundary data for ψ and Ψ is provided by the following discretisation of the temperature equations (4.40) and (4.49): given $\theta^n_j = \Theta^n_j + \psi_N D^{(1)}_z {C_N}^n_j + \psi_S D^{(1)}_z {C_S}^n_j$ find $\theta^{n+1}_0, \theta^{n+1}_{\mathcal{N}} \in V_{q_h}$ and $\Theta^{n+1}_0, \Theta^{n+1}_{\mathcal{N}} \in V_{q_h}$ such that

$$a_1(\theta^{n+1}_0, \phi) = l^n_{3,0} \text{ and } a_1(\theta^{n+1}_{\mathcal{N}}, \phi) = l^n_{3,\mathcal{N}} \text{ for all } \phi \in V_{q_h}, \tag{4.88}$$

$$\text{and } a_1(\Theta^{n+1}_0, \phi) = l^n_{4,0} \text{ and } a_1(\Theta^{n+1}_{\mathcal{N}}, \phi) = l^n_{4,\mathcal{N}} \text{ for all } \phi \in V_{q_h}. \tag{4.89}$$

4.3 Solvability and Error Estimates

The discrete problem at each timestep is solvable. Consider the problem in matrix form given by (4.59) and (4.73). The first matrix equation solves for potential vorticity. To show that this system can be solved set $\mathcal{N} = 3$ for simplicity giving the augmented coefficient matrix

$$\left[\begin{array}{ccc|c} L^0 & 0 & 0 & F_0^n \\ 0 & L^0 & 0 & F_1^n \\ 0 & 0 & L^0 & F_2^n \end{array}\right] \tag{4.90}$$

where

$$L^0 = (1 + \tau C_D \theta_m) A. \tag{4.91}$$

Applying row reduction to this matrix gives

$$\left[\begin{array}{ccc|c} 1 & 0 & 0 & L_0^{-1} F_0^n \\ 0 & 1 & 0 & L_0^{-1} F_1^n \\ 0 & 0 & 1 & L_0^{-1} F_2^n \end{array}\right], \tag{4.92}$$

therefore, for this system to be solvable $\tau C_D \theta_m \neq -1$ which is clearly true since $\tau, C_D > 0$ and $\theta_m \geq 0$. Also, the finite element matrix A must be invertible which is true since it is positive definite due to the coercivity of the bilinear form $a_1(\cdot, \cdot)$.

The streamfunction can be solved by (4.73); from the finite difference coefficients in Table 4.1 and the symmetry of the invertible finite element matrices A_1 and A_2, the matrix is strictly diagonally dominant and therefore solvable.

It is shown in [20], for the inviscid two-dimensional QGE, that the velocity solution $\boldsymbol{u_g}^n$ follows the error estimate

$$||\boldsymbol{u_g} - \boldsymbol{u_g}^n||_{L^2(\Omega)} = O(h^p) \tag{4.93}$$

where h is the mesh size, and p is the polynomial order of the discrete finite element space basis functions. It is also suggested that the potential vorticity q follows this error estimate, however, their numerical results indicate that the streamfunction ψ and potential vorticity q have $O(h^{p+1})$ convergence which is optimal for a discontinuous finite element method [105]. Since the finite element discretisation presented in this thesis is in the horizontal plane, similar results are expected given a high

order finite difference approximation in the vertical, at least for zero diffusion and fixed Dirichlet boundary conditions.

4.4 Implementation Details

The method is implemented using the C++ programming language within the Distributed and Unified Numerics Environment (DUNE) [16, 17, 18, 28, 29]. Using the finite element framework provided by `dune-fem` [41, 42] a module was created in the dune project called `dune-qg-dg` relying on the 2.5 version release of the core modules. The framework is built upon the code in `dune-fem-howto`. The structure of the code is split into classes for elliptic operators, models, problems and a finite element scheme. Two elliptic operators are written for continuous and discontinuous spaces. The potential vorticity and temperature discontinuous solutions are solved using the discontinuous elliptic operator that interfaces with models for the potential vorticity and temperature equations. Similarly, the continuous elliptic operator is used to recover the streamfunction. The finite element scheme handles the discretisation scheme by initialising the solutions using the problem class and assembling and solving the system matrices using the elliptic operators. The auxiliary integrals used to calculate the unknown streamfunction boundary values are handled by a freeslipconstraints class. This class calculates the discrete integrals using the same quadrature rules as the finite element scheme and stores the boundary values.

The grid implementation `YASPGRID` was used to enable periodic boundary treatment with quadrilateral elements. As the method uses a finite element approximation only in the horizontal direction, a two-dimensional computational grid was used via setting the preprocessor parameters `WORLDDIM=GRIDDIM=2`. This way the finite element framework can be used unchanged and a finite difference class can be written separately to handle the vertical discretisations. This finite difference class takes advantage of the dimension of the range of the discrete functions being set to the number of vertical layers in the grid. The number of vertical layers is controlled using the preprocessor variable `VERTICAL_LAYERS`. The finite element polynomial basis function order is set with the variable `POLORDER`. The DUNE interface for the PETSc solvers [13, 14, 15] was used to solve the linear systems, where the MUMPS solver was found to be particularly efficient. For data output, a wrapper class transfers the layered data onto a three-dimensional grid written into .vtu files suitable for visualisation in ParaView [2, 10] or similar software.

The variables stored during runtime include; the streamfunction ψ^n, new and previous timestep zero-boundary streamfunction Ψ^n and Ψ^{n-1}, potential vorticity q^n, velocity $\boldsymbol{u_g}^n$, vorticity ω^n, temperature θ^n and zero-boundary temperature Θ^n. The algorithm for solving the system, assuming data is known at timestep n, is shown in the flowchart in Figure 4.3.

Checkpointing is implemented to periodically store the current state of the solutions and the streamfunction boundary values. The minimal set of solutions required to recover from a checkpoint are; the potential vorticity q^n, temperature θ^n and Θ^n at the vertical boundaries as well the streamfunction horizontal boundary values C_N^n and C_S^n at timestep n. The remainder of the data can be recovered from this.

4.4.1 Coriolis Parameter

Section 2.2 introduced the β-plane approximation to the Coriolis parameter $f \approx f_0 + \beta y$ where $f_0 = 2\Omega \sin\varphi_0$ and $\beta = (2\Omega/a)\cos\varphi_0$ for Earth's radius a where the meridional coordinate y is measured as a perturbation from the reference latitude φ_0. Due to restrictions in the code, computations were performed on a $[0, L/L_x] \times [0,1] \times [0,1]$ domain which places the reference latitude at the south boundary of the domain. This means that the β-plane approximation is less accurate at the north boundary than at the south. If not for the $(0,0,0)$ grid origin restriction one could simply use a $[0, L/L_x] \times [-1/2, 1/2] \times [0,1]$ computational grid. This is resolved by moving the reference latitude to the centre of the domain which requires the coordinate change $y' = y - y_0$ where $y' = y_0$ corresponds to the reference latitude in the centre of the domain. This coordinate change does not effect any of the dynamics in the QGE except for the βy term in (2.100b) where the meridional coordinate appears explicitly, which now becomes $\beta(y - y_0)$. This provides a more consistent approximation of the Earth's rotational forces throughout the domain.

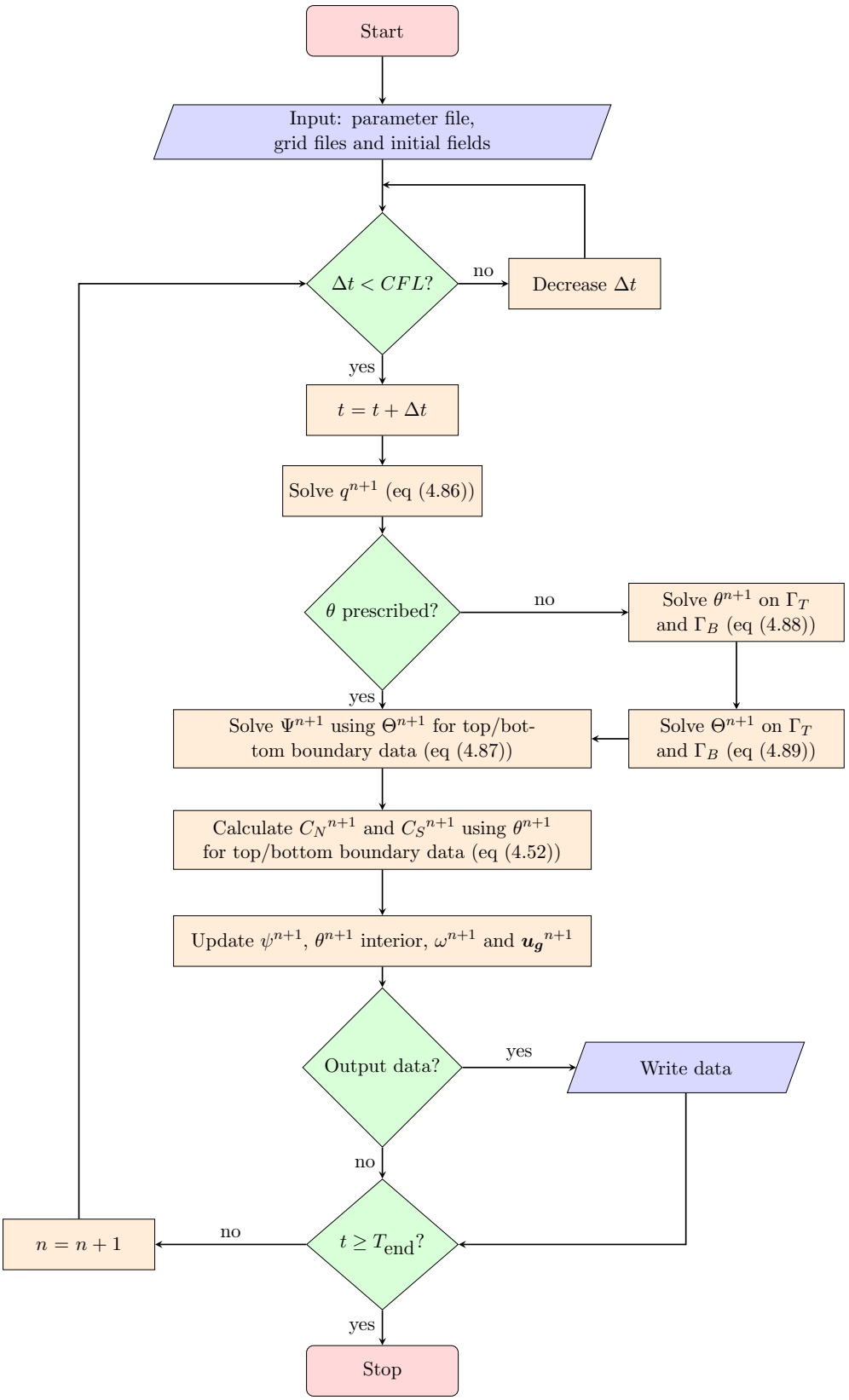

Figure 4.3: Program flow chart detailing full solution algorithm.

Chapter 5

Numerical Tests

5.1 Travelling Wave (TW2D)

Documented here is a test used to verify the two-dimensional implementation of the equations during development, similar to tests used in [20]. The numerical method used is detailed in Section 4.1.1 where the three-dimensional term is replaced with the two-dimensional term $-Bu^{-1}\psi$. Due to this being a two-dimensional problem, no finite difference approximations are required. The two-dimensional QGE are [86],

$$\partial_t q + J(\psi, q) = \mathcal{F} + C_D \Delta\psi \tag{5.1a}$$

$$q = \Delta\psi - Bu^{-1}\psi + \beta y. \tag{5.1b}$$

where the bottom friction C_D and Burger number $Bu = (N_0 H/f_0 L)^2$ are dimensionless constants. The boundary conditions are $\psi = 0$ at the north and south boundaries and zonally periodic. The finite element method is verified by testing the two-dimensional formulation with a travelling wave solution. This test uses the exact solution

$$\psi(x, y, t) = \sin(2\pi x - ct)\sin(2\pi y) \tag{5.2}$$

$$q(x, y, t) = -(8\pi^2 + Bu^{-1})\sin(2\pi x - ct)\sin(2\pi y) + \beta y. \tag{5.3}$$

For these to provide an exact solution to (5.1) set,

$$\begin{aligned}\mathcal{F}(x, y, t) = \quad & [(8\pi^2 + Bu^{-1})c + 2\pi\beta]\cos(2\pi x - ct)\sin(2\pi y) \\ & + 8C_D\pi^2 \sin(2\pi x - ct)\sin(2\pi y).\end{aligned} \tag{5.4}$$

A computational domain $[0, 1]^2$ is used with parameter values shown in Table 5.1.

Take note that the choice of the wave speed constant c simplifies the forcing term.

Parameter	Value
Bu	1
C_D	10^{-3}
β	1
c	$-2\pi\beta/(8\pi^2 + Bu^{-1})$

Table 5.1: Parameter values used for 2D travelling wave test.

L^2 errors for the streamfunction ψ, potential vorticity q and velocity $\boldsymbol{u_g}$ are listed in Table 5.2 for linear elements and Table 5.3 for quadratic elements. The streamfunction and potential vorticity are seen to converge according to $O(h^{p+1})$ and velocity to $O(h^p)$ for grid spacing h. The velocity convergence is an order lower because it is directly calculated from the gradient of the streamfunction. This is in agreement with optimal convergence rates of $O(h^{p+1})$ for a finite element scheme using pth order polynomial basis functions of the discrete finite element spaces, indicating a $(p+1)$th order scheme [105]. This test shows that the finite element discretisation of the advection term and recovery of the streamfunction from a discontinuous potential vorticity is successful and can be advanced in time whilst retaining optimal convergence.

Grid Size	L^2 Error ψ	EOC ψ	L^2 Error q	EOC q	L^2 Error $\boldsymbol{u_g}$	EOC $\boldsymbol{u_g}$
8×8	0.043593	-	4.28992	-	1.0196	-
16×16	0.00868395	2.32767	0.919827	2.22152	0.503512	1.01791
32×32	0.00233053	1.89769	0.219522	2.067	0.251826	0.999602
64×64	0.000543162	2.1012	0.0474644	2.20945	0.125908	1.00005
128×128	0.000126787	2.09897	0.010588	2.16442	0.0629559	0.999958

Table 5.2: **Linear elements 2D**. L^2 errors and experimental order of convergence (EOC) for the streamfunction ψ, potential vorticity q and velocity $\boldsymbol{u_g}$ for travelling wave test run for 2D QGE using linear elements ($p = 1$) at $t = 8\pi^2 + 1$.

Grid Size	L^2 Error ψ	EOC ψ	L^2 Error q	EOC q	L^2 Error $\boldsymbol{u_g}$	EOC $\boldsymbol{u_g}$
8×8	0.00229405	-	0.476252	-	0.102612	-
16×16	0.000254975	3.16947	0.0571252	3.05953	0.0255342	2.0067
32×32	3.09147e-05	3.04399	0.00692878	3.04345	0.00638298	2.00013
64×64	3.85486e-06	3.00354	0.000860197	3.00986	0.00159584	1.99992

Table 5.3: **Quadratic elements 2D**. L^2 errors and experimental order of convergence (EOC) for the streamfunction ψ, potential vorticity q and velocity $\boldsymbol{u_g}$ for travelling wave test run for 2D QGE using quadratic elements ($p = 2$) at $t = 8\pi^2+1$.

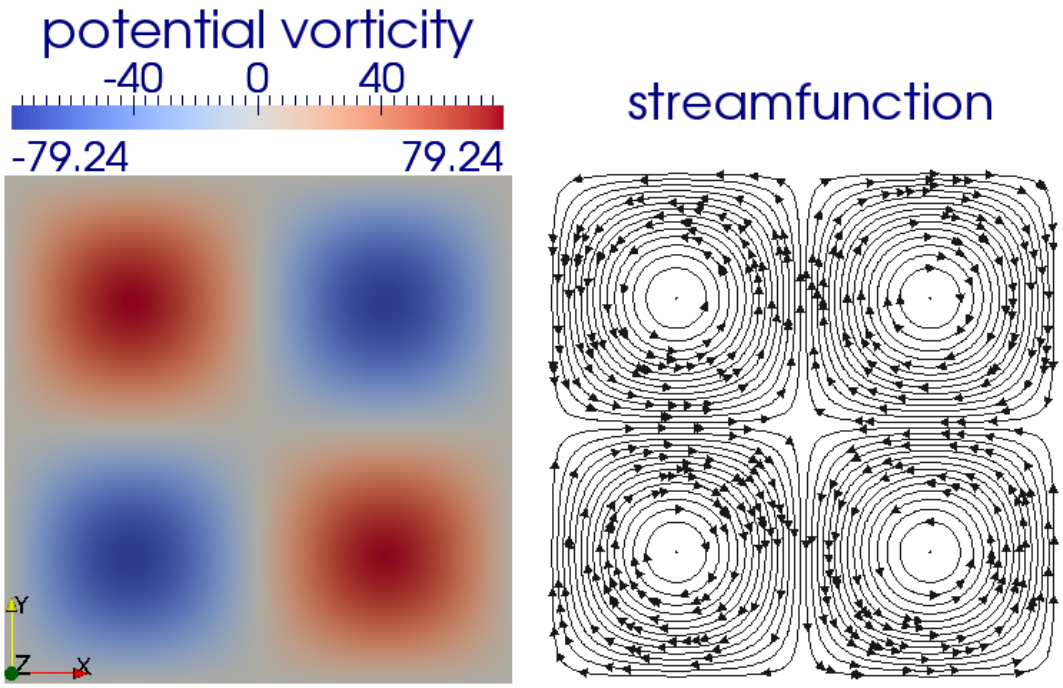

Figure 5.1: (Left) Potential vorticity q and (Right) streamfunction ψ for the travelling wave test TW2D at $t = 8\pi^2 + 1$ using linear elements. Computed on $[0, 1]^2$ domain with 128×128 grid.

5.2 Travelling Wave 3D Full Mechanics (TW3DF)

To test the full finite element / finite difference discretisation for the quasi-geostrophic model (2.101) that will be used to investigate frontogenesis, the previous test from [20] is extended to a three-dimensional travelling wave example. This is with horizontal momentum and vertical buoyancy diffusion terms ($\mathcal{A}_H > 0, \mathcal{K}_V > 0$) and bottom friction ($C_D > 0$) with the full vertical boundary conditions (2.102) that require temperature to be solved on the top and bottom boundaries using (2.103). This test uses the exact solution

$$\psi(x, y, t) = \sin(2\pi x - ct)\sin(2\pi y)\sin(2\pi z) \tag{5.5}$$

$$q(x, y, t) = -\left(8\pi^2 + \frac{4\pi^2}{Bu\,N^2}\right)\sin(2\pi x - ct)\sin(2\pi y)\sin(2\pi z) + \beta y. \tag{5.6}$$

For these to satisfy the equations set the forcing term,

$$\begin{aligned}\mathcal{F}(x,y,t) = \quad & \left[\left(8\pi^2 + \frac{4\pi^2}{Bu\,N^2}\right)c + 2\pi\beta\right]\cos(2\pi x - ct)\sin(2\pi y)\sin(2\pi z) \\ & - \left[64\pi^4 A_H + \frac{16\pi^4}{N^2}K_{V_1} + 8\pi^2 C_D\right]\sin(2\pi x - ct)\sin(2\pi y)\sin(2\pi z).\end{aligned} \tag{5.7}$$

Two different runs were performed; one with the streamfunction fixed to zero at the north-south boundaries and another with free-slip boundaries where the boundary values are calculated as described in Section 2.3.3. Tests with both linear and quadratic elements were done and L^2 errors and EOCs at $t = 12\pi^2$ were calculated.

Parameter	Value
$\mathcal{K}_V$	$10^{-5}\,\mathrm{m^2 s^{-1}}$
$\mathcal{A}_H$	$0.01\,\mathrm{m^2 s^{-1}}$
$\mathcal{C}_D$	$0.1\,\mathrm{s^{-1}}$
β	$1\,\mathrm{m^{-1} s^{-1}}$
f_0	$1\,\mathrm{s^{-1}}$
N	$1\,\mathrm{s^{-1}}$
c	$-\beta/2\pi(2 + Bu^{-1}N^{-2})$
U	$1\,\mathrm{ms^{-1}}$
L	$1\,\mathrm{m}$
L_x	$1\,\mathrm{m}$
H	$1\,\mathrm{m}$

Table 5.4: Parameter values used for three-dimensional travelling wave test with full mechanics. Since the characteristic values are set to 1, the above parameters are equal to the non-dimensional parameters.

Grid Size	L^2 Error ψ	EOC ψ	L^2 Error q	EOC q	L^2 Error $\boldsymbol{u_g}$	EOC $\boldsymbol{u_g}$
$8 \times 8 \times 15$	0.139772	-	20.7081	-	2.7481	-
$16 \times 16 \times 15$	0.0276283	2.33886	4.41112	2.23098	1.3357	1.04084
$32 \times 32 \times 15$	0.00677504	2.02784	1.04021	2.08427	0.666707	1.00247
$64 \times 64 \times 15$	0.00128219	2.40162	0.204547	2.34637	0.333137	1.00094
$128 \times 128 \times 15$	0.000182996	2.80873	0.0417762	2.29168	0.166578	0.999921

Table 5.5: **Linear elements with zero Dirichlet boundaries.** L^2 errors and EOCs for the streamfunction ψ, potential vorticity q and velocity $\boldsymbol{u_g}$ for travelling wave test run for 3D QGEs with full mechanics (TW3DF) and fixed $\psi = 0$ boundary conditions using linear elements.

The parameters used for this test are in Table 5.4 and the experimental convergence

Grid Size	L^2 Error ψ	EOC ψ	L^2 Error q	EOC q	L^2 Error $\boldsymbol{u_g}$	EOC $\boldsymbol{u_g}$
$8 \times 8 \times 15$	0.00776318	-	2.142	-	0.276004	-
$16 \times 16 \times 15$	0.000671369	3.53147	0.230193	3.21805	0.0675882	2.02985
$32 \times 32 \times 15$	0.000212143	1.66207	0.0271393	3.08439	0.0169798	1.99295
$64 \times 64 \times 15$	0.000203956	0.0567762	0.00430776	2.65537	0.00459478	1.88575
$8 \times 8 \times 23$	0.0092559	-	2.07106	-	0.343144	-
$16 \times 16 \times 23$	0.000885614	3.38562	0.220849	3.22924	0.0847133	2.01815
$32 \times 32 \times 23$	0.000116862	2.92187	0.0259789	3.08765	0.0211763	2.00014
$64 \times 64 \times 23$	5.94814e-05	0.96625	0.00526677	2.30234	0.00531805	1.99348

Table 5.6: **Quadratic elements with zero Dirichlet boundaries.** L^2 errors and EOCs for the streamfunction ψ, potential vorticity q and velocity $\boldsymbol{u_g}$ for travelling wave test run for 3D QGEs with full mechanics (TW3DF) and fixed $\psi = 0$ boundary conditions using quadratic elements. The convergence suffers from the low vertical resolution and improves with greater vertical resolution as seen in the second set of tests with 23 vertical layers.

results for the fixed boundary value run are shown in Table 5.5 for linear elements and 5.6 for quadratic elements. The suboptimal convergence rates in the quadratic element run are due to the low vertical resolution, and improve with finer vertical resolution. It is evident that increasing the order of the horizontal finite element discretisation is overshadowed by the vertical resolution and first order time discretisation. Despite the optimal convergence observed with the linear elements, the discrete velocity solution contains large discontinuities. It is for these reasons that quadratic elements will be used for all further tests and calculations in this thesis.

The convergence results displayed in Table 5.7 and 5.8 were produced from the run with free-slip north and south boundaries. It is evident that the boundary value calculation causes an error increase, most notable in the coarsest grids and interferes with the optimal convergence of the finite element method. This is to be expected since the boundary value calculation involves integration over gradient approximations at the boundary, which improve with finer grids. It was found that convergence was sensitive to the diffusion parameter $\mathcal{A}_H$ when using free-slip boundaries. This is likely due to the no-flux boundary condition $\omega = 0$ on the north and south boundaries that accompanies the horizontal momentum diffusion term, which is weakly enforced by the $\mathcal{A}_H$ term as seen in the linear form (4.82). If $\mathcal{A}_H$ is not sufficiently large, then errors on the boundary will lead to poor accuracy in the calculation of the streamfunction boundary values using (2.117).

Grid Size	L^2 Error ψ	EOC ψ	L^2 Error q	EOC q	L^2 Error $\boldsymbol{u_g}$	EOC $\boldsymbol{u_g}$
$8 \times 8 \times 15$	1.55217	-	169.006	-	13.4619	-
$16 \times 16 \times 15$	0.58696	1.40296	59.4951	1.50624	5.25068	1.35831
$32 \times 32 \times 15$	0.137608	2.09269	14.2832	2.05845	1.39821	1.90892
$64 \times 64 \times 15$	0.03797	1.85764	3.92194	1.86468	0.475683	1.55551
$128 \times 128 \times 15$	0.00988741	1.94120	1.01737	1.94672	0.188563	1.33495

Table 5.7: **Linear elements with free-slip boundaries.** L^2 errors and EOCs for the streamfunction ψ, potential vorticity q and velocity $\boldsymbol{u_g}$for travelling wave test run for 3D QGEs with full mechanics (TW3DF) using linear elements and free slip boundary treatment.

Grid Size	L^2 Error ψ	EOC ψ	L^2 Error q	EOC q	L^2 Error $\boldsymbol{u_g}$	EOC $\boldsymbol{u_g}$
$8 \times 8 \times 15$	0.639233	-	68.9266	-	5.28244	-
$16 \times 16 \times 15$	0.0365257	4.12936	3.5196	4.29158	0.31465	4.06938
$32 \times 32 \times 15$	0.00496421	2.87927	0.474554	2.89077	0.0442313	2.83061
$64 \times 64 \times 15$	0.000634833	2.96712	0.0585782	3.01814	0.00671889	2.71877

Table 5.8: **Quadratic elements with free-slip boundaries.** L^2 errors and EOCs for the streamfunction ψ, potential vorticity q and velocity $\boldsymbol{u_g}$ for travelling wave test run for 3D QGEs with full mechanics (TW3DF) using quadratic elements and free slip boundary treatment. Convergence is less effected by the vertical resolution than in Table 5.6, suggesting that convergence is somewhat determined by the free-slip boundary value calculations. Only three refinements were performed due to computational limits.

5.3 Numerical Conservation of Energy and Enstrophy

The energy and enstrophy are conserved quantities of the inviscid QGE (2.65) as shown in Theorems 2.5 and 2.7, it is therefore desirable for these quantities to be conserved numerically as tested in [20]. Define the energy of the numerical solution as

$$\mathcal{E}_h = \frac{1}{2}\|\nabla\psi^n\|_{L^2}^2 + \frac{1}{2}\left\|\frac{f_0}{N}\frac{\partial\psi^n}{\partial z}\right\|_{L^2}^2 \tag{5.8}$$

and the enstrophy (dissipation energy) of the numerical solution as

$$Z_h = \frac{1}{2}\|q^n\|_{L^2}^2, \tag{5.9}$$

where the L^2 norms are taken over the whole computational domain. Figure 5.2 shows the energy and enstrophy plotted over time of the TW3DF test with quadratic basis functions and free-slip boundaries (Table 5.8). The numerical quantities of the travelling wave solution can be seen to converge towards the analytical values for energy $\mathcal{E} = 3\pi^2/4 \approx 7.4022$ and enstrophy $Z = 9\pi^4 + 1/6 \approx 876.8485$ as $h \to 0$.

Furthermore, the relative changes in numerical energy and enstrophy from the initial values decreases as the horizontal grid spacing h decreases indicating that the spatial discretisation conserves these quantities.

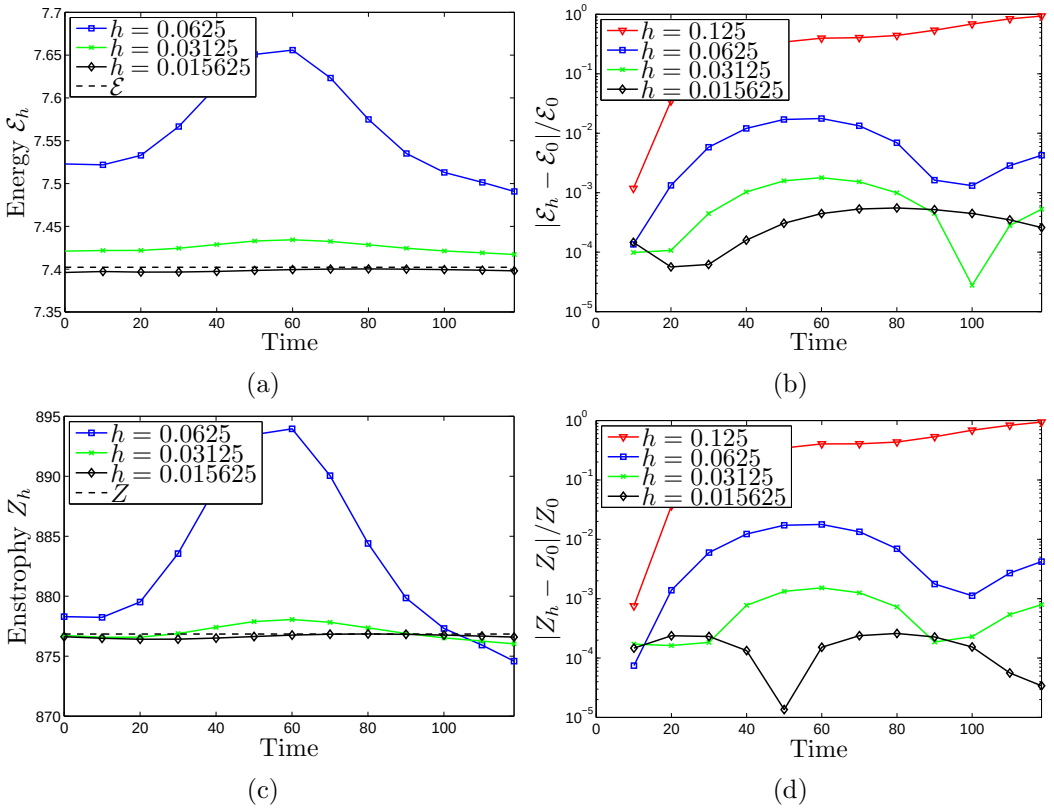

Figure 5.2: Numerical conservation of energy and enstrophy with refinement in grid spacing h. Solutions are taken from the test in Table 5.8. (Left) Energy and enstrophy for the numerical solutions converge to true values $\mathcal{E}$ and Z as $h \to 0$. (Right) Change in numerical energy and enstrophy relative to initial values $\mathcal{E}_0$ and Z_0 at $t = 0$. The initial values are calculated after projection of the initial conditions onto the grid. The quantities from the coarsest grid ($h = 0.125$) have been excluded from the plots on the left to provide a clearer view of the more refined solutions.

5.4 Vortex Pair without Rotation (VPwoR)

This section tests the motion of a vortex pair as described in [1, 62], similar to tests performed in [75, 91, 121], where a vortex pair of opposing vorticities will propagate along their axis of separation. Set diffusion and rotation to zero ($f_0 = \beta = 0$) so that the QGE are reduced to the vorticity equation for the two-dimensional Euler

equations

$$\frac{\partial q}{\partial t} + (\boldsymbol{u_g} \cdot \nabla) q = 0 \tag{5.10}$$

where the potential vorticity is now equivalent to relative vorticity $q = \Delta\psi$, north/-south boundaries are free-slip and east/west boundaries are periodic. The stream-function of a point vortex with infinite vorticity at a position (x_0, y_0) and zero vorticity everywhere else is given by

$$\psi = -\frac{\Gamma}{4\pi} \log((x - x_0)^2 + (y - y_0)^2). \tag{5.11}$$

Clearly, one must add a small constant δ into this formulation to remove the singularity for computational purposes. Therefore, an initial two-dimensional vortex of strength $\Gamma_0 = \Gamma$ at (x_0, y_0) is given by,

$$\psi(x, y, 0) = -\sum_{i=0}^{2} \frac{\Gamma_i}{4\pi} \log((x - x_i)^2 + (y - y_i)^2 + \delta^2), \tag{5.12a}$$

$$u_g(x, y, 0) = -\frac{\partial \psi}{\partial y} = \sum_{i=0}^{2} \frac{\Gamma_i}{2\pi} \frac{y - y_i}{(x - x_i)^2 + (y - y_i)^2 + \delta^2}, \tag{5.12b}$$

$$v_g(x, y, 0) = \frac{\partial \psi}{\partial x} = -\sum_{i=0}^{2} \frac{\Gamma_i}{2\pi} \frac{x - x_i}{(x - x_i)^2 + (y - y_i)^2 + \delta^2}, \tag{5.12c}$$

$$q(x, y, 0) = -\sum_{i=0}^{2} \frac{\Gamma_i}{\pi} \frac{\delta^2}{((x - x_i)^2 + (y - y_i)^2 + \delta^2)^2}, \tag{5.12d}$$

where image vortices, at $(x_1, y_1) = (x_0, -y_0)$ and $(x_2, y_2) = (x_0, 2L_y - y_0)$ for domain width L_y in the $y-$direction of strengths $\Gamma_1 = \Gamma_2 = -\Gamma$, ensure the no-flow through boundary condition $\boldsymbol{u_g} \cdot \boldsymbol{n} = 0$ is satisfied.

Using the above equations to ensure boundary conditions are satisfied, a vortex pair is placed with vortices at $(0.5, 0.4)$ and $(0.5, 0.6)$ with strengths $-\Gamma$ and Γ respectively where $\Gamma = 0.005$. The computational domain is a two-dimensional unit square $[0, 1]^2$. Such a configuration generates a westward flow on the structure, indeed, the pair propagates westward as shown in Figure 5.3. The approximate velocity at which this vortex pair should travel is given by the velocity that each vortex induces on the other

$$u_g = -\frac{\partial \psi}{\partial y} = \frac{\Gamma}{2\pi} \frac{0.4 - 0.6}{(0.5 - 0.5)^2 + (0.4 - 0.6)^2} = -\frac{\Gamma}{0.4\pi} \approx -0.004. \tag{5.13}$$

This velocity is reduced slightly by the effect of the north and south boundaries that create the effect of counter-rotating image vortices on the other side of the boundaries. The closest image vortices at $(0.5, 1.4)$ and $(0.5, -1.4)$ induce a velocity of

$$\frac{\Gamma}{2\pi}\frac{0.8}{(0.8)^2} = \frac{\Gamma}{1.6\pi} \approx 0.001 \tag{5.14}$$

on the structure which gives the total velocity of the vortex pair to be approximately -0.003. Therefore, at $t = 50$ the vortex pair should have travelled approximately a distance of 0.15 across the domain to $x = 0.35$. As seen in Figure 5.3c, the pair has moved slightly less than this due to the vorticity that the vortex pair sheds as it propagates, weakening the structure. This test shows that the numerical scheme can produce accurate dynamics of a vortex pair.

5.5 Boundary Image Vortex without Rotation (VwoR)

This section tests the method with a vortex near the free-slip boundary similar to the test in [108]. The vortex is expected to propagate along the boundary as if an image vortex (of opposite vorticity) is on the opposite side of the boundary creating a vortex pair [1, 62]. Therefore, the vortex propagates along the boundary in a similar way to a vortex pair as shown in Figure 5.4. The vortex propagates slightly faster than the vortex pair because it experiences less distortion from the north boundary than in the vortex pair test case and has a propagation velocity of approximately -0.0035, therefore, moving to around $x = 0.325$ at $t = 50$. This shows that the free-slip boundaries have been implemented correctly in the numerical scheme and vortex dynamics behave as expected near the boundaries.

5.6 Vortex in a β-plane (VwR)

Now, set $\beta = 1$ to observe the β-plane effect on a vortex as tested in [86, 88]. The equation is now (5.10) with $q = \Delta\psi + \beta y$. The same initial conditions (5.12) are used with the vortex initially placed at $(0.5, 0.1)$.

An explanation for the behaviour of the vortex in the β-plane found in [86] is outlined in the following. For a characteristic velocity scale U and length scale L, one can estimate a scaling ratio between the β-term and vorticity advection in the potential

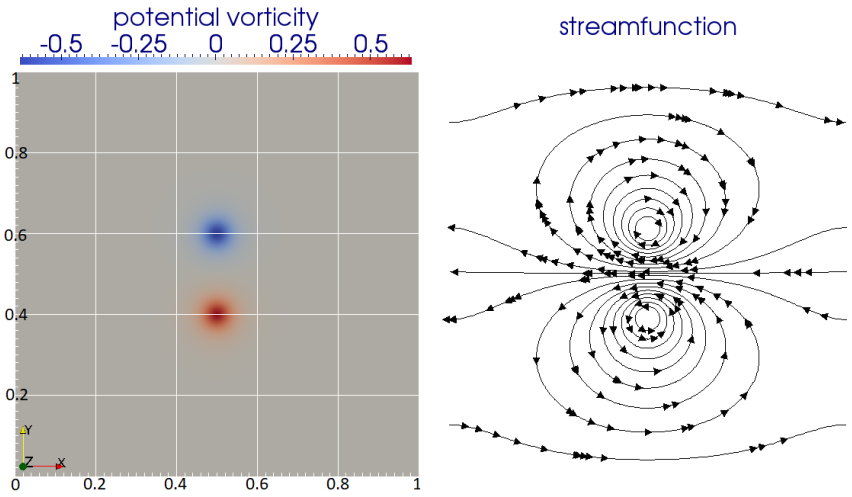

(a) Initial vortex pair $t = 0$.

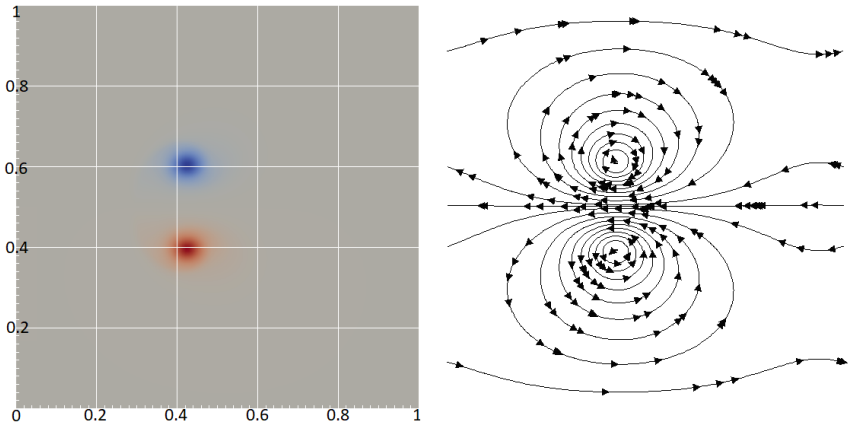

(b) Vortex pair begins to propagate westward, moving as a single structure, $t = 25$.

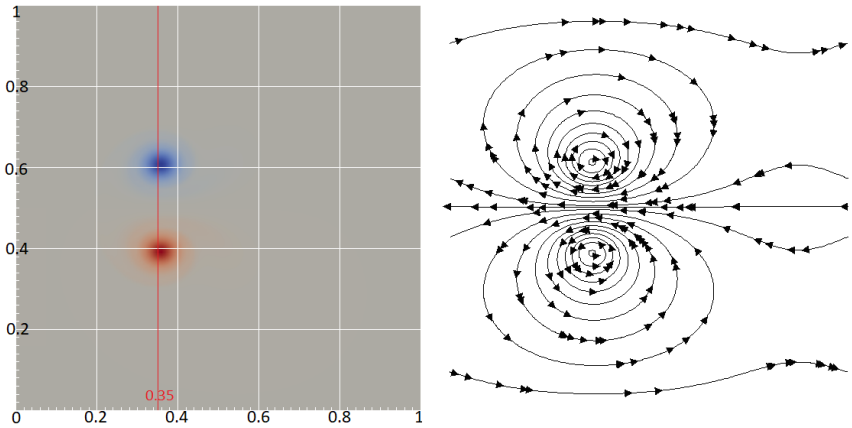

(c) Fluid moves around the vortex pair as it propagates and sheds vorticity, $t = 50$.

Figure 5.3: A vortex pair propagating westward due to the velocity each vortex induces on the other, computed on a 128×128 grid with quadratic elements and free-slip boundaries.

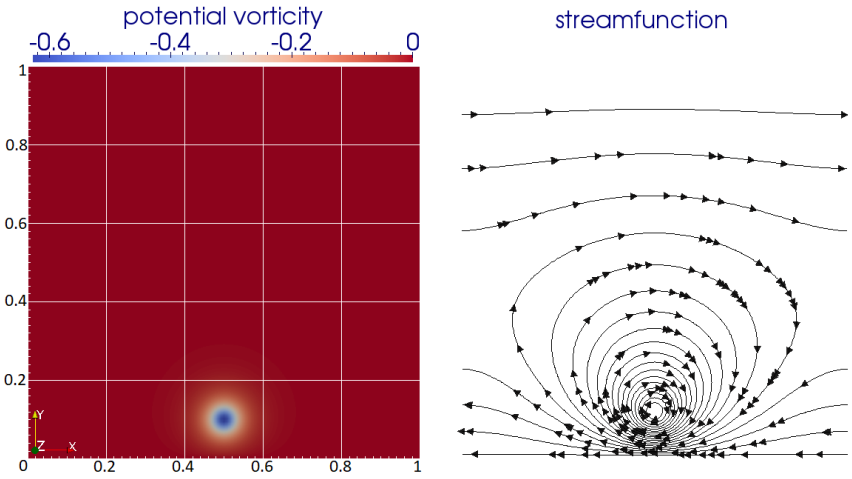

(a) Initial vortex at $t = 0$.

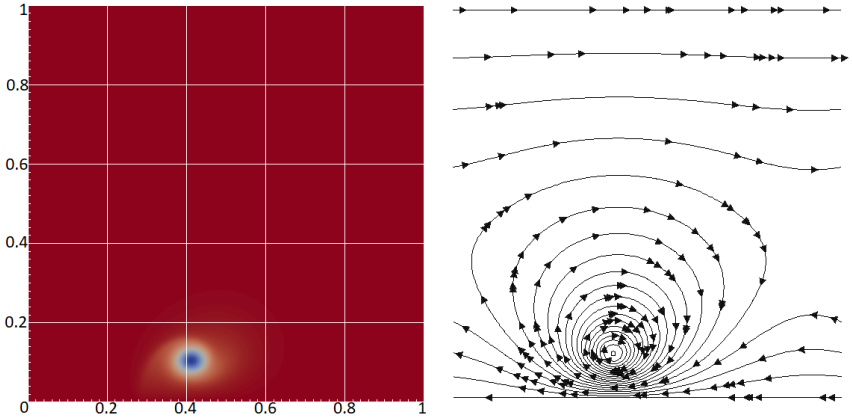

(b) Vortex begins to propagate westward as if there is a counter-rotating vortex on the other side of the solid boundary, $t = 25$.

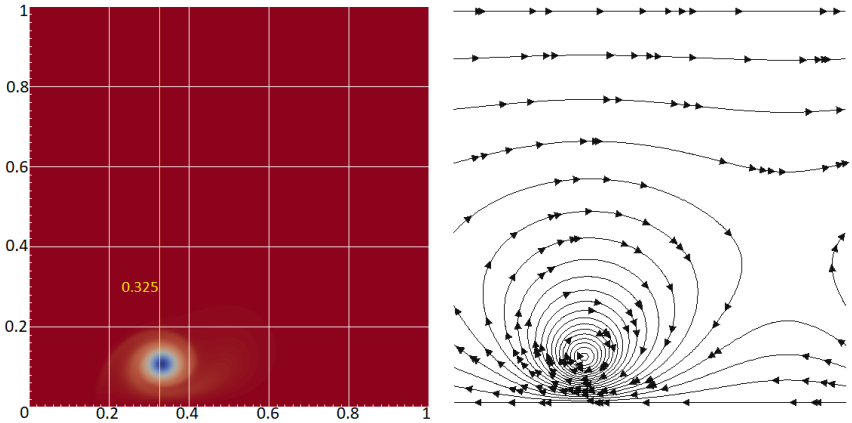

(c) The vortex sheds vorticity and weakens slightly as it propagates along the boundary, $t = 50$.

Figure 5.4: Potential vorticity and streamlines with arrows indicating fluid velocity direction of a vortex propagating westward along the south boundary as if part of a vortex pair, computed on a 128×128 grid.

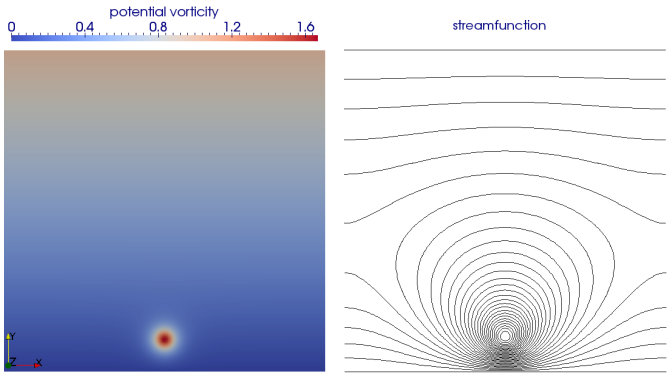

(a) Initial vortex near south boundary at $t = 0$.

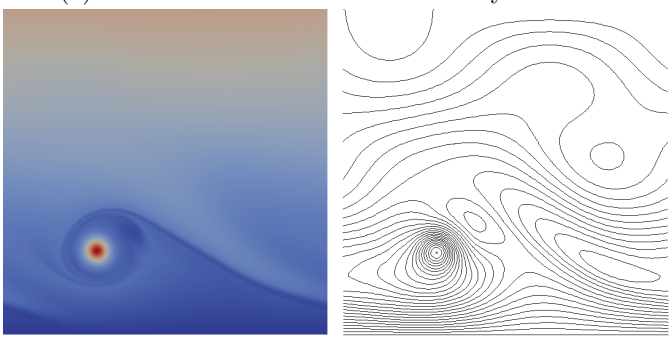

(b) Vortex at $t = 100$, westward motion becomes dominant over the boundary propagation.

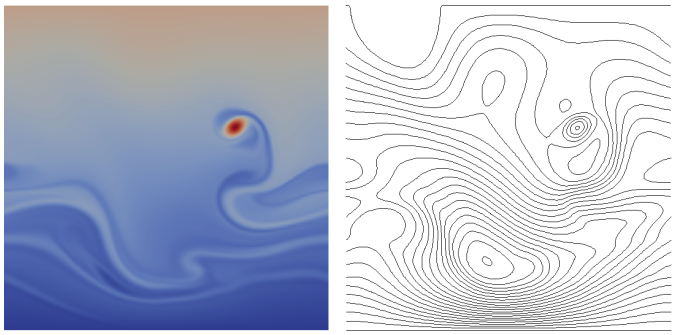

(c) Vortex at $t = 250$, Rossby waves shed in the wake of the vortex.

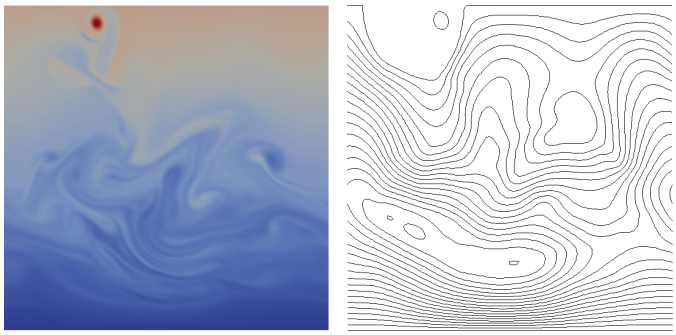

(d) Vortex hits the north boundary at $t = 500$

Figure 5.5: A cyclonic vortex propagating northwest due to β-plane rotation effects. The vortex propagates along the boundary in the eastward direction for a short time, but as it moves north due to the rotation effects, the westward motion dominates. Rossby waves can be seen in the wake of the vortex.

vorticity equation (5.10),

$$\mathcal{R} = \frac{\beta v}{\boldsymbol{u} \cdot \nabla \omega} \sim \frac{\beta U}{(U/L)(U/L)} = \frac{\beta L^2}{U}, \tag{5.15}$$

where vorticity $\omega = \Delta\psi$. The β influence is strong when $\mathcal{R}$ is large. When this is true, the initially axisymmetric streamfunction ψ propagates westward and changes shape by Rossby wave dispersion. To understand this propagation, observe when the flow is primarily an axisymmetric vortical flow $\psi(x, y) \approx \Psi_a(r)$, the β-term creates a forcing term in (5.10) since

$$(\boldsymbol{u} \cdot \nabla)\beta y = \beta \frac{\partial \psi}{\partial x} \approx \beta \frac{\partial}{\partial x} \Psi_a(r) = \beta \cos(\theta) \frac{d\Psi_a}{dr}. \tag{5.16}$$

The $\cos(\theta)$ represents a dipole structure, which generates an advective flow. Initially, the dipole centres are separated in the zonal direction (east-west), but after time this is rotated by azimuthal (angular) advection from Ψ_a towards a more meridional (north-south) separation. This results in an approximately westward advection. The dipole centre separation is not completely meridional, so the vortex propagation is not exactly westward. The north-south motion is dependent on the sign of $d\Psi_a/dr$: if it is positive, then the motion will be to the north as in Figure 5.5 and if it is negative, then motion will be to the South as in Figure 5.6. Rossby waves can be seen in the wake of the vortices, where weather fronts often form in the atmosphere. Such low/high pressure systems can be carried eastward by the Northern Hemi-sphere jet stream, causing weather fronts to precede the cyclone/anticyclone. Clearly the vortices in the numerical tests behave in accordance with this theoretical explanation, demonstrating that the planetary rotation effects have been implemented correctly.

5.7 Vortex in an f-plane with East-West Tilt (VEWT)

This test is constructed using an initial vortex with an east-west tilt with height is used to test the effects of the f-plane. For this test set $\beta = 0, f_0 = 10$ and $N = 1$ with the unforced ($\mathcal{F} = 0$), inviscid ($\mathcal{A}_H = \mathcal{K}_V = 0$) three-dimensional QGE (2.65) in a unit cube domain $[0, 1]^3$ to observe strong rotation effects. Figure 5.7 shows how the initial vortex evolves. The vortex becomes flattened in the y-direction and rotates anti-clockwise. Over time, this flattening and rotating of the vortex structure forms into a vertical vortex column aligned with the global rotation axis as would be expected in a strongly rotating fluid due to the Taylor-Proudman theorem [39].

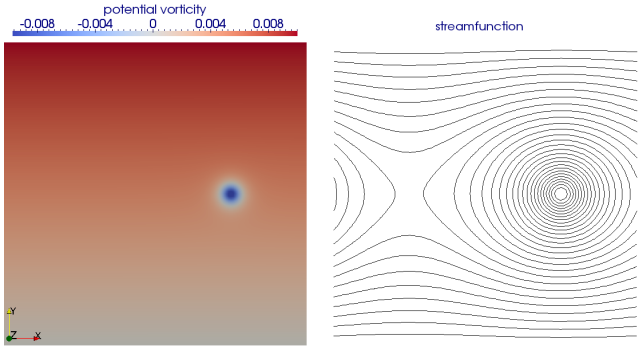

(a) Initial vortex at $t = 0$.

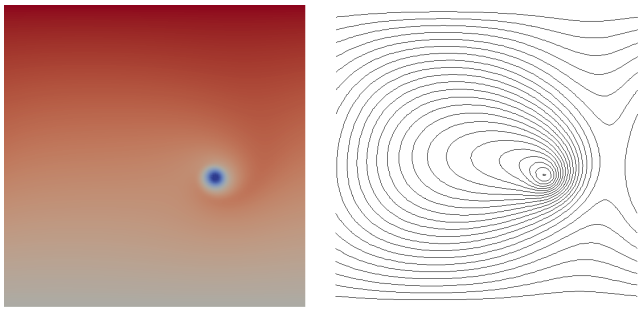

(b) Vortex begins to experience rotational effects at $t = 150$.

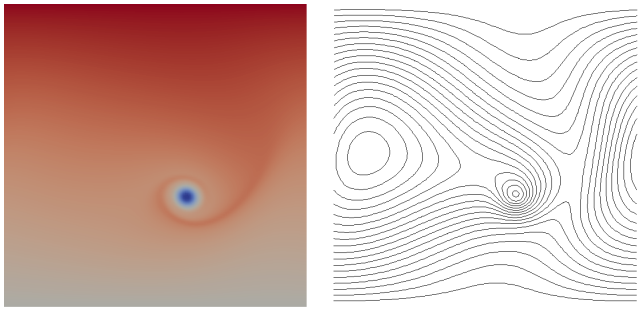

(c) Vortex propagating southwest at $t = 300$.

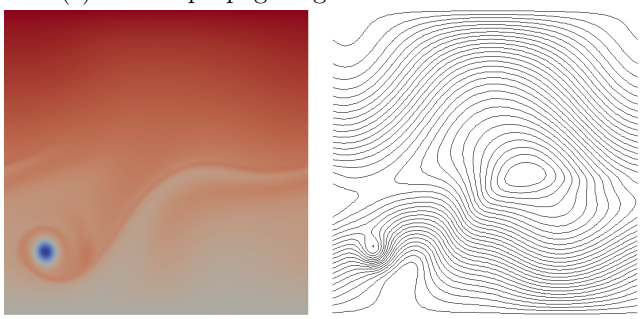

(d) Vortex at $t = 1000$.

Figure 5.6: Potential vorticity and streamlines of an axisymmetric anti-cyclonic vortex propagating southwest due to β-plane rotation effects.

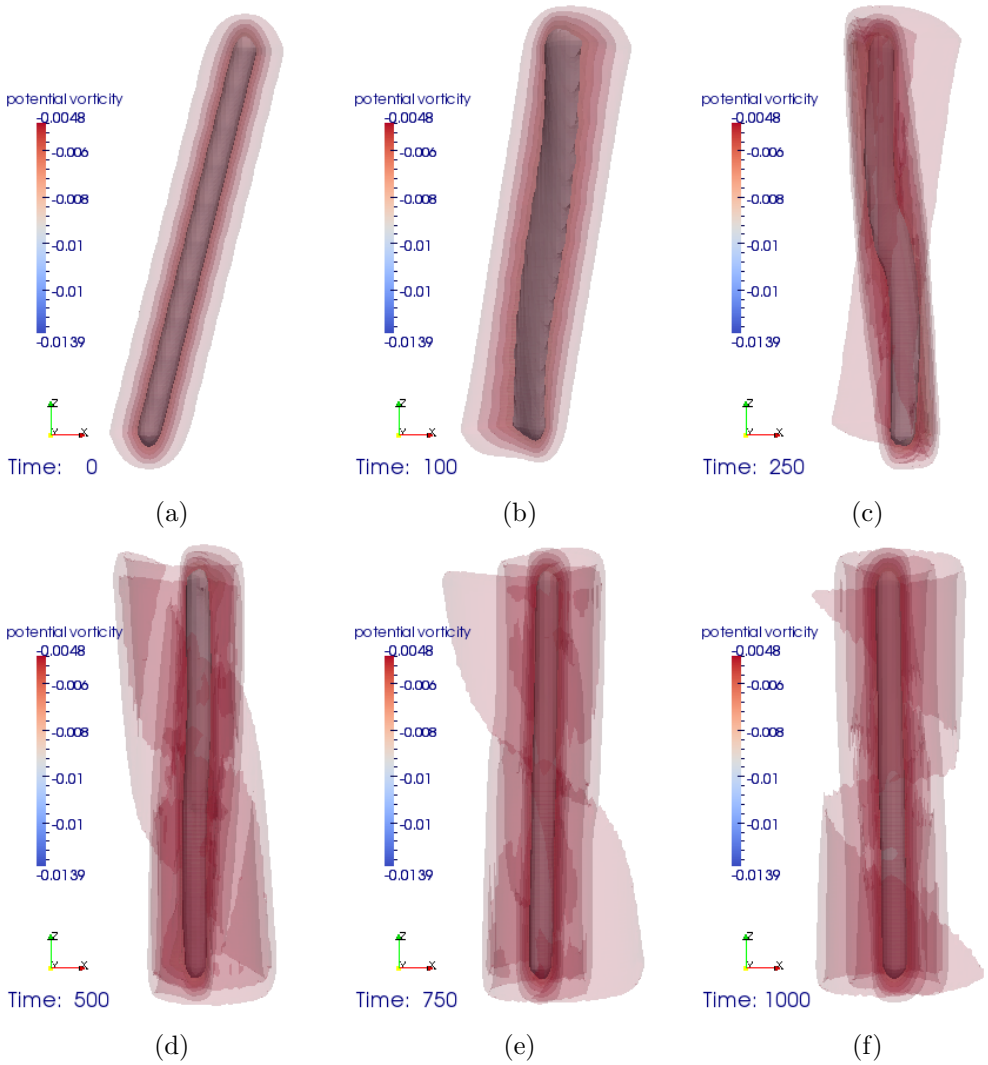

Figure 5.7: Potential vorticity isosurfaces of an anti-cyclonic vortex with an east-west tilt evolving in an f-plane. The initially tilted vortex straightens up and becomes more uniform with height. This demonstrates that the numerical method exhibits the expected behaviour of rapidly rotating flows. Computed on $[0, 1]^3$ domain with $128 \times 128 \times 15$ grid using quadratic elements and free-slip boundaries.

Chapter 6

Quasi-geostrophic Frontogenesis

The goal of this chapter is to use a reduced model for the formation of weather fronts and from this gain insight into their origin and the role of frontal dynamics upon atmospheric flows. The following presents a brief discussion of how weather is generated in Earth's atmosphere from [86]. The mean circulation patterns for the ocean and atmosphere are unstable to perturbation and are therefore intrinsically variable, despite the invariant compositions of the ocean and atmosphere and fixed land and sea-floor topography. The statistics of this variability may be considered stationary in time under steady-state external influences; generating a statistical equilibrium comprised of unstable mean flows, turbulent eddies, waves, and vortices generated by the instabilities. On longer time scales, the mean eddy fluxes of momentum, heat, potential vorticity, and material tracers shape the structure of the mean circulation and material distributions.

Synoptic scale or mesoscale mean circulations are approximately geostrophic, hydrostatic and subject to two broad groups of instabilities: Barotropic instability: the mean horizontal shear is the principal energy source for the eddies, and horizontal momentum flux (Reynolds stress) is the dominant eddy flux. Baroclinic instability: the mean vertical shear and horizontal buoyancy gradient (related through the thermal wind) is the energy source, and the vertical momentum and horizontal buoyancy fluxes are the dominant eddy fluxes, with Reynolds stress playing a secondary role.

Under some circumstances, the mean flows are unstable to other smaller scale types of instability: convective, Kelvin-Helmholtz, or centrifugal, which are relatively rare as direct instabilities of the mean flows on the planetary scale. More often these instabilities arise either in response to locally forced flows such as in boundary lay-

ers or as secondary instabilities of the synoptic and mesoscale flows as part of a general cascade of variance toward dissipation on very small scales. The mean zonal wind pattern in the mid-latitude troposphere is a result of geostrophic flow with an associated meridional temperature gradient created by tropical heating and polar cooling.

This wind profile is baroclinically unstable to extra-tropical fluctuations on the synoptic scale of O(103) km. This is the primary origin of weather, and in turn weather events collectively cause a poleward heat flux that limits the strength of the zonal wind and its geostrophically balancing meridional temperature gradient.

This chapter will demonstrate that the QGE can produce fronts using a horizontal deformation field acting on a temperature gradient. This then sets the stage for a more dynamic channel model that generates fronts along a strong zonal jet within geostrophic turbulence. The goal of this chapter is to characterise the resulting fronts in terms of profiles and horizontal spectra that could eventually be compared to atmospheric data or further reduced models.

6.1 Deformation Field Front Formation

There are many mechanisms involved in the formation of fronts, one of the most important being a horizontal deformation field acting upon a temperature gradient [61, 112, 128, 129, 130]. A deformation field with an axis of contraction perpendicular to a temperature gradient will intensify the gradient. Frontogenesis using the quasi-geostrophic equations has been achieved analytically [130] and numerically [87, 129]. Williams analytically and numerically solved the quasi-geostrophic equations by decomposing the streamfunction into one part describing the deformation field and another part independent of x to get the non-dimensionalised equations (after a change of coordinates)

$$\begin{aligned} \frac{\partial q}{\partial t} - y\frac{\partial \psi}{\partial y} &= 0 \\ \frac{\partial^2 \psi}{\partial t \partial z} - y\frac{\partial^2 \psi}{\partial y \partial z} + w &= 0 \end{aligned} \tag{6.1}$$

where

$$q = \frac{\partial^2 \psi}{\partial y^2} + \frac{\partial^2 \psi}{\partial z^2}, \tag{6.2}$$

removing the x dependence. These equations are solved in a vertical slice with a $y-z$ plane streamfunction with a simple setup to achieve frontogenesis [129, 130]; impose a deformation field with horizontal velocity and length scales U and L,

$$u_d = \frac{U}{L}\left(x - \frac{L}{2}\right) \quad v_d = -\frac{U}{L}\left(y - \frac{L}{2}\right) \tag{6.3}$$

and initial temperature field with vertical length scale H,

$$\theta = \frac{\partial \theta_I}{\partial z}\left(z - \frac{H}{2}\right) - A\left(\frac{2}{\pi}\right)\arctan\left(\sinh\left(\alpha\left[y - \frac{L}{2}\right]\right)\right), \tag{6.4}$$

where A is the variation in temperature and $\alpha = 1/(2L_f)$ for frontal length scale $L_f = HN/f_0$. This choice of temperature disturbance is close to the large time analytical solution found by Williams and the particular value of α used is such that the length scale of the initial disturbance is no smaller than the frontal scale (or Rossby deformation radius) L_f. Otherwise, the vertical motions of rising warm air and falling cool air will be dominant over the frontogenesis causing frontolysis (weakening of the front) to occur [130]. Williams' numerical results displayed an increase in the meridional temperature gradient, however, oscillations near the boundary occurred due to the inexactness of the constant flux boundary conditions [129]. Despite this, the results clearly indicate formation of a front within the quasi-geostrophic and non-geostrophic settings, with the non-geostrophic equations producing a front with more realistic vertical sloping.

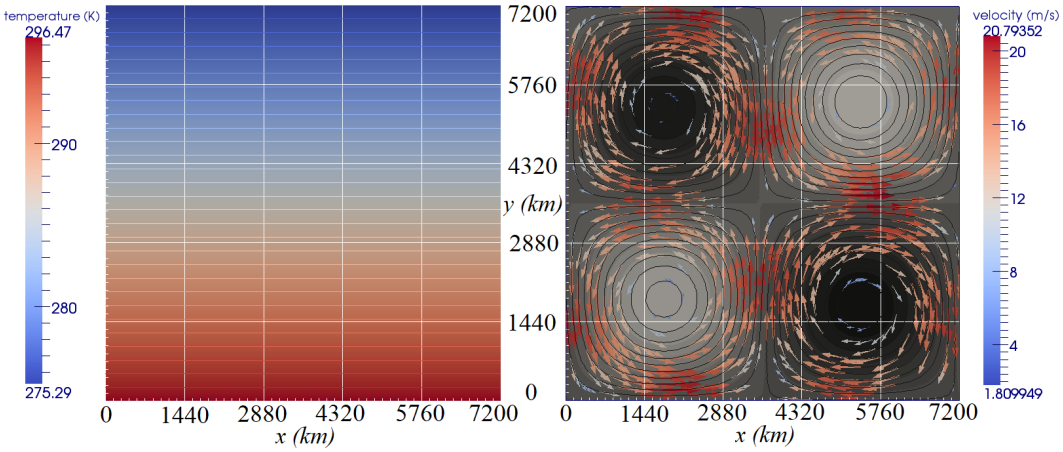

Figure 6.1: (Left) Initial potential temperature (6.7) and (Right) velocity field (6.6) with streamlines (contours of (6.8)) at $z = 900\,\mathrm{m}$.

Within this thesis, an attempt is made to reproduce the inviscid quasi-geostrophic

Parameter	Value
$\mathcal{K}_V$	$0\,\mathrm{m^2 s^{-1}}$
$\mathcal{A}_H$	$0\,\mathrm{m^2 s^{-1}}$
$\mathcal{C}_D$	$0\,\mathrm{s^{-1}}$
β	$1.4 \times 10^{-11}\,\mathrm{m^{-1} s^{-1}}$
f_0	$1.1 \times 10^{-4}\,\mathrm{s^{-1}}$
γ	$3.3 \times 10^{-3}\,\mathrm{K^{-1}}$
N	$0.0114\,\mathrm{s^{-1}}$
θ_0	$300\,\mathrm{K}$
$\partial\theta_I/\partial y$	$-3 \times 10^{-6}\,\mathrm{K m^{-1}}$
$\partial\theta_I/\partial z$	$4 \times 10^{-3}\,\mathrm{K m^{-1}}$
g	$9.806\,65\,\mathrm{K m^{-1}}$
L	$7.2 \times 10^6\,\mathrm{m}$
L_x	$7.2 \times 10^6\,\mathrm{m}$
H	$9000\,\mathrm{m}$
U	$20\,\mathrm{m\,s^{-1}}$

Table 6.1: Parameter values used for deformation field.

results, using an approach similar to that used by Williams [130]. The equations will be the unforced, inviscid dimensional quasi-geostrophic equations

$$\frac{\partial q}{\partial t} + (\boldsymbol{u_g} \cdot \nabla) q = 0, \tag{6.5a}$$

with

$$q = \Delta\psi + \frac{\partial}{\partial z}\left(\frac{f_0^2}{N^2}\frac{\partial \psi}{\partial z}\right) + \beta y, \tag{6.5b}$$

with rigid north, south, top and bottom boundaries and periodicity in the zonal direction. Instead of using the deformation field given by (6.3), this work uses the sinusoidal field,

$$u_d = U \sin\left(\frac{2\pi}{L}\left(x - \frac{L}{2}\right)\right)\cos\left(\frac{2\pi}{L}\left(y - \frac{L}{2}\right)\right), \tag{6.6a}$$

$$v_d = -U \cos\left(\frac{2\pi}{L}\left(x - \frac{L}{2}\right)\right)\sin\left(\frac{2\pi}{L}\left(y - \frac{L}{2}\right)\right), \tag{6.6b}$$

and an initial temperature field with a linear north-south gradient

$$\theta = \frac{\partial \theta_I}{\partial y}\left(y - \frac{L}{2}\right) + \frac{\partial \theta_I}{\partial z}\left(z - \frac{H}{2}\right) + \theta_0. \tag{6.7}$$

Here θ_0 is a reference temperature with $\partial\theta_I/\partial y = -3 \times 10^{-6}\,\mathrm{Km}^{-1}$ and $\partial\theta_I/\partial z = 4 \times 10^{-3}\,\mathrm{Km}^{-1}$ being the horizontal and vertical temperature variations of the initial field. The vertical potential temperature variation $\partial\theta_I/\partial z$ is taken to be positive as in a stable atmosphere. This produces the initial streamfunction

$$\begin{aligned}\psi =& \frac{g\gamma}{f_0}\left[-\frac{UL}{2\pi}\sin\left(\frac{2\pi}{L}\left(x-\frac{L}{2}\right)\right)\sin\left(\frac{2\pi}{L}\left(y-\frac{L}{2}\right)\right)\right.\\ &\left.+\left(\frac{\partial\theta_I}{\partial y}\left(y-\frac{L}{2}\right)+\frac{1}{2}\frac{\partial\theta_I}{\partial z}\left(z-H\right)+\theta_0\right)z\right],\end{aligned} \tag{6.8}$$

where g is the gravitational acceleration and γ is the thermal expansion coefficient. Initial potential vorticity is then

$$q = \frac{4\pi U}{L}\sin\left(\frac{2\pi}{L}\left(x-\frac{L}{2}\right)\right)\sin\left(\frac{2\pi}{L}\left(y-\frac{L}{2}\right)\right)+\frac{f_0^2}{N^2}\frac{\partial\theta_I}{\partial z}+\beta y. \tag{6.9}$$

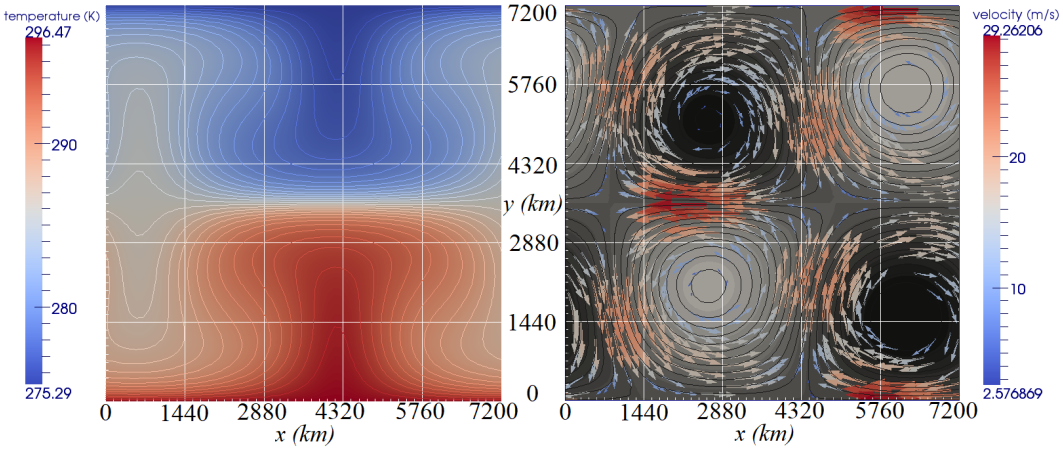

Figure 6.2: Formation of a front at $t = 30\,\mathrm{h}$, horizontal slice at $z = 900\,\mathrm{m}$. Strong temperature gradients can be seen at $y = 3600\mathrm{km}$ between $x = 2160 - 6480\mathrm{km}$. The deformation field and front formation have drifted east due to the geostrophic winds that form to balance the meridional temperature gradient. The vertical structure of the front is seen in Figure 6.4. Computed on a $64 \times 64 \times 15$ grid.

This setup is similar to that used by Stone [112], and the spurious oscillations near the boundary should not occur with the zero flux boundary conditions. This initial temperature gradient is representative of the average natural state of the atmosphere, with warmer air near the equator and cold air at the poles. Note that, because the temperature gradient extends over the whole domain, only $L > L_f$ is required to observe frontogenesis. The choice of deformation field also means that $u_d \approx x, v_d \approx -y$ for (x, y) close to $(L/2, L/2)$, thereby resembling the simple defor-

mation fields used by Stone and Williams. This is the region where frontogenesis is expected to be observed.

Initial conditions at $z = 900\,\text{m}$ above ground are shown in Figure 6.1. The initial linear temperature gradient in the left hand image shows warm air in the South and cool air in the North. The right image shows the deformation field following streamlines (depicted with contours). Figure 6.2 shows the evolution of the flow after 30 hours. A strong concentration of temperature contours indicate that a clear frontal zone has formed near the centre of the domain. The temperature gradients in turn induce a geostrophic westerly wind that has caused the front to drift towards the East.

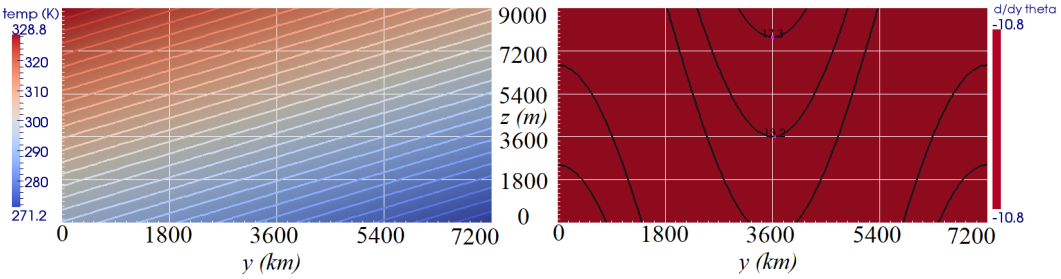

Figure 6.3: (Left) Initial potential temperature and (Right) meridional temperature gradient with zonal velocity (contours) at $x = 4176\,\text{km}$. Vertical temperature variation is that of a stable atmosphere ($N^2 > 0$).

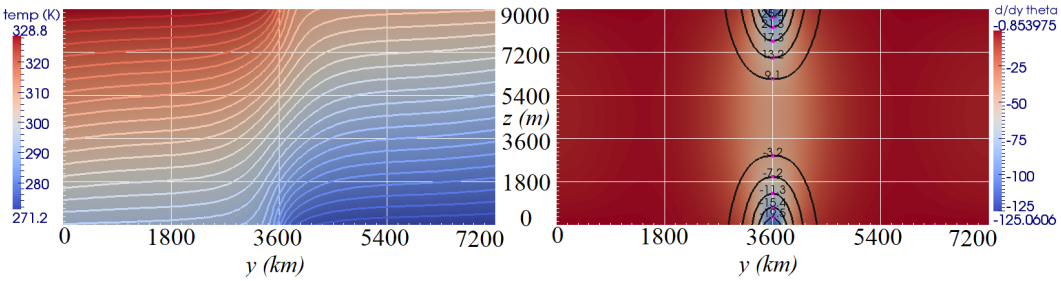

Figure 6.4: Formation of a front at $t = 30\,\text{h}$, vertical slice at $x = 4176\,\text{km}$. The temperature gradients clearly intensify with the strongest gradient occurring near the top and bottom boundaries. A strong westerly jet develops at the top boundary due to the strong temperature gradients. An opposing jet develops near the ground due to the movement of air along the frontal zone.

Observing the development of the front in a vertical slice taken at $x = 4176\text{km}$, one can see that the initially stable temperature profile (Figure 6.3) becomes de-

formed with strong temperature gradients around $y = 3600$km as seen in Figure 6.4. The strongest temperature gradients occur near the top and bottom boundaries. Strong jets also form near the boundaries; at the top boundary a strong westerly jet is induced by the strong meridional temperature gradient, whilst at the bottom boundary an easterly jet is formed by the motion of air along the frontal zone.

6.2 Channel Model

This section investigates a turbulent zonal jet for a geometry known to generate fronts when simulated by McWilliams et al. [87, 89] and Holland et al. [56, 57]. The domain is as previously assumed: $[0, L_x] \times [0, L] \times [0, H]$ with periodicity in the zonal direction and rigid top, bottom, north and south boundaries. The configuration assumes that there is a constant forcing at the top of the domain in the form of a stress wind representing the geostrophic wind generated by a meridional temperature gradient. Neither heating ($\mathcal{H}_t = 0$) nor vertical diffusion ($\mathcal{K}_V = \mathcal{A}_V = 0$) is used since McWilliams and Chow [87] found these had a negligible effect on the dynamics of the flow. This zonal wind blows eastward and is strongest in the centre of the domain; this effect can be incorporated into the model by letting

$$\boldsymbol{\tau} = \tau_0 \sin\left(\frac{\pi y}{L}\right) \hat{\boldsymbol{x}}, \tag{6.10}$$

where $\hat{\boldsymbol{x}} = (1, 0, 0)$, then the forcing term in the quasi-geostrophic equations is given by

$$\mathcal{F} = \begin{cases} H_w^{-1}(\nabla \times \boldsymbol{\tau}) \cdot \hat{\boldsymbol{z}} = -\dfrac{\tau_0 \pi}{L H_w} \cos\left(\dfrac{\pi y}{L}\right) & \text{if } z \geq |H - H_w| \\ 0 & \text{if } z < |H - H_w| \end{cases} \tag{6.11}$$

where H_w is the depth of the wind and $\hat{\boldsymbol{z}} = (0, 0, 1)$. The energy in the system is damped by a bottom friction

$$\mathcal{C}_D = \begin{cases} \mathcal{C}_D' & \text{if } z \leq H_D \\ 0 & \text{if } z > H_D \end{cases} \tag{6.12}$$

applied to the bottom of the domain, where $H_D < H$ is some height. Let us recall the dimensional quasi-geostrophic equations (2.65) in this setting;

$$\frac{\partial q}{\partial t} + J(\psi, q) = \mathcal{F} + \mathcal{A}_H \Delta^2 \psi - \mathcal{C}_D \Delta \psi$$

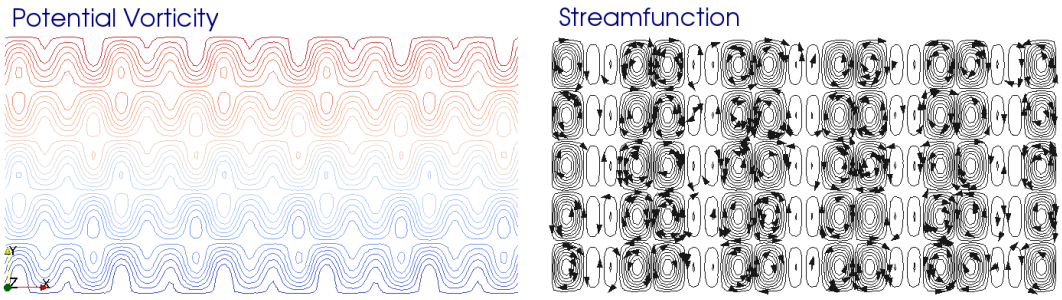

Figure 6.5: Initial perturbations seen as horizontal slices taken at height of 4500 m. (Left) Potential vorticity contours. (Right) Streamlines with flow direction indicated by arrows. Sinusoidal perturbations make up the initial flow to provide the conditions for a growing instability.

with potential vorticity

$$q = \Delta\psi + \frac{\partial}{\partial z}\left(\frac{f_0^2}{N^2}\frac{\partial\psi}{\partial z}\right) + \beta y. \tag{6.13}$$

The boundary conditions are free-slip with no-flux that is

$$\frac{\partial\psi}{\partial\boldsymbol{\tau}} = \mathcal{A}_H\frac{\partial^2\psi}{\partial\boldsymbol{n}^2} = 0 \text{ on north and south boundaries,} \tag{6.14a}$$

$$w = 0 \text{ on top and bottom boundaries} \tag{6.14b}$$

with periodic boundaries in the zonal direction. The values of the streamfunction at the north and south boundaries are calculated using equations (2.117).

Table 6.2 shows a summary of similar numerical experiments. McWilliams and Chow uses a three-layer model with a higher order "triharmonic" viscosity term $-A_4\Delta^3\psi$ to dampen small grid level oscillations and a vertical momentum diffusion term which was found to have insignificant effects on the flow. As stated in [56], the reason for using this higher order viscosity term is computational. The purpose of these horizontal diffusion terms and bottom friction is to dissipate energy with corresponding decay rates $\delta_m = 8\mathcal{A}_H\pi^2/L_e^2$, $\delta_4 = 32A_4\pi^4/L_e^4$ and $\delta_D = \mathcal{C}_D$ where L_e is an eddy length scale. From this it is clear that the decay times $1/\delta_m$ and $1/\delta_4$ become much longer for larger eddies, but the diffusive effects of the A_4 term drop more rapidly than the $\mathcal{A}_H$ term at larger scales. When introducing bottom friction, horizontal diffusion is still desired for numerical stability. It is for this reason that the higher order diffusion is more commonly used in conjunction with bottom friction.

Paper	Scheme Order	h	Δz	$\mathcal{A}_H$ (m^2s^{-1})	A_4 (m^4s^{-1})	$\mathcal{C}_D$ (s^{-1})	Comments
McWilliams 1981 Equilibrium Geostrophic Turbulence [87]	2nd Finite Diff	38.5 km	3 layer	0	10^{11}	10^{-7}	
McWilliams 1981 [87]	2nd Finite Diff	19.2 km	3 layer	0	10^{10}	10^{-7}	
McWilliams 1981 [87]	2nd Finite Diff	9.6 km	3 layer	0	10^{9}	10^{-7}	
McWilliams 1978 Antarctic Curcumpolar Currents [89]	2nd Finite Diff	19.6 km	3 layer	0	10^{10}	10^{-7}	Uses time varying oscillation in wind stress. Experimented with larger A_4 but no discernible changes in streamfunction patterns. Uses smallest A_4 possible that is consistent with computational stability.
Holland 1978 Wind Driven QG Model [56]	2nd Finite Diff	20 km	2 layer	$0, 100, 330, 2600$	8×10^9	10^{-7}	Smaller $\mathcal{A}_H$ results in more vigorous jet meanders. $\mathcal{A}_H = 0$ when using bottom friction. A_4 used with bottom friction term to replace $\mathcal{A}_H$. Instability completely suppressed for $\mathcal{A}_H = 2600$.

Table 6.2: Channel model literature.

Triharmonic damping is rapid at small scales and drops off rapidly at larger scales. Although, the same effect can be achieved with the derived horizontal momentum diffusion term $\mathcal{A}_H \Delta^2 \psi$ using a smaller value of $\mathcal{A}_H$ and increase in horizontal resolution. These parameters are chosen in the literature to be as small as possible without allowing grid level noise to develop. Holland tests the model with $\mathcal{A}_H \neq 0$, with values ranging from $100\,\mathrm{m^2 s^{-1}}$ to $2600\,\mathrm{m^2 s^{-1}}$ with a 20 km resolution and found that the flow became more non-linear with decreasing $\mathcal{A}_H$. Holland introduces a bottom friction term when replacing the $\mathcal{A}_H$ term with the higher order diffusion. In this section, the $\mathcal{A}_H$ term is retained to avoid imposing greater timestep restrictions on the explicit numerical scheme.

Parameter	Oceanic Value	Atmospheric Value
$\mathcal{K}_V$	$0\,\mathrm{m^2 s^{-1}}$	$0\,\mathrm{m^2 s^{-1}}$
$\mathcal{A}_H$	$1\,\mathrm{m^2 s^{-1}}$	$1\,\mathrm{m^2 s^{-1}}$
$\mathcal{C}_D$	$10^{-7}\,\mathrm{s^{-1}}$	$4 \times 10^{-6}\,\mathrm{s^{-1}}$
β	$1.4 \times 10^{-11}\,\mathrm{m^{-1} s^{-1}}$	$1.6 \times 10^{-11}\,\mathrm{m^{-1} s^{-1}}$
f_0	$1.1 \times 10^{-4}\,\mathrm{s^{-1}}$	$1.1 \times 10^{-4}\,\mathrm{s^{-1}}$
γ	$2 \times 10^{-4}\,^\circ\mathrm{C^{-1}}$	$3.5 \times 10^{-3}\,^\circ\mathrm{C^{-1}}$
N	$0.002\,\mathrm{s^{-1}}$	$0.011\,\mathrm{s^{-1}}$
τ_0	$10^{-4}\,\mathrm{m^2 s^{-2}}$	$0.1\,\mathrm{m^2 s^{-2}}$
L	$10^6\,\mathrm{m}$	$8 \times 10^6\,\mathrm{m}$
L_x	$2 \times 10^6\,\mathrm{m}$	$16 \times 10^6\,\mathrm{m}$
H	$5000\,\mathrm{m}$	$9000\,\mathrm{m}$
H_w	$500\,\mathrm{m}$	$900\,\mathrm{m}$
H_D	$3250\,\mathrm{m}$	$5850\,\mathrm{m}$
U	$1\,\mathrm{m\,s^{-1}}$	$60\,\mathrm{m\,s^{-1}}$

Table 6.3: Parameter values used for channel model.

Experiment	Grid	Resolution	$\mathcal{A}_H$	$\mathcal{C}_D$
1	$64 \times 32 \times 5$	31.25 km	$175\,\mathrm{m^2 s^{-1}}$	$10^{-7}\,\mathrm{s^{-1}}$
2	$64 \times 32 \times 5$	31.25 km	$4\,\mathrm{m^2 s^{-1}}$	$10^{-7}\,\mathrm{s^{-1}}$
3	$64 \times 32 \times 5$	31.25 km	$0.1\,\mathrm{m^2 s^{-1}}$	$10^{-7}\,\mathrm{s^{-1}}$
4	$64 \times 32 \times 5$	31.25 km	$100\,\mathrm{m^2 s^{-1}}$	$0\,\mathrm{s^{-1}}$
5	$128 \times 64 \times 7$	15.625 km	$1\,\mathrm{m^2 s^{-1}}$	$10^{-7}\,\mathrm{s^{-1}}$
6	$256 \times 128 \times 5$	7.8125 km	$1\,\mathrm{m^2 s^{-1}}$	$10^{-7}\,\mathrm{s^{-1}}$
7	$128 \times 64 \times 5$	125 km	$1\,\mathrm{m^2 s^{-1}}$	$4 \times 10^{-6}\,\mathrm{s^{-1}}$

Table 6.4: Horizontal diffusion and bottom friction parameters used in different experiments.

The system is perturbed by an arbitrary arrangement of horizontal sinusoidal waves that are uniform with height,

$$\psi(x, y, z, 0) = \frac{100}{UL} \sin\left(\frac{5\pi y}{L}\right) \left[\sin\left(\frac{5\pi x}{L_x}\right) + \sin\left(\frac{10\pi x}{L_x}\right)\right]. \tag{6.15}$$

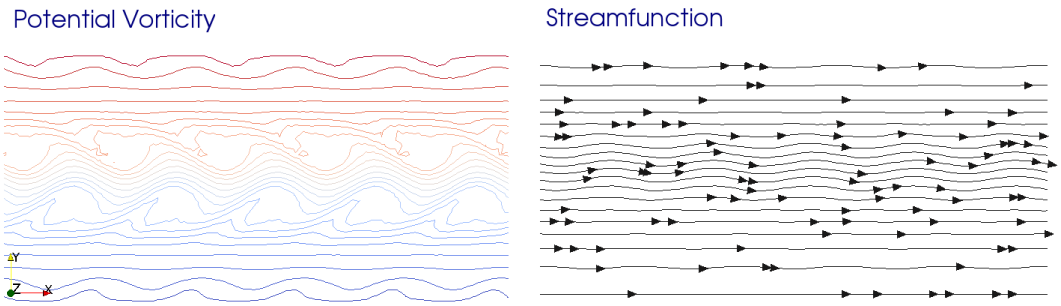

Figure 6.6: Horizontal slices taken at height of 4500 m of channel Experiment 1 at $t = 1800$ days. (Left) Potential vorticity contours closely packed together show the development of a zonal jet in the centre of the domain. (Right) Streamlines with velocity direction indicated by arrows. The oscillations with the jet represent the Rossby wave growth. The dominant, most unstable x-wavelength is 400 km, other perturbation modes have not grown as quickly.

The parameters used for the simulations are listed in Table 6.3 and the different diffusion parameters experimented with are detailed in Table 6.4. Experiments 1-6 use parameters based on those used in [87] and more closely resemble an ocean channel, however, as McWilliams and Chow argues in [87], the flow characteristics are still applicable to the atmosphere. Experiment 7 uses the atmospheric parameters listed in Table 6.3 based on [111]. The first experiment used a relatively low 31.25 km horizontal resolution with a $64 \times 32 \times 5$ grid and $\mathcal{A}_H = 175\,\mathrm{m^2 s^{-1}}$ and since it was found that the vertical diffusion coefficients had little effect on the average dynamics of the channel flow $\mathcal{K}_V = 0\,\mathrm{m^2 s^{-1}}$ was chosen. Experiments 2, 3 and 4 confirm the findings of Holland [56], reducing $\mathcal{A}_H$ results in a more turbulent flow. Experiment 5 used a slightly increased vertical resolution, but did not reveal any further flow dynamics. Experiment 6 uses a finer resolution than in previous literature and produced eddies of various length scales as can be seen in Figures 6.7 and 6.8. The analysis discussed will refer to Experiment 6 unless otherwise specified.

The initial state begins almost at rest with the flow consisting only of the small sinusoidal perturbation (6.15). The wind stress then generates meridional streamfunction, potential vorticity and temperature gradients that propagate down through the flow creating a zonal jet that grows in strength. For the first 1000 days the flow remains strongly linear with no visible perturbations until a growing Rossby wave

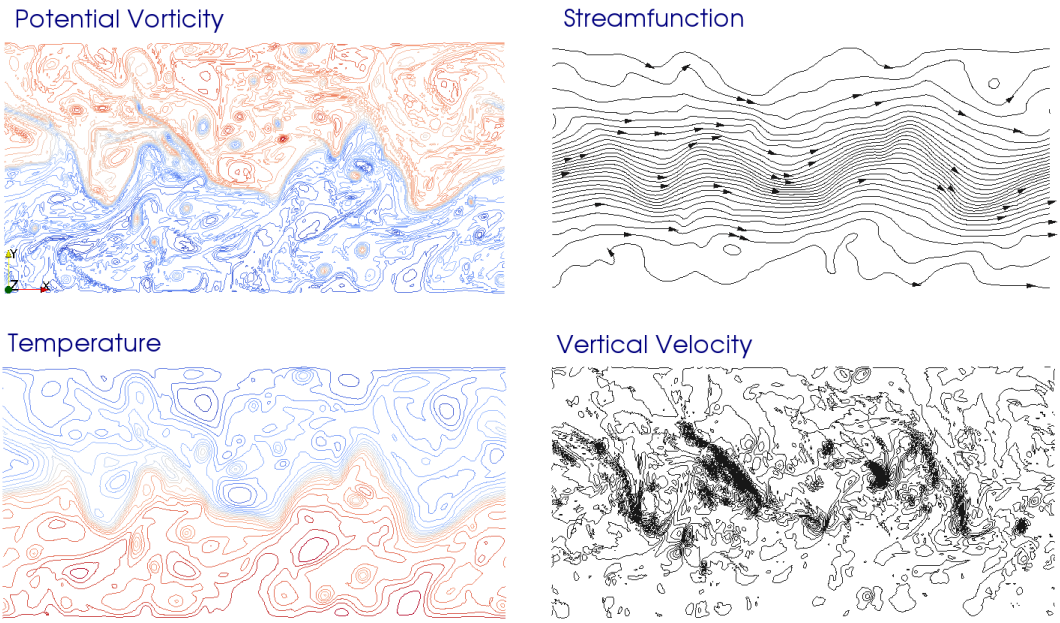

Figure 6.7: Horizontal slices taken at 4500 m of channel Experiment 6 ($\mathcal{A}_H = 1\,\mathrm{m^2 s^{-1}}$) at $t = 2055$ days. Contours are displayed for potential vorticity, streamfunction, temperature and vertical velocity. Arrows on the streamlines indicate flow direction. The flow has developed turbulent behaviour with the jet meandering in an irregular fashion and large eddies are visible.

with wavelength approximately 400 km becomes visible in the centre of the jet, as seen in Figure 6.6 (see Appendix A for more information on Rossby waves and jet streams). These waves steadily grow in amplitude until around day 1700 when the jet becomes baroclinically unstable and develops the turbulent behaviour seen in Figure 6.7. Note that, the turbulent behaviour here is geostrophic where vortices are primarily generated by the break up of the baroclinic jet (see Sections 1.2 and 1.3). The kinetic energy in Figure 6.11 steadily increases during the growth of the perturbation and spikes as the flow transitions to turbulence, the potential energy increases until day 1700 where it rapidly releases energy into eddy generation. Figure 6.8 shows strong temperature gradients along the jet with areas of large vorticity on each side of the temperature gradient with opposing signs, this is indicative of frontal regions.

The long time state of the flow was found to be independent of the initial state, provided there is a large enough perturbation. This was tested using different initial

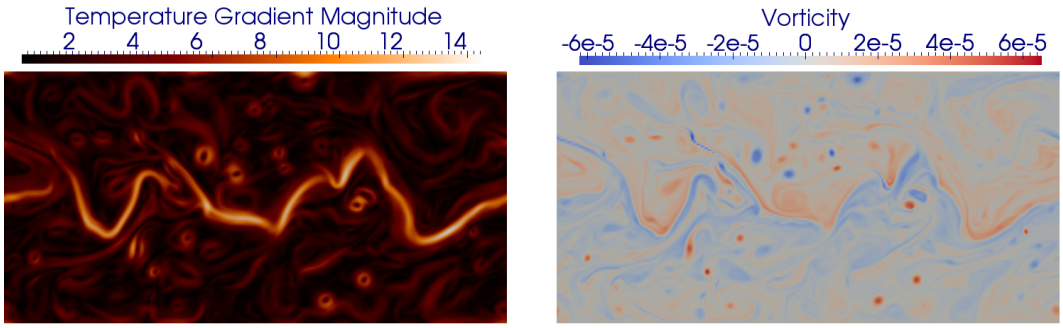

Figure 6.8: Horizontal slices taken at 4500 m of channel Experiment 6 at $t = 2055$ days. Strong temperature gradients ($^{\circ}C(1000\,\mathrm{km})^{-1}$) can be seen along the jet axis with a build up of positive and negative vorticity (s^{-1}) on opposing sides of the temperature gradients. This indicates the formation of frontal regions along the jet.

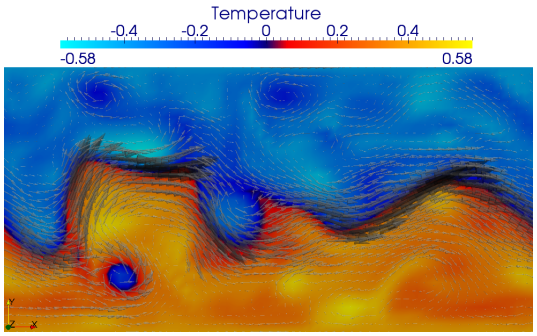

Figure 6.9: Horizontal slice taken at 4500 m of channel Experiment 2 with contrasting temperature scale to exaggerate temperature fluctuations ($^{\circ}C$). Arrows indicate the fluid velocity. The meandering jet displays physically observed features; a low pressure cell forms in the South of the channel as cold fluid is pinched off from the north side of the jet stream.

perturbations in addition to (6.15),

$$\psi(x,y,z,0) = \frac{100}{UL}\sin\left(\frac{5\pi y}{L}\right)\left[\sin\left(\frac{5\pi x}{L_x}\right)+\sin\left(\frac{15\pi x}{L_x}\right)\right], \tag{6.16}$$

$$\psi(x,y,z,0) = \frac{100}{UL}\sin\left(\frac{10\pi y}{L}\right)\left[\sin\left(\frac{10\pi x}{L_x}\right)+\sin\left(\frac{15\pi x}{L_x}\right)\right], \tag{6.17}$$

$$\psi(x,y,z,0) = \frac{100}{UL}\sin\left(\frac{\pi y}{L}\right)\sin\left(\frac{20\pi x}{L_x}\right). \tag{6.18}$$

Whilst the different perturbations grew at varying rates and became baroclinically unstable at different times, all simulations eventually entered the same state of a meandering jet in geostrophic turbulence.

The jet displays some of the physical features of atmospheric jets including the for-

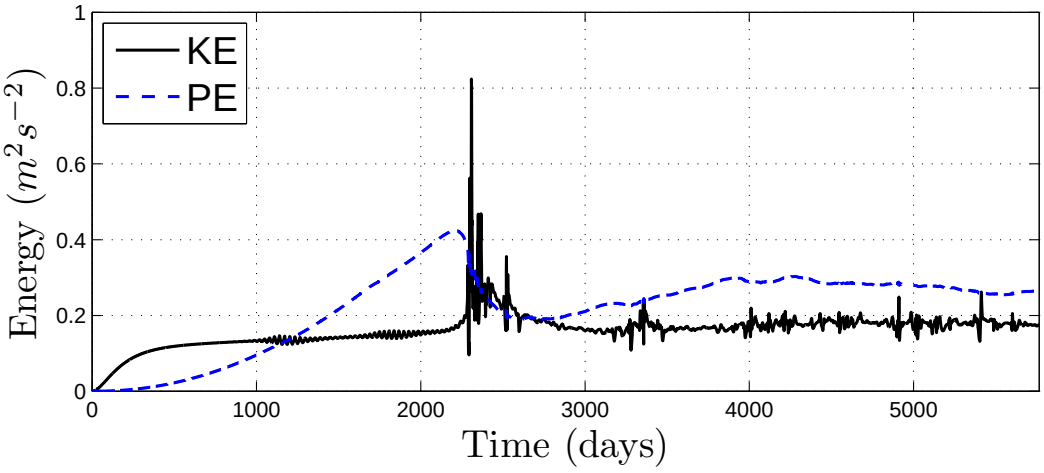

Figure 6.10: Kinetic energy (solid black) and potential energy (dashed blue) per unit mass of Experiment 1 sampled at 1 day intervals. The kinetic and potential energies steadily increase until a surge of potential to kinetic energy occurs as the flow becomes baroclinically unstable. The energies then level out as the flow reaches a statistical equilibrium, with occasional small dips in PE and spikes in KE coincide with periods of strong frontal regions forming in the jet meanders. The coarseness of this experiment ($64 \times 32 \times 5$) allowed for long time integration.

mation of cyclones which become more frequent as $\mathcal{A}_H$ is decreased. Figure 6.9 displays a region of cold air separating from the north side of the jet stream and becoming surrounded by the warmer air in the South. The low pressure cell then generates a cyclone as motions are deflected anti-clockwise around the cell by the Coriolis effect [82].

As detailed in Section 2.3.1, the kinetic energy is calculated as

$$KE = \int_\Omega \frac{1}{2} |\nabla \psi|^2 \, \mathrm{d}\boldsymbol{x}, \tag{6.19}$$

the potential energy as

$$PE = \int_\Omega \frac{1}{2} \frac{f_0^2}{N^2} \left(\frac{\partial \psi}{\partial z} \right)^2 \mathrm{d}\boldsymbol{x}, \tag{6.20}$$

and transfer from potential to kinetic energy as given in equations (2.86) and (2.87)

$$PE \to KE = f_0 \int_\Omega w \frac{\partial \psi}{\partial z}. \tag{6.21}$$

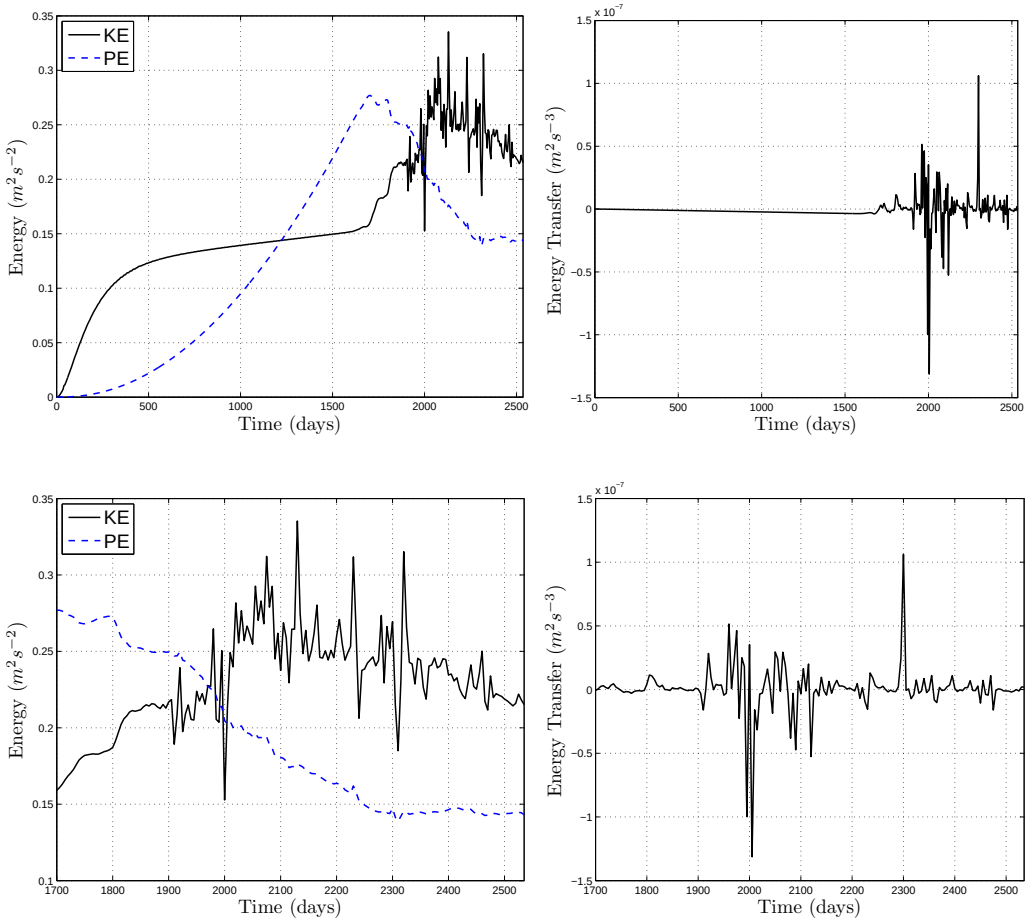

Figure 6.11: (Left) Kinetic energy (solid black) and potential energy (dashed blue) per unit mass of Experiment 6 sampled at 5 day intervals. (Right) Potential energy to kinetic energy transfer rate. Bottom figures are restricted to after the flow transitions to turbulence. Potential and kinetic energy increase with a small but gradually increasing transfer from KE to PE, until around day 1700 when the jet becomes unstable and turbulent where KE spikes and there are large fluctuations in energy transfer.

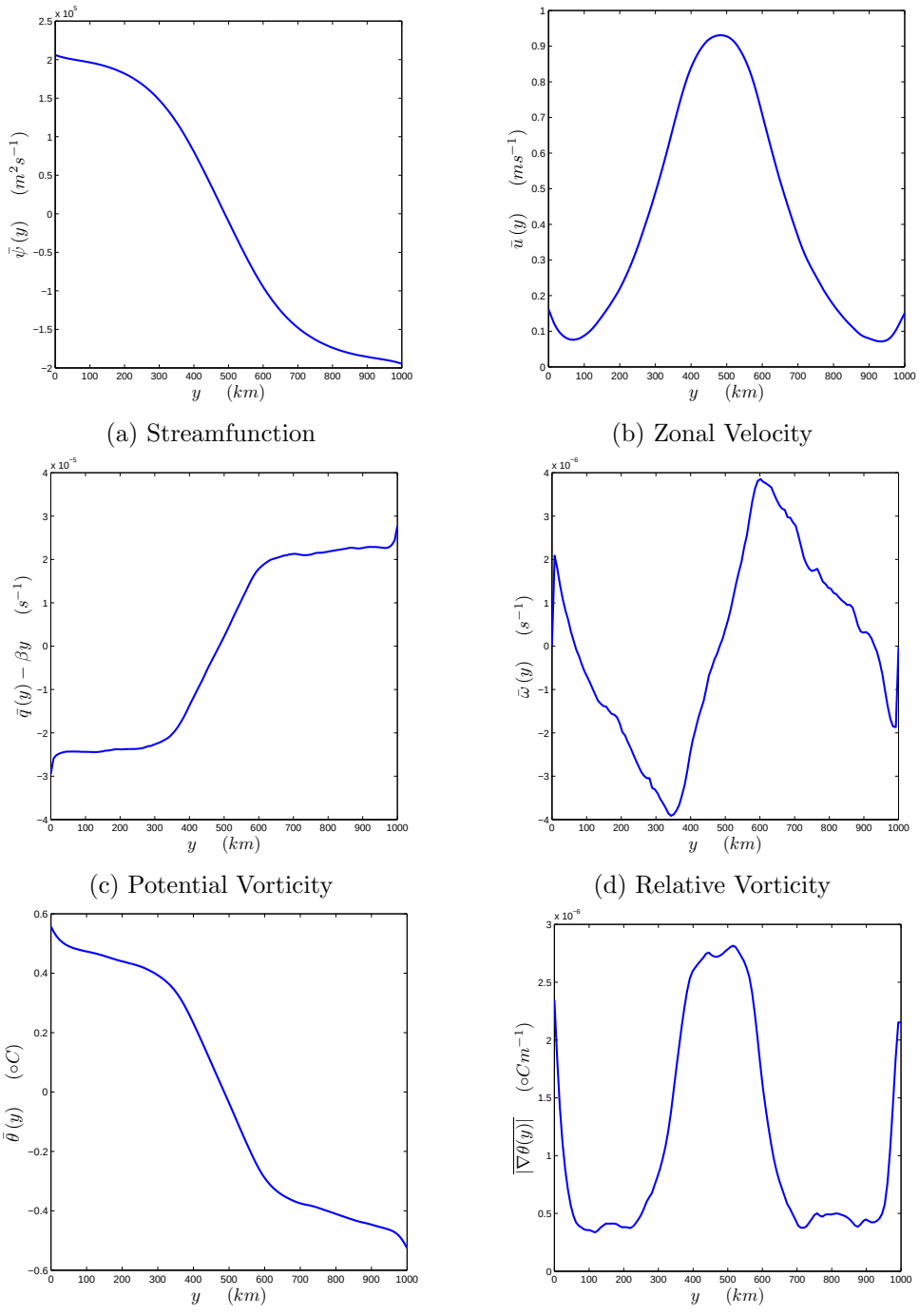

(a) Streamfunction

(b) Zonal Velocity

(c) Potential Vorticity

(d) Relative Vorticity

(e) Temperature

(f) Temperature Gradient

Figure 6.12: Mean fields as a function of the meridional coordinate y taken at $z = 4500\,\mathrm{m}$ for Experiment 6. Average over 405 days taken at 5 day intervals from $t = 1950 - 2355$ days. The zonal velocity peaks in the center of the domain where the jet develops, and there is warm fluid to the south and cool fluid to the north of the jet. Temperature gradients spike around the jet where frontal regions form. There are also spikes at the boundaries caused by the large vortices that break off from the jet and travel along the north and south boundaries of the channel.

The kinetic and potential energy are plotted over time in Figure 6.11. There is an increase in both kinetic and potential energy until the baroclinic instability sets in and there is a transfer from potential to kinetic energy as the flow becomes strongly turbulent. Energy transfers then continue to fluctuate within the turbulent flow. A longer time integration, as done for Experiment 1, reveals the energies then level out to enter a statistical equilibrium state (Figure 6.10) as described in [87], where the flow is still turbulent with a strong meandering zonal jet and the energy injection from the wind stress at the top of the domain is balanced by dissipation.

Figure 6.12 shows various mean fields of the turbulent flow. There is a strong zonal velocity in the centre of the domain where the jet is strongest and sharp vorticity and temperature gradients across the jet.

Figure 6.13 shows the temperature profile across a front at different times as it forms within the jet. The temperature profiles collapse over the 10 days that it was observed. Clearly, the zonal jet is a prominent feature of the flow, characterised by strong fronts that develop and break up as the jet meanders. At times, the jet consists of a continuous front with warm fluid in the South and cooler fluid in the North. At other times, the jet can break up generating large eddies around the resulting cooler/warmer fluid. The meanders in the jet cause frontal regions to bend up against each other. Uplifting and strong vertical stretching are observed in these regions as seen in Figure 6.14.

The one-dimensional energy spectrum can be calculated by taking the Fourier transform of the kinetic energy, for wavevector magnitude $k = |k_x|$, [40]

$$E(k) = \frac{1}{4\pi} \int \langle u_g(x,y,z) \cdot u_g(x+r,y,z) \rangle e^{-ikr}\, dr = \frac{1}{2} \left| \widehat{u_g}(k_x,y,z) \right|^2, \qquad (6.22)$$

where $\langle \cdot \rangle$ denotes an ensemble average and

$$\widehat{u_g}(k_x,y,z) = \frac{1}{2\pi} \int u_g(x,y,z) e^{-ik_x x}\, dx. \qquad (6.23)$$

McWilliams and Chow observed a k^{-3} regime in the time averaged kinetic energy spectra at $y = L/2$, however, higher resolution quasi-geostrophic channel calculations have shown a shallower -2.3 slope at the top of the domain [93, 111].

Figure 6.16 shows time averaged spectra of the zonal and meridional velocities. The

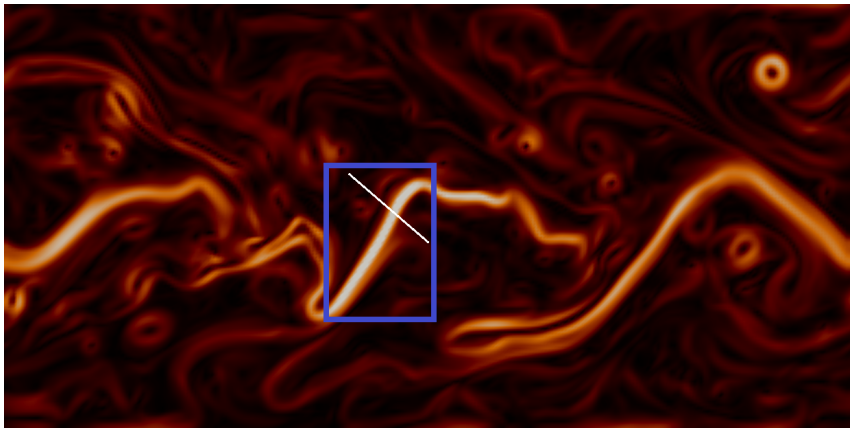

(a)

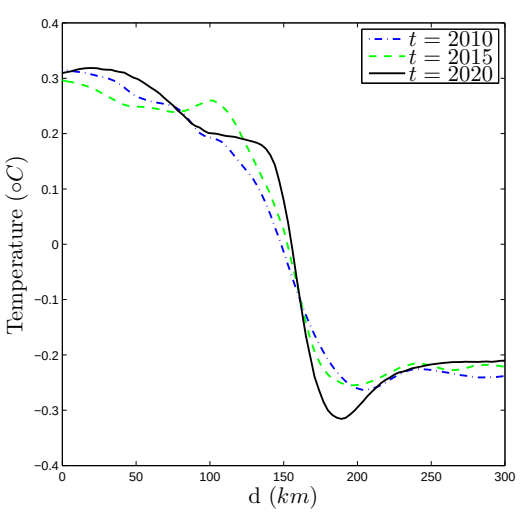

(b)

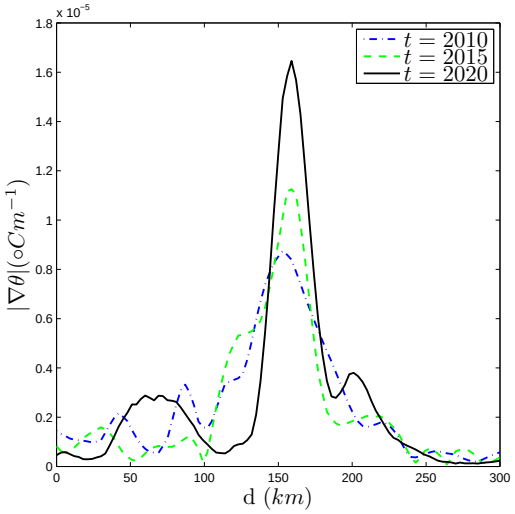

(c)

Figure 6.13: Temperature profiles across a forming front traced over 10 days (highlighted above in the temperature gradient magnitude slice at $t = 2020$ days). The profiles are taken along a 300 km long one-dimensional line perpendicular to the front (white line in (a)). The bottom axis represents the distance d along these cross-front lines which begin on the warm side of the front and end on the cold side. The temperature profiles show that the front is collapsing.

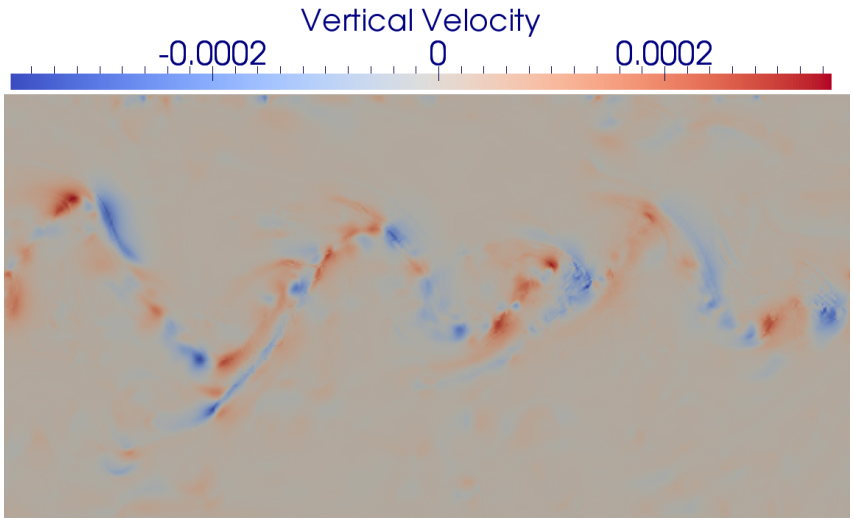

(a) Vertical velocity w (ms^{-1}), shows uplifting around fronts.

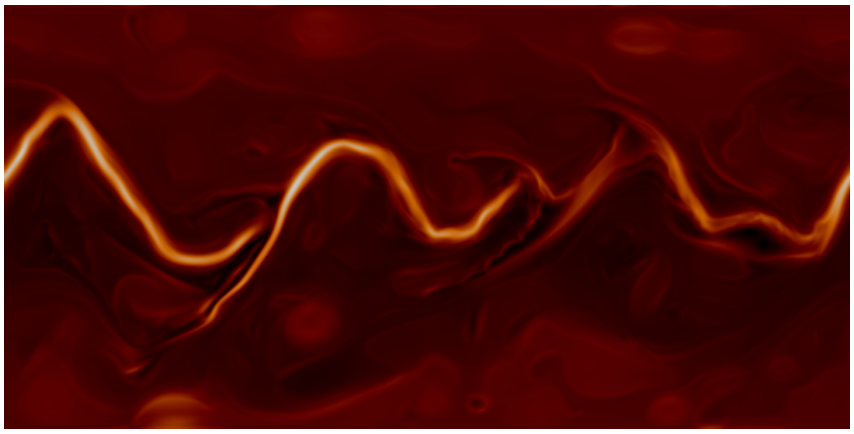

(b) Temperature gradient magnitude.

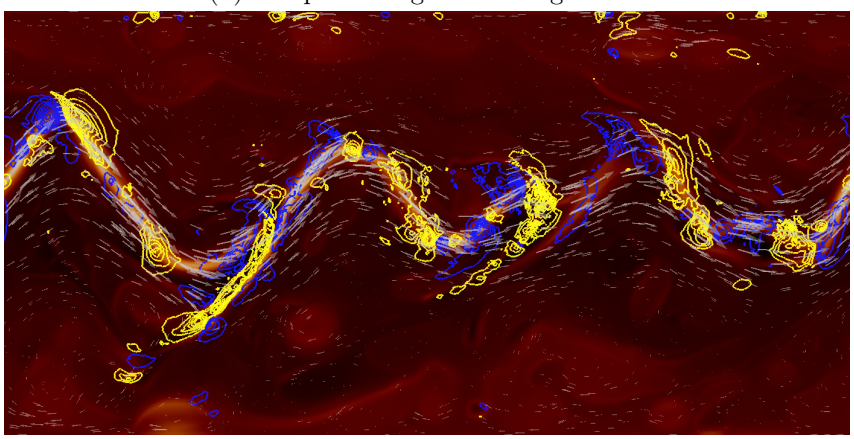

(c) Strong vertical stretching $\partial w/\partial z > 0$ (yellow contours) and subsidence $\partial w/\partial z < 0$ (blue contours) located around jet meanders where frontal regions bend up. Velocity indicated with arrows.

Figure 6.14: Horizontal slices taken at a height of $z = 4500\,\mathrm{m}$ at $t = 2583$ days of Experiment 6 with resolution increased to 512×256.

spectra are taken from one-dimensional zonal lines and averaged over the meridional coordinate and in time over a period of 405 days at 5 day intervals. The compensated spectra indicate a short $k^{-5/3}$ regime at the larger scales. Figures 6.17 and 6.18 show that this short $k^{-5/3}$ regime (or at least something less steep than k^{-3}) at large scales appears to be more prominent away from the central jet axis. In this region, baroclinic instability forms meanders in the jet that can cause the jet to bend up on itself creating closely packed frontal regions with strong vertical stretching as seen in Figure 6.14. This concentration and stretching of sharp interfaces is known to cascade energy to small scales and produce a $k^{-5/3}$ regime in spiral vortex stretching models [81]. Greater computational resources or a more efficient implementation of the numerical scheme, would allow a higher resolution simulation which may reveal a longer $k^{-5/3}$ regime to confirm this.

6.2.1 Atmospheric Channel Model

As shown in Tables 6.3 and 6.4, Experiment 7 was run with atmospheric valued parameters. The flow has very similar characteristic to the oceanic simulations with the instability developing at $t = 150$ days, much quicker than the oceanic simulations. The jet displays large meanders with wavelengths around 4000 km as seen in Figure 6.15.

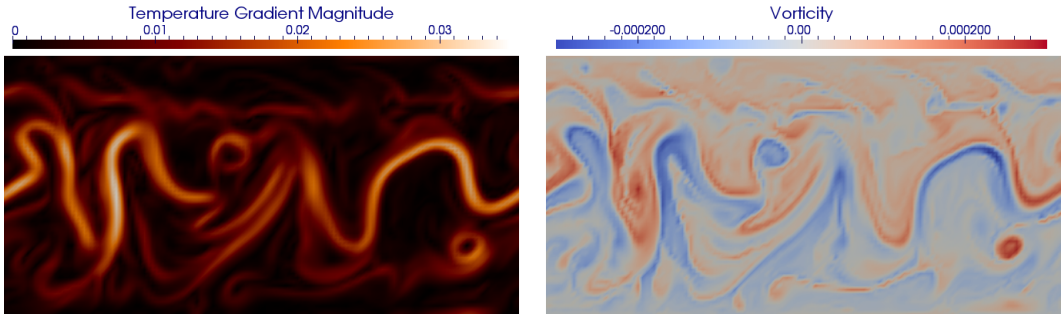

Figure 6.15: Horizontal slices taken at 8100 m of atmospheric channel Experiment 7 at $t = 225$ days. Simulation run on a $128 \times 64 \times 5$ grid. Strong temperature gradients ($^{\circ}C\text{km}^{-1}$) can be seen along the jet axis with a build up of positive and negative vorticity (s^{-1}) on opposing sides of the temperature gradients. Meandering jet has similar characteristics to the ocean jet with large amplitude waves of wavelength around 4000 km.

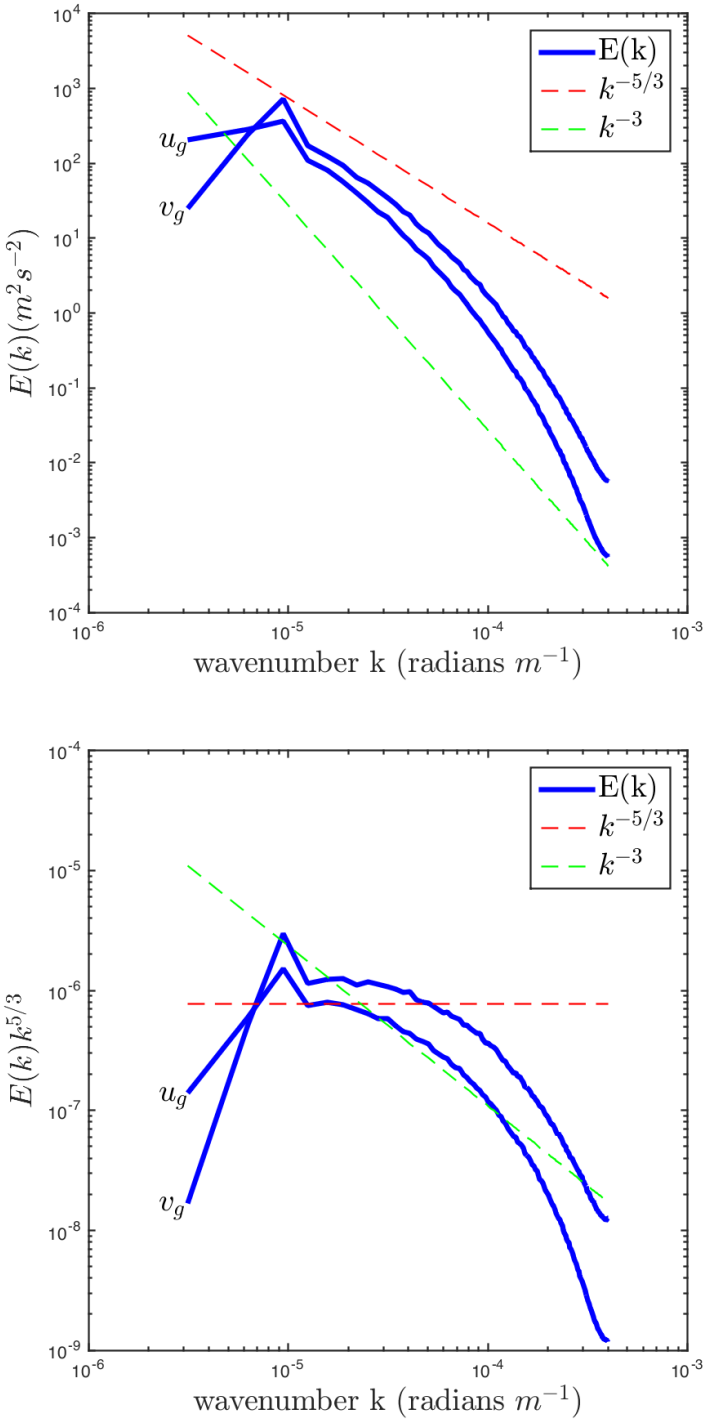

Figure 6.16: **Average channel spectra**. Instantaneous one-dimensional energy spectra of the zonal velocity u_g and meridional velocity v_g averaged over $t = 1950 - 2355$ days of Experiment 6. The spectra were taken in the zonal x direction and averaged over the meridional y coordinate and $z = 4400\,\text{m}$ to $5000\,\text{m}$. (Top) Energy spectra $E(k)$ (Bottom) Compensated energy spectra $E(k)k^{5/3}$. The red and yellow dashed lines are $k^{-5/3}$ and k^{-3} slopes respectively. There are signs of a short $k^{-5/3}$ regime at large scales.

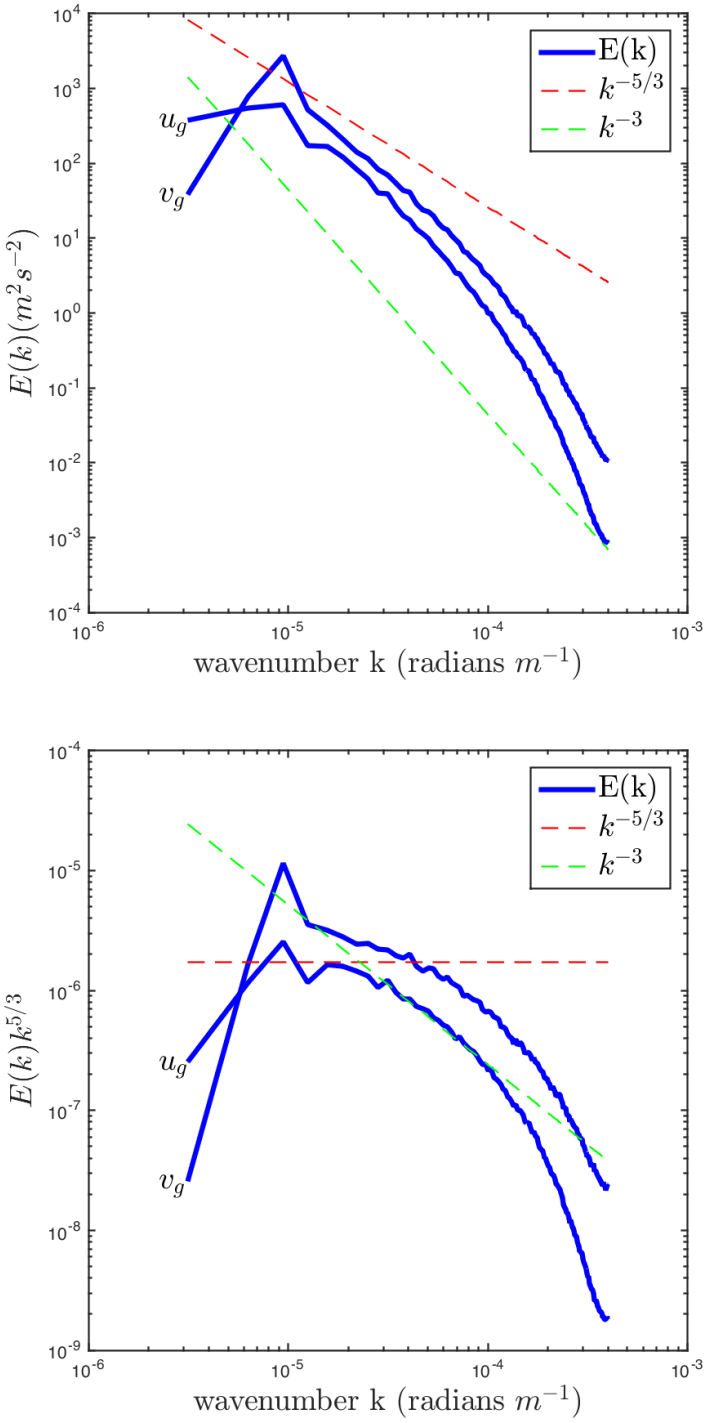

Figure 6.17: **Average jet spectra**. Instantaneous one-dimensional energy spectra of the zonal velocity u_g and meridional velocity v_g averaged over $t = 1950 - 2355$ days of Experiment 6. The spectra were taken in the zonal x direction along the zonal jet at $y = 500\,\text{km}$ and averaged over $z = 4400\,\text{m}$ to $5000\,\text{m}$. (Top) Energy spectra $E(k)$ (Bottom) Compensated energy spectra $E(k)k^{5/3}$. The red and yellow dashed lines are $k^{-5/3}$ and k^{-3} slopes respectively. There are signs of something less steep than k^{-3} at large scales.

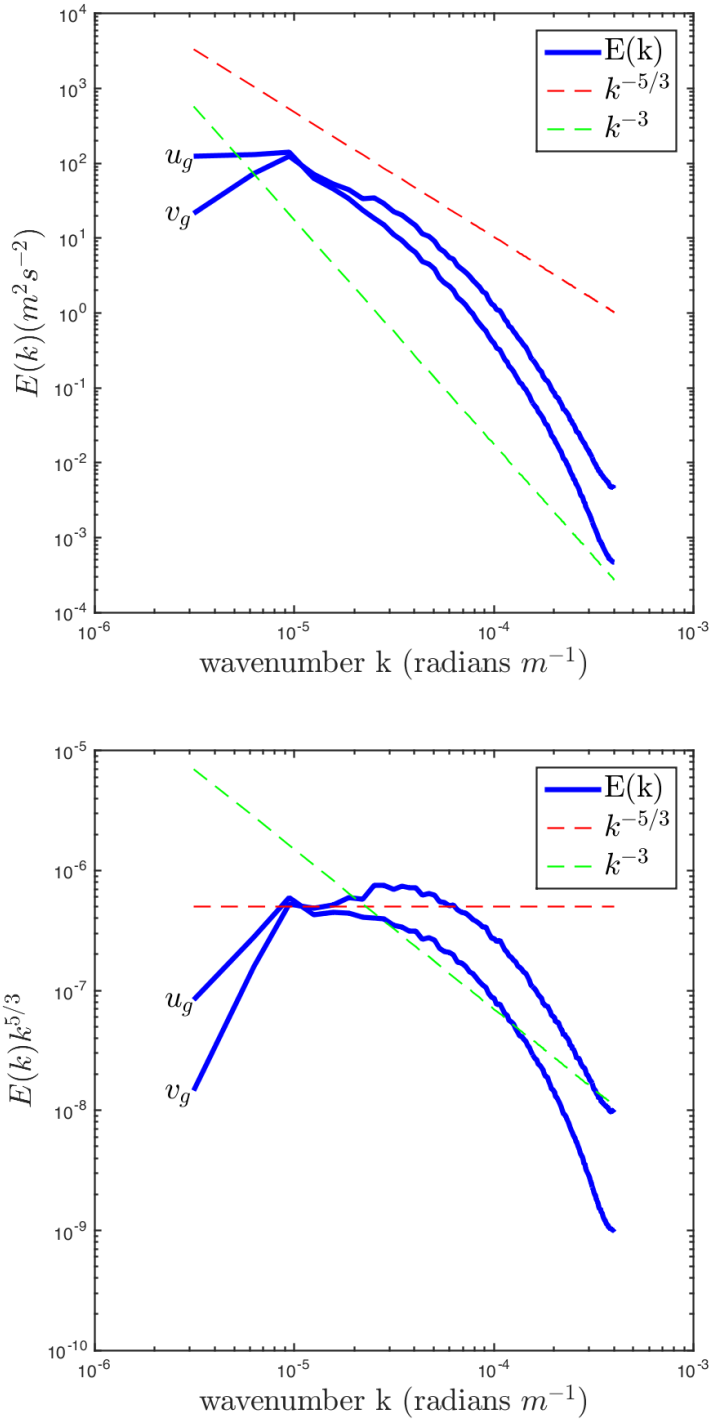

Figure 6.18: **Average outer flow spectra**. Instantaneous one-dimensional energy spectra of the zonal velocity u_g and meridional velocity v_g averaged over $t = 1950 - 2355$ days of Experiment 6. The spectra were taken in the zonal x direction away from the central zonal jet at $y = 750\,\text{km}$ and averaged over $z = 4400\,\text{m}$ to $5000\,\text{m}$. (Top) Energy spectra $E(k)$ (Bottom) Compensated energy spectra $E(k)k^{5/3}$. The red and yellow dashed lines are $k^{-5/3}$ and k^{-3} slopes respectively. There are signs of a short $k^{-5/3}$ regime at large scales.

Chapter 7

Conclusion

There is strong evidence for a ubiquitous $k^{-5/3}$ energy spectrum regime in the atmosphere for mesoscales. Despite the advances in weather forecast modelling and computing, some current models fail to display this energy spectrum [9]. The atmosphere displays strong stratification suggesting that two-dimensional dynamics may play a role in the transfer of energy to small scales. Strongly stratified horizontally homogeneous turbulence is one possible mechanism for generating this $k^{-5/3}$ energy spectrum at small scales. Whilst this mechanism maybe valid high up in the stratosphere, in the troposphere (boundary layer) vertical motions are important. Therefore, this thesis investigates frontogenesis as another other possible mechanism.

A numerical code was developed for the three-dimensional quasi-geostrophic equations using a mixed (dis)continuous Galerkin finite element and finite difference method. The finite element discretisation places the streamfunction in a continuous space allowing the velocity to be single valued in the normal direction along element edges. The potential vorticity was discretised using a discontinuous finite element space and the vertical direction using a fourth order finite difference method allowing for a simplified finite element discretisation in the directions of primary interest. Time advancement was facilitated by a forward Euler method which reduced computational costs for each timestep, however, placed strong restrictions on the timestep size. A third order explicit Runge-Kutta time discretisation may reduce restrictions on the timestep.

The code was tested with a travelling wave solution in two and three-dimensional versions of the code to verify the numerical method and show convergence of the solution with increasing grid resolution. The method displayed expected convergence

results for fixed boundary conditions. Solutions calculated using free-slip boundary conditions did not display optimal convergence of the finite element discretisation, which is likely due the dependence on accurate calculation of the boundary values via the integrals in (2.117). Further testing included a vortex propagating along a boundary with no rotation, making this a test of the Euler equations. The vortex propagated much like a vortex pair of opposite signs, which was also tested to verify correct reproduction of vortex dynamics. The following tests introduced rotation on a vortex. For an anti-clockwise rotating vortex, there was an overall motion towards the Northwest, whilst a clockwise vortex moved towards the Southwest, with Rossby waves appearing in the wakes.

Frontogenesis was observed by imposing a horizontal deformation field upon a north-south temperature gradient. The temperature gradient increased along the axis of contraction with steeper gradients observed near ground level. Frontal dynamics generated an easterly jet near the surface whilst geostrophic winds balancing the north-south temperature gradient developed a westerly jet high in the atmosphere.

A channel model was investigated using a zonal wind stress at the top of the domain blowing eastward with energy dissipated through lateral friction as well as bottom friction. A small sinusoidal perturbation was used to disturb the strong zonal flow which grew until the flow became baroclinically unstable and transitioned into geostrophic turbulence with a strong meandering zonal jet in the centre of the domain. Strong temperature gradients formed along the jet axis accompanied by a build up of positive and negative vorticity on opposing sides of the temperature gradients indicating frontal regions. The energy spectrum of the zonal and meridional velocities show a short $k^{-5/3}$ regime at large scales for the 256×128 grid calculation, suggesting that the numerical model has captured a mechanism responsible for this regime. This regime appeared to be more prominent on the outer regions of the jet where large meanders cause the sharp fronts to bend up against each other and experience vertical stretching. This behaviour is known to produce a $k^{-5/3}$ regime in spiral vortex stretching [81], perhaps a similar mechanism can be generated in the bends of a jet.

7.1 Further Work

Further investigation into vertical stretching of folded fronts, generated in the meanders of a zonal jet with higher resolution simulations is necessary to determine

whether this is a valid mechanism for a downscale energy cascade in the atmosphere.

Extensions to the work presented here could include introduction of a bottom topography simulating mountains and other geographical features. Observing what effects these features have on the dynamics could provide further understanding of what role the shape of the Earth's surface plays in the development of weather formations. Whilst the use of a finite difference approximation in the vertical simplified the horizontal finite element discretisation and allowed for easy control of vertical resolution, the inclusion of topographical features would be more naturally suited to a full three-dimensional finite element method.

The quasi-geostrophic equations provide a simple model of mid-latitude atmospheric motions, however, this means that the relevance of the results is also limited. Implementing a finite element method for the primitive equations or Boussinesq equations to remove the restriction to mid-latitudes and including more ageostrophic motions would allow the observation of more realistic frontal characteristics [129]. This could provide further insight into the transfer of kinetic energy to small scales by observing the energy spectra when these more realistic fronts bend up against each other. Taking this further, one could implement the primitive equations on a sphere to better approximate the effects of the curvature of the Earth and remove the restrictive north-south boundaries. Other processes such as latent heat release and radiation could also be included for a more complete model.

Appendix A

Further Background

The information presented here is taken from standard geophysical fluid dynamics texts [39, 86].

A.1 Rossby Waves

Atmospheric Rossby waves are responsible for the meandering of the jet stream in Earth's atmosphere. Rossby waves emerge due to shear in rotating fluids so that the Coriolis force changes along the sheared coordinate. Barotropic Rossby waves can be derived from the non-dimensionalised two-dimensional QGE

$$\partial_t q + J(\psi, q) = 0 \tag{A.1}$$

$$q = \Delta\psi - Bu^{-1}\psi + \beta y, \tag{A.2}$$

which can be linearised as

$$\frac{\partial \Delta\psi}{\partial t} - Bu^{-1}\frac{\partial \psi}{\partial t} + \beta\frac{\partial \psi}{\partial x} = 0. \tag{A.3}$$

To find the dispersion relation put $\psi = \hat{\psi}e^{i(k_x x + k_y y - \omega_d t)}$ into the linearised equation to get

$$\omega_d = -\frac{\beta k_x}{k_x^2 + k_y^2 + Bu^{-1}}. \tag{A.4}$$

The phase speed with $k = |\boldsymbol{k}|$ is then,

$$c_{ph} = \frac{\omega_d}{k^2}\boldsymbol{k} = -\beta\left(\frac{k_x^2}{k(k + Bu^{-1})}, \frac{k_x k_y}{k(k + Bu^{-1})}\right), \tag{A.5}$$

notice that the x-component is negative, therefore, waves propagate only to the

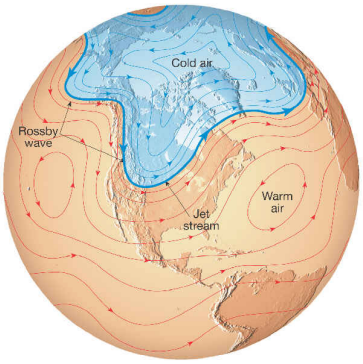

Figure A.1: Jet stream in the Northern Hemisphere. Cold air filled troughs can pinch off and form low pressure cyclones. The jet stream transports weather systems around. [Figure in [82], © 2013. Reprinted by permission of Pearson Education, Inc., New York, New York.]

west. The group speed is

$$c_g = (\partial_k, \partial_l)\omega_d = \beta \left(\frac{k_x^2 - k_y^2 - Bu^{-1}}{(k^2 + Bu^{-1})^2}, \frac{2k_x k_y}{(k^2 + Bu^{-1})^2} \right). \tag{A.6}$$

This group speed may be in either direction, consider long waves with the x-direction wavelength λ_x larger than the y-direction wavelength λ_y, ie. $1/k_x > 1/k_y$ or $k_y > k_x$. Then, the x-component of the group velocity $c_{g,x} < 0$, so long waves move west. However, for short waves with $\lambda_y > \lambda_x$ or $k_y < k_x$ then $c_{g,x} > 0$ and so short waves move east. The jet stream blows east and carries weather fronts with it.

Baroclinic Rossby waves can be derived from the non-dimensional three-dimensional QGE and have dispersion relation [39]

$$\omega = -\frac{\beta k_x}{k_x^2 + k_y^2 + k_z^2 Bu^{-1}/N^2}, \tag{A.7}$$

hence the phase speed is

$$c_{ph} = -\frac{\beta}{k^2(k_x^2 + k_y^2 + k_z^2 Bu^{-1}/N^2)}(k_x^2, k_x k_y) \tag{A.8}$$

indicating westward propagation.

A.2 Two-Layer QGE and Baroclinic Instability

Baroclinic instabilities are caused by the presence of a horizontal temperature gradient in a rapidly rotating, strongly stratified fluid like the atmosphere. This instability can be studied using a two-layer quasi-geostrophic model with layer thicknesses $H_1 = H_2 = H/2$ and density ρ_1 and ρ_2 as in Figure A.2 [39, 86],

$$\frac{\partial q_1}{\partial t} + J(\psi_1, q_1) = 0, \tag{A.9}$$

$$\frac{\partial q_2}{\partial t} + J(\psi_2, q_2) = 0, \tag{A.10}$$

where for reduced gravity $g' = g(\rho_2 - \rho_1)/\rho_0$, the potential vorticities in the layers are

$$q_1 = \Delta\psi_1 + \beta y - \frac{f_0^2}{g' H_1}(\psi_1 - \psi_2), \tag{A.11}$$

$$q_2 = \Delta\psi_2 + \beta y + \frac{f_0^2}{g' H_2}(\psi_1 - \psi_2). \tag{A.12}$$

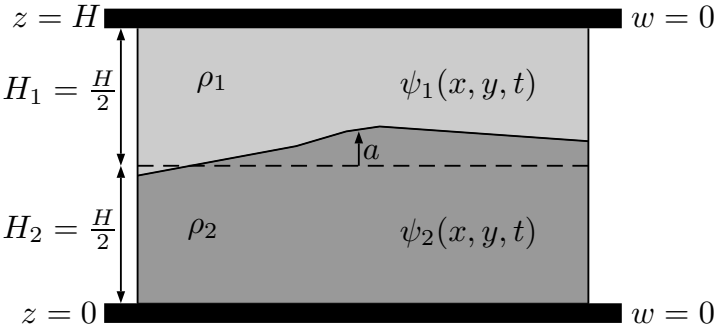

Figure A.2: Representation of the vertical stratification by two layers of uniform density in a quasi-geostrophic model. The vertical displacement $a = (f_0/g')(\psi_2 - \psi_1)$.

Note that, the last terms in potential vorticity equations are equivalent to a finite difference approximation of the term $\frac{\partial}{\partial z}\left(\frac{f_0^2}{N^2}\frac{\partial \psi}{\partial z}\right)$ in the full three-dimensional quasi-geostrophic equations. Linearising these equations with an average flow $\overline{\psi}_1 = -Uy$ and $\overline{\psi}_2 = Uy$ gives

$$\frac{\partial q_1'}{\partial t} + U\frac{\partial q_1'}{\partial x} + v_1'\left[\beta + \frac{U}{R^2}\right] = 0, \tag{A.13}$$

$$\frac{\partial q_2'}{\partial t} - U\frac{\partial q_2'}{\partial x} + v_2'\left[\beta - \frac{U}{R^2}\right] = 0 \tag{A.14}$$

where $R = \sqrt{g'H}/2f_0$ is the baroclinic radius of deformation and

$$q_1' = \Delta\psi_1' - \frac{f_0^2}{g'H_1}(\psi_1' - \psi_2'), \tag{A.15}$$

$$q_2' = \Delta\psi_2' + \frac{f_0^2}{g'H_2}(\psi_1' - \psi_2'). \tag{A.16}$$

Now, assume the fluctuating component to be a wave solution of the form $\psi_j' = \hat{\psi}_j \exp\left(i(k_x x + k_y y - \omega t)\right)$ for layers $j = 1, 2$. Using this in the above equations gives

$$(\omega - k_x U)\left[k^2\hat{\psi}_1 + \frac{1}{2R^2}(\hat{\psi}_1 - \hat{\psi}_2)\right] + k_x\left[\beta + \frac{U}{R^2}\right]\hat{\psi}_1 = 0, \tag{A.17}$$

$$(\omega + k_x U)\left[k^2\hat{\psi}_2 - \frac{1}{2R^2}(\hat{\psi}_1 - \hat{\psi}_2)\right] + k_x\left[\beta - \frac{U}{R^2}\right]\hat{\psi}_2 = 0. \tag{A.18}$$

Using $C_x = \omega/k_x$ and defining the barotropic and baroclinic components of the Fourier coefficients,

$$\hat{\psi}_{\text{tr}} = \frac{1}{2}(\hat{\psi}_1 + \hat{\psi}_2) \text{ and } \hat{\psi}_{\text{cl}} = \frac{1}{2}(\hat{\psi}_1 - \hat{\psi}_2), \tag{A.19}$$

the equations now become

$$[C_x k^2 + \beta]\hat{\psi}_{\text{tr}} - Uk^2\hat{\psi}_{\text{cl}} = 0 \tag{A.20}$$

$$-U(k^2 - R^{-2})\hat{\psi}_{\text{tr}} + [C_x(k^2 + R^{-2}) + \beta]\hat{\psi}_{\text{cl}} = 0. \tag{A.21}$$

A pure barotropic wave occurs when $U = 0$ and $\hat{\psi}_{\text{cl}} = 0$ then $C_x = -\beta/k^2$, which is the same wavespeed derived for planetary Rossby waves using the Charney equation.

A pure baroclinic wave occurs when $U = 0$ and $\hat{\psi}_{\text{tr}} = 0$ then $C_x = -\beta/(k^2 + R^{-2})$, which is the same wavespeed derived for planetary Rossby waves using the single-layer two-dimensional quasi-geostrophic equations.

When $U \neq 0$, the barotropic and baroclinic components are coupled. Note that, (A.20) and (A.21) form a system of line equations in $\hat{\psi}_{\text{tr}}$ and $\hat{\psi}_{\text{cl}}$ and can be written in matrix form

$$\underbrace{\begin{bmatrix} [C_x k^2 + \beta] & -Uk^2 \\ -U(k^2 - R^{-2}) & [C_x(k^2 + R^{-2}) + \beta] \end{bmatrix}}_{A} \begin{bmatrix} \hat{\psi}_{\text{tr}} \\ \hat{\psi}_{\text{cl}} \end{bmatrix} = \begin{bmatrix} 0 \\ 0 \end{bmatrix}. \tag{A.22}$$

If the matrix A is invertible then the solutions are trivial, $\hat{\psi}_{\text{tr}} = 0$ and $\hat{\psi}_{\text{cl}} = 0$. Therefore, the non-trivial solutions are when the matrix A is not invertible and so the determinant $|A| = 0$. That is

$$[C_x k^2 + \beta][C_x(k^2 + R^{-2}) + \beta] - U^2 k^2 (k^2 - R^{-2}) = 0. \tag{A.23}$$

To get the wavespeed C_x, calculate the discriminant $\mathcal{P}$ of the quadratic equation (A.23) for C_x. Doing this gives

$$C_x = -\frac{\beta(2k^2 + R^{-2}) \pm \sqrt{\mathcal{P}}}{2k^2(k^2 + R^{-2})} \tag{A.24}$$

where

$$\mathcal{P} = \beta^2 R^{-4} + 4U^2 k^4 (k^{-4} - R^{-4}). \tag{A.25}$$

The solution is stable when $\mathcal{P} > 0$. Otherwise, $\mathcal{P} < 0$ and the wavespeed has an imaginary, growing component, ie unstable. It can be shown that the wave is stable for

$$U \leq \beta R^2. \tag{A.26}$$

Recall that the layers had average flows of speed U in opposite directions, therefore, the greater the vertical shear, the more likely that it will breach the threshold of instability.

A.3 Jet Stream

The motion of vortices in the jet stream develop planetary Rossby waves which can be explained in terms of baroclinic instability [113]. Figures A.3 and A.4 show how a vertical vortex column can be subjected to baroclinic instability, causing it to oscillate in the north-south direction.

The atmosphere is thinner near the poles since the air is cooler and heavier, so the thickness $H = h_0 - h'y$ decreases towards the poles. This can also be represented by two fluid layers using a sloping density surface as shown in Figure A.4 with the stratosphere acting like a rigid lid to the troposphere since it is so strongly stratified and stable. The Coriolis parameter $f = f_0 + \beta y$ increases towards the poles. Given that the relative vorticity $\omega = 0$ at point 1, it is required that the potential vorticity

$$q = \frac{f + \omega}{H} = \frac{f}{H} \tag{A.27}$$

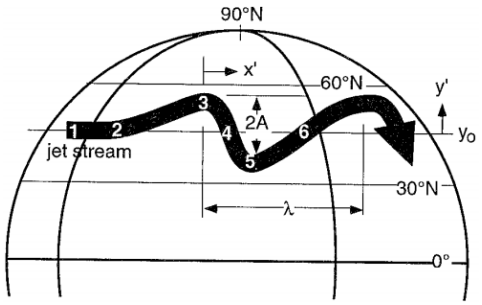

Figure A.3: Initially zonal flow at point 1, if disturbed at point 2, will develop north-south meanders called Rossby waves. Figure in [113].

be conserved. Suppose at point 2 the flow is perturbed towards the north, the air is now moving to greater latitudes where f increases and H decreases. Therefore, to conserve potential vorticity q, the relative vorticity ω must decrease to the point of becoming negative at point 3 and turning anti-cyclonic (clockwise), causing the jet to point southeast.

Now moving south, the jet experiences a decrease in f and an increase in H, therefore, to conserve q the vorticity ω increases. At point 4 the vorticity has increased so much that it is now positive and the jet turns cyclonic (anti-clockwise) heading back northeast. The initially stable jet at point 1 has become unstable. One can see this Rossby wave requires variation of the Coriolis parameter f and thickness H (due to stratification) with latitude to create the baroclinic instability.

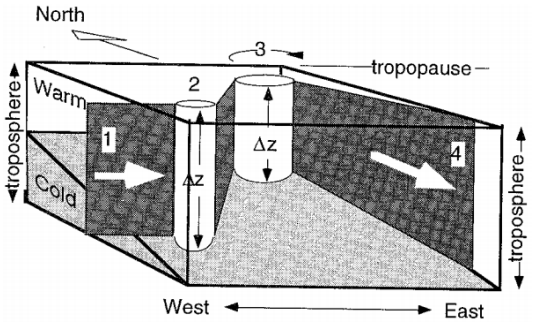

Figure A.4: Dark grey ribbon represents jet stream axis, white columns indicate absolute vorticity. Figure in [113].

Appendix B

Alternative Methods

The following includes several alternative approaches to discretising the QGE that were considered or proved unsuccessful.

B.1 Vertical Spectral Discretisation

A spectral discretisation for the vertical direction was considered. The basic idea behind a spectral approximation is to decompose the solution into a combination of sinusoidal functions. The difference between spectral methods and finite differences is that a finite difference is a local approximation only taking into account neighbouring points, whereas spectral methods are global approximations using the whole domain. The advantage of spectral methods is the exponential accuracy achieved and the simplicity with which derivatives are calculated. For zero Dirichlet boundary conditions, use a sine basis,

$$q(x,y,z,t) = \sum_{k_z=-K}^{K} \widehat{q}_k \sin(k_z z), \qquad \psi(x,y,z,t) = \sum_{k_z} \widehat{\psi}_k \sin(k_z z),$$
$$\boldsymbol{u}(x,y,z,t) = \sum_{k} \widehat{\boldsymbol{u}}_k \sin(k_z z) \tag{B.1}$$

where the Fourier coefficients are calculated using the Discrete Sine Transforms

$$\widehat{q}(x,y,k,t) = \frac{1}{\mathcal{N}} \sum_{n=0}^{\mathcal{N}} q_n \sin(k_z z), \qquad \widehat{\psi}(x,y,k,t) = \frac{1}{\mathcal{N}} \sum_{n=0}^{\mathcal{N}} \psi_n \sin(k_z z),$$
$$\widehat{\boldsymbol{u}}(x,y,k,t) = \frac{1}{\mathcal{N}} \sum_{n=0}^{\mathcal{N}} \boldsymbol{u}_n \sin(kz). \tag{B.2}$$

Then derivatives can be easily calculated as

$$\frac{\partial^2 \psi_j}{\partial z^2} = \widehat{\frac{\partial^2 \psi_j}{\partial z^2}} = -\widehat{k_z^2 \psi_j} = \sum_r \left[\frac{1}{\mathcal{N}} \sum_{k_z} -k_z^2 \sin(k_z z_j) \sin(-k_z z_r) \right] \psi_r. \tag{B.3}$$

The disadvantage of this method, however, is that this results in a dense matrix problem as well as limitation on the boundary conditions. Therefore, a finite difference approach was better suited for the purpose of this thesis.

B.2 Discontinuous Galerkin Streamfunction Spatial Discretisation

Presented here is an alternative discretisation method that uses a discontinuous Galerkin finite element method to solve for the streamfunction ψ and calculate the potential vorticity by recovering the divergence properties of the velocity field using a Raviart-Thomas projection [47]. The results produced unstable solutions and therefore this method was not used to produce the results presented in this thesis. However, the method is discussed as it demonstrates the difficulties that arise from a discontinuous velocity field. The equations are the non-dimensionalised quasi-geostrophic equations,

$$\frac{\partial q}{\partial t} + J(\psi, q) = A_V \frac{\partial^2 \Delta \psi}{\partial z^2} \tag{B.4}$$

where the potential vorticity is

$$q = \Delta \psi + Bu^{-1} \frac{\partial}{\partial z} \left(\frac{1}{N^2} \frac{\partial \psi}{\partial z} \right) + \beta y. \tag{B.5}$$

The only diffusion term included here is the vertical momentum diffusion to demonstrate how the finite element and finite difference methods are combined. The use of finite difference methods in the vertical simplifies the finite element discretisation in the horizontal. For simplicity, also fix the boundary conditions to $\psi = 0$ on horizontal boundaries and $\partial\psi/\partial z = 0$ on vertical boundaries. Approximate all z derivatives with a finite difference approximation, with the vertical direction being discretised into $\mathcal{N} + 1$ sheets. Then $\psi_j : \Omega_j \to \mathbb{R}$ with $j \in \{0, ..., \mathcal{N}\}$ denotes the function $\psi|_{\Omega_j} = \psi(x, y, j\Delta z)$ on the j^{th} vertical level, that is with $z = j\Delta z$. The term on the right hand side of (B.4) will be approximated with such a finite difference, for

example, a second order approximation is given by

$$\frac{\partial^2 \psi}{\partial z^2} \approx \frac{\psi_{j+1} - 2\psi_j + \psi_{j-1}}{\Delta z^2}. \tag{B.6}$$

The second term in the potential vorticity equation (B.5) will also be approximated with finite differences, for example,

$$Bu^{-1} \frac{\partial}{\partial z}\left(\frac{1}{N^2}\right)\frac{\partial \psi}{\partial z} + \frac{Bu^{-1}}{N^2}\frac{\partial^2 \psi}{\partial z^2} \approx L_z(\psi) := \tag{B.7}$$
$$\frac{Bu^{-1}}{2\Delta z}\left[\left(\frac{1}{N^2}\right)_{j+1} - \left(\frac{1}{N^2}\right)_{j-1}\right]\left(\frac{\psi_{j+1} - \psi_{j-1}}{2\Delta z}\right) + \left(\frac{Bu^{-1}}{N^2}\right)_j \frac{\psi_{j+1} - 2\psi_j + \psi_{j-1}}{\Delta z^2}.$$

To simplify notation let us define the following,

$$\kappa := A_V \frac{\tau}{\Delta z^2}, \tag{B.8}$$

$$\lambda_j := \frac{Bu^{-1}}{4\Delta z^2}\left[\left(\frac{1}{N^2}\right)_{j+1} - \left(\frac{1}{N^2}\right)_{j-1}\right], \tag{B.9}$$

$$\mu_j := \left(\frac{1}{N^2}\right)_j \frac{Bu^{-1}}{\Delta z^2}. \tag{B.10}$$

Combining the finite difference approximations with a theta-method in time with timestep τ, equation (B.4) becomes

$$\begin{aligned} &q_j^{n+1} - \theta_m \kappa(\Delta\psi_{j+1}^{n+1} - 2\Delta\psi_j^{n+1} + \Delta\psi_{j-1}^{n+1}) \\ &= q_j^n - \tau J(\psi_j^n, q_j^n) + (1-\theta_m)\kappa(\Delta\psi_{j+1}^n - 2\Delta\psi_j^n + \Delta\psi_{j-1}^n). \end{aligned} \tag{B.11}$$

with equation (B.5) yielding

$$q_j^{n+1} = \Delta\psi_j^{n+1} + \lambda_j\left(\psi_{j+1}^{n+1} - \psi_{j-1}^{n+1}\right) + \mu_j\left(\psi_{j+1}^{n+1} - 2\psi_j^{n+1} + \psi_{j-1}^{n+1}\right) + \beta y. \tag{B.12}$$

Define the elliptic operator

$$\begin{aligned} L\left(\psi_j^{n+1}\right) :=& \Delta\psi_j^{n+1} + \lambda_j\left(\psi_{j+1}^{n+1} - \psi_{j-1}^{n+1}\right) + \mu_j\left(\psi_{j+1}^{n+1} - 2\psi_j^{n+1} + \psi_{j-1}^{n+1}\right) + \beta y \\ &- \theta_m \kappa\left(\Delta\psi_{j+1}^{n+1} - 2\Delta\psi_j^{n+1} + \Delta\psi_{j-1}^{n+1}\right) \end{aligned} \tag{B.13}$$

Then

$$L\left(\psi_j^{n+1}\right) = \underbrace{q_j^n - \tau J(\psi_j^n, q_j^n) + (1-\theta_m)\kappa(\Delta\psi_{j+1}^n - 2\Delta\psi_j^n + \Delta\psi_{j-1}^n)}_{F_j^n}. \tag{B.14}$$

Writing in matrix form,

$$\begin{bmatrix} L_0^0 & L_1^+ & 0 & 0 & \cdots & 0 \\ L_0^- & L_1^0 & L_2^+ & 0 & \cdots & 0 \\ 0 & \ddots & \ddots & \ddots & \vdots & \vdots \\ \vdots & \cdots & 0 & L_{\mathcal{N}-2}^- & L_{\mathcal{N}-1}^0 & L_{\mathcal{N}}^+ \\ 0 & \cdots & 0 & 0 & L_{\mathcal{N}-1}^- & L_{\mathcal{N}}^0 \end{bmatrix} \begin{bmatrix} \psi_0^{n+1} \\ \psi_1^{n+1} \\ \vdots \\ \psi_{\mathcal{N}-1}^{n+1} \\ \psi_{\mathcal{N}}^{n+1} \end{bmatrix} = \begin{bmatrix} F_0^{n+1} \\ F_1^{n+1} \\ \vdots \\ F_{\mathcal{N}-1}^{n+1} \\ F_{\mathcal{N}}^{n+1} \end{bmatrix} \tag{B.15}$$

where the linear operators

$$L_j^+ = \mu_j + \lambda_j - \theta_m \kappa \Delta \tag{B.16}$$

$$L_j^0 = -2\mu_j + (1 + 2\theta_m \kappa)\Delta \tag{B.17}$$

$$L_j^- = \mu_j - \lambda_j - \theta_m \kappa \Delta. \tag{B.18}$$

Now, apply a finite element scheme to each layer. Consider a tessellation $\mathcal{T}_h$ on a horizontal domain Ω, and assume that the tessellation is identical on each layer. Considering (B.14), multiply by a test function ϕ in the discontinuous Galerkin (DG) space $V_{q_h} \subset V_q$ to get

$$\begin{aligned} &\sum_{T\in\mathcal{T}_h} \int_T \Delta\psi_j^{n+1}\phi + \sum_{T\in\mathcal{T}_h} \int_T \lambda_j \left(\psi_{j+1}^{n+1} - \psi_{j-1}^{n+1}\right)\phi + \sum_{T\in\mathcal{T}_h} \int_T \mu_j \left(\psi_{j+1}^{n+1} - 2\psi_j^{n+1} + \psi_{j-1}^{n+1}\right)\phi \\ &- \sum_{T\in\mathcal{T}_h} \int_T \theta_m\kappa \left(\Delta\psi_{j+1}^{n+1} - 2\Delta\psi_j^{n+1} + \Delta\psi_{j-1}^{n+1}\right)\phi + \sum_{T\in\mathcal{T}_h} \int_T \beta y\phi = + \sum_{T\in\mathcal{T}_h} \int_T F_j^n \phi. \end{aligned} \tag{B.19}$$

Apply the DG version of integration by parts (Theorem (3.10)) on the Laplacian terms,

$$\begin{aligned} \sum_{T\in\mathcal{T}_h} \int_T \Delta\psi_j^{n+1}\phi = &- \sum_{T\in\mathcal{T}_h} \int_T \nabla\psi_j^{n+1}\cdot\nabla\phi + \sum_{e\in\mathcal{I}_h} \int_e \{\nabla\psi_j^{n+1}\}\cdot[\phi] + \cancelto{0}{\sum_{e\in\mathcal{I}_h} \int_e [\nabla\psi_j^{n+1}]\{\phi\}} \\ &+ \sum_{e\in\mathcal{I}_h^\partial} \int_e \nabla\psi_j^{n+1}\cdot\boldsymbol{n}_e^+\phi, \end{aligned} \tag{B.20}$$

where the third term is dropped due to the fact that the true solution ψ is continuous so $[\nabla\psi] = 0$. One can add in a penalty term [105]

$$P^{\sigma,\alpha}(\psi,\phi) = \sum_{e\in\mathcal{I}_h\cup\mathcal{I}_h^\partial} \beta_e \int_e [\psi][\phi], \tag{B.21}$$

and a symmetry term

$$S^{\epsilon}(\psi,\phi) = \epsilon \sum_{e\in\mathcal{I}_h\cup\mathcal{I}_h^{\partial}} \int_e \{\nabla\phi\}[\psi], \tag{B.22}$$

without effecting consistency since $[\psi] = 0$. Here, β_e is a penalty parameter and ϵ is a symmetry parameter. The method is symmetric if $\epsilon = -1$. Now, turning attention to the Jacobian term, notice that

$$J(\psi,q) = \boldsymbol{u_g}\cdot\nabla q = \nabla\cdot(\boldsymbol{u_g}q), \tag{B.23}$$

due to incompressibility. Multiplying by a test function $\phi \in V_{q_h}$, integrating over an element T, summing over all elements and applying integration by parts,

$$\begin{aligned}
\sum_{T\in\mathcal{T}_h}\int_T \nabla\cdot(\boldsymbol{u_g}q)\phi &= \sum_{e\in\mathcal{I}_h\cup\mathcal{I}_h^{\partial}}\int_e [\boldsymbol{u_g}q\phi] - \sum_{T\in\mathcal{T}_h}\int_T q\boldsymbol{u_g}\cdot\nabla\phi \\
&= \sum_{e\in\mathcal{I}_h\cup\mathcal{I}_h^{\partial}}\int_e \{\boldsymbol{u_g}q\}\cdot[\phi] + \sum_{e\in\mathcal{I}_h}\int_e [\boldsymbol{u_g}q]\{\phi\} + \sum_{e\in\mathcal{I}_h^{\partial}}\int_e \underbrace{\boldsymbol{u_g}\cdot\boldsymbol{n_e}}_{0} q\phi \\
&\quad - \sum_{T\in\mathcal{T}_h}\int_T q\boldsymbol{u_g}\cdot\nabla\phi \\
&= \sum_{e\in\mathcal{I}_h}\int_e \hat{\boldsymbol{u}}_e(q)\cdot[\phi] - \sum_{T\in\mathcal{T}_h}\int_T q\boldsymbol{u_g}\cdot\nabla\phi =: b(\psi,q,\phi),
\end{aligned} \tag{B.24}$$

where

$$\hat{\boldsymbol{u}}_e = \begin{cases} q|_{T_{e^+}}\boldsymbol{u_g} & \text{if } \boldsymbol{u_g}\cdot\boldsymbol{n}_e^+ \geq 0 \\ q|_{T_{e^-}}\boldsymbol{u_g} & \text{if } \boldsymbol{u_g}\cdot\boldsymbol{n}_e^+ < 0 \end{cases}. \tag{B.25}$$

To deal with the discontinuous velocity, perform averaging over the intersections and use a Raviart-Thomas projection [47] so that $\nabla\cdot\boldsymbol{u_g}$ exists, this is to combat stability issues due to the discontinuity of the velocity. Define the bilinear forms

$$\begin{aligned}
a_1(\psi,\phi) &= \sum_{T\in\mathcal{T}_h}\int_T \nabla\psi\cdot\nabla\phi - \sum_{e\in\mathcal{I}_h\cup\mathcal{I}_h^{\partial}}\int_e [\phi]\cdot\{\nabla\psi\} - \sum_{e\in\mathcal{I}_h}\int_e [\nabla\psi]\{\phi\} \\
&\quad - \sum_{e\in\mathcal{I}_h^{\partial}}\int_e \nabla\psi\cdot\boldsymbol{n}_e\phi + P^{\sigma,\alpha}(\psi,\phi) + S^{\epsilon}(\psi,\phi),
\end{aligned} \tag{B.26}$$

$$a_2(\psi,\phi) = \sum_{T\in\mathcal{T}_h}\int_T \psi\phi. \tag{B.27}$$

Now, the problem can be written as; given ψ_j^n for each $j \in \{0, ..., \mathcal{N}\}$ find $\psi_j^{n+1} \in V_{q_h} \subset V_q$ such that

$$\begin{aligned} -a_1(\psi_j^{n+1}, \phi) + \lambda_j a_2(\psi_{j+1}^{n+1} - \psi_{j-1}^{n+1}, \phi) + \mu_j a_2(\psi_{j+1}^{n+1} - 2\psi_j^{n+1} + \psi_{j-1}^{n+1}, \phi) \\ +\theta_m \kappa a_1(\psi_{j+1}^{n+1} - 2\psi_j^{n+1} + \psi_{j-1}^{n+1}, \phi) = l_j^n(\phi) \text{ for all } \phi \in V_{q_h}, \end{aligned} \tag{B.28}$$

where the right hand side is given by the linear form

$$\begin{aligned} l_j^n(\phi) = &- a_1(\psi_j^n, \phi) + \lambda_j a_2(\psi_{j+1}^n - \psi_{j-1}^n, \phi) + \mu_j a_2(\psi_{j+1}^n - 2\psi_j^n + \psi_{j-1}^n, \phi) \\ &- \tau b(\psi_j^n, q_j^n, \phi) - (1 - \theta_m)\kappa a_1(\psi_{j+1}^n - 2\psi_j^n + \psi_{j-1}^n, \phi). \end{aligned} \tag{B.29}$$

The potential vorticity can be recovered each timestep by solving

$$\begin{aligned} a_2(q_j^{n+1}, \phi) = -a_1(\psi_j^{n+1}, \phi) + \lambda_j a_2(\psi_{j+1}^{n+1} - \psi_{j-1}^{n+1}, \phi) + \mu_j a_2(\psi_{j+1}^{n+1} - 2\psi_j^{n+1} + \psi_{j-1}^{n+1}, \phi) \\ +\theta_m \kappa a_1(\psi_{j+1}^{n+1} - 2\psi_j^{n+1} + \psi_{j-1}^{n+1}, \phi) \text{ for all } \phi \in V_{q_h}. \end{aligned} \tag{B.30}$$

The finite element decomposition into basis functions $\{\varphi_i\}_i$ is demonstrated using a Lagrange element with nodal variables

$$\boldsymbol{B} = \left\{ N_1(p) = p(0,0), N_2(p) = p(1,0), N_3(p) = p(0,1) : p \in P^1 \right\}, \tag{B.31}$$

that is point evaluations at the vertices. The monomial basis for P^1 is $\{1, x, y\}$, so any function u on the triangular element can be approximated by a linear function

$$u(x, y) = \alpha_1 + \alpha_2 x + \alpha_3 y. \tag{B.32}$$

In particular, the i^{th} basis function for the Lagrange triangle can be written as

$$\varphi_i(x, y) = \alpha_1^i + \alpha_2^i x + \alpha_3^i y. \tag{B.33}$$

Considering the reference triangle $\hat{K}$ as in Figure (B.1) with vertices labeled anti-clockwise as in basis $\boldsymbol{B}$, write the values of a function u at each vertex

$$\begin{aligned} u_1 &= u(0,0) = \alpha_1 \\ u_2 &= u(1,0) = \alpha_1 + \alpha_2 \\ u_3 &= u(0,1) = \alpha_1 + \alpha_3 \end{aligned} \tag{B.34}$$

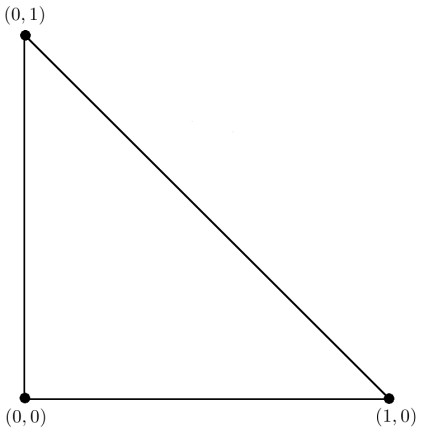

Figure B.1: Lagrange Element

which in matrix form is

$$\boldsymbol{u} = M\boldsymbol{\alpha} \tag{B.35}$$

where $\boldsymbol{u} = (u_1, u_2, u_3)$ and $\boldsymbol{\alpha} = (\alpha_1, \alpha_2, \alpha_3)$ and

$$M = \begin{bmatrix} 1 & 0 & 0 \\ 1 & 1 & 0 \\ 1 & 0 & 1 \end{bmatrix}. \tag{B.36}$$

Inverting the matrix M,

$$M^{-1} = \begin{bmatrix} 1 & 0 & 0 \\ -1 & 1 & 0 \\ -1 & 0 & 1 \end{bmatrix}. \tag{B.37}$$

Then,

$$\boldsymbol{\alpha} = M^{-1}\boldsymbol{u} \tag{B.38}$$

and from this,

$$u(x, y) = u_1(1 - x - y) + u_2 x + u_3 y, \tag{B.39}$$

so the nodal basis $\boldsymbol{\Phi} = \{\varphi_1, \varphi_2, \varphi_3\}$ is given by

$$\begin{aligned} \varphi_1(x, y) &= 1 - x - y \\ \varphi_2(x, y) &= x \\ \varphi_3(x, y) &= y. \end{aligned} \tag{B.40}$$

Observe that, this nodal basis $\boldsymbol{\Phi}$ of P^1 is the dual basis to the N_i and satisfies the

desired condition

$$N_i(\varphi_j) = \delta_{i,j} = \begin{cases} 1 & \text{if } i = j \\ 0 & \text{otherwise.} \end{cases} \tag{B.41}$$

In order to work on the reference element, introduce the mapping from the reference element $\hat{T}$ to an element $T \in \mathcal{T}_h$ given by

$$F(\hat{\boldsymbol{x}}) = \begin{bmatrix} x_2 - x_1 & x_3 - x_1 \\ y_2 - y_1 & y_3 - y_1 \end{bmatrix} \begin{bmatrix} \hat{x} \\ \hat{y} \end{bmatrix} + \begin{bmatrix} x_1 \\ y_1 \end{bmatrix}, \tag{B.42}$$

where $\{(x_1, y_1), (x_2, y_2), (x_3, y_3)\}$ are the coordinates of the vertices of the element T. One can express any function $v \in V_{q_h}$ as a linear combination of basis functions, in particular for a solution ψ_j^n of (B.28),

$$\psi_j^n = \sum_{k=1}^{P} c_k(j, n)\varphi_k \tag{B.43}$$

where the vector $(c_1, c_2, c_3, ..., c_P) \in \mathbb{R}^P$ is unique and $P = dim(V_{q_h})$. Then the problem is equivalent to

$$\begin{aligned} \sum_{k=1}^{P} -c_k(j, n+1)a_1(\varphi_k, \varphi_l) \\ +\lambda_j(c_k(j+1, n+1) - c_k(j-1, n+1))a_2(\varphi_k, \varphi_l) \\ +\mu_j(c_k(j+1, n+1) - 2c_k(j, n+1) + c_k(j-1, n+1))a_2(\varphi_k, \varphi_l) \\ +\theta_m\kappa(c_k(j+1, n+1) - 2c_k(j, n+1) + c_k(j-1, n+1))a_1(\varphi_k, \varphi_l) \\ = l_j^n(\varphi_l). \end{aligned} \tag{B.44}$$

Writing the degrees of freedom in a vector

$$\boldsymbol{c}_j^n = \begin{bmatrix} c_1(j, n) \\ c_2(j, n) \\ c_3(j, n) \\ \vdots \\ c_P(j, n) \end{bmatrix}, \tag{B.45}$$

defining the finite element matrix

$$A_i = \begin{bmatrix} a_i(\varphi_1,\varphi_1) & \dots & a_i(\varphi_P,\varphi_1) \\ \vdots & \ddots & \vdots \\ a_i(\varphi_1,\varphi_P) & \dots & a_i(\varphi_P,\varphi_P) \end{bmatrix}, \quad F_j^n = \begin{bmatrix} l_j^n(\varphi_1) \\ \vdots \\ l_j^n(\varphi_P) \end{bmatrix} \tag{B.46}$$

and rearranging to get,

$$\begin{aligned} &(\theta_m\kappa A_1 + (\lambda_j+\mu_j)A_2)\boldsymbol{c}_{j+1}^{n+1} - ((1+2\theta_m\kappa)A_1 + 2\mu_j A_2)\boldsymbol{c}_j^{n+1} \\ &+ (\theta_m\kappa A_1 + (\mu_j-\lambda_j)A_2)\boldsymbol{c}_{j-1}^{n+1} = F_j^n. \end{aligned} \tag{B.47}$$

Finally, the problem is given in matrix form as

$$\begin{bmatrix} L_0^0 & L_1^+ & 0 & 0 & \cdots & 0 \\ L_0^- & L_1^0 & L_2^+ & 0 & \cdots & 0 \\ 0 & \ddots & \ddots & \ddots & \vdots & \vdots \\ \vdots & \cdots & 0 & L_{\mathcal{N}-2}^- & L_{\mathcal{N}-1}^0 & L_{\mathcal{N}}^+ \\ 0 & \cdots & 0 & 0 & L_{\mathcal{N}-1}^- & L_{\mathcal{N}}^0 \end{bmatrix} \begin{bmatrix} \boldsymbol{c}_0^{n+1} \\ \boldsymbol{c}_1^{n+1} \\ \vdots \\ \boldsymbol{c}_{\mathcal{N}-1}^{n+1} \\ \boldsymbol{c}_{\mathcal{N}}^{n+1} \end{bmatrix} = \begin{bmatrix} F_0^{n+1} \\ F_1^{n+1} \\ \vdots \\ F_{\mathcal{N}-1}^{n+1} \\ F_{\mathcal{N}}^{n+1} \end{bmatrix} \tag{B.48}$$

with

$$\begin{aligned} L_j^+ &= (\theta_m\kappa A_1 + (\lambda_j+\mu_j)A_2) \\ L_j^0 &= -((1+2\theta_m\kappa)A_1 + 2\mu_j A_2) \\ L_j^- &= (\theta_m\kappa A_1 + (\mu_j-\lambda_j)A_2). \end{aligned} \tag{B.49}$$

A Krylov space iterative solver method is used to solve this matrix. As it is non-symmetric, one cannot guarantee convergence of a conjugate-gradient method, therefore, a bi-conjugate-gradient stabilised method, GMRES or direct method will be needed.

B.3 Third Order Runge-Kutta

A popular high order time discretisation is the third order Runge-Kutta explicit method, suppose

$$\frac{\partial q}{\partial t} = F(t,q) \tag{B.50}$$

then the method is applied as follows,

$$q^{n+1} = q^n + \frac{1}{6}\left(k_1 + 4k_2 + k_3\right), \tag{B.51}$$

where

$$k_1 = \Delta t F(t^n, q^n), \tag{B.52}$$

$$k_2 = \Delta t F\left(t^n + \Delta t/2, q^n + k_1/2\right), \tag{B.53}$$

$$k_3 = \Delta t F\left(t^n + \Delta t, q^n - k_1 + 2k_2\right), \tag{B.54}$$

and $t^n = t^0 + n\Delta t$. This is often used in fluid dynamics codes due to its stability and conservation properties and would be a good improvement on forward Euler.

Bibliography

[1] Acheson, D. *Elementary Fluid Dynamics.* Oxford University Press, 2009.

[2] Ahrens, J., Geveci, B., and Law, C. *ParaView: An End-User Tool for Large Data Visualization, Visualization Handbook.* Elsevier, 2005.

[3] Arnold, D. N. An interior penalty finite element method with discontinuous elements. *SIAM Journal on Numerical Analysis 19* (1982), 742–760.

[4] Arnold, D. N., Brezzi, F., Cockburn, B., and Marini, L. D. Unified analysis of discontinuous galerkin methods for elliptic problems. *SIAM Journal on Numerical Analysis 39*, 5 (2002), 1749–1779.

[5] Aubin, J. P. Approximation des problèmes aux limites non homogènes pour des opérateurs non linéaires. *Journal of Mathematical Analysis and Applications 30* (1970), 510–521.

[6] Augier, P., and Billant, P. Onset of secondary instabilities on the zigzag instability in stratified fluids. *JFM 682* (2011), 120–131.

[7] Augier, P., Billant, P., and Chomaz, J.-M. Spectral analysis of the transition to turbulence from a dipole in stratified fluid. *JFM 713* (2012), 86–108.

[8] Augier, P., Billant, P., and Galtier, S. Kolmogorov laws for stratified turbulence. *JFM 709* (2012), 659–670.

[9] Augier, P., and Lindborg, E. A new formulation of the spectral energy budget of the atmosphere, with application to two high-resolution general circulation models. *Journal of the Atmospheric Sciences 70*, 7 (2013), 2293–2308.

[10] Ayachit, U. *The ParaView Guide: A Parallel Visualization Application.* Kitware, 2015.

[11] Babuška, I. The finite element method with penalty. *Mathematics of Computation 27* (1973), 221–228.

[12] Babuška, I., and Zlámal, M. Nonconforming elements in the finite element method with penalty. *SIAM Journal on Numerical Analysis 10* (1973), 863–875.

[13] Balay, S., Abhyankar, S., Adams, M. F., Brown, J., Brune, P., Buschelman, K., Dalcin, L., Eijkhout, V., Gropp, W. D., Kaushik, D., Knepley, M. G., McInnes, L. C., Rupp, K., Smith, B. F., Zampini, S., Zhang, H., and Zhang, H. PETSc users manual. Tech. Rep. ANL-95/11 - Revision 3.7, Argonne National Laboratory, 2016.

[14] Balay, S., Abhyankar, S., Adams, M. F., Brown, J., Brune, P., Buschelman, K., Dalcin, L., Eijkhout, V., Gropp, W. D., Kaushik, D., Knepley, M. G., McInnes, L. C., Rupp, K., Smith, B. F., Zampini, S., Zhang, H., and Zhang, H. PETSc Web page, 2016. http://www.mcs.anl.gov/petsc.

[15] Balay, S., Gropp, W. D., McInnes, L. C., and Smith, B. F. Efficient management of parallelism in object oriented numerical software libraries. In *Modern Software Tools in Scientific Computing* (1997), E. Arge, A. M. Bruaset, and H. P. Langtangen, Eds., Birkhäuser Press, pp. 163–202.

[16] Bastian, P., Blatt, M., Dedner, A., Engwer, C., Fahlke, J., Gräser, C., Klöfkorn, R., Nolte, M., Ohlberger, M., and Sander, O. DUNE Web page, 2011. http://www.dune-project.org.

[17] Bastian, P., Blatt, M., Dedner, A., Engwer, C., Klöfkorn, R., Kornhuber, R., Ohlberger, M., and Sander, O. A Generic Grid Interface for Parallel and Adaptive Scientific Computing. Part II: Implementation and Tests in DUNE. *Computing 82*, 2–3 (2008), 121–138.

[18] Bastian, P., Blatt, M., Dedner, A., Engwer, C., Klöfkorn, R., Ohlberger, M., and Sander, O. A Generic Grid Interface for Parallel and Adaptive Scientific Computing. Part I: Abstract Framework. *Computing 82*, 2–3 (2008), 103–119.

[19] Bergeron, T. *Über die dreidimensional verknüpfende Wetteranalyse*. Geofys. Publikationer, 1928.

[20] Bernsen, E., Bokhove, O., and can der Vegt, J. J. W. A (dis)continuous finite element model for generalized 2D vorticity dynamics. *Journal of Computational Physics 211* (2006), 719–747.

[21] Billant, P. Zigzag instability of vortex pairs in stratified and rotating fluids. part 1. general stability equations. *JFM 660* (2010), 354–395.

[22] Billant, P. Zigzag instability of vortex pairs in stratified and rotating fluids. part 2. analytical and numerical analyses. *JFM 660* (2010), 396–429.

[23] Billant, P., and Chomaz, J.-M. Experimental evidence for a new instability of a vertical columnar vortex pair in a strongly stratified fluid. *JFM 418* (2000), 167–188.

[24] Billant, P., and Chomaz, J.-M. Theoretical analysis of the zigzag instability of a vertical columnar vortex pair in a strongly stratified fluid. *JFM 419* (2000), 29–63.

[25] Billant, P., and Chomaz, J.-M. Three-dimensional stability of a vertical columnar vortex pair in a stratified fluid. *JFM 419* (2000), 65–91.

[26] Billant, P., and Chomaz, J.-M. Self-similarity of strongly stratified inviscid flows. *Physics of Fluids 13*, 1645 (2001).

[27] Billant, P., Chomaz, J.-M., and Otheguy, P. Elliptic and zigzag instabilities on co-rotating vertical vortices in a stratified fluid. *JFM 553* (2006), 253–272.

[28] Blatt, M., and Bastian, P. The iterative solver template library. In *Applied Parallel Computing. State of the Art in Scientific Computing* (2007), B. Kågström, E. Elmroth, J. Dongarra, and J. Waśniewski, Eds., vol. 4699 of *Lecture Notes in Computer Science*, Springer, pp. 666–675.

[29] Blatt, M., and Bastian, P. On the generic parallelisation of iterative solvers for the finite element method. *Int. J. Comput. Sci. Engrg. 4*, 1 (2008), 56–69.

[30] Brenner, S., and Scott, R. *The Mathematical Theory of Finite Element Methods*. Texts in Applied Mathematics. Springer New York, 2007.

[31] Brethouwer, G., Billant, P., Lindborg, E., and Chomaz, J.-M. Scaling analysis and simulation of strongly stratified turbulent flows. *J. Fluid Mech. 585* (2007), 343–368.

[32] Bethouwer, G., and Lindborg, E. Vertical dispersion by stratified turbulence. *JFM 614* (2008), 303–314.

[33] Bruggemann, N., and Eden, C. Routes to dissipation under different dynamical conditions. *Journal of Physical Oceanography 45* (2015), 2149–2168.

[34] Charney, J. G. Some remaining problems in numerical weather prediction. *Advances in numerical weather prediction* (1966), 61–70.

[35] Cho, J. Y. N., and Lindborg, E. Horizontal velocity structure functions in the upper troposphere and lower stratosphere 1. Observations. *Journal of Geophysical Research 106* (2001), 10223–10232.

[36] Chynoweth, S., and Sewell, M. J. Dual variables in semigeostrophic theory. *Proceedings of the Royal Society of London, Series A, Mathematical and Physical Sciences 424* (1989), 155–186.

[37] Cockburn, B., and Shu, C.-W. Rungekutta discontinuous galerkin methods for convection-dominated problems. *Journal of Scientific Computing 16*, 3 (2001), 173–261.

[38] Cullen, M. J. P., and Purser, R. J. An extended lagrangian theory of semi-geostrophic frontogenesis. *Journal of the Atmospheric Sciences 41*, 9 (1984), 1477–1497.

[39] Cushman-Roisin, B., and Beckers, J.-M. *Introduction to Geophysical Fluid Dynamics: Physical and Numerical Aspects.* Academic Press, 2009.

[40] Davidson, P. *Turbulence: An Introduction for Scientists and Engineers.* Oxford University Press, 2004.

[41] Dedner, A., Klöfkorn, R., Nolte, M., and Ohlberger, M. A Generic Interface for Parallel and Adaptive Scientific Computing: Abstraction Principles and the DUNE-FEM Module. *Computing 90*, 3–4 (2010), 165–196.

[42] Dedner, A., Klöfkorn, R., Nolte, M., and Ohlberger, M. DUNE-FEM Web page, 2011. http://dune.mathematik.uni-freiburg.de.

[43] Deloncle, A., Billant, P., and Chomaz, J.-M. Nonlinear evolution of the zigzag instability in stratified fluids: a shortcut on the route to dissipation. *JFM 599* (2008), 229–239.

[44] Eady, E. T. Long waves and cyclone waves. *Tellus 1*, 3 (1949), 33–52.

[45] Edelmann, W. On the behaviour of disturbances in a baroclinic channel. Summary Rep. No. 2, Research in Objective Weather Forecasting, Part F. Contract AF61 (052)-373. *Deutscher Wetterdienst, Offenbach* (1963).

[46] Elliott, W. P., Brown, H. A., and Baer, L. *A synoptic study of horizontal deformation.* Texas A & M University, Department of Oceanography, 1956.

[47] Ern, A., Nicaise, S., and Vohralik, M. An accurate H(div) flux reconstruction for discontinuous Galerkin approximations of elliptic problems. *Comptes Rendus Mathematique 345* (2007), 709–712.

[48] Evans, L. *Partial Differential Equations.* Graduate studies in mathematics. American Mathematical Society, 1998.

[49] Fornberg, B. Generation of finite difference formulas on arbitrarily spaced grids. *Mathematics of Computation 51*, 184 (1988), 699–706.

[50] Foster, E. *Finite Elements for the Quasi-Geostrophic Equations of the Ocean.* PhD thesis, Virginia Polytechnic Institute and State University, 2013.

[51] Foster, E., Iliescu, T., and Wang, Z. A finite element discretisation of the streamfunction formulation of the stationary quasi-geostrophic equations of the ocean. *Comput. Methods Appl. Mech. Engrg. 261–262* (2012), 105–117.

[52] Frisch, U. *Turbulence: The legacy of A. N. Kolmogorov.* Cambridge University Press, 1995.

[53] Gledzer, A. E., Gledzer, E. B., Khapaev, A. A., and Chkhetiani, O. G. Effect of three-dimensional structures on the dynamics of turbulence in thin layers of fluid in a laboratory experiment. *Atmospheric and Oceanic Physics 49* (2013), 187–200.

[54] Gupta, K. K., and Meek, J. L. A brief history of the beginning of the finite element method. *International Journal for Numerical Methods in Engineering 39* (1996), 3761–3774.

[55] Herring, J., and Metais, O. Numerical experiments in forced stably stratified turbulence. *JFM 202* (1989), 97–115.

[56] Holland, W. R. The role of mesoscale eddies in the general circulation of the ocean - numerical experiments using a wind-driven quasi-geostrophic model. *Journal of Physical Oceanography 8* (1978), 363–392.

[57] Holland, W. R., and Lin, L. B. On the origin of mesoscale eddies and their contribution to the general circulation of the ocean. I. a preliminary numerical experiment. *Journal of Physical Oceanography 5* (1975), 642–657.

[58] Holt, M. W. Semigeostrophic moist frontogenesis in a lagrangian model. *Dynamics of Atmospheres and Oceans 14* (1990), 463–481.

[59] Holton, J. R. *An Introduction to Dynamic Meteorology*, 4th ed. Elsevier Academic Press, 2004.

[60] Hoskins, B. J. The mathematical theory of frontogenesis. *Annual Review of Fluid Mechanics 14* (1982), 131–151.

[61] Hoskins, B. J., and Bretherton, F. P. Atmospheric frontogenesis models: Mathematical formulation and solution. *Journal of the Atmospheric Sciences 29* (1972), 11–37.

[62] Houghton, E. L., and Carpenter, P. W. *Aerodynamics for Engineering Students*, 5th ed. Butterworth-Heinemann, 2003.

[63] Iliescu, E. F. T., and Wells, D. A two level finite element discretisation of the streamfunction formulation of the stationary quasi-geostrophic equations of the ocean. *Computers and Mathematics with Applications. 66* (2012), 1261–1271.

[64] Jacobson, M. Z. *Fundamentals of Atmospheric Modeling*, 2nd ed. Cambridge University Press, 2005.

[65] Julien, K., Peterson, M. R., and Weiss, J. B. Vortex cores, strain cells, and filaments in quasigeostrophic turbulence. *Physics of Fluids 18*, 026601 (2006), 1–11.

[66] Kerr, R., De Santi, F., Tordella, D., and Parmar, A. Stratified zig-zags on vortex pairs using vertically shifted perturbations. In *accepted XXIII ICTAM, Beijing, China, 19-24 August* (2012).

[67] Kerr, R. M. Is there a 2d cascade in 3d convection? *Contemp. Math. 283* (2001).

[68] Kerr, R. M. Swirling, turbulent vortex rings formed from a chain reaction of reconnection events. *Physics of Fluids 25*, 065101 (2013).

[69] Kerr, R. M., and King, G. P. Evidence for a mid-latitude, mesoscale downscale energy cascade from the marine boundary layer. (Unpublished), 2009.

[70] Kerr, R. M., Meneguzzi, M., and Gotoh, T. An inertial range crossover in structure functions. *Physics of Fluids 13*, 7 (2001), 1985–1994.

[71] Kolmogorov, A. N. Dissipation of energy in locally isotropic turbulence. *Proc. Roy. Soc. London A 434* (1991), 15–17. (Original 1941).

[72] Kolmogorov, A. N. The local structure of turbulence in incompressible viscous fluid for very large reynolds number (reprinted 1991). *Proc. Roy. Soc. London A 434* (1991), 9–13. (Original 1941).

[73] Kraichnan, R. H. Inertial ranges in two-dimensional turbulence. *Physics of Fluids 10* (1967), 1417–1423.

[74] Kubatko, E. J., Dawson, C., and Westerink, J. J. Time step restrictions for Runge-Kutta discontinuous Galerkin methods on triangular grids. *Journal of Computational Physics 227*, 23 (2008), 9697 – 9710.

[75] Leweke, T., Le Dizès, S., and Williamson, C. H. Dynamics and instabilities of vortex pairs. *Annual Review of Fluid Mechanics 48* (2016), 507–541.

[76] Lindborg, E. Can the atmospheric kinetic energy spectrum be explained by two-dimensional turbulence? *Journal of Fluid Mechanics 388* (1999), 259–288.

[77] Lindborg, E. The energy cascade in a strongly stratified fluid. *JFM 550* (2006), 207–242.

[78] Lindborg, E., and Bretthouwer, G. Stratified turbulence forced in rotational and divergent modes. *JFM 586* (2007), 83–108.

[79] Lindborg, E., and Cho, J. Horizontal velocity structure functions in the upper troposphere and lower stratosphere 2. Theoretical considerations. *Journal of Geophysical Research 106* (2001), 10233–10241.

[80] Lions, J.-L. Problèmes aux limites non homogènes à donées irrégulières: Une méthode d'approximation. *Numerical Analysis of Partial Differential*

Equations (C.I.M.E. 2 Ciclo, Ispra, 1967), Edizioni Cremonese, Rome (1968), 283–292.

[81] Lundgren, T. Strained spiral vortex model for turbulent fine structure. *The Physics of Fluids 25*, 12 (1982), 2193–2203.

[82] Lutgens, F. K., Tarbuck, E. J., and Tasa, D. *The Atmosphere: An Introduction to Meteorology*, 12th ed. Pearson Education, 2013.

[83] Martinsen-Burrell, N., Julien, K., Peterson, M. R., and Weiss, J. B. Merger and alignment in a reduced model for three-dimensional quasi-geostrophic ellipsoidal vortices. *Physics of Fluids 18*, 057101 (2006), 1–14.

[84] McWilliams, J. C. A note on a consistent quasigeostrophic model in a multiply connected domain. *Dynamics of Atmospheres and Oceans 1* (1977), 427–441.

[85] McWilliams, J. C. The emergence of isolated coherent vortices in turbulent flow. *Journal of Fluid Mechanics 146* (1984), 21–43.

[86] McWilliams, J. C. *Fundamentals of Geophysical Fluid Dynamics*. Cambridge University Press, 2006.

[87] McWilliams, J. C., and Chow, J. H. S. Equilibrium geostrophic turbulence i: A reference solution in a β-plane channel. *Journal of Physical Oceanography 11* (1981), 921–949.

[88] McWilliams, J. C., and Flierl, G. R. On the evolution of isolated, nonlinear vortices. *Journal of Physical Oceanography 9*, 6 (1979), 1155–1182.

[89] McWilliams, J. C., Holland, W. R., and Chow, J. H. S. A description of numerical antarctic circumpolar currents. *Dynamics of Atmospheres and Oceans 2* (1978), 213–291.

[90] McWilliams, J. C., Weiss, J. B., and Yavneh, I. The vortices of homogeneous geostrophic turbulence. *Journal of Fluid Mechanics 401* (1999), 1–26.

[91] Meleshko, V., Konstantinov, M. Y., Gurzhi, A., and Konovaljuk, T. Advection of a vortex pair atmosphere in a velocity field of point vortices. *Physics of Fluids A: Fluid Dynamics 4*, 12 (1992), 2779–2797.

[92] Metais, O., and Herring, J. Numerical simulations of freely evolving turbulence in stably stratified fluids. *JFM 202* (1989), 117–148.

[93] Morss, R. E., Snyder, C., and Rotunno, R. Spectra, spatial scales, and predictability in a quasigeostrophic model. *Journal of the Atmospheric Sciences 66*, 10 (2009), 3115–3130.

[94] NASA. Visible Earth Website. https://www.visibleearth.nasa.gov, [Accessed: 27 February 2018].

[95] Nastrom, G. D., and Gage, K. S. A climatology of atmospheric wavenumber spectra of wind and temperature observed by commercial aircraft. *Journal of the Atmospheric Sciences 42* (1985), 950–960.

[96] Nitsche, J. A. Über ein Variationsprinzip zur Lösung Dirichlet-Problemen bei Verwendung von Teilräumen, die keinen Randbedingungen unteworfen sind. *Abhandlungen aus dem Mathematischen Seminar der Universität Hamburg 36* (1971), 9–15.

[97] Palmer, T., Shutts, G., Hagedorn, R., Doblas-Reyes, F., Jung, T., and Leutbecher, M. Representing model uncertainty in weather and climate prediction. *Annu. Rev. Earth Planet. Sci. 33* (2005), 163–193.

[98] Palmer, T. N. A nonlinear dynamical perspective on model error: A proposal for non-local stochastic-dynamic parametrization in weather and climate prediction models. *Quarterly Journal of the Royal Meteorological Society 127*, 572 (2001), 279–304.

[99] Pedlosky, J. *Geophysical Fluid Dynamics*, 2nd ed. Springer Verlag, 1987.

[100] Pope, S. *Turbulent Flows*. Cambridge University Press, 2000.

[101] Provenzale, A. Transport by coherent barotropic vortices. *Annual Review of Fluid Mechanics 31* (1999), 55–93.

[102] Provost, C. L., Bernier, C., and BLayo, E. A comparison of two numerical methods for integrating a quasi-geostrophic multilayer model of ocean circulations: Finite element and finite difference methods. *Journal of Computational Physics 110* (1994), 341–359.

[103] Puel, M., and Vasseur, A. F. Global weak solutions to in inviscid 3D quasi-geostrophic equation. *Communications in Mathematical Physics 339* (2015), 1063–1082.

[104] Riley, J., and deBruynKops, S. Dynamics of turbulence strongly influenced by buoyancy. *Physics of Fluids 15*, 2047 (2003).

[105] Rivière, B. *Discontinuous Galerkin Methods for Solving Elliptic and Parabolic Equations*. Society for Industrial and Applied Mathematics, 2008.

[106] Rognes, M. E., Kirby, R. C., and Logg, A. Efficient assembly of h(div) and h(curl) conforming finite elements. *SIAM Journal on Scientific Computing 31*, 6 (2009), 4130–4151.

[107] Roux, D. L., and Pouliot, B. Analysis of numerically induced oscillations in two-dimensional finite element shallow water models part ii: Free planetary waves. *SIAM J. Sci. Comput. 30* (2008), 1971–1991.

[108] Saffman, P. The approach of a vortex pair to a plane surface in inviscid fluid. *Journal of Fluid Mechanics 92*, 3 (1979), 497–503.

[109] Sanders, F. Investigation of the structure and dynamics of an intense surface frontal zone. *Journal of Meteorology 12* (1955), 542–552.

[110] Shutts, G. A kinetic energy backscatter algorithm for use in ensemble prediction systems. *Quarterly Journal of the Royal Meteorological Society 131*, 612 (2005), 3079–3102.

[111] Snyder, C., Hamill, T. M., and Trier, S. B. Linear evolution of error covariances in a quasigeostrophic model. *Monthly weather review 131*, 1 (2003), 189–205.

[112] Stone, P. H. Frontogenesis by horizontal wind deformation fields. *Journal of the Atmospheric Sciences 23*, 5 (1966), 455–465.

[113] Stull, R. *Meteorology for Scientists and Engineers*, 3rd ed. Brooks/Cole, 2011. Creative Commons Attribution-NonCommercial-ShareAlike 4.0 International License, https://creativecommons.org/licenses/by-nc-sa/4.0/.

[114] Takahashi, Y. O., Hamilton, K., and Ohfuchi, W. Explicit global simulation of the mesoscale spectrum of atmospheric motions. *Geophysical Research Letters 33*, 12 (2006), 1–4. L12812.

[115] Tritton, D. J. *Physical Fluid Dynamics*, 2nd ed. Oxford University Press, 2011.

[116] Trudinger, N. S. *Elliptic partial differential equations of second order*, third ed. Springer, 1998.

[117] Tung, K. K., and Orlando, W. W. The k^{-3} and $k^{-5/3}$ energy spectrum of atmospheric turbulence: Quasigeostrophic two-level model simulation. *Journal of the Atmospheric Sciences 60* (2002), 824–835.

[118] Turner, M. J., Clough, R. W., Martin, H. C., and Topp, L. T. Stiffness and deflection analysis of complex structures. *Journal of the Aeronautical Sciences 25* (1956), 805–823.

[119] Vallis, G. *Atmospheric and Oceanic Fluid Dynamics: Fundamentals and Large-scale Circulation*. Cambridge University Press, 2006.

[120] van Rees, W., Hussain, F., and Koumoutsakos, P. Vortex tube reconnection at Re = 10^4. *Physics of Fluids 24*, 075105 (2012).

[121] van Rees, W. M., Novati, G., and Koumoutsakos, P. Self-propulsion of a counter-rotating cylinder pair in a viscous fluid. *Physics of Fluids 27*, 6 (2015), 063102.

[122] Venaille, A., Nadeau, L.-P., and Vallis, G. Ribbon turbulence. *Physics of Fluids 26*, 12 (2014), –.

[123] Visram, A. R., Cotter, C. J., and Cullen, M. J. P. A framework for evaluating model error using asymptotic convergence in the eady model. *Quarterly Journal of the Royal Meteorological Society 140*, 682 (2014), 1629–1639.

[124] von Hardenberg, J., McWilliams, J. C., Provenzale, A., Shchepetkin, A., and Weiss, J. B. Vortex merging in quasi-geostrophic flows. *Journal of Fluid Mechanics 412* (2000), 331–353.

[125] Waite, M., and Bartello, P. Stratified turbulence generated by internal gravity waves. *JFM 546* (2006), 313–339.

[126] Waite, M., and Smolarkiewicz, P. Instability and breakdown of a vertical vortex pair in a strongly stratified fluid. *JFM 606* (2008), 239–273.

[127] Wendt, J., Anderson, J., and for Fluid Dynamics, V. K. I. *Computational fluid dynamics: an introduction*. Von Karman Institute book. Springer, 1996.

[128] Williams, R. T. Atmospheric frontogenesis : A numerical experiment. *Journal of the Atmospheric Sciences 24* (1967), 627–641.

[129] Williams, R. T. Quasi-geostrophic versus non-geostrophic frontogenesis. *Journal of the Atmospheric Sciences 29*, 1 (1972), 3–10.

[130] Williams, R. T., and Plotkin, J. Quasi-geostrophic frontogenesis. *Journal of the Atmospheric Sciences 25* (1968), 201–206.